CEREBELLAR AND SENSORY CONTRIBUTIONS TO THE OPTOMOTOR RESPONSE IN LARVAL ZEBRAFISH

ANDREAS M. KIST

Dissertation zur Erlangung des akademischen Grades
des Doktors der Naturwissenschaften (Dr. rer. nat.)

an der Fakultät für Biologie der
Ludwig-Maximilians-Universität München

München, Februar 2019

It's not a question, but a lesson learned in time.
It's something unpredictable, but in the end it's right.

— Billie Joe Armstrong

Für meine Pinzoma.

EIDESSTATTLICHE ERKLÄRUNG

Ich versichere hiermit an Eides statt, dass die vorgelegte Dissertation von mir selbständig und ohne unerlaubte Hilfe angefertigt ist.

München, 28. Februar 2019

Andreas M. Kist

ABSTRACT

A main question in systems neuroscience is how sensory information is processed to yield a behavior best suited for the current situation. In this thesis, we use the larval zebrafish model system, an emerging model organism in neuroscience due to its optical and genetic accessibility allowing non-invasive tracking of neural activity.

We first shed light on the feature space that drives swimming behavior of larval zebrafish. The optomotor response, an innate reflex to directional whole-field motion, is widely used across animal species to induce swimming behavior, however, the properties of the visual stimulus are not yet clearly defined. Here, we show with reverse correlation and thorough parameter evaluation that the optomotor response is best elicited by global whole-field motion together with a local light-dark transition. We further find active units across the brain that react specifically to this stimulus. We can also show that a generalized linear model is capable of modeling the observed behavior better than chance.

We next were interested how visual sensory information and behavior is encoded in Purkinje cells, a principal cell type in the cerebellum important in sensorimotor control. We show that Purkinje cells in larval zebrafish exhibit the same hallmarks as in mammals, such as planar dendritic trees. Interestingly, we observed that Purkinje cells show a different signal compartementalization compared to mammalian ones. Using two-photon calcium imaging with novel transgenic lines that we developed, we are able to show that visual information is spatially clustered across the cerebellum. With the help of electrophysiology, we could show that the inferior olive provides the sensory context for Purkinje cell activity. Granule cells seem to be the major carrier of motor-related information and provide this context homogenously across the cerebellum. When manipulating Purkinje cell activity, larval zebrafish show a longer latency to initiate swimming in an optomotor response paradigm, suggesting that Purkinje cells have an impact on motor initiation.

Finally, we characterized the *in vivo* performance of a novel far-red fluorescence protein termed mCarmine, that expresses well in larval zebrafish and outperforms an established cyan-fluorescent protein mTFP1.

In summary, we find novel aspects in the sensorimotor transformation of visual stimuli to behavior and provide new insights in how behavior is driven and how sensorimotor contexts are represented in the brain.

ZUSAMMENFASSUNG

Eine wichtige Frage in den systemischen Neurowissenschaften ist es herauszufinden, wie sensorische Informationen verarbeitet werden, um in jeder Situation die beste Verhaltensstrategie hervorzurufen. In der vorliegenden Arbeit verwenden wir die Zebrabärblingslarve - ein Modellorganismus, der in der systemischen Neurowissenschaft immer mehr Zuspruch findet. Durch ihre Transparenz ist es möglich das Innere zu mikroskopieren, ohne den Organismus zu verletzen. Weiterhin ist es durch etablierte Methoden einfach, transgene Organismen zu erzeugen.

Zuerst untersuchen wir, welche Eigenschaften visueller Stimuli Zebrabärblingslarven zum Schwimmen bringen. Diese so genannte optomotorische Antwort (*optomotor response*) ist ein angeborener Reflex, der ausgelöst wird, wenn die Zebrabärblingslarve globale, gerichtete Bewegung wahrnimmt. Wir können hier allerdings zeigen, dass die optomotorische Antwort am besten ausgelöst wird, wenn die globale Bewegungswahrnehmung mit einem lokalen hell-dunkel Übergang kombiniert wird. Zusätzlich finden wir aktive Areale im Zebrabärblingslarvengehirn, die stark mit diesem Stimulus korrelieren. Weiterhin können wir mit Hilfe eines mathematischen Modells zeigen, dass dieser Stimulus besser das Verhalten vorhersagt als rein stochastisches Schwimmen.

Um herauszufinden, wie sensorische Signale motorische Verhaltensweisen beeinflussen, haben wir Purkinje-Zellen, ein wichtiger Zelltyp des Kleinhirns, untersucht. Wir können zeigen, dass Purkinje-Zellen in der Zebrabärblingslarve ähnlich zum Säugetier planare Dendritenbäume besitzen, aber eine andere Signalkompartementalisierung haben. Mit Hilfe von Zwei-Photonen-Mikroskopie und neuen transgenen Linien sehen wir, dass sensorische Informationen im Kleinhirn räumlich organisiert sind, motorische Information aber einheitlich verfügbar ist. Mit Hilfe der Elektrophysiologie können wir zeigen, dass die untere Olive die räumliche Organisation herstellt, und Körnerzellen homogen über das Kleinhirn motorische Informationen zur Verfügung stellt. Durch die aktive Manipulation in Purkinje-Zellaktivität mit Hilfe von optogenetischen Methoden haben wir beobachtet, dass Purkinje-Zellen einen Einfluss auf die Bewegungsinitiation haben.

Zuletzt haben wir charakterisiert, wie sich ein neues Fluoreszenzprotein namens mCarmine *in vivo* verhält. Das ins tief-rote verschobene Fluoreszenzprotein lässt sich gut in Nervenzellen transgener Zebrabärblingslarven exprimieren und zeigt eine bessere Leistung als ein etabliertes cyan-fluoreszierendes Protein (mTFP1).

Zusammenfassend legen wir neue Grundsteine für das Verständnis wie die optomotorische Antwort in der Zebrabärblingslarve hervorgerufen wird, und wie sensorische und motorische Signale in Purkinje-Zellen zusammentreffen, und welchen Einfluss Purkinje-Zellen auf das Verhalten von Zebrabärblingslarven haben.

PUBLICATIONS

Fabritius, Arne, David Ng, **Andreas M. Kist**, Mutlu Erdogan, Ruben Portugues, and Oliver Griesbeck (Dec. 2018). "Imaging-Based Screening Platform Assists Protein Engineering." In: *Cell Chemical Biology* 25.12, 1554–1561.e8. DOI: 10.1016/j.chembiol.2018.08.008.

Kist, Andreas M., Laura D. Knogler, Daniil A. Markov, Tugce Yildizoglu, and Ruben Portugues (2017). "Whole-Brain Imaging Using Genetically Encoded Activity Sensors in Vertebrates." en. In: *Decoding Neural Circuit Structure and Function*. Springer, Cham, pp. 321–341. DOI: 10.1007/978-3-319-57363-2_13.

Kist, Andreas M. and Ruben Portugues (2018). "Optomotor Swimming in Larval Zebrafish Is Driven by Global Whole-Field Visual Motion and Local Light-Dark Transitions." In: *in preparation*.

Knogler, Laura D., **Andreas M. Kist**, and Ruben Portugues (Jan. 2019). "Motor Context Dominates Output from Purkinje Cell Functional Regions during Reflexive Visuomotor Behaviours." In: *eLife* 8. Ed. by Indira M. Raman, e42138. DOI: 10.7554/eLife.42138.

Štih, Vilim, Luigi Petrucco, **Andreas M. Kist**, and Ruben Portugues (Dec. 2018). "Stytra: An Open-Source, Integrated System for Stimulation, Tracking and Closed-Loop Behavioral Experiments." en. In: *bioRxiv*, p. 492553. DOI: 10.1101/492553.

CONTENTS

In this thesis you will find additional information embedded, such as hyperlinks (shown in blue) to Github repositories or multimedia files. The latter are usually linked via quick response (QR) codes. You can scan these QR codes using your phone. Here is a QR code example that brings you to my Github account:

ACRONYMS

AFs   aborization fields

AMPA α-amino-3-hydroxy-5-methyl-4-isoxazolepropionic acid

BTA   behavioral triggered average

ca8   *carbonic anhydrase 8*

CaM   calmodulin

ChR   channelrhodopsin

CFP   cyan fluorescent protein

CMTK   Computational Morphometry Toolkit

DCN   deep cerebellar nuclei neurons

DLP   digital light processing

DMD   digital micromirror device

DNA   desoxyribonucleic acid

dpf   days post fertilization

EC   eurydendroid cell

EGFP   enhanced green fluorescent protein

fps   frames per second

FRET   Förster resonance energy transfer

GECI   genetically encoded calcium indicators

GFP   green fluorescent protein

GLM   generalized linear model

IPN   interpositus nucleus

IR   infra-red

LED   light emitting diode

LiCl   Lithium chloride

LNP   linear-nonlinear-poisson

LTD   long-term depression

LTP	long-term potentiation
NA	numerical aperture
NEB	New England biolabs
NLS	nuclear localization signal
NMDA	N-methyl-D-aspartate
nMLF	medio-lateral fasciculus
NRRD	Nearly Raw Raster Data
OKR	optokinetic response
OMR	optomotor response
ORF	open reading frame
PCR	polymerase chain reaction
PI	performance index
PSF	point-spread function
ReAChR	red-activated channelrhodopsin
RGB	red, blue and green
RGCs	retinal ganglion cells
ROC	receiver operating characteristic
ROI	region of interest
SNR	signal to noise ratio
STA	spike-triggered average
STC	spike-triggered covariance
TB	terrific broth
TE	Tris-EDTA
TIFF	Tagged Image File Format
TL	Tüpfel-Longfin
TTL	transistor-transistor logic
UAS	upstream activation sequence
YFP	yellow fluorescent protein

INTRODUCTION

Understanding how the brain works is the main task in systems neuroscience. We not only know that different species have different brains or brain structures, but also that the brain between individuals in the same species is different on a micro, and yet so similiar on a macro level. Interestingly, we commonly ask *how* the brain works, rather than *why* it exists. However, the *why* seems to be important in the light of the following studies.

1.1 NEUROSCIENCE, OR WHY WE HAVE A BRAIN

Daniel Wolpert, a figure in sensorimotor control research at Cambridge University, UK, who recently moved to Columbia, gave a great TED talk about the real reason why we have brains. He mentions that the one and only reason for us having a brain is in the light of *adaptable* behavior[1]. To illustrate this, he uses the example of the sea squirt, a small aquatic organism that has a (rudimentary) brain after birth. As a larva, it swims through the water until it founds a decent spot to settle down. After attaching to the stone, it does not move anymore, because it remains on the very same spot its entire life. And because there is no more locomotion, it presumable does not need its brain anymore. This is why it digests its own brain immediately and undergoes metamorphosis (Margulis and Chapman 2009).

While behaving, we interact with our environment and we need to be able to also sense the dynamic nature of the environment. Our brain not only controls behavior, but also receives sensory input through different sensory modalities, such as the tactile, vestibular and visual senses, enabling the organism to dynamically modulate its behavior. In systems neuroscience, we use the following general schematic to illustrate this connection, from sensory information to behavior (Figure 1).

Why we have a brain.

---

1 https://www.ted.com/talks/daniel_wolpert_the_real_reason_for_brains/transcript

Figure 1: The dogma of systems neuroscience. Sensory information is processed by the brain and the most appropriate behavior is chosen and elicited.

Classical neuroscience research is often conducted in rodents, especially mice. Mice are vertebrates and mammals, and thus, have a highly similar brain structure compared to humans. However, there are also limitations using this model organism. Monitoring neural activity involves invasive preparations that may lead to unphysiological conditions. Mice brains have a huge amount of neurons, where only a small part is accessible for each experiment and animal, limiting the field of view to a very narrow area. Although the generation time of mice is rather short (around ten weeks from birth to giving birth), experiments using viral transductions can take up months. It starts with raising mice to a proper age, injection, incubation/waiting, (invasive) preparations and ends with elaborate experiments (such as electrophysiology or imaging). If mice should perform a learned task, time for training is also needed. Further, it is a nocturnal animal leading to a different metabolism and also shows no cortex folding, something visible in non-human primates and humans (del Toro et al. 2017).

Recently, the larval zebrafish has been shown to be a very useful model organism in developmental biology (Dawid 2004), but also in systems neuroscience (Ahrens et al. 2012). Because it is also a vertebrate like a mammal, the larval zebrafish shares some homologous brain structures with mammals, such as the hypothalamus or the cerebellum. For further reading regarding development and anatomy, the reader is directed to two great publications: Kimmel et al. 1995 and Müller and Wullimann 2015. Only recently, researchers were able to image for the first time the whole brain of a non-anesthetized vertebrate, i.e. larval zebrafish, during behavior in a virtual environment (Ahrens et al. 2012). With the use of genetically encoded calcium indicators (GECI) expressed in all neurons, neural activity could be determined by reading out the fluorescence of single neurons (see also review Rose et al. 2014). A major break-through in imaging neural activity was the development of very sensitive GECIs with high signal-to-noise (T.-W. Chen et al. 2013, see also following paragraphs).

1.1.1 *Larval zebrafish*

The larval zebrafish (*Danio rerio*) is a powerful model organism in systems neuroscience (Figure 2). Larval zebrafish show already a huge variety of different behaviors (see 1.1.2). They are also optical transparent, especially with the *nacre* mutation (homozygous defect of the melanophores gene *mitfa*, Lister et al. 1999). This allows anatomical and functional imaging *in vivo* using endogenously expressed fluorescent proteins or GECIs. Luckily, the zebrafish also offers easy genetic access by using the *tol2* transposase system (Asakawa et al. 2008). With this, foreign DNA can be integrated stably in the zebrafish genome by injecting a plasmid harboring a gene of interest flanked by two

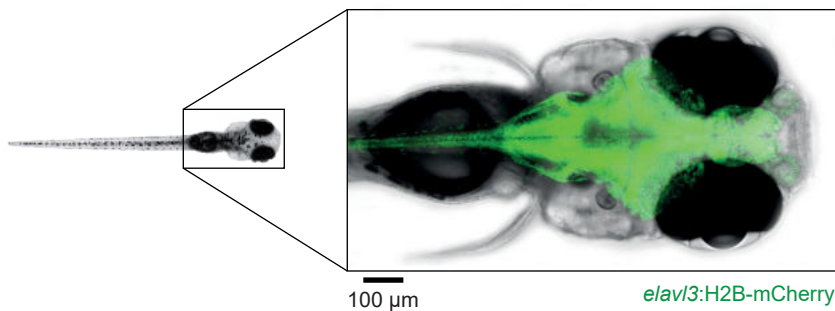100 µm   *elavl3*:H2B-mCherry

Figure 2: The larval zebrafish is a useful model organism in systems neuroscience. Larval zebrafish are around four mm long at around six to eight days post fertilization (dpf). Transgenic modified fish can be utilized to express genes, such as a fluorescent protein, in a tissue-specific manner. Here, a transgenic fish expressing mCherry in all neurons (green) is shown.

direction-selective *tol2* arms and the *tol2* transposase mRNA. The *in vivo* translated *tol2* transposase recognizes the *tol2* arms and integrates the gene of interest randomly in the genome. This is a stochastic process and can yield a various amount of integration events. Using this technique, a lot of different molecular tools could be used, such as enhancer trap screening (Scott et al. 2009), direct expression of reports under the control of tissue-specific promotors or enhancers (Matsui et al. 2014; Park et al. 2000), or the Gal4/UAS² system (Scott et al. 2007, explained and used in study III). An example is shown in Figure 2: there, we utilized the *elavl3* promotor to label all neurons using a fluorescent protein.

1.1.2 *Behavioral repertoire*

The larval zebrafish has a rich behavioral repertoire that develops very quickly (nicely reviewed by Michael B. Orger and de Polavieja 2017). Three or four days post fertilization (dpf), larvae track rotating stimuli with their eyes, a reflexive behavior called the optokinetic response (OKR) (Brockerhoff et al. 1995; D. Clark 1981; J. Easter S. S. and Nicola 1996; S. S. Easter and Nicola 1997). Around five dpf, fish swim in the direction of perceived motion to stabilize themselves in respect to the visual environment. This reflex is called the optomotor response (OMR) (D. Clark 1981; Neuhauss et al. 1999). The OMR can be elicited in freely swimming fish and also in a preparation where the head is restrained in low-melting point agarose (Portugues and Engert 2011), see also Figure 3. It is important to note, that the OMR is not restricted to larval zebrafish, but also visible in flies (Borst et al. 2010), mice (Matsuo et al. 2018; Shi et al. 2018) and other species (Dieringer et al. 1982).

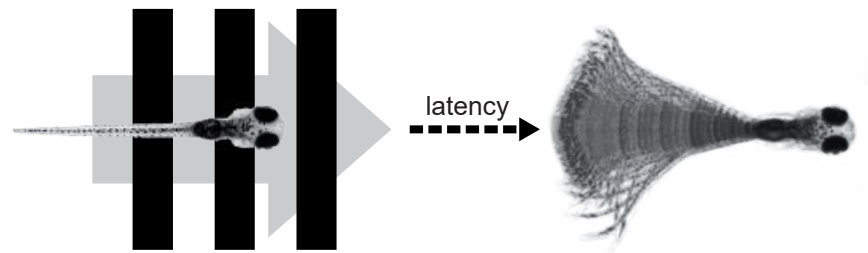2 see also study III; upstream activation sequence (UAS)

Figure 3: The innate optomotor response (OMR) is elicited in freely and head-restrained fish when presented with forward moving visual stimuli, such as a binary grating.

Behaviorally, OMR swimming has been shown to be driven by green and red cones (Michael B. Orger and Baier 2005), Fourier and non-Fourier visual motion (M. B. Orger et al. 2000), depend on the speed of fixed period square gratings (Portugues et al. 2015; Severi et al. 2014) and on the visual reafference perceived during swimming[3] (Ahrens et al. 2012; Portugues and Engert 2011).

Larval zebrafish do not swim continously, but rather swim in discrete swimming events called bouts. Bouts are tail oscillations of a given frequency, typically around 25 to 30 Hz, and can be grouped using several features into distinct behaviors (Marques et al. 2018), such as forward swims, turns and approaches.

In terms of neuronal processing, despite a number of elegant studies characterizing the projection of retinal ganglion cells (RGCs) to the ten retino-recipient areas in the zebrafish brain (Burrill and S. S. Easter 1994; Robles et al. 2014), the functional involvement of these RGC aborization fields (AFs) in the OMR remains unclear (Burgess et al. 2010; Muto et al. 2005; Nikolaou et al. 2012; Roeser and Baier 2003; Temizer et al. 2015). In addition, two studies, (Kubo et al. 2014; Naumann et al. 2016) have implicated the pretectum as an important hub where OMR sensory drive is represented.

Study I   Despite the fact that we know that very simple visual stimuli such as binary gratings are capable inducing OMR (Neuhauss et al. 1999; M. B. Orger et al. 2000), we don't know features in the visual stimulus that trigger or at least significantly contribute to the OMR. In the first *Results* part of this thesis, hereafter refered to as *Study I*, I describe the contribution of different visual features. In addition, we perform whole-brain imaging experiments and identify neural populations, downstream of retinal ganglion cells, that react to these features and may play a role in driving the OMR.

---

3 I was involved in studies focusing on the timing aspect of reafference together with Daniil Markov. Because of their own field of complexity, they are not part of this thesis.
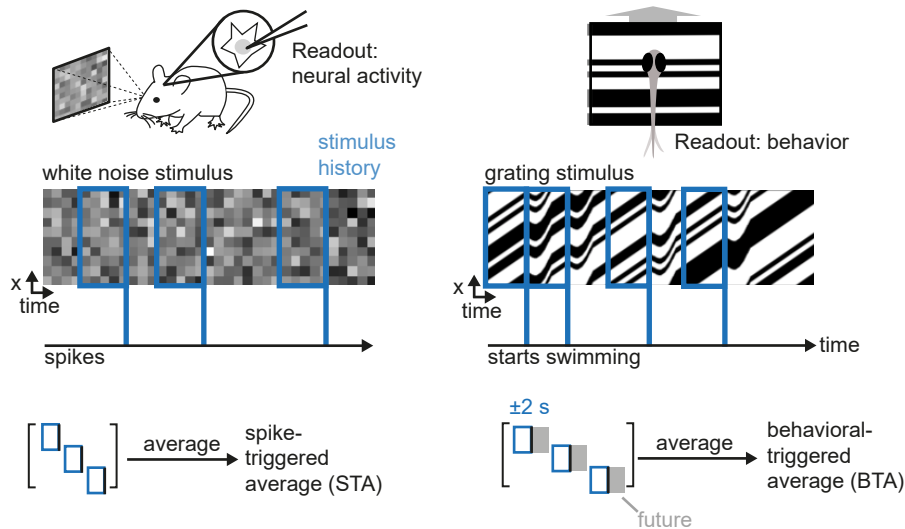
Figure 4: Spike- and behavior-triggered average. Left panel: Spikes are recorded from a neuron using patch clamp while a visual white noise stimulus is presented to the mouse's eye. Computing the spike-triggered average yields a linear filter. Right panel: Here, we record not spikes, but behavior, especially when the fish starts swimming. We present larval zebrafish with a forward-moving binary grating that provides visual feedback while the fish is swimming. We compute the behavioral-triggered average based on the swim starts.

1.1.3 *Behavior-triggered average*

A typical question in systems neuroscience is what the optimal stimulus is to make a neuron fire. One approach to answer this question for an example neuron located in the primary visual cortex of a mouse would be to present different stimuli to the eye of the mouse, and record simultaneously from that particular neuron electrophysiologically (Figure 4, left panel). After accumulating many spikes in a recording, one would go back to the stimulus presented and average all the sequences of stimuli leading to a spike (stimulus history). This method, also known as reverse correlation or spike-triggered average (STA) has been extensively used to characterize receptive fields of neurons (reviewed by Schwartz et al. 2006, see Figure 4, left panel).

The STA can be used as a linear filter in a linear-nonlinear-poisson (LNP) cascade model (Figure 5), previously used to describe firing patterns of neurons in the visual pathway (Pillow et al. 2008). To showcase the method, Figure 5 shows all steps using play data: the aim is to retrieve a (here, *a priori* set) linear filter using STA. We first designed a linear filter (weight vector) *k*. The dot product of *k* and the stimulus, for example a gaussian white noise stimulus, yields the linear filtered stimulus, or in other words a "raw firing rate". Applying a nonlinearity, such as a half-square rectification, we get an

instantaneous firing rate resembling the probability of a neuron to spike. Feeding the instantenous firing rate into a stochastic Poisson process, one yields discrete spikes. Reverse correlating the stimulus with the spikes should ideally return the linear filter *k*.

The STA, however, only describes a stimulus subspace. Especially when the nonlinearity is symmetric, the STA does not provide any visible structure. Here, spike-triggered covariance (STC) is capable of extracting these linear filters. To further show how STA and STC works, a detailed Jupyter notebook[4] is attached to this thesis. All code is available through the LNP repository on my Github account.

BTA   In study I, we use a similar approach to determine the optimal stimulus required to elicit a forward OMR swimming response in larval zebrafish (Figure 4, right panel). This approach yields a behavioral triggered average (BTA) as has been used previously to map the response of zebrafish to fluctuations in heat (Haesemeyer et al. 2015). By presenting visual stimuli consisting of black and white bars of randomly varying widths moving at different speeds in uniform forward direction, we compute the BTA (see Figure 4) and show that the optimal stimulus that will evoke the OMR consists of two features: whole-field, global motion and a caudal to rostral light to dark luminance transition crossing the larva's head, which has not been previously described in the literature.

1.1.4   *Neural activity indicators*

The classical approach and gold standard to determine neuronal activity is electrophysiology. Whole-cell or cell-attached recordings reveal detailed information about the activity of single neurons, while microelectrode arrays can be used to record from a population *in vivo*. However, using the latter method, it is hard to determine from which neurons one recorded. If the cells share a similar spiking pattern, it is hard to decode if the measured signal arises from one or multiple sources.

To overcome this invasive method and to better resolve the activity of many neurons recorded simultaneously, optical activity indicators were developed (Tsien 1981; Williams et al. 1985). In particular, many neuroscience labs have adopted functional imaging techniques that report cell activity by measuring intracellular calcium levels. Calcium levels change upon depolarization in a neuron by the release of internal calcium storages, such as the endoplasmatic reticulum, or by influx via calcium channels, such as NMDA or AMPA receptors[5]. Early attempts used organic dyes to report calcium, such as Oregon Green BAPTA-1

---

4 A Jupyter notebook is a web-based platform to execute Python programming code with rich-text annotations and inline plots.

5 The receptors are named according to their agonists: N-methyl-D-aspartate (NMDA) and α-amino-3-hydroxy-5-methyl-4-isoxazolepropionic acid (AMPA)
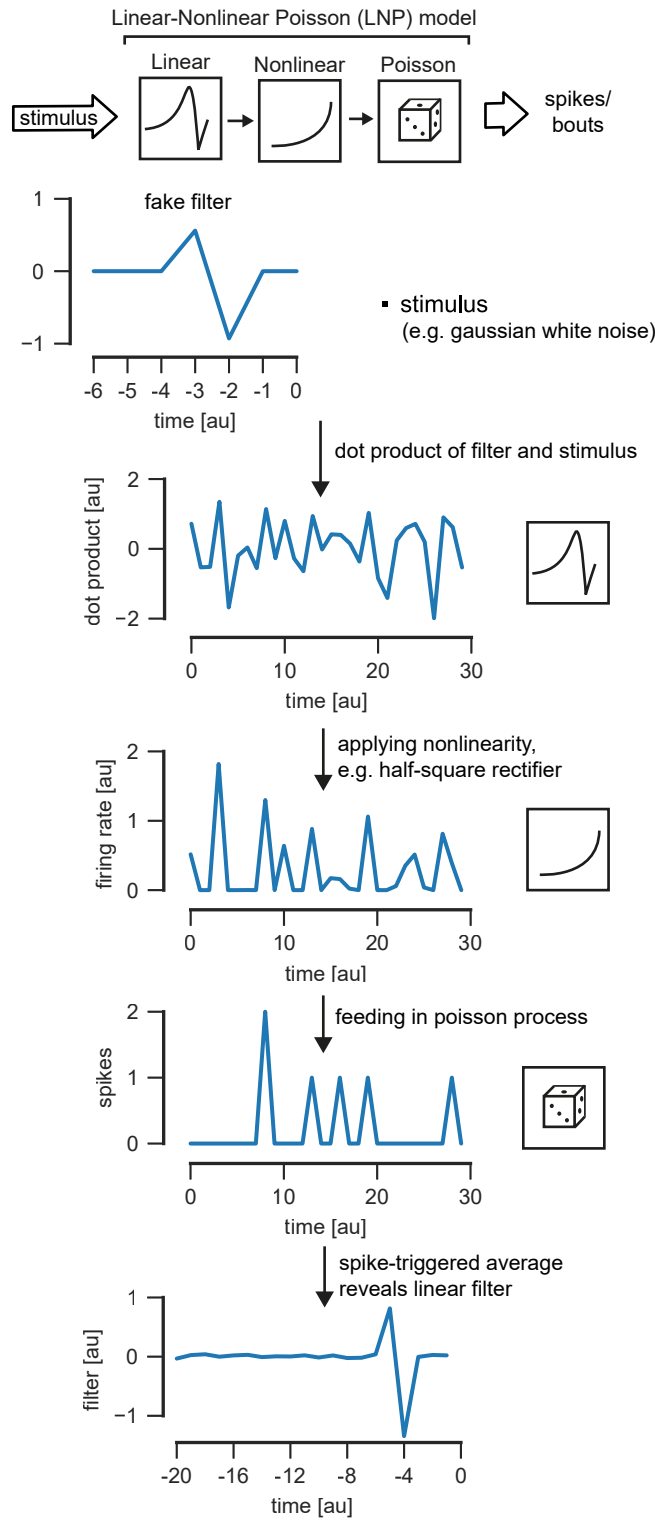
Figure 5: The linear-nonlinear Poisson process cascade. A stimulus is linearily filtered using a weight vector or filter k. The filtered stimulus is passed to a nonlinearity function, such as an exponential or a half-squared rectification, yielding an instantenous firing rate. This is fed into a stochastic Poisson process producing discrete spikes. Using the spikes and the spike-inducing stimulus, reverse correlation or spike-triggered average yields the linear filter k (if the nonlinearity is not symmetric).

Figure 6: The GCaMP protein. a) The cartoon scheme of GCaMP. A circular-permuted GFP contains an calmodulin (CaM) and an M13 domain that are connected with linkers to the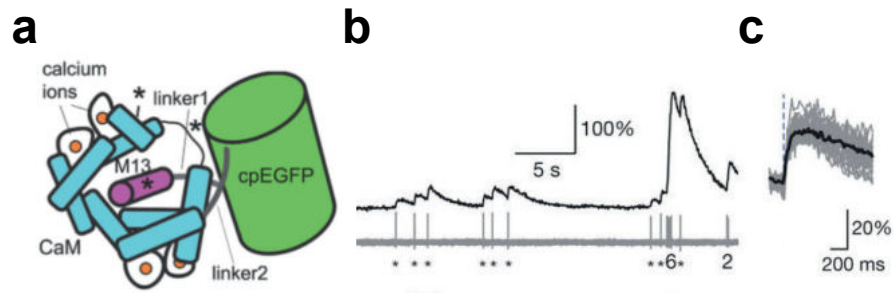 GFP barrel. Four calcium ions can be bound to the CaM domain. Image taken from Akerboom et al. 2012. Reprinted with permission. b) A fluorescence trace (changed fluorescence relative to baseline fluorescence) of GCaMP6s is shown above a simultaneous electrophysiology trace of the very same cell. Note the sharp onset and long decay of the calcium signal. c) the average calcium response to a single action potential. b) and c) were taken from T.-W. Chen et al. 2013. Reprinted with permission.

or Fura-4. It is, however, hard to translocate the dye into the cell. Thus, most researchers use genetic encoded fluorescent proteins that were genetically engineered to fluoresce relative to the cell's voltage or calcium levels (see Figure 6b). These indicators are mostly based on green fluorescent protein (GFP) derivates that consist of one or more GFP-like molecules. A very famous example is the GCaMP family, originally developed by Nakai et al. 2001, that consists of a circular-permuted GFP with a calcium sensitive domain based on the M13 peptide and Calmodulin (see Looger and Griesbeck (2012) and Rose et al. (2014) for review, see also Figure 6a). However, there are also ratiometric calcium sensors based on the troponin C domain of the toadfish, that uses two fluorescent proteins, cyan fluorescent protein (CFP) and yellow fluorescent protein (YFP), that show a given Förster resonance energy transfer (FRET) efficiency depending on the ambient calcium levels (Thestrup et al. 2014). Due to the ease of use of single fluorophore reporters, the GCaMP family is the major calcium reporter used to date and was also utilized in our imaging experiments (see study I and study II).[6]

1.1.5   *Fluorescent proteins*

Fluorescent proteins are the basis of the aforementioned calcium indicators and consist of a β-barrell structure with the fluorophore being inside of the barrell. The fluorophore is a combination of three

---

[6] I was involved in developing a new calcium indicator in collaboration with the Griesbeck lab, which is still an ongoing project, and its description is beyond the scope of this thesis.
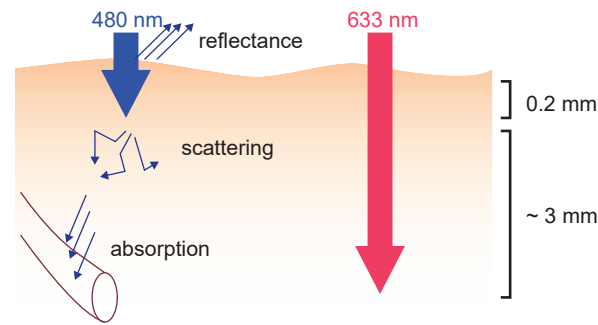
Figure 7: Light is scattered, reflected and absorbed depending on its wavelength. Longer wavelengths are capable to penetrate tissue easier with less reflectance, absorption and scattering than light with shorter wavelengths.

amino acids that rearrange spontaneously and show distinct features for excitation and emission. The most common fluorophore is the enhanced green fluorescent protein (EGFP) and is nowadays widely used to label transfected cells or to track proteins by fusing EGFP to the N- or C-terminus of the protein of interest. EGFP is classically excited using blue light with a peak around 488 nm. Emission is generally shifted to longer wavelengths, and in case of EGFP, the emission produces photons with a peak in the green spectrum. As the most common GCaMP variants are based on EGFP, they are also excited with blue light and emit green light.

However, high energetic blue light is prone to scatter when it interacts with matter. When imaging deep into the brain, blue light scatters and loses power in the focus. Interestingly, the longer the wavelength, the deeper the penetration and the less scattering occurs (Figure 7). When focusing on fluorescent proteins of other species than the *Aequorea victoria* derived EGFP, new red-(emission-)shifted variants were found, such as DsRed. Using several rounds of mutagenesis, the original tetrameric protein was turned monomeric and several variants with different excitation and emission spectra were found (Shaner et al. 2004). One red-shifted variant from this study, mCherry[7], is nowadays widely used and very often combined with EGFP to perform two color imaging. Further, due to the fact that the spectra are red-shifted, mCherry performs better in deeper tissues than EGFP, despite its lower overall brightness.

Scattering depends on wavelength

When looking at the fluorescent proteins known to date, there is an abundance of green/yellow emitting fluorescent proteins, however, a lack of bright far-red emitting fluorescent proteins, that are in particular useful to study deep brain regions (Figure 8). In this thesis, we describe a collaboration effort where Arne Fabritius developed a new far-red shifted protein named mCarmine that was evolved using an

Study III

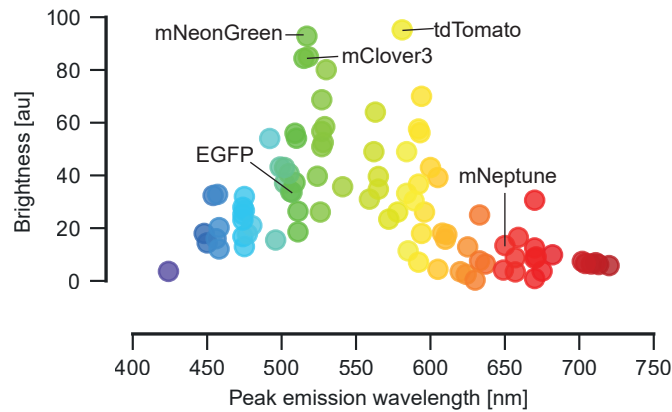7 the *m* in mCherry stands for monomeric

Figure 8: Bright fluorescent proteins are accumulated in the green/yellow emission spectrum. The brightest fluorescent proteins known are mClover3 and mNeonGreen in the green, and tdTomato in the yellow/red spectrum. mCarmine was evolved using a mNeptune variant. Copyright to Kurt Thorn and Talley Lambert. Reprinted with permission.

automatic screening platform and outperforms cyan light emitting fluorescent proteins in larval zebrafish *in vivo*.

1.1.6 *Expression of genes of interest*

Tissue-specific promotors and/or enhancers allow specific expression of genes of interest, such as the aforementioned GCaMP. In study II, we utilize the *carbonic anhydrase 8* (ca8) enhancer element to specifically label Purkinje cells. In this case, Matsui et al. 2014 found that an only 253 bp long fragment upstream of the transcription start is needed to specifically drive expression in Purkinje cells. In study III, we used the *elavl3* promotor, that drives expression specifically in neural tissue (Park et al. 2000).

Ideally, scientists would like to target tissues or cell populations specifically. However, sometimes little is known about the molecular expression profiles of specific cell types. Strategies like enhancer trapping were used to create transgenic species that label a specific tissue without a priori knowledge of the existence and/or location of the enhancer, for example valuable driver lines for granule cells (Takeuchi et al. 2015) used in study II.

1.2   THE CEREBELLUM

The small brain   The cerebellum, the Latin name of the orginally Greek term parencephalis introduced already by Aristotle, is a small structure adjacent to the brain stem and the cerebrum (brain). In the 19th century, Rolando discovered that a damaged cerebellum leads to impairment

human

mouse

zebrafish
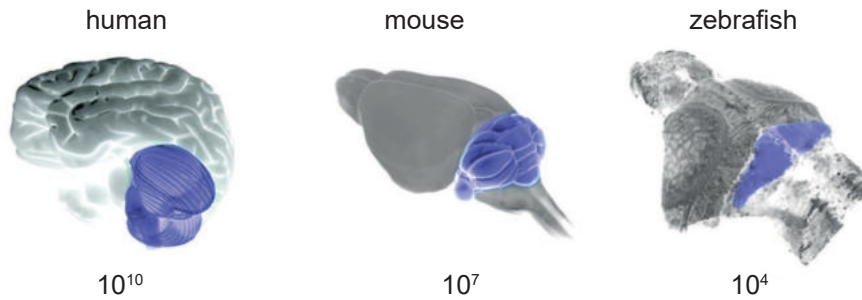
10^{10} 10^7 10^4

Figure 9: The cerebellum is conserved across vertebrates. The whole brain is shown in gray, the cerebellum is highlighted in purple. The number of neurons in the cerebellum differ across species in orders of magnitude: humans have around ten billion, mice around ten million and larval zebrafish approximately tens of thousand neurons in the cerebellum.

of motor function, pioneering the idea that the cerebellum is important for proper motor behavior (the history of the cerebellum is nicely reviewed by Coco and Perciavalle 2015). Later, it was related to coordination and motor learning, as well as conditioning (Thompson 1986; Thompson and Steinmetz 2009, for review). Conditioning is a form of learning, where a neutral, i.e. conditioned, stimulus that typically evokes no behavior, is paired with a behavior-inducing stimulus, called the unconditioned response. The cerebellum mediates this learning by bringing together both, sensory and motor information.

The main cell types of the cerebellum, namely granule cells and Purkinje cells (as well as interneurons and neurons in the deep cerebellar nuclei) were already drawn and described by Ramon y Cajal in the 19th century. Interestingly, the cerebellum is conserved across vertebrates, including mice, birds and the larval zebrafish (Figure 9).

1.2.1 *Circuitry*

The same microcircuit is repeated as unit across the entire cerebellum (Figure 10): Mossy fibers carrying sensory and motor signals from several brain areas and the spinal cord, synapse onto granule cells. Granule cells (as shown in Figure 11c) are excitatory, have three to five claw-like dendritic arms and send long axons in the molecular layer that form parallel fiber sheets. Purkinje cells reside with their soma in a layer above the granule cells (Purkinje cell layer) and receive input from various parallel fibers. Their elaborate planar dendritic tree is arranged such that parallel fibers are orthogonal to the dendritic tree plane (Figure 12c). Purkinje cells are the sole output of the cerebellar cortex, are GABAergic (inhibitory) and synapse on deep cerebellar nuclei neurons (DCN). DCN axons leave the cerebellum. In addition, the inferior olive, a structure outside of the cerebellum and located in
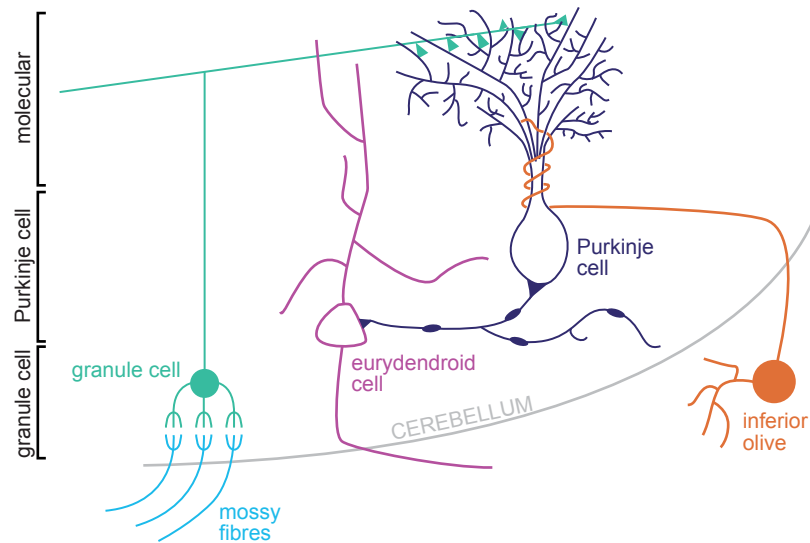
Microcircuitry

Figure 10: The cerebellar circuitry in larval zebrafish. Adapted from Bae et al. 2009 and Okamoto 2014. Note that a fraction of Purkinje cell axons are also leaving the cerebellum (vestibular cerebellum). Eurydendroid cells are in the same layer as Purkinje cells. Neurons of the inferior olive are located outside of the cerebellum.

the brain stem, sends climbing fibers to Purkinje cells that wrap around the main dendritic arbor. It is thought that the inferior olive sends error signals and acts as a teaching signal to allow learning (Albus 1971; Marr David 1969). In larval zebrafish, we observe the same cell types as in mammals (Bae et al. 2009), except that in zebrafish no DCN exist, however, they have a homologous cell type termed eurydendroid cell (EC) (Alonso et al. 1992; Meek et al. 1992). Further, no basket cells have been described so far. Fortunately, we have a body of available transgenic fish lines that are either enhancer trap drivers or direct lines that selectively label specific cerebellar cell types (Matsui et al. 2014; Takeuchi et al. 2015).

1.2.2 *Granule cells*

Granule cells have been shown to be highly conserved across species, including larval zebrafish (Knogler et al. 2017). We can utilize enhancer trap lines that label a subset of granule cells (see Figure 11a) to study granule cell function (Takeuchi et al. 2015). They have also three to five claws where they receive dendritic input (Figure 11c). They send long axons to the molecular layer in the cerebellum known as parallel fibers, that contact Purkinje cell dendrites (Figure 11b). Already early studies suggest that cerebellar learning can occur on the parallel fiber - Purkinje cell synapse by using long-term depression (LTD), see Suvrathan and Raymond 2018 for review. However, stimuli have to be
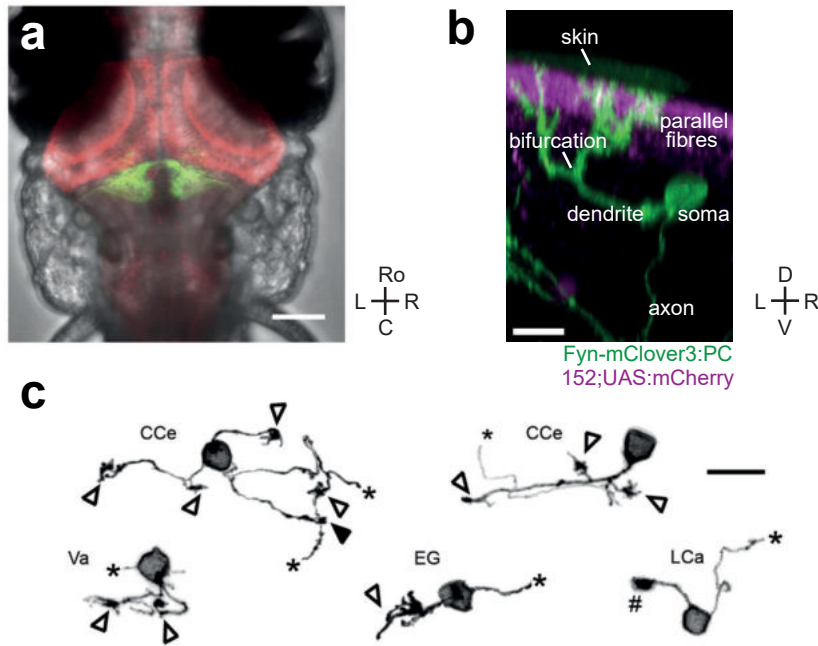
Figure 11: Granule cells in larval zebrafish. a) a confocal maximum intensity projection with a pan-neuronal pattern in red, and a large population of granule cells in green (combination of many transgenic lines). Scale bar represents 100 μm. b) a single Purkinje cell (labelled with Fyn-mClover3:PC, green) that spans its dendritic tree to the parallel fiber layer (gSA2AzGFF152B;UAS:mCherry, magenta). c) Examples of sparse labelled granule cells using electroporation. Open arrowheads indicate dendritic claws, black arrowheads indicate dendritic branches without claws, pound indicates putative growth cone, and the truncated parallel fiber axons for all cells are marked with asterisks. The scale bar represents 10 μm. Data from (a) and (c) was taken from Knogler et al. 2017. Reprinted with permission.

exactly timely locked that LTD and thus, learning occurs, otherwise one can likely get long-term potentiation (LTP). Meek argued that parallel fibers are parallel so that Purkinje cells can act as coincidence detectors (Meek 1992). However, it is barely known what kind of parallel fiber signals make downstream Purkinje cells spike.

1.2.3   *Purkinje cells*

Purkinje cells are the sole output of the cerebellar cortex. They are known to be involved in mediating cerebellar learning via long-term depression on the parallel-fiber-Purkinje-cell synapse and can shape motor coordination (Bosch et al. 2015; Gallimore et al. 2018; Kono et al. 2018; Ransdell et al. 2017; Suvrathan and Raymond 2018). As shown in Figure 10, Purkinje cells receive two major sources of input: granule cell input via the parallel fibers and inferior olive input via climbing fibers. These two inputs can be characterized in Purkinje cell activity: Purkinje cells fire simple spikes intrinsically and in response to parallel fiber input, or complex spikes due to climbing fiber activity (see Figure 12a). Interestingly, in mammals calcium imaging can separate simple and complex spike activity depending on the signal location (Figure 12b): somata show most likely simple spikes, whereas dendrites show complex spike activity (Ramirez and Stell 2016).

Purkinje cells are of inhibitory nature and can be selectively stained using antibodies against Parvalbumin. Alternatively, they can be genetically selectively labelled using for example the L2 or *aldolase c* promotor. In mammals, we see interesting alternating patterns of *aldolase c*, also known as zebrin II, because it generates these beautiful zebra-like patterns across the cerebellum (see Figure 12d). Interestingly, Purkinje cells in larval zebrafish are all *aldolase c*/Zebrin II+ (Bae et al. 2009; Takeuchi et al. 2015), similar to other teleost fish, where Purkinje cells are the only Zebrin II+ population (Meek et al. 1992). Interestingly, a small enhancer fragment of the *carbonic anhydrase 8* enhancer is capabable of driving Purkinje cell specific expression in larval zebrafish (Matsui et al. 2014) and across species (Namikawa et al. 2019). Interestingly, *ca8* as well as *aldolase c* are members of the glucose cycle, emphasizing the importance of energy production in these highly active neurons. Further, Parvalbumin 7 (*Parv7*) has been utilized to label Purkinje cells using immunohistochemistry to determine the average number of Purkinje cells in zebrafish at 7 dpf being between roughly 180 and 350 (Hamling et al. 2015).

Using the *tol2* transposon system (as introduced above) and a reporter, such as GFP, one can selectively image Purkinje cell morphology and create stable transgenic fish lines labelling Purkinje cells *in vivo*. For the work presented here, I was generating transgenic fish lines in order to characterize Purkinje cell morphology and topography (see study II), selectively activate Purkinje cells using channelrhodopsin (ChR), similar to Matsui et al. 2014, and red-activated channelrhodopsin (ReaChR) (Lin et al. 2013), and functionally image Purkinje cell activity using state-of-the-art genetically encoded calcium indicators.

Similar to mammals, Purkinje cells in larval zebrafish are spontaneously active and receive input from granule cells and from the
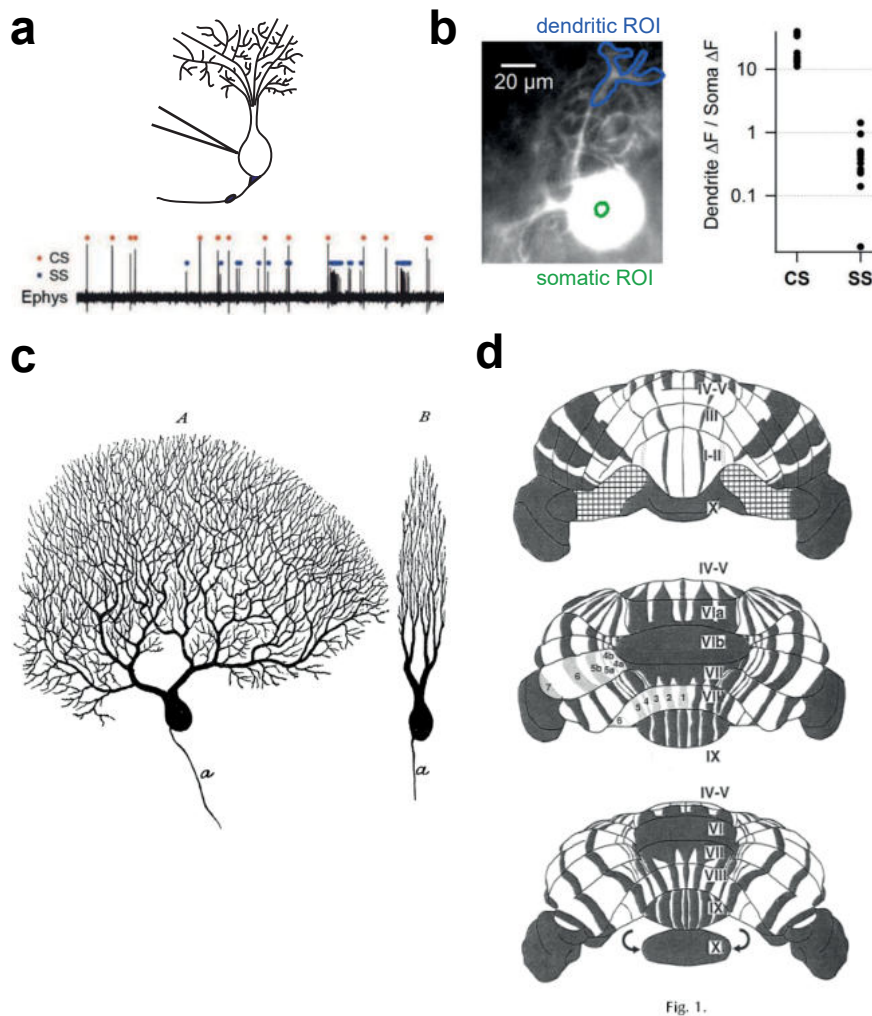
Figure 12: Purkinje cells have specific activity patterns, anatomy and molecular identity. a) A loose-patch recording of a zebrafish Purkinje cell (holds true for other model organisms as well). Data taken from Knogler et al. 2019. b) Dendritic calcium responses are due to complex spikes, whereas somatic calcium responses are due to simple spikes, observed in a mammalian brain slice preparation. Taken from Ramirez and Stell 2016. c) Purkinje cells have planar dendrites. They expand in one dimension, but are very compact orthogonal to the other. Image taken from Piersol and Dwight 1916. d) Zebrin divides the cerebellum in sagittal stripes. Figure taken from Hawkes and Herrup 1995. Panels b) to d) were reprinted with permission.

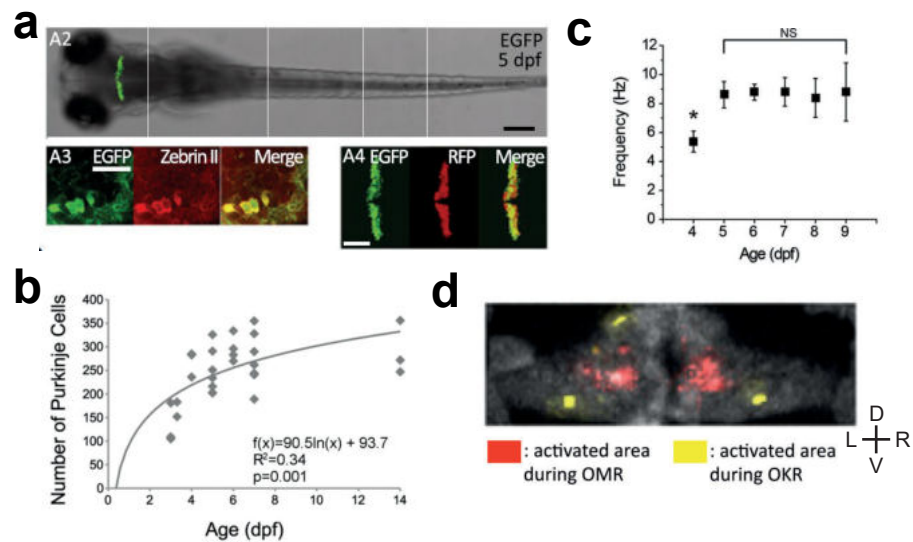Figure 13: Studies on Purkinje cells in larval zebrafish. a) Matsui et al. 2014 showed that the *ca8* enhancer labels Purkinje cell specifically. b) Hamling et al. 2015 quantified the number of Purkinje cells in zebrafish. c) Hsieh et al. 2014 showed that Purkinje cell mature with 5 dpf. d) Matsui et al. 2014 performed preliminary imaging experiments showing a coarse OMR and OKR distribution across the cerebellum. All panels were reprinted with permission.

inferior olive via climbing fibers (Hsieh et al. 2014; Sengupta and Thirumalai 2015). Previously, it has been shown that larval zebrafish Purkinje cells matured already at five dpf, only two days after they were born (Hsieh et al. 2014). As well, it was shown that larval zebrafish Purkinje cells exhibit diverse activity patterns (Scalise et al. 2016). However, important anatomical features have not been investigated yet, such as a comprehensive, high-quality single Purkinje cell morphology and a topography analysis (see study II and Appendix).

Internal models   Purkinje cells are also thought to be part of cerebellar internal models contributing to smooth behaviorals and motor learning (Wolpert et al. 1995, 1998) and known to be involved in some variants of spinocerebellar ataxias (Matilla-Dueñas et al. 2014; Meera et al. 2016). The cerebellum is known to have a certain topography, such that vestibular information is highly processed in the floccolus and lobules involved in oculomotor behavior include lobule V, IV and VII (Voogd and Barmack 2006). However, it is nearly impossible to map the whole *Study II*   mammalian cerebellum due to its size and inaccessibility. Given the unique conditions in larval zebrafish such as optical accessibility, we were able to use whole-cerebellar population imaging to map visual inputs and motor signals to the whole Purkinje cell layer (study II). Using single-cell electrophysiological studies in combination with functional calcium imaging, we could determine that Purkinje cell calcium transients are due to both, complex spikes and simple spike

bursts, and the spike type cannot be inferred from calcium traces (study II).

We could show that Purkinje cells located caudal-laterally in the cerebellum project outside of the cerebellum and respond almost exclusively to optokinetic stimuli with complex spike transients, suggesting that these cells resemble the zebrafish homologue of the flocculus.

1.2.4 *Eurydendroid cells*

The zebrafish homologue to mammalian DCN are eurydendroid cells (Ikenaga et al. 2006). They reside in the same layer as Purkinje cells and are similar in many ways. ECs also send their dendrites to the molecular layer (see Figure 14a) and potentially get input from granule cells (Ikenaga et al. 2006). This is different from the classical microcircuitry and introduces new potential computational models. Previously it was shown that ECs in zebrafish leave the cerebellum ipsilaterally and contacts the optic tectum (Heap et al. 2013), however, with recent data from Virginia Palieri we were able to label a supposedly different subtype of ECs that project contralaterally (data shown in Virginia's master thesis, not published, line used shown in Figure 14b).

Eurydendroid cells share, however, more features with their mammalian counterparts. They also are tonically active (observation by Laura Knogler, not yet reported), and are aspartergic and glutamatergic (Ikenaga et al. 2005, and own data, see appendix). Interestingly, ECs fall in at least two molecularily different groups: olig2+Calretinin- and olig2-Calretinin+ (Bae et al. 2009; Biechl et al. 2016; McFarland et al. 2008). The enhancer trap line we use in the lab hspzGFFgDMC156A (Takeuchi et al. 2015) labels both EC populations, olig2+ and olig- (see Figure 14c). We further developed an EC-optimized UAS:GCaMP6s reporter line to functionally image EC populations using two-photon and light-sheet calcium imaging.

1.2.5 *Inferior olive*

The inferior olive is part of the cerebellar circuitry and an important signal source, however, the location of the inferior olive neuron somata is outside of the cerebellum in the rhombencephalon. The inferior olive neurons send long so-called climbing fibers to the cerebellum that "climb up" the different cerebellar layers and wrap the Purkinje cell dendrite. They form a very strong synaptic connection based on voltage-gated calcium channels to the Purkinje cell dendrite, that lead to an extraordinary large depolarization. This depolarization is known as complex spikes, in contrast to simple spikes that are elicited by granule cells (see Figure 12a).

The inferior olive is thought to be an error detector since the early 1970s (Ito 2013). According to this theory, inferior olive neurons only
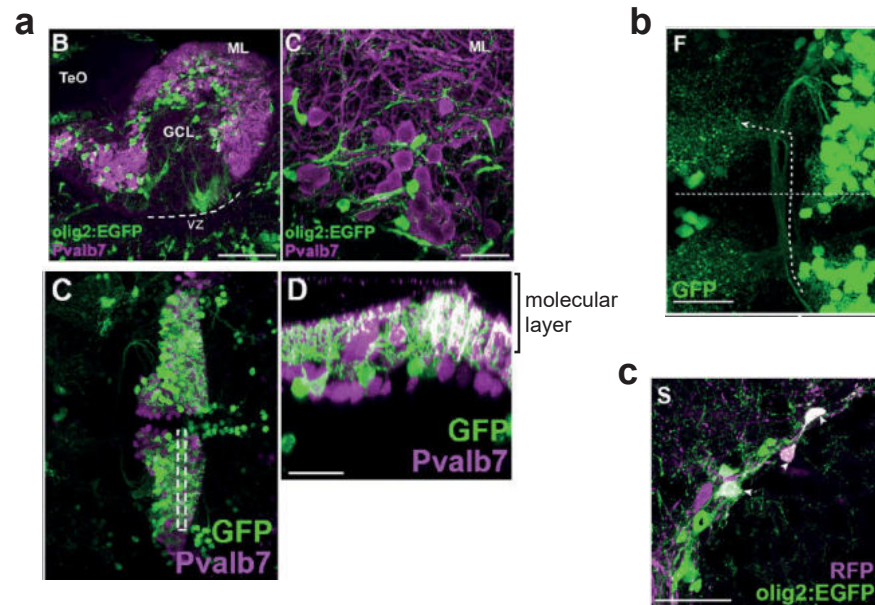
Figure 14: Eurydendroid cells are distinct from Purkinje cells. a) GFP+ eury-
dendroid cells do never overlap with Pvalb7+ Purkinje cells (top
panels from Bae et al. 2009, lower panels from Takeuchi et al. 2015).
Interestingly, eurydendroid cells extend their dendrites into the
molecular layer. b) Eurydendroid cells leave the cerebellum and
send their axon contralaterally to rostral circuits. c) Some eury-
dendroid cells in the line hspzGFFgDMC156A are olig2+. b) and
c) were taken from Takeuchi et al. 2015. All panels were reprinted
with permission.

fire when an error occurs. The effect of which is to weaken the granule cell - Purkinje cell synapse and to evoke learning. However, there is an increasing body of evidence, that the inferior olive does not simply function as an error detector, but rather has a specific role in timing and shows predictive encoding. A recent review tries to unify all experimental knowledge in one single hypothesis, termed "dynamic encoding hypothesis" (Streng et al. 2018).

In study II, we elucidate how the inferior olive contributes to Purkinje cell activity observed by electrophysiology (Knogler et al. 2019, see also Appendix) and functional calcium imaging (see the following chapters).

METHODOLOGY

In this thesis we performed behavioral experiments, anatomical imaging experiments, or functional imaging experiments together with visual stimulation and behavioral recordings (see also **Kist** et al. 2017). Transgenic fish lines were either stable lines (F0 offspring, F1+), such as *elavl3*:GCaMP6s used in the first study and PC:GCaMP6s in the second study, or transient lines (F0 generation, injected with constructs, see below) to achieve single cell labelling as in the second study to identify and image single cells.

2.1 FISH HUSBANDRY

Adult zebrafish fish were bred in house at the Max Planck Institute of Neurobiology fish facility and kept at a 14/10 h day/night cycle. Six to eight dpf larvae were used for either behavioral or imaging experiments. For pure behavioral experiments we used Tüpfel-Longfin (TL) wildtype fish. For imaging experiments, we used fish that have a deficiency in the *mitfa* gene, responsible for forming melanophores (Lister et al. 1999). These so-called *nacre* fish lack dark pigments and are very well suited for *in vivo* imaging purposes. For imaging experiments in study I, we used a transgenic line that expresses GCaMP6s under the pan-neuronal *elavl3* promoter (Kim et al. 2017). For imaging experiments in study II, we expressed GCaMP6s using the *ca8* enhancer (PC:GCaMP6s) in Purkinje cells, or used the enhancer trap line gSA2AzGFF152B (Takeuchi et al. 2015) to drive UAS:GCaMP6s in granule cells. For single Purkinje cell labelling, we used *aldoca*:gap43-mCherry fish (Takeuchi et al. 2015) as a reference for morphing *z* stacks to each other. For behavioral optogenetics experiments, we used ChR2-Venus:PC:R-GECO1 fish (Matsui et al. 2014). For evaluation of mCarmine, we used *elavl3*:Gal4 fish (Kimura et al. 2008). For counting Purkinje cells, we used PC:NLS-GCaMP6s. All experiments were approved by the Regierung von Oberbayern via TVA 55-2-1-54-2532-82-2016.

2.2 CREATING TRANSGENIC LINES

Cloning

The common strategy across cloning attempts is to linearize the desired backbone by restriction enzyme digestion because linearization via polymerase chain reaction (PCR) is either non feasible due to huge plasmid sizes (around 16 kb), AT-rich streches or repetitive se-

quences. Inserts are prepared using PCR on either plasmid backbones provided by Addgene or the Baier lab or commercially synthetized desoxyribonucleic acid (DNA) sequences. Final constructs were assemblied in a one-pot-reaction via either Gibson assembly (Gibson et al. 2009), NEBuilder or most commonly SLiCE (Zhang et al. 2012). PCR, gel purification and construct assemblies were performed according to the manufacturer's recommendations with slight variations. The cloning strategy as well as a protocol is located in the Appendix. An example to clone EGFP in the *ca8* enhancer plasmid is shown in Figure 7. For convenience, we termed all constructs and fish using the *ca8* enhancer "PC". For example, if Fyn-tagRFP and Cre are inserted in the left and the right cassette, respectively, the construct or fish would be called Fyn-tagRFP:PC:Cre. An example cloning protocol for creating the construct PC:EGFP is shown in Figure 15.

Assembly mixes were transformed in chemically competent bacteria based on the DH5α strain. We made our own competent bacteria using either the Zymo Mix&Go kit or using TSS buffer (see protocol in Appendix, similar to the original publication of Chung et al. 1989), both with equally good performance. Usually, 100 μl bacteria were transformed with one to two μl of assembly mix, incubated on ice for around 30 minutes and heat-shocked at 42°C for 30 seconds. After a short incubation on ice (typically less than five minutes), bacteria were plated on pre-warmed LB plates containing 1:1000 Ampicillin (plates acquired from the central media service).

Colony PCR

The colony PCR protocol was improved for maximum efficiency and reduced costs. A protocol is in the Appendix. Briefly, a mastermix containing the 2x OneTaq MasterMix with Standard buffer from New England biolabs (NEB), forward and reverse primer and water was aliquotted in 15 μl reactions. Colonies were picked using a fresh filter tip, spread on a fresh plate and the tip was subsequently added to the PCR mix well. After a short incubation, tips were removed and the PCR tubes moved to a thermocycler. Optimal performance have been observed when initial denaturation was three to five minutes.

Positive clones were inoculated in terrific broth (TB) medium (Carl Roth, X972.1) supplemented with Ampicillin (100 mg/ml, Carl Roth, K029) in a ratio of 1:1000 for a final concentration of 100 μg/ml and grown overnight at 37°C while shaking.

Plasmid preparation

2 mL of overnight culture was spun down in 2 mL microfuge tubes and plasmid DNA was purified using plasmid extraction kits from Machery Nagel (NucleoSpin). Kits were used according to the manufacturer's instructions. Plasmid was eluted normally in RNAse and DNase-free water. Plasmids for long-term storage or gained from
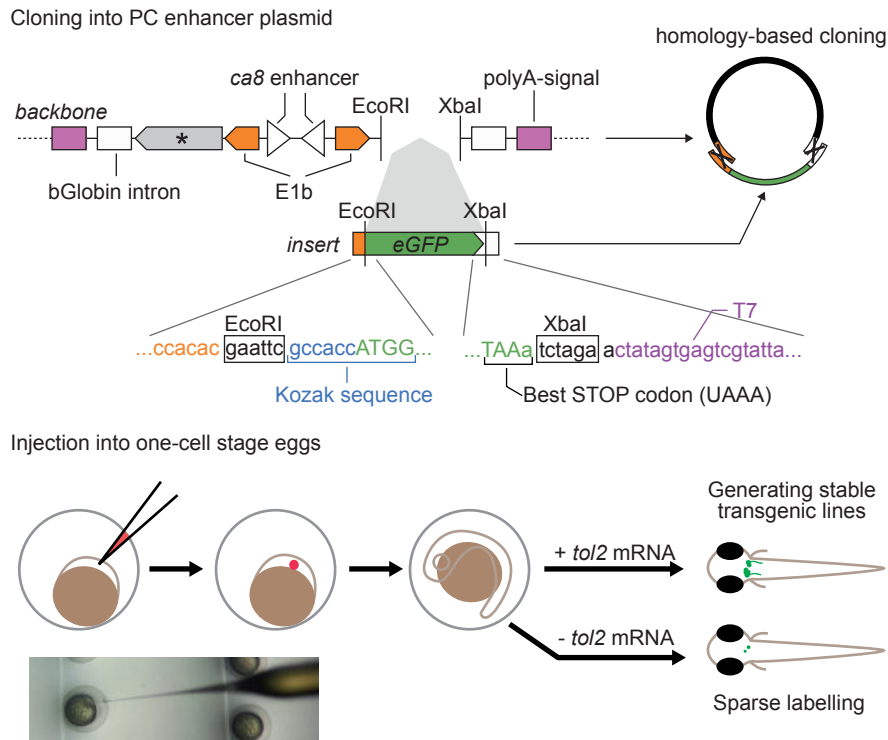
Figure 15: Cloning of EGFP in the PC enhancer plasmid using homology-dependent cloning, such as SLiCE. Flanking DNA sequences are color coded according to the plasmid or the PCR product above. In brief, the 5' sequence should have a 20-30 bp homology to the E1b promotor, as well as the EcoRI restriction site and a Kozak sequence (gccaccATGG), where ATGG are the first 4 bases of the protein of interest, here EGFP. The 3' end should have the UAAA stop codon, which is known to efficiently stop translation and boost expression *in vivo*. Further, the XbaI restriction site and the 20 bp homology to the T7 promotor adjacent to the β-Globin intron should be included. For injection, a mix of Phenol red, DNA and optional *tol2* mRNA and water is injected in the one-cell stage of freshly laid eggs. At 3-4 dpf one can screen for fluorescence, e.g. the cloned EGFP. If *tol2* mRNA was added, one would expect a comprehensive pattern, without *tol2* mRNA the labelling efficiency is low, thus getting sparse labelling. The fish injected with construct and *tol2* mRNA can be raised and the offspring screened for fluorescence ending in a stable transgenic fish line. (*): we have plasmids that contain already Fyn-tagRFP or Fyn-mClover3 here. A list of available constructs is in the Appendix.

Midi Preps (Machery Nagel or Zymo) were typically stored in Tris-EDTA (TE) buffer.

Cas9 protein preparation

For CRISPR/Cas9 experiments, we subcloned NLS-Cas9-NLS[1] as published by Hruscha et al. 2013 in pCoofy4 (Scholz et al. 2013) to be expressed by the Max Planck Institute of Biochemistry protein core facility. Purified Cas9 protein was mixed with sgRNA prepared either with direct *in vitro* transcription from oligos or directly ordered from IDT.

tol2 *mRNA preparation*

A detailed protocol to create *tol2* mRNA is attached in the Appendix. Briefly, the open reading frame (ORF) of tol2 was cloned into a plasmid adjacent to a SP6 promotor for in vitro transcription. Using the Ambion SP6 mMessage mMachine kit, the mRNA is transcribed from that linearized plasmid. Further modifications, such as capping and poly-adenylation, are performed to achieve a high quality mRNA. RNA is precipitated using Lithium chloride (LiCl) overnight at -80°C and then eluted in RNase and DNase free high pure water. Concentration is adjusted to 175 ng/μl and aliquotted in PCR tubes (4 μl each) and stored at -20 °C until further use.

Injection

Constructs for direct drivers were injected in an incross of *nacre* or *casper* fish, whereas Gal4 and UAS constructs were injected in an outcross of the desired UAS or Gal4 line and nacre or casper, respectively. Fish were setup in mating boxes with separator. In the morning of the next day, the divider was lifted and fish mated. Laid eggs were immediately collected and injected during the single cell state using a picospritzer (see Figure 15, bottom panel). The injection mix consists of *tol2* mRNA (around 25 ng/ul), plasmid DNA (less or equal concentration as *tol2* mRNA) and phenol red (1:10 dilution). Injection volume was estimated by eye to be around 1 nL. Injected eggs were kept in Danieau solution and cleaned once a day. Depending on the driver line, successful integration was screened using fluorescence between one (e.g. *olig2*:KalTA4 and *elavl3*) or three to four dpf (e.g. bleeding heart transgenesis marker or *ca8* enhancer). Sparse labelling for optogenetics, electrophysiology or anatomical characterization was performed by omitting *tol2* mRNA (see Figure 15).

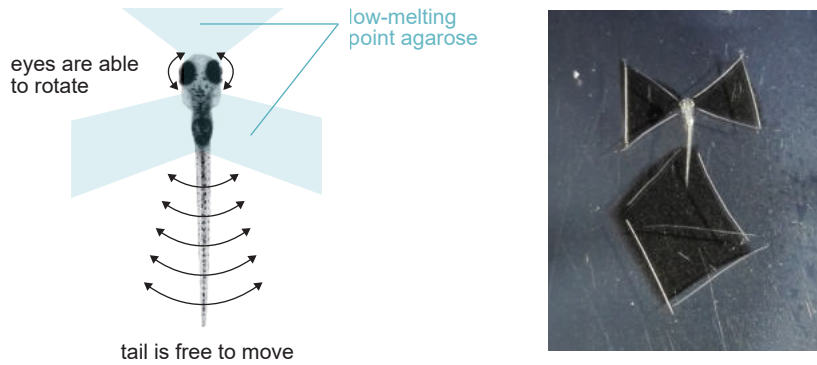
1 nuclear localization signal (NLS)

Figure 16: Preparation of larval zebrafish for head-restrained experiments. The fish is completely immobilized in low-melting point agarose. After the agarose set, the agarose around the eyes and the tail is removed, so fish are able to move their eyes and tail.

2.3 PREPARATION

We embedded six to eight day old larval zebrafish in low-melting point agarose (Thermo Scientific, Invitrogen UltraPure #16520050) dissolved in fish water. The tail (and depending on the experiment, the eyes as well) is freed and the head and trunk stay restrained in agarose (see Figure 16). We use 35 mm dishes (Falcon, #353001) for behavioral and two-photon experiments, and a micro knife (Fine Science Tools, #10315-12) for preparation. For light-sheet experiments, I developed a custom light-sheet chamber optimized for behavior tracking, stimulus presentation, illumination and imaging. A detailed document is appended to this thesis.

2.4 BEHAVIORAL EXPERIMENTS

In this thesis, larval zebrafish behavior was assessed using head-restrained larval zebrafish as described in 2.3. The behavioral setup consists of two parts, hard- and software. In general, I refer to the hardware as the behavioral setup.

2.4.1 Behavioral setup

The behavioral setup (Figure 17) itself resides on an aluminium breadboard attached to isolators (Thorlabs). On the breadboard, we mounted a stage from laser-cut acrylic to position the embedded fish, i.e. the petri dish. On the stage, we added a screen based on white paper or opaque foil to project a stimulus pattern from below. For stimulus presentation, we used a commercially available projector, such as the ASUS P3E. We used a cold mirror to place the projector horizontally on
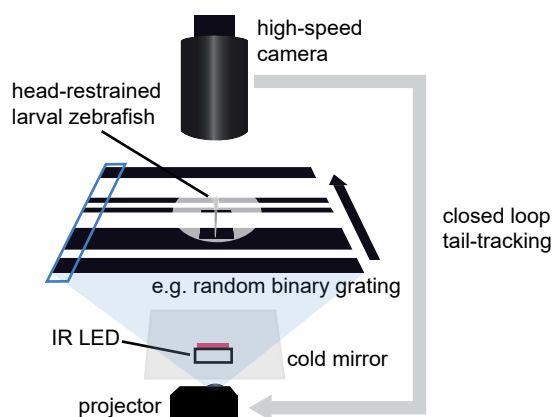
Figure 17: Schematic of the behavioral setup. A forward moving binary grating is presented from below to a head-restrained, tail-freed zebrafish larva. The visual stimulus, i.e. grating, is generated in 1D (x, blue rectangle) and stretched in y.

the breadboard and to allow simultaneously infra-red (IR) illumination from below.

The IR illumination was custom-made based on a high-power light emitting diode (LED) (e.g. OSRAM Black series, peak wavelength around 830 - 850 nm), pre-mounted on a star plate. The star plate was attached to an SM1 cap using thermal pads. Two holes were drilled to allow two cables passing through the cap from behind. The cables were soldered on the plus and minus pads as indicated on the star plate. These cables were connected to a buck pack (e.g. RCD-24-1.00/W/X3) that allows a constant current supply (recommended for high-power leds). The voltage applied to the LED is automatically regulated by the buck pack. We further connected the buck pack to a power supply that supplies around 12 V (such as Voltcraft ESPS-1500).

The illuminated fish was tracked using a high-speed camera (AVT Pike, XIMEA MQ003MG-CM, XIMEA MQ013RG-ON, or PointGrey BlackFly S BFS-U3-04S2M-CS) mounted on an optical rail (Thorlabs) using custom-made holders (Max-Planck workshop) and connected either with FireWire (AVT Pike) or USB3 (XIMEA and PointGrey models) to the computer. The camera speed was between 200 and 450 frames per second with 8 bit and VGA resolution (usually 640x480, 720x540 for PointGrey models). The camera was equipped with a Navitar tele-objective (TC.5028, Hinze Optoelectronics, Hamburg).

To avoid the stimulus bleed-through to the camera, we used IR long-pass filters (#66-106, Edmund Optics). A commercially available computer (Intel i5 family recommended) is sufficient for operating the closed-loop stimulus and online tracking of the fish's behavior; a special arrangement of petri dishes allows two fish being assessed on the same setup with one computer connected to two cameras.
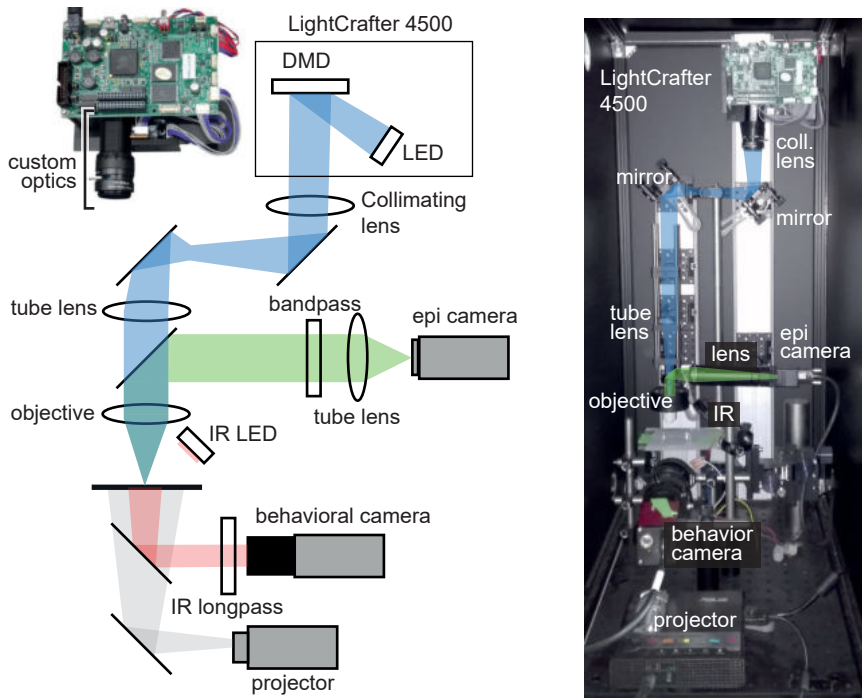
Figure 18: DMD-based optogenetic stimulation setup. The illumination light (blue) is generated by an LED. Light, that hit mirrors oriented into the active light path, is reflected that it can pass the collimating lens, is reflected by two mirrors that adjust the beam, and is focused by the tube lens. The tube lens images the DMD on the back aperture of the objective. The fluorescent sample emits green light that is collected by the objective and reflected by a 500 nm short pass dichroic. A lens coupled with an IR blocking filter focuses the light on a camera chip. The fish is tracked from below using a high-speed camera equipped with a macro lens. A projector provides visual stimulation from below.

2.4.2 *DMD-based optogenetic stimuluation*

To show an image on an liquid crystal display, pixels are set to a value between 0 (off) and 255 (max intensity). Depending on the pixel value, a different amount of light passes through an opaque layer. This happens three times, once per color (RGB[2]), and then forms a colorful image. In a commercial digital light processing (DLP) projector, a similar procedure is used. Instead of liquid crystals, a mirror assembly is used. For each pixel, a single mirror can be instructed to move out (0) or completely into the light path (255). Intermediate intensities can be achieved by only slightly moving the mirror into the light path (1-254). A device using this kind of mirror matrix is called digital micromirror device (DMD).

---

2 three main colors used in additive mixing, red, blue and green (RGB)

We utilized an evaluation DLP projector (Texas Instruments LightCrafter 4500) with blue, green and red LEDs - as shown in the top left and top right in figure 18 - loosely based on a previously described protocol (Zhu et al. 2012). We removed the original, diverging lens array and replaced it by a collimating convex lens (Thorlabs). By coupling it with another lens, we imaged the DMD chip on the back aperture of a 20x water immersion objective (Leica HCX APO L U-V-I, 0.5 numerical aperture (NA)). For alignment, we used a special slide that emits green fluorescences upon blue illumination (Thorlabs, FSK2). For fluorescence microscopy, we used the blue LED for illumination and collected the green fluorescence using a 500 nm dichroic mirror and focused the light on a XIMEA camera.

DMD repository   To interface the DMD, I programmed a software based on Python and the dlpc350 library. This program is available through the Portugues lab Github account. For aligning the DMD with the camera, we moved a rectangle region of interest (ROI) over the camera field of view and used three positions at the corner of the field of view. Using the center of mass of both, the rectangles shown on the DMD and the rectangles on the camera image, we calculated an affine transformation matrix. This transformation matrix is stored and used for optical stimulation.

Optical stimulation pattern can be arbitrarily defined using custom polygonal ROIs on the camera live image (Figure 19). These ROIs are stored as separate illumination files for further use. During a behavioral experiment, these patterns are used to optically stimulate Purkinje cells during a specific stimulus or behavior. To drive Channelrhodopsin, we used the blue and green LED together with a 488/10 band-pass filter.

Visual stimulation for behavioral experiments is projected from below using commercially available projectors (see *Behavioral setup* section). Behavior tracking was implemented from below in combination with an IR illumination from above.

2.4.3 *Software*

Visual stimulation and behavioral tracking is based on custom written software in Python 3.6, and uses the numpy, PyQt4/5, pyqtgraph and OpenCV library. The interface as shown in Figure 20 consists of a graph depicting the tail trace, the tail vigor, the speed of the visual stimulus, and, depending on the experiment, the eye trace. Further, a live image of the fish and tracking is presented. A textbox logging all events is available in the bottom right and stored as text file after the experiment.

Classically, each experiment saves an image of the fish, the data collected during the experiment, such as time, tail trace, vigor, speed of the grating, conditions of the experiment and trial number, as csv
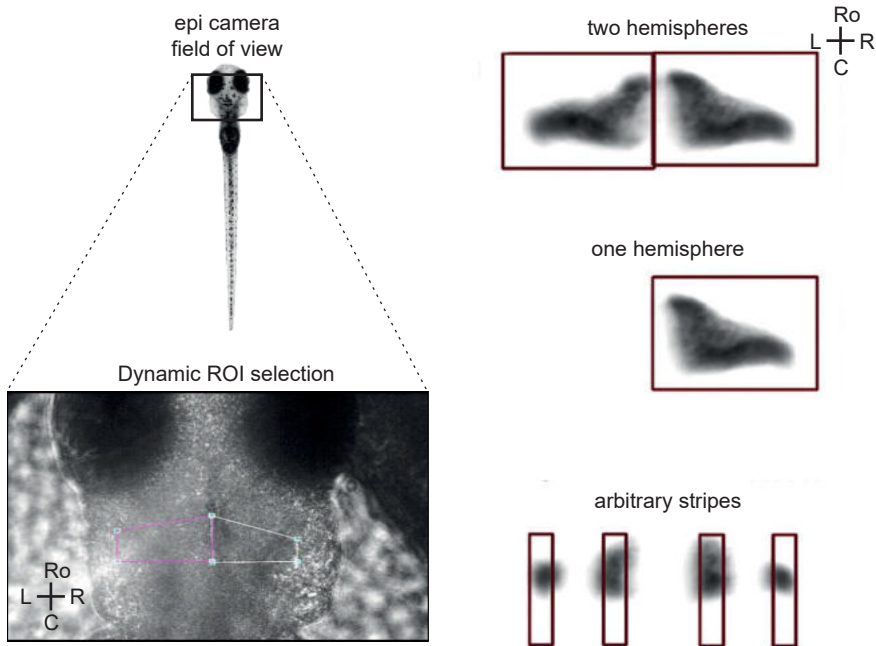
Figure 19: Stimulation specificty with ROIs drawn on the live camera top view. The field of view of the camera is depicted on the left (black rectangle on the larva and zoom-in). The DMD chip covers the camera's whole field of view. ROIs can be selected dynamically. ROIs can have arbitrary shapes (as shown on the right). Purkinje cell fluorescence is reliably restricted by the ROI selection pattern.

(comma separated values) or npy (pickled numpy array), and a log file containing relevant information regarding the experiment. Further, tail trunk and tail tip positions used for tail tracking are saved.

Visual stimuli are presented using an OpenCV or Qt widget. The visual stimulus is updated at 60 Hz, matching the refresh rate of the projector. For most behavioral experiments, binary gratings with a period (one black and white bar) of 10 mm were used. If not stated otherwise, forward speed of the grating was 10 mm/s. For closed loop experiments (the stimulus reacts on the fish's behavior, Figure 17), the following formula for visual feed-back calculation was used:

$$s = s_0 - \alpha * v$$

where s is the corrected speed of the grating, s_0 is the maximum speed of the grating, v the vigor of the fish, that is the standard deviation of a 50 ms rolling buffer of the tail trace, and α the strength of the fish. For α=0, the stimulus runs in open loop. α is typically set to a value, that s during swimming reaches around -20 mm/s (Portugues and Engert 2011).
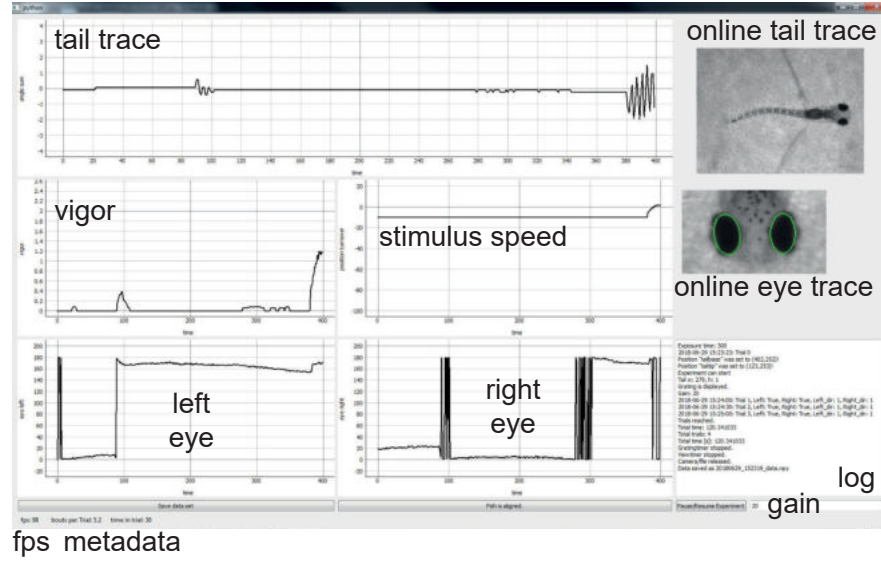
Figure 20: Software to operate behavioral rigs. A screenshot of the graphical
user interface showing the online behavior tracking and stimulus
features, and metadata, such as frames per second (fps)

Tail tracing

Tail tracing was performed as previously described (Portugues and En-
gert 2011), re-implemented from LabVIEW in Python. Briefly, the tail
trunk and the tail tip are either manually by clicking or automatically
defined. The latter can be implemented using a multilayer perceptron
(based on the seminal work of Rosenblatt 1961) as explained in detail
in the Appendix and shown in Figure 21.

The two points between tail trunk and tail tip define the length of
the tail L. The length L is divided in 10 segments. For the first segment,
an arc of -90° to 90° where 0° pointing towards the tail tip is drawn,
and an intensity profile I is determined. As the tail is dark on a bright
background, the minimum is determined:[3]

$$\beta = argmin\ I(\beta)$$

Iteratively, for each subsequent tail segment, another -90° to 90° arc
is drawn. The 180° arc is relatively set depending on the angle β of the
previous segment to allow the algorithm to follow the tail cuverture
(Figure 22). The tail sum T is the cumulative sum of all angles β:

$$T = \sum_{i=1}^{10} \beta_i$$

.

For a given bout, the tail oscillates around the resting position (see
Figure 22 for resting position and deflection).

---

3 In some cases the fish is bright on dark background, for example in light-sheet or
2-photon microscopy, then the image is inverted.

1. Annotation of features

3. Training multilayer perceptron

Input layer

1st hidden layer
(16-32 units)

output layer
(4 classes)

ReLU

ReLU

Softmax

2. Building library of features

head
tail trunk
tail tip
background

4. Feature probability map

head

tip

trunk

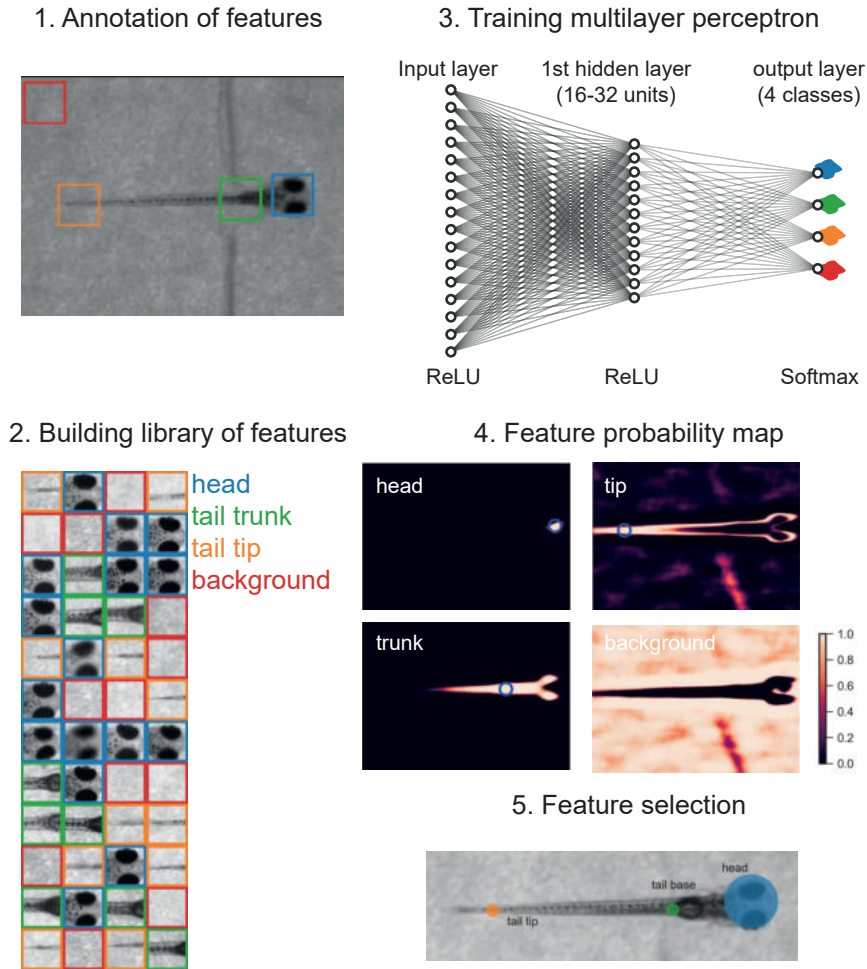background

5. Feature selection

head
tail base
tail tip

Figure 21: Determination of head, tail trunk and tail tip via a multilayer perceptron. First, features were annotated for 405 fish using log-files of previous experiments. Second, a library was constructed of 80x80 px segments. Third, a multilayer perceptron with 32 units in the first hidden layer with rectifier linear unit (ReLU) activation and a four units in the output layer with a softmax activation function performed very well. Fourth, for a given image the feature probabilty can be estimated. The peak probability is indicated by a blue circle. Fifth, the feature positions were initialized automatically by the multilayer perceptron for downstream tail and eye tracings.
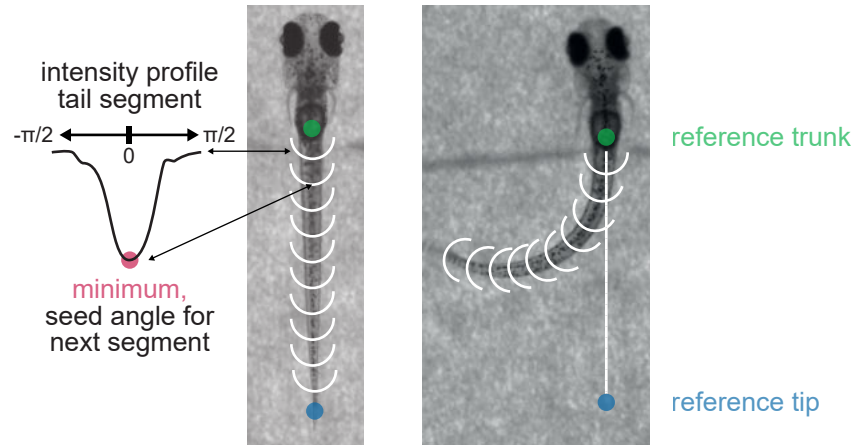
Figure 22: Tail tracking procedure. Tail is indexed using a manually or auto-
matically chosen label for trunk and tail tip (indicated by green
and blue circles). Here, the algorithm divides the tail in ten equally
spaced segments and iteratively approaches the tail tip by finding
the minimum of the intensity profile of a half circle drawn at every
segment. The minimum of a circle (indicated by a red dot) is the
current segment angle and the seeding angle for the next segment,
that allows us to calculate the tail curvature (compare left and
right example).

Eye tracing

Eyes are tracked using established methods. In very high (signal to
noise ratio (SNR)) scenarios, the tracking algorithm is as follows (and
shown in Figure 23):

1. The image is thresholded to extract bright eyes from a dark back-
   ground (note this is inverted in Figure 23 for display purposes)

2. The two largest contours in the thresholded image are identified.
   The image can be cropped to the head position using template
   matching, a neural network (Figure 21) or manual selection. The
   initial sorting is according to size and not to their spatial location,
   thus, the contours are sorted spatially to ensure eye identity.

3. Ellipses are fit to the sorted contours

4. The rotation angle of the ellipse's major axis (or vertex) in respect
   to the body axis of the fish is determined.

An example eye tracing code is located in the Appendix. For com-
plex offline tracking scenarios with low quality eye recordings, an
interactive Jupyter notebook is available to test different algorithms,
for example for local, i.e. adaptive, thresholding. I could apply local
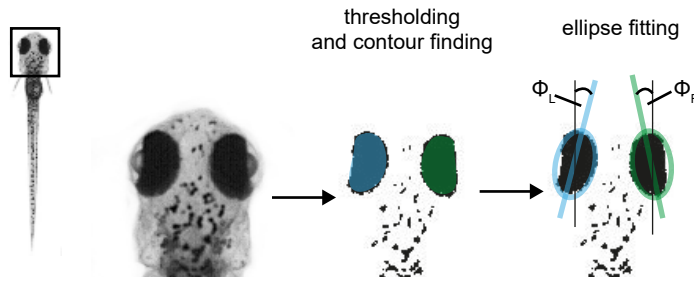thresholding with further post-processing successfully to a behav-

Figure 23: Eye tracking. For fast image processing, we crop the full image to the immediate surrounding of the eyes. The image is first globally thresholded. Then, contours are found (blue and green for left and right eye, respectively). For each contour, an ellipse is fitted and the rotation angle (ϕ_L and ϕ_R) will be determined. Depending on the implementation, we correct the angle such that positive values are nasal and negative values are temporal.

ioral dataset[4] with very low quality recordings that had a very dim illumination and poor contrast.

Recently, we created an effort to standardize the behavioral tracking and the stimulus presentation in a software termed stytra, that is publicly available via Github and currently in revision, but available as preprint (Štih et al. 2018).[5]

Stimuli sets

For the first study, the visual stimulus consisted of random binary, i.e. black and white, bars of given sizes (0.5 mm, 2.5 mm, 5 mm and 10 mm). The stimuli were presented at different speeds (5, 10, 15 and 20 mm/s). Stimuli were generated by choosing white and black bars from a uniform distribution to ensure on average even gray. For experiments that probed the filter dependence on white-to-black bar ratio, we changed the threshold such that we ensure on average 25, 50 or 75% white bars (i.e. a 1:3, 1:1 and 3:1 white to black bar ratio). The stimulus presentation was updated at 60 Hz (projector in-built refreshing rate). The stimulus scene was a square window that was centered on the fish's head and spans 30 mm in each cardinal direction.

For behavioral experiments, the fish experiences three different conditions: open loop (no visual feedback), closed loop (visual feedback) and replay. In study I, the first experiments that determined the BTA and its dependency on parameters where performed in closed loop. Later, the BTA (also refered to as filter) was replayed to head-restrained larvae (the total 6 s in open loop). As a control we shuffled the pixel values to disrupt the spatial correlation by keeping the same overall

---

4 Martinsried two-photon experiments of inferior olive activity during sensorimotor control
5 stytra is a visual stimulation and behavior tracking tool developed by Vilim Stih and Luigi Petrucco with my input

Stimuli

Expo22

luminance. We also used the intensity profile on bout start of the filter, stretched this in 2D and then presented this in whole-field motion ensuring that filter replay and whole-field motion filter were probed the same amount of times. These stimuli are embedded in the linked movie. The imaging experiment visual stimuli were shown in open loop.

For Purkinje cell imaging experiments, we showed the fish a battery of different stimuli including translational and rotational gratings that induce robustly OMR and OKR, respectively, as well as whole-field flashes of different luminance. The experiments were performed in open loop. The exact sequence of stimuli and durations are located in the Appendix (condensed format) and are available as an Excel spreadsheet.

2.5 IMAGING

In the presented studies we use either a confocal microscope[6] for anatomical imaging studies or a custom built two-photon microscope (Denk et al. 1990; Tsai and Kleinfeld 2009) for functional imaging studies (see Figure 24). We also could show that a custom-built light-sheet microscope has comparable signals when testing the same fish with both imaging modalities (**Kist** et al. 2017). However, in one-photon light-sheet microscopy blue light is needed to excite GCaMP and monitor neural activity, which can potentially interfere with behavior, as blue light is known to be adversive to fish (Guggiana-Nilo and Engert 2016; Villamizar et al. 2014). We thus used two-photon microscopy for our functional imaging experiments since the imaging laser is in the infrared spectrum (tuned to 905 nm for our imaging experiments) and invisible to the fish.

We monitored neural activity at a framerate of around 3-10 Hz, depending on the behavioral paradigm and the field of view being imaged. The tail and eyes were monitored at approximately 150 to 200 Hz using an IR illumination from the side for the tail and through the objective for the eyes (see Figure 24). Code for tracking both, tails and eyes, as well as stimulus presentation, were implemented in custom written software in Python similar to the behavioral rig software. Stimuli were triggered by the imaging system using a transistor-transistor logic (TTL) pulse via a LabVIEW-Python bridge[7]. Code for tail and eye tracking is attached to this thesis and available through Github and stytra.

---

6 Zeiss LSM700 or Leica SP8, available through imaging core facility

7 known as the anki listener vi, that writes a file to the listener folder upon receiving a TTL pulse.
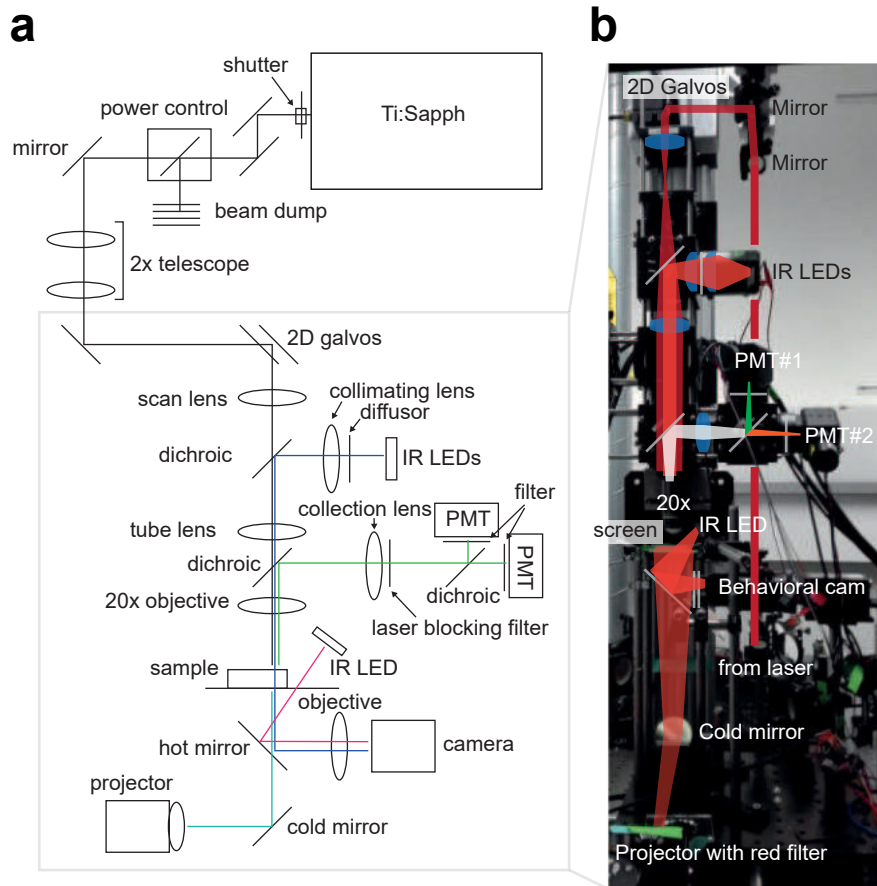
Figure 24: Custom built two-photon microscope. a) Schema of the lab two-photon microscope. Note that there are IR LED paths to illuminate the sample, i.e. the fish, decently to allow tail and eye tracking. The latter is achieved by illuminating the head through the objective. Visual stimuli are shown using a commercial projector from below. Behavior is also tracked from below. We imaged using a pulsed IR Ti:Sapphire laser that was tuned to 905 nm. Images were acquired using scanning with 2D galvos. b) Photograph of two-photon microscope with partial annotation of important elements as depicted in a). Light paths are colored according to the approximate wavelength (IR is colored reddish). Lenses are indicated with semi-transparent blue shapes. Mirrors or filters are indicated by grayish lines.
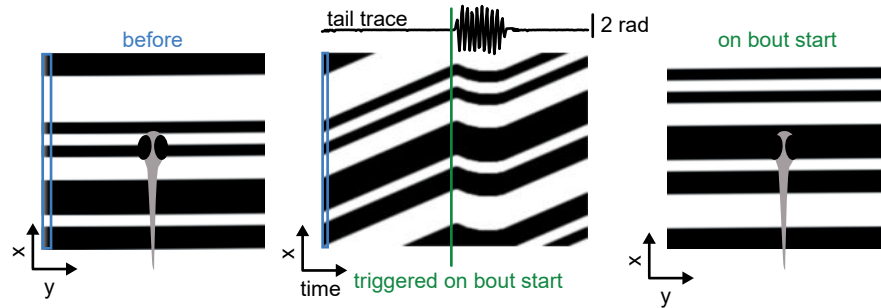
Figure 25: Behavioral triggered average. Visual stimulus is normally 2D, however, the information of x is repeated in y, thus, we reduce the stimulus to 1D and use time as the second dimension. This shows the visual stimulus over time relative to the fish (fish is not to scale). It moves forward in time, potentially evoking OMR. After the experiment, we compute the visual stimulus patterns triggered on bout start with an interval of ± 2 s.

2.6   DATA ANALYSIS

Data analysis was performed using Python 3.6 using the Anaconda environment. Packages used to analyze and handle the data include numpy, scipy, pandas, scikit-learn, scikit-image, deepdish, multiprocessing, Keras, OpenCV, gspread, and glob. Data shown in this thesis are plotted using matplotlib and seaborn. Single cell neurons were traced using NeuTube. Figure arrangement and image postprocessing was performed using Adobe Illustrator and Photoshop CS5.

2.6.1   *Behavioral data*

Behavioral data was acquired using custom written software in Python (see 2.4.3). Next to the time stamps for each camera frame, we saved relevant behavioral data such as cumulative tail angle, vigor, grating speed and position of the grating. To identify bouts, we set a threshold vigor to identify swimming (above threshold) and resting (below threshold) periods. Next, by taking the difference of the trace in time, we identify bout starts (1) and bout ends (-1). Using bout starts and bout ends, we compute the mean bout duration (i.e. swimming time) and the mean interbout duration (time between two consecutive bouts).

Behavioral-triggered average (BTA)

In the first study, we computed the stimulus history for each bout start, in other words, performing reverse correlation to determine which stimulus was leading to a bout (see also Figure 4 and 25). Empirically, we found that a history of two seconds is sufficient. We were also

identifying a two seconds window into the future, to investigate if the mean stimulus showed some structure after bout start. Every bout longer than 150 ms was considered as a proper bout and was included in the analysis, to avoid contamination with struggles and escapes. We reduced the stimulus dimensionality to 1D, because the stimulus is only unique in one dimension (rostral to caudal), and stretched in the other (left to right). We generated stimulus patterns using spatio-temporal stimuli with two dimensions: space (1D as described before) and time. We calculated the behavioral triggered average (BTA) by averaging all generated patterns across bouts, and then across individual fish, analogous to the spike-triggered average as introduced before (Schwartz et al. 2006):

$$BTA = \frac{1}{N} \sum_i^N \frac{1}{n_i} \sum_j^{n_i} \vec{s}_j$$

Where N is the number of total fish, n_i the number of bout starts and $\vec{s}_j$ the spatio-temporal stimulus with a history of one to two seconds.

To extract the grating directly from the camera image, we took a background image without presenting any stimulus. We focused on a part close to the border of the image to avoid contamination with behavior and background subtracted every camera image with the background image. We subsequently applied a threshold to this image to gain binary bars. The eye of the fish was always centered on the center of the camera chip (XIMEA MG022RG-CM).

Nonlinearities were determined using the binned dot product of the BTA with the stimulus over time (Schwartz et al. 2006). The nonlinearity is the ratio between stimuli in each bin at bout triggered events and occurrences of all stimuli in that bin.

Behavioral-triggered covariance analysis (BTC)

Similar to the spike triggered covariance (Schwartz et al. 2006), the behavioral triggered covariance is calculated using the following formula:

$$BTC = \frac{1}{n_{bouts} - 1} \sum_i^n (\vec{s}_i - BTA)(\vec{s}_i - BTA)^T$$

We pooled all bouts from all fish together (N=52 fish) and subtracted the overall mean (i.e. the behavioral triggered average, *BTA*) of the whole dataset. We retrieved the eigenvalues and eigenvectors using singular-value decomposition of the *BTC* matrix using the scipy's implementation of the LAPACK SVD solver.

Generalized Linearized Model (GLM)

We fitted a generalized linear model (GLM) similar to the one described in (Haesemeyer et al. 2015). We fitted the following equation by min-

imizing the negative log likelihood. The input to the model is the grating history leading to a bout x_i. The model tries to predict the labels given the features, i.e. binary bout starts (0 no bout start, 1 bout start). We used 60 Hz as time basis.

$$min_{\beta_0,\beta} \frac{1}{N} \sum_{i=1}^{N} L(y_i, \beta_0 + \beta^T \dot{x}_i + \lambda[0.5(1-\alpha)]||\beta||_2^2 + \alpha||\beta||_1$$

We set $\alpha = 0$, thus neglecting L_1 regularization, because the model does not converge otherwise. The model with best performance as determined by receiver operating characteristic (ROC) analysis had a $\lambda = 0.088$. We used the pyglmnet package for fitting the data. Data was fitted on an 80% fraction of total bouts and model performance was evaluated for the whole data set of a given fish. To evaluate model performance we performed bootstrapping by shuffling the labels and determines true and false positive and negative rates. We shuffled 100 times and present the average with standard deviation across shuffles.

2.6.2 *Imaging data*

h5viewer   Imaging data was acquired using custom-written LabVIEW programs and stored as chunked, uncompressed Tagged Image File Format (TIFF) files. For further processing, TIFF files were combined, compressed and stored in HDF5[8] file format to achieve a single file per trial and plane. The deepdish library was used to interface PyTables and to load and save HDF5 files. An easy way to visualize compressed HDF5 files is to use the *h5viewer* (private repository on the Portugues lab Github account). It features not only HDF5 files, but also Nearly Raw Raster Data (NRRD)[9] and TIFF files, works with Drag&Drop, accepts pasting from clipboard and has easy shortcuts to invert a stack or image or to create maximum intensity or sum projection across z or time.

2.6.2.1 *Deinterlacing*

The two-photon microscope creates an interlacing artifact by scanning the laser beam back and forth. Further, due to the optical properties of scan lens and tube lens, that are just achromatic doublets with no theta correction, the beam wavefront cuvature is bent causing non-linear abberations in the far field of view. To compensate for these artifacts, we estimate a non-linear transformation matrix of each half-image,

---

8 HDF5 is a hierarchical data format that efficiently stores large amounts of data and widely supported by many software platforms, such as Java, Matlab, Python, R and Julia.
9 NRRD files are multidimensional files similar to TIFF files, can be, however, much better compressed, have richer metadata, and are usually used when working with CMTK.
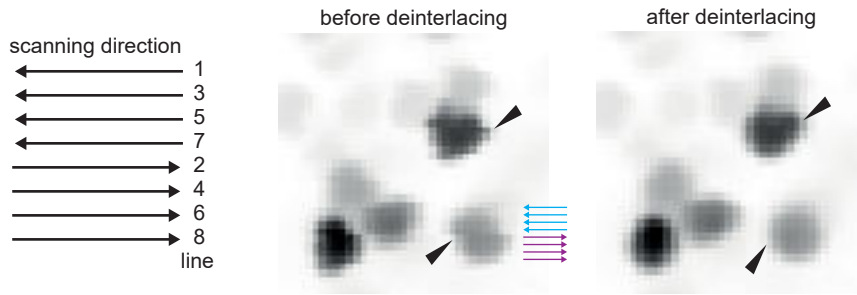
Figure 26: Deinterlacing procedure. The galvo mirros scan the laser beam back and forth over the whole image plane in multiples of the eight line scheme. Without deinterlacing, there are image artifacts visible (black arrow heads). After deinterlacing, nuclei look nicely round.

that has an offset of four lines to each other (see Figure 26). The non-linear affine transformation is estimated across the stack and applied to each acquired frame.

2.6.2.2 *Registration*

Individual frames are registered either to the mean of the stack or the first ten frames, depending on the experiment. Registering is performed using the cross-correlation in the fourier domain of the image (Guizar-Sicairos et al. 2008). For sub-pixel precision, the discrete fourier transformation is upsampled in a small neighbourhood. An rigid transformation is applied to shift the target image to the reference image using the functions shipped with scipy or skimage. *in plane*

After registering the stack for each trial or plane, the stack is registered across trials and planes from the center to the dorsal and ventral planes of the acquired stack. *across planes*

2.6.2.3 *Anatomy-based segmentation*

Anatomical segmentation was performed on datasets that were acquired in fish where the calcium indicator was restricted to the nucleus of the neuron via an $H2B^{10}$ or an NLS tag (see Figure 26 as example). For segmentation we used the template matching algorithm implemented in scikit-image. Using empirical studies, we saw that either a random nucleus or a gaussian is efficient in detection of nuclei. The template matching algorithm returns a correlation map between the template (i.e. random cell or gaussian) and the image anatomy stack. Here, it is important to note that the standard deviation across imaging frames instead of the sum projection gave rise to a higher sensitivity of event detection.

A 2D version of that algorithm was implemented in the data analysis pipeline in a collaboration with Reinhard Köster and Jakob von Trotha *Braunschweig*

---

10 H2B is a histone, part of the DNA packaging machinery.

at the TU Braunschweig for light-sheet imaging analysis. A 3D version was used to count Purkinje cells in a confocal dataset (see Figure 52 and Knogler et al. 2019) and to segment Purkinje cells in a two-photon imaging dataset focusing on the role of Purkinje cells during closed and open loop (data not shown).

2.6.2.4 *Correlation-based segmentation*

Correlation-based segmentation was performed as introduced in Portugues et al. 2014 and explained in depth in Michael B. Orger and Portugues 2016. Briefly, for each imaged plane, i.e. an image stack of time x width x height, every spatial pixel is correlated with the summed activity of 5x5 neighbouring pixels. This results in a correlation map that is used to find seeds for the ROI growing algorithm.

ROIs are grown by iteratively adding neighbouring pixels that correlate highly with the seed pixel. Other implementations, however, use the correlation of the new neighbour pixel with the mean of all already added pixels to the ROI. If a neighbouring pixel exceeds a given euclidean distance to the seed pixel or its correlation value with the seed pixel is below a pre-defined threshold, the ROI growing routine is finished. Next, a new seed pixel is selected and fed into the ROI growing routine. This process continues until the seeding correlation is below a given threshold or a maximum number of seeds are drawn from a given stack.

Algorithms are implemented in Python using mainly numpy and numba, and perform well in a multi-threaded environment using the *threading* library.

2.6.2.5 *Extracting activity from calcium signals*

Neural activity was determined either with $\frac{\Delta F}{F}$ or using normalized, i.e. *z*-scored activity $\hat{F}$, where $\overline{F}$ is the mean fluorescence over time, and σ_F denotes the standard deviation of the fluorescence over time:

$$\frac{\Delta F}{F} = \frac{F_t - F_0}{F_0}$$

$$\hat{F} = \frac{F - \overline{F}}{\sigma_F}$$

2.6.2.6 *Clustering*

The scikit-learn implementation of the *k*-means algorithm was used to cluster activity traces in an unsupervised manner. The number of clusters were determined empirically.

2.6.2.7 *Regression*

To determine if neurons are specifically coding for sensory stimuli and/or behavioral components, we built regressors that would re-

semble an ideal neural activity. Because neural activity is acquired as a transient fluorescence signal related to calcium, we convolve the regressor with the calcium kernel. The calcium kernel describes the risetime and decay time of the fluorescence signal upon an action potential. We assume an infinitely fast rising time and a one-exponential decay for the dissociation of calcium and the calcium sensor (as described previously in Akerboom et al. 2012; T.-W. Chen et al. 2013). The following equation explains the mathematical procedure:

$$R(t) = r(t) * k(t),$$
$$k(t) = e^{-\tau t},$$

where $R(t)$ is the convolved regressor $r(t)$ with the function, i.e. convolutional kernel, $k(t)$ that is a single exponential function with a decay time constant τ, that is typically set to the decay time of the calcium sensor. Previous studies suggested around 1 to 1.5 seconds for GCaMP6s (T.-W. Chen et al. 2013; Dunn et al. 2016b).

Regression analysis was performed either on ROIs extracted using anatomical or correlation-based segmentation or voxel-wise across an acquired volume. The latter computes in an unbiased way the correlation of each voxel with the regressor chosen. For multiple regressors, we used multilinear regression. Multilinear regression tries to find a linear combination of regressors $r_i(t)$ to match accurately the fluorescence signal $F(t)$:

$$F(t) = w_0 + w_1 r_1(t) + w_2 r_2(t) + \ldots + w_n r_n(t),$$

where w_i is the weight of each $r_i(t)$ and w_0 the bias term. The linear equation is solved using the scikit-learn implementation of LinearModel. In these studies, we did not use any regularization terms, because the performance of the LinearModel itself was sufficient.

For the swimming correlation map shown in the first study (Figure 48), we created a regressor using the swimming vigor for each plane and convolved it with the GCaMP6s kernel. ROIs that are correlated more than 0.8 were considered swimming related ROIs.

Brain region identification

To identify brain regions, we used the annotations provided by the Z-brain atlas (Randlett et al. 2015). First, we morphed the Tg(*elalv3*:GCaMP5g) confocal stack provided by the Z-brain atlas to our reference brain (as used in Knogler et al. 2017) using the Computational Morphometry Toolkit (CMTK) to compute a general transformation matrix. We used this transformation matrix to morph each annotation map to our reference brain. Then, we iterated over every voxel in our cluster map and determined if this voxel is contained in any annotated map. Annotations with high coverage were considered being present in the cluster.

Injection of Fyn-mClover3:PC
in aldoca:gap43-mCherry inx

Imaging at high-resolution
for cellular anatomy

Imaging at lower resolution and zoom
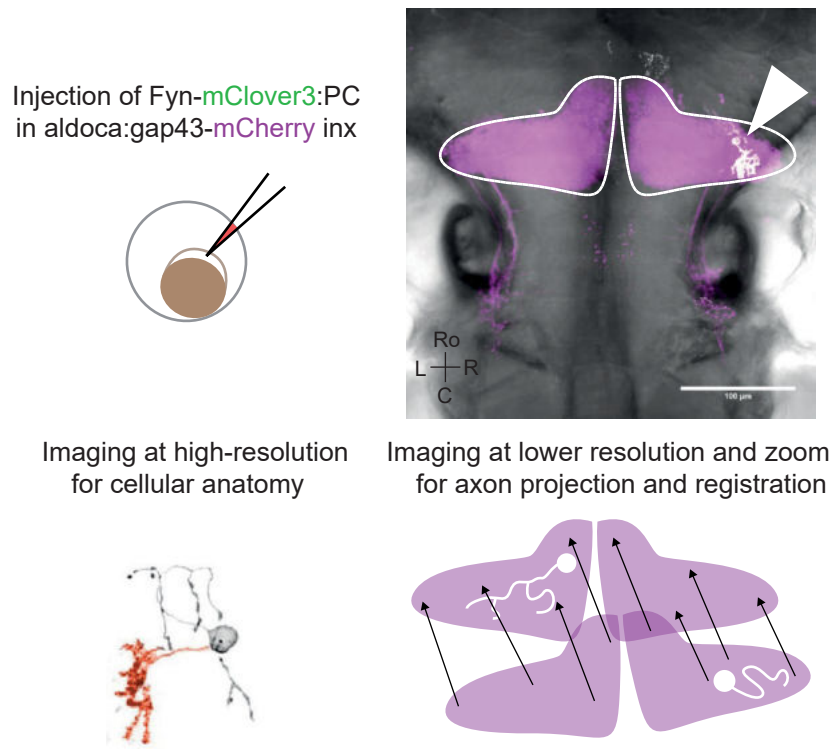for axon projection and registration

Figure 27: Sparse labelling of Purkinje cells. Embryos were injected with a construct specifically labelling Purkinje cells in green (Fyn-mClover3:PC). We injected in an incross of the *aldoca*:gap43-mCherry background (Casper fish, that lack melanophores and iridophores, *mitfa*$^{-/-}$;*roy*$^{-/-}$, described in White et al. 2008). This allowed us to image the sparse labelled Purkinje cells in reference to all Purkinje cells. Two stacks were acquired: one for high-resolution imaging (bottom left panel) and the other for axon tracing and registration (bottom right panel, see text).

regionfinder   This feature is part of a program called *regionfinder* and is available in the Github repository of the lab. It can also be used to easily look at morphed stacks in relation to our reference brain.

2.6.2.8   *Single neuron tracings*

For Purkinje cell single cell labelling, Fyn-mClover3:PC was injected in an incross of *aldoca*:gap43-mCherry (see Figure 27). The *aldoca* fish label all Purkinje cells with a red fluorescent indicator. This red channel was used as a reference template to morph individual fish together. Sparse Purkinje cells were imaged in the green channel (excited with a 488 nm laser) at a high-resolution close to the diffraction limit (ca. 125 nm sampling for each px).

High-resolution images were deconvolved using Richardson-Lucy deconvolution (Lucy 1974; Richardson 1972) as implemented in the FIJI plugin DeconvolutionLab. The point-spread function (PSF) used for deconvolution was created using the PSF Generator plugin for FIJI. The

PSF was based on the Born&Wolf model. Settings were 1.0 NA, 1.333 for refractive index (water immersion), step size 500 nm, px-width depending on acquistion settings, on average 125 nm/px. Excitation wavelength: 488 nm. The Richardson-Lucy algorithm works iteratively, for our purposes 10 to 20 iterations were sufficient and avoided the occurence of artifacts. Note: Other implementations of the Richardson-Lucy algorithm were tested (skimage and own implementation in Python), however, the DeconvolutionLab software was significantly faster than all other implementations tested. After deconvolution, all stacks were manually inspected and background fluorescence, autofluorescent skin and artifacts were manually removed. All cells were interpolated to an xy spacing of 200 nm.

Neurons were traced using NeuTube (Feng et al. 2015). Tracing information was stored in swc file format (Cannon et al. 1998)[11]. Using custom written software in Python, the swc file was automatically transformed into a TIFF stack by drawing lines in 3D between each two adjacent, connected nodes. Drawing functions already implemented in scikit-image or OpenCV only work in 2D. To draw lines in 3D, I re-implemented the Bresenham algorithm (Bresenham 1965). A sphere at the location of the soma with a radius of 5 μm was also drawn and was implemented by drawing 2D intersections of the sphere, i.e. circles, using the plane spacing in z. This program circumvented the tedious operations in FIJI and gave the same results. The drawing functions are available on my and the Portugues lab Github account.

Drawing in 3d

Reference channels (see Figure 27) were morphed to the Purkinje cell reference stack that has been morphed to the lab reference brain (as used in Knogler et al. 2017) using CMTK (Rohlfing and Maurer 2003). The same transformation matrix was used to morph the traced neurons to the reference brain. For intepretation reasons, we also morphed all neurons to the same hemisphere.

Evaluation of mCarmine

We excited mTFP1 and mCarmine with a 442 and a 633 nm laser, respectively. To compare mTFP1 and mCarmine quantitatively, we determined a performance index (PI) in a deconvolved z-stack (Richardson-Lucy algorithm with a theoretical PSF for mTFP1 and mCarmine) (Kirshner et al. 2013; Sage et al. 2017) that covers the interpositus nucleus (IPN) (around 240 ± 28 μm deep) with re-adjusted laser settings. The PI shows the relation of signal (the higher the fluorescence, the better) to brightness (the brighter the fluorophore, the easier it is to emit photons and thus, cause fluorescence) and laser power (the less

---

11 The swc file format is a standardized, ASCII-based file format to save 3D structural information of nodes and their connection to each other.

laser power is needed to emit photons, the better). Thus, the following equation describes the PI

$$PI = \frac{\overline{F}}{b \cdot \beta},$$

with $\overline{F}$ being the mean fluorescence in a given frame, b the brightness of the fluorophore (54.0 and 6.0 for mTFP1 and mCarmine, respectively, brightness is the product of quantum yield and the molar extinction coefficient) and β the laser power used in that frame (ranging from 0 to 1, where 0 is off and 1 is maximum laser power). The PI was normalized to the mean PI of mTFP1.

Statistics

Significance was tested using Student's t-test where applicable. P-values below 0.05 were treated as significant, corrected by Bonferroni correction for multiple tests. All error bars represent standard error of the mean unless otherwise stated. Confidence intervals show 95% of variance (i.e. two standard deviations).

RESULTS

3.1 STUDY I:

OPTOMOTOR SWIMMING HAS LOCAL AND GLOBAL FEATURES.

In the first study, we investigate what visual features contribute to evoking the OMR. We first behaviorally tested fish with random binary gratings to use reverse correlation, similar to the spike-triggered average for receptive fields. The so called behavioral-triggered average (BTA), to determine if there is some structure in the visual stimulus triggering the OMR (see introduction and Methods). Next, we were looking at the stimulus parameters, if they alter the main visual feature identified in the BTA, the light-dark transition. Then, we tested the performance of a replay of the BTA and some variants and could show, that both, global whole-field and local light dark transitions contribute to the OMR significantly. We used two-photon whole-brain calcium imaging to identify units correlated with a whole-field filter light-dark transition stimulus. Lastly, we tested if a generalized linear model is suitable to explain the data.

3.1.1 *The optomotor response is preferentially elicited after a light-dark transition*

To determine which features of the binary grating induce swimming behavior, we presented head-restrained larval zebrafish with forward-moving whole-field visual stimuli consisting of black and white bars from below (see Figure 17). The visual stimulus was generated randomly for each experiment, such that black and white bars occurred with equal probability (see Methods). In other words, when picking random instances of the visual stimulus across the experiment, the average visual stimulus across the field was gray. Using real-time behavioral tail tracking, we provided the fish visual feedback by changing the visual stimulus speed in proportion to the swimming strength of the fish (see Figure 28, top left panel, and movie).

Example bout

For every fish we computed the reverse correlation of the presented visual stimulus with behavioral onset to gain the BTA (see Methods and Figures 25 and 28). The BTA consists of a spatiotemporal filter (the history part of the BTA, Figure 28, right panel) that is stereotypical across individuals (Figure 29).

The BTA filter is globally largely unstructured one to two seconds before bout start. Structure emerges around 500 ms before bout start that comprises a local light and dark luminance band moving forward,
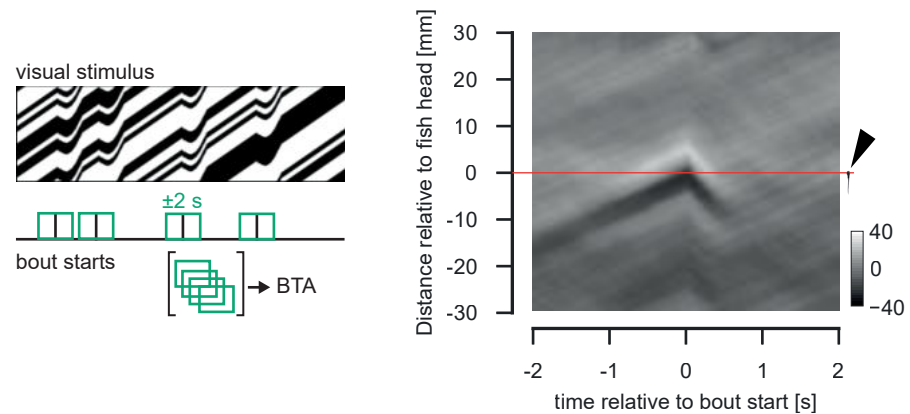
Figure 28: The behavioral triggered average contains structure. From the visual stimulus shown to the fish, we extracted the bout starts from the tail trace and triggered the visual stimulus on the bout start with a window of ± 2 s. On the right, the BTA resulting from averaging the individual BTAs of 52 fish is shown. The position of the fish's head is indicated by the red line and positive y values denote positions in front of the fish. The larva on the right, indicated by the black arrow head, is drawn to scale. The z-scale denotes luminance intensity variations from baseline.
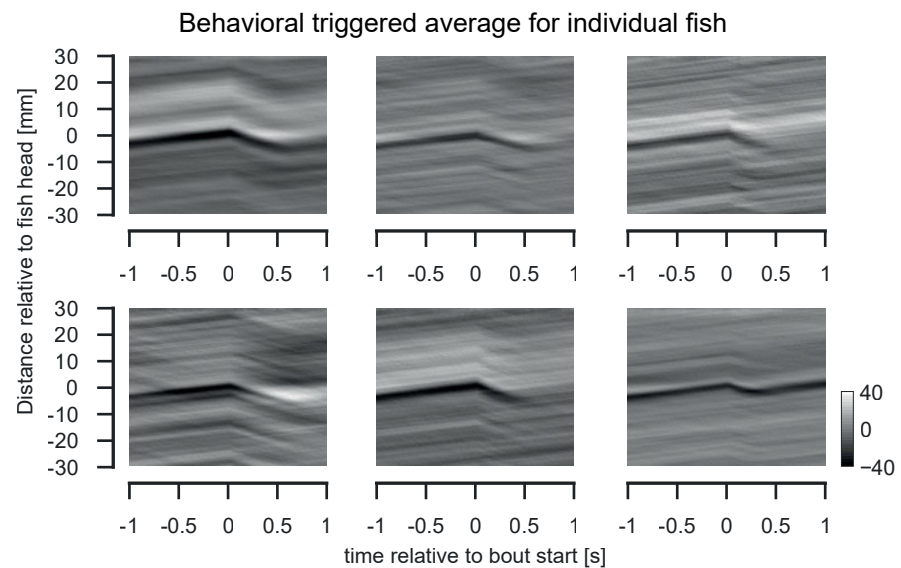

Figure 29: The BTA aligned to bout starts for different six individual fish. The same light-dark transition trend is apparent across fish. In individual fish is more noise apparent than in the total average of 52 fish. Heatmaps indicate relative luminance intensity.
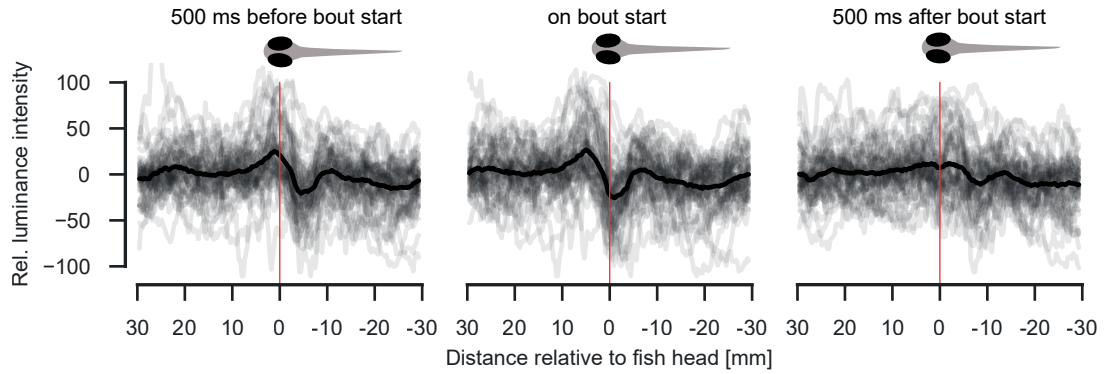
Figure 30: Fish experience a light stimulus compared to baseline, and then swim after perceiving a light-dark transition. After swimming, the luminance is homogenously at baseline.

that coincides with bout start when the border from the light to dark area reaches the head of the fish (Figure 30 and 31a).

The fish experiences this light-dark transition (Figure 31b,c) with a peak-to-peak duration of around 500 ms. Interestingly, these luminance changes are very local, roughly ± 5 mm away from the head of the fish (Figure 31c). The results shown in Figure 31a and Figure 31c further indicate that fish don't start swimming at the local luminance minimum, but rather on the light-dark transition itself. Roughly 500 ms after swimming, the average luminance levels of the filter are not different from the luminance levels during the unstructured period before bout onset (Figure 31b,d).

In line with an LNP model, we computed the nonlinearity for the BTA across fish (Figure 32) and saw that it is in line with an asymmetric point-linearity as seen in STA nonlinearities (Schwartz et al. 2006).

In order to confirm these results, we repeated these experiments in higher spatial and temporal resolution to better extract the exact stimulus presented in the near visual field of the fish as suggested by Figure 30 directly from the camera image to avoid stimulus uncertainties due to technical limitations (see Methods). These findings confirmed that the filter indeed shows fish swim at a local light-dark transition (Figure 33).

As we observe structure in the average stimulus that triggers behavior, we next asked if there is a structure in the stimulus ending the bouts. Thus, we performed a similar analysis for bout ends, however, in contrast to bout starts, we found no apparent structure in the bout end-triggered average filter (Figure 34a). As suggested by Figure 31a and Figure 34b, we tested if that unstructured gray is able to trigger ending the bout. We performed an experiment where the whole visual field turns gray after detection of bout onset. Fish swim significantly shorter (328 ± 13 ms vs. 367 ± 13 closed-loop, $p<0.05$, Student's t-test, Figure 34c), but this effect was very small, indicating that the local
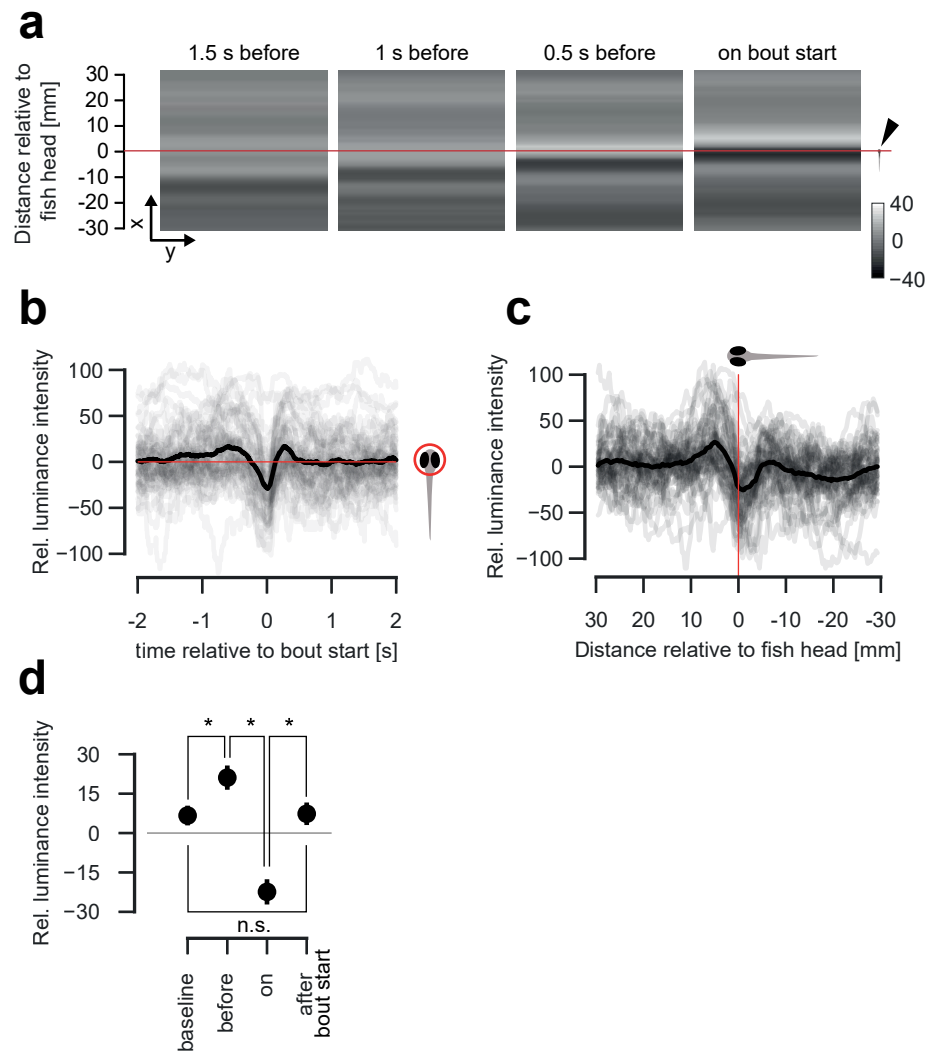
Figure 31: Fish swim after a light-dark transition. (a) The average visual stimulus in 500 ms steps leading to bout start. As in Figure 30, the fish's position is indicated with a red line and black arrow head. (b) The average luminance profile over time on fish head across fish (black) with averages for individual fish (light gray). (c) Average luminance intensity across fish (black) relative to fish's position with averages for individual fish (light gray). (d) Average luminance across fish on fish head at baseline, 500 ms before bout, on bout and 500 ms after bout. Note, that baseline luminance levels and luminance levels 500 ms after the bout do not differ. Asterisks show significance levels with $p<0.05$. Error bars indicate S.E.M.
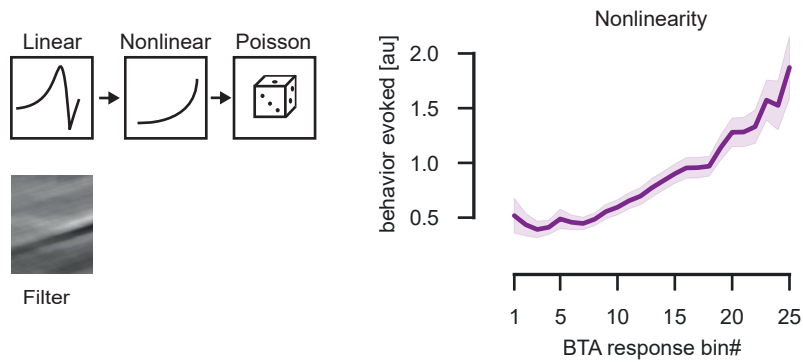
Figure 32: Nonlinearity is as expected in an LNP model. Details see Methods. On the left side, a schematic of an LNP model is shown, with the linear filter gained from the BTA analysis.
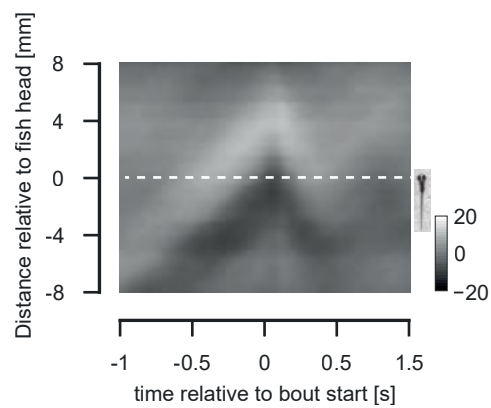

Figure 33: Local filter across twelve fish. Local luminance levels were gained by extracting the grating directly from the camera image. A representative fish is shown right next to the filter for a size comparison. Same filter is present as indicated by experiments with a greater field of view (Figure 28).

luminance levels are important to trigger swimming but that other factors may contribute to controlling swim duration and stopping.

In summary, these experiments show that a forward moving whole-field visual stimulus exhibits on average a striking local and not global structure that is stereotypic across fish and consists of a local light-dark transition.

Light-dark transition is largely unaffected by stimulus parameters.

To understand the visual features that optimally drive OMR swimming, we next investigated how the BTA filter depends on the stimulus parameters, as it has been shown previously that grating speeds influence behavior (Severi et al. 2014). Changing the bar width or stimulus speed did not affect the most salient features of the filter (compare Figure 31c and Figure 35), namely the light to dark transition centered on the larva's head. Small changes in filter features, such as increased peak to peak magnitude can be accounted by the different stimulus statistics (Figure 35, left panel, and Appendix). With low stimulus speeds the light-dark transition is pronounced, however, fades with increasing speeds, indicating that fish are presumably faced with sensorimotor processing delays (Figure 35, right panel, and Appendix). Behavioral parameters, such as mean bout duration and mean inter-bout duration (i.e. time between bouts) is not affected by these changes in stimulus parameters (Figure 36). The BTA across stimulus parameters is highly similar to the one shown in Figure 28, incorporating more variance because of the higher stimulus space (Figure 37).

We next were interested if the BTA is dependent on the average global luminance levels. When we varied the ratio of white to black bars, the average is not gray, but shifted to darker or lighter luminance levels, respectively. When determining the BTA filter for these different white:black bar ratio stimuli, we observed a similar light dark transition compared to the BTA shown in Figure 37, indicating that fish likely adapt to the average luminance level of the stimulus (Figure 38, see Appendix). We also verified that the fish behavior and filter nonlinearities stayed constant across white:black bar ratios (Figure 38).

In certain cases, reverse correlation may not reveal all stimuli that drive a response. If both a stimulus and its inverse are equally likely to elicit a spike/behavior, then the average of these stimuli would have little structure (Schwartz et al. 2006). We therefore performed behavior triggered covariance analysis (Schwartz et al. 2006, and methods) on our dataset focusing on the two seconds prior to bout start to look for evidence of symmetric filters (Figure 39a). Using singular-value decomposition on the covariance matrix, we obtained eigenvectors of the stimulus covariance matrix, sorted by their eigenvalues, that provide directions which explain the most variance. We performed the same analysis on our dataset with shuffled bout start labels. We sorted the eigenvalues in descending order and found that eigenvalues
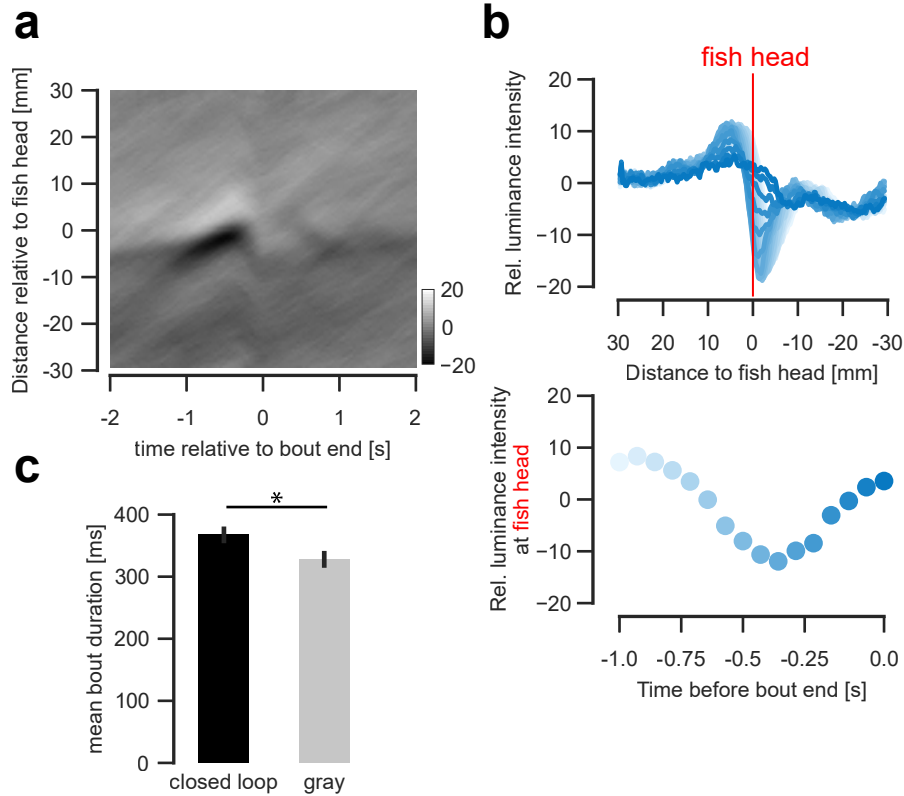
Figure 34: Bout end triggered average shows no filter response. a) Bout end triggered average across fish, grating speeds and bar sizes. The bout inducing filter is still apparent. Heatmap shows relative luminance levels b) Relative luminance profile for visual scene (upper panel) and at fish head (indicated by red line), color coded in time (one second before bout end to bout end depicted in increasing blue saturations). The mean luminance profile approaches an average even luminance across the visual field. Around 400 ms before bout end (the average bout duration of a fish, as seen in c)), the luminance at fish head is minimal, and during swimming the luminance increases again. c) Mean bout duration of fish when provided normal closed-loop reafference or only even gray that relates to the grating with 0% contrast by overall constant luminosity. With this neutral stimulus, swim significantly less (p<0.05), but still close to normal closed-loop bouts. Shaded area indicate S.E.M.
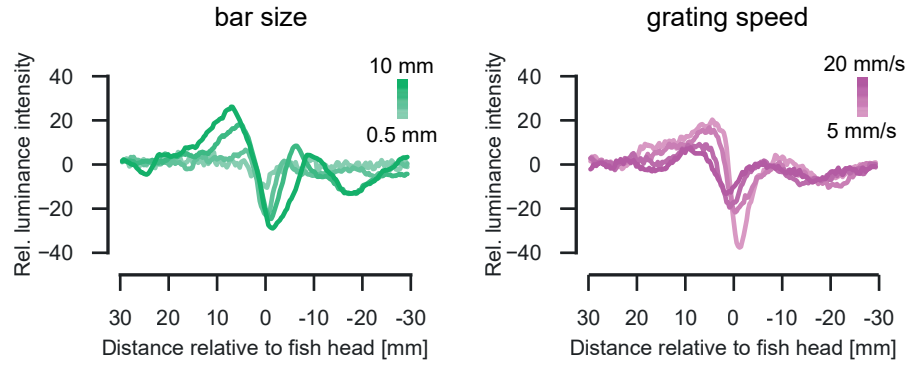
Figure 35: Left panel: mean luminance intensity profiles at bout start for different bar sizes (0.5 mm, 2.5 mm, 5 mm and 10 mm, shown from light to dark green). Right panel: mean luminance intensity profiles for different grating speeds (5, 10, 15 and 20 mm/s shown in light to dark magenta).
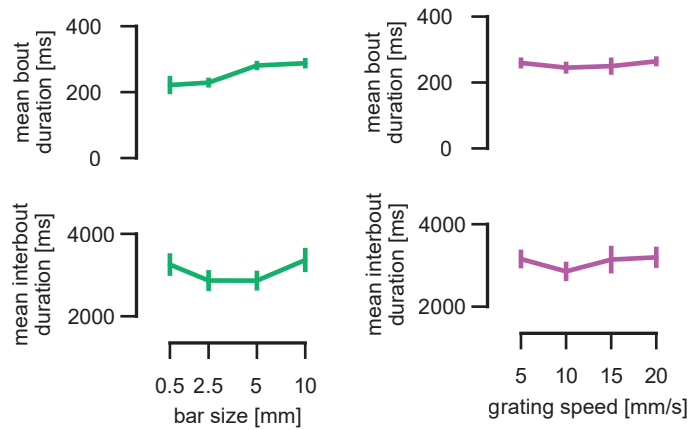

Figure 36: Mean bout and interbout duration for different bar sizes (left, green) and grating speeds (right, magenta), respectively. See also Figure 35. Error bars indicate S.E.M.
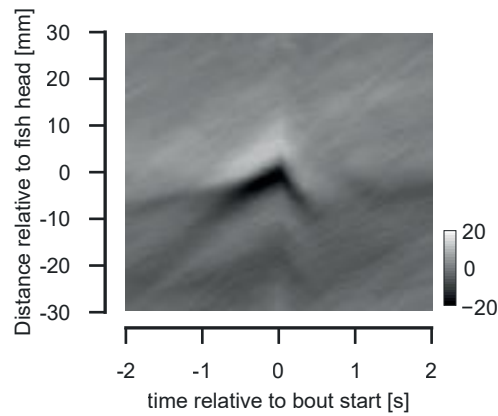
Figure 37: Average BTA for all grating speeds and bar sizes across 52 individual fish BTAs. The structure is highly apparent roughly one second before bout start and disappears rapidly earlier than one second before bout start and almost immediately after bout start.
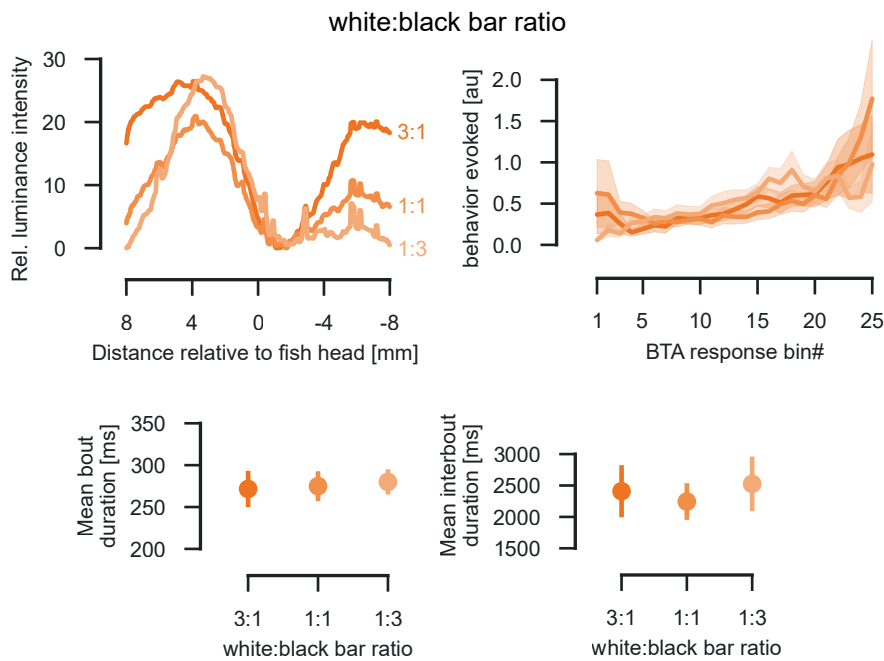

Figure 38: Left panel: relative intensity profiles aligned to the minimum for a local random binary grating experiment with varying white-to-black bar ratios, for 1:3, 1:1 and 3:1, respectively. Right panel: Nonlinearities for all bar ratios (compare to Figure 32). Bottom panels: mean bout and mean interbout duration for different white-to-black-bar ratios. Error bars indicate S.E.M. Top right panel: nonlinearities for different white-to-black bar ratios with shaded error shows S.E.M.

for shuffled bout starts and true bout starts are very close to each other. Eigenvalues from shuffled bout starts covariance analysis tend to explain more variance than true bout starts (Figure 39b).

When looking at the eigenvectors, we found that eigenvectors were also very similar between random instances and bout starts. Interestingly, eigenvectors cover a whole-field, global forward moving sine-like stimulus that increases its frequency along higher eigenvalues and -vectors (Figure 39c). Later eigenvectors do not show any structure compared to first eigenvectors (Figure 39c). Given the similarities between shuffled and bout starts, we propose that the covariance analysis does not yield further symmetric filters to be further considered in specific behavior triggering. Noteworthy, it showed that global whole-field motion is symmetric, as this global whole-field motion becomes gray in the BTA.

To summarize, we could show that the BTA's light-dark transition is stable across a variety of stimulus conditions, which underlines the BTA's importance in OMR swimming. Together with our covariance analysis, we show that symmetric global whole-field motion accompanied by a local light to dark transition close to the larva's head is an integral part of OMR.

3.1.2   *Behavioral response onset is mediated by the light-dark transition gradient*

Stimuli

To precisely examine the importance of both global and local motion in eliciting OMR swimming we presented larvae with visual stimuli that differentially provide relevant global and local information (see movie). The first one, which we refer to as filter replay, consisted of the BTA as shown in Figure 37. It is replayed to the fish as shown in Figure 31a, for the full duration of three seconds before and following when the optimal visual trigger for the bout would occur. The second, which we term whole-field motion, consisted of the BTA's luminance profile at bout start (see Figure 31c) stretched in 2D and moved over the fish in a caudal to rostral direction. The third stimulus consisted of the BTA shuffled in space (i.e. at every instance in time, the spatial profile of the BTA was shuffled), to avoid motion inducing two-point correlations. For the space-time profile of the filter replay and the whole-field motion stimulus see the first two panels in Figure 43b.

By definition, the BTA should comprise a close to ideal stimulus to evoke the behavior. When comparing the individual visual stimuli used to generate the BTA to the average BTA obtained across trials and across fish, we see that the BTA in fact contains no global and only local motion and is mostly unstructured (compare to Figure 37). We found that the filter replay was nonetheless capable of evoking swimming (Figure 40). We observed, however, that the whole-field motion stimulus, was more effective than the filter replay in eliciting
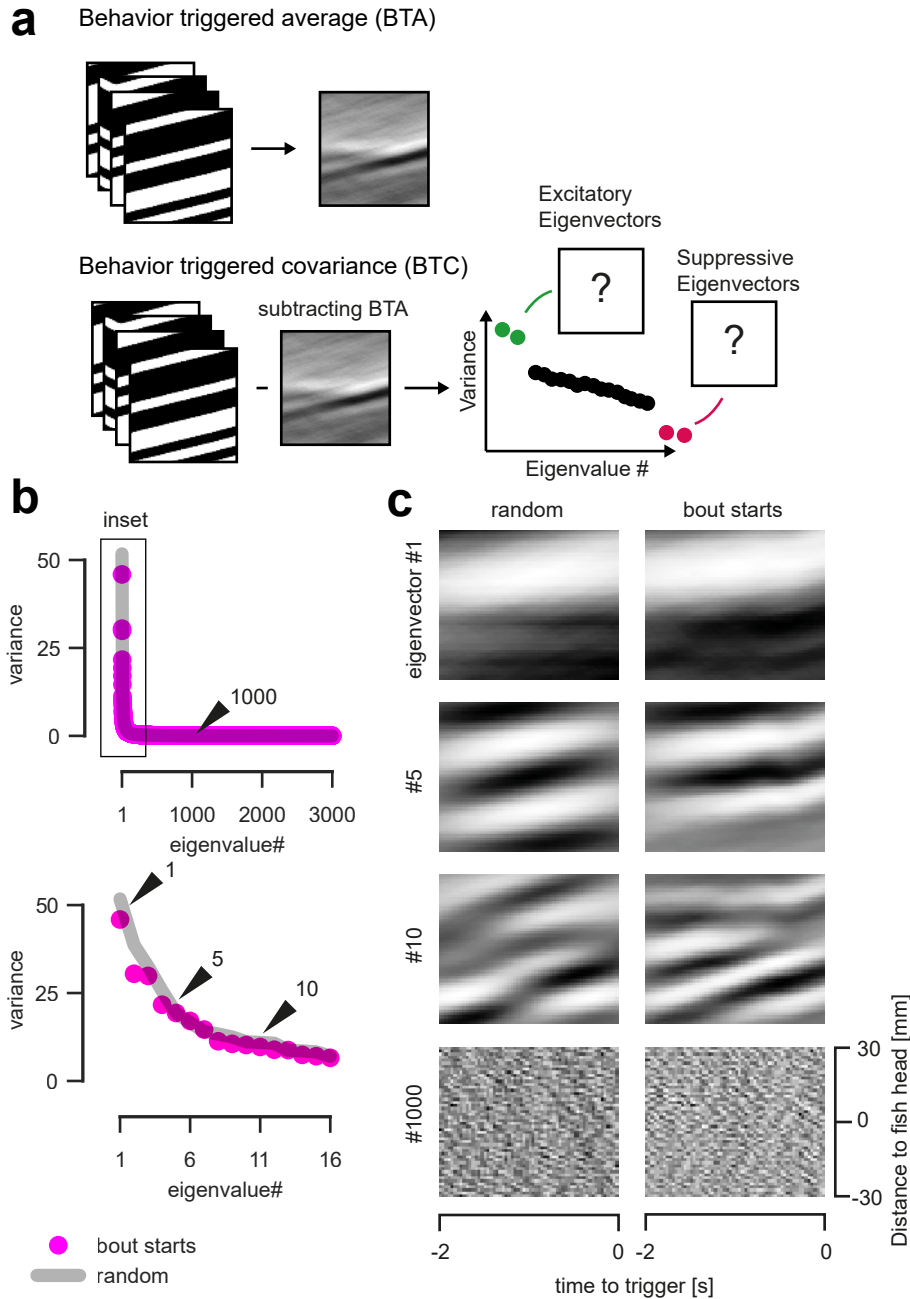
Figure 39: Behavior triggered covariance analysis did not reveal further feature subspace. a) We determined the first filter by performing BTA to determine if more filters contribute to the OMR. b) Eigenvalues gained from singular-value decomposition of the covariance matrix of bout starts (magenta circles). The gray shade indicates the eigenvalues gained from a singular-value decomposition of the covariance matrix of shuffled bout starts. Example eigenvectors shown in c) are labeled with a black arrowhead and the respective eigenvalue number. Lower panel shows the black rectangle inset enlarged. c) Example eigenvectors for random and bout-triggered instances as derived from b).
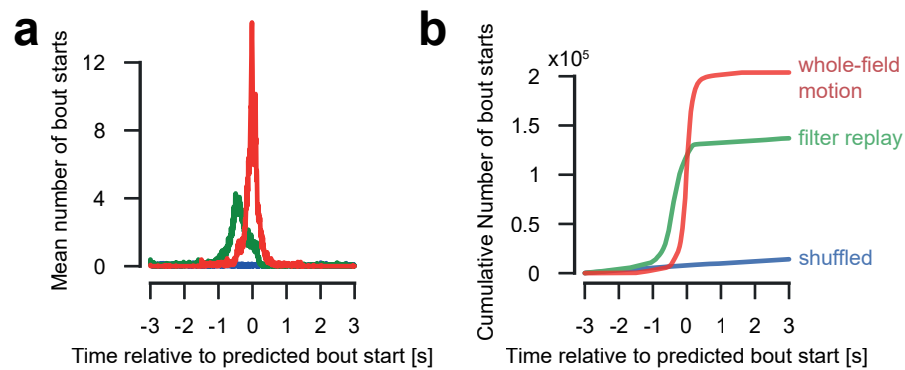
Figure 40: Whole-field filter, but not filter replay evokes predicted behavior. a) Mean number of bout starts at given time points relative to predicted bout start. Blue lines represent when the grating was shuffled, green filter replay and red whole-field motion of average trigger (N=28). b) Cumulative distribution of bout starts (shuffled = 1414, filter replay = 13699, whole-field motion = 20380) as shown in a). The midpoint for filter replay is -0.41 s before predicted bout start, for whole-field motion it is -0.15 s. The shuffled bouts are distributed equally across the trial. Colors as in a).

swims, indicating that whole-field motion is an important feature for triggering OMR, however, its structure seems to be irrelevant (see Figure 28).

In addition, swims in response to the whole-field motion stimulus occurred closer to the predicted time of bout start, whereas filter replay-elicited bouts occurred earlier than expected (Figure 40). We therefore hypothesized that it was the difference in the stimulus presented in the far visual field that was responsible for the different behavioral profiles observed between the filter replay and the whole-field motion stimulus.

To test this hypothesis we presented fish with the filter replay locally, in an 8 mm window surrounding the larva, and combined this with different stimuli in the far caudal visual field (see Figure 41, Figure 42, and Methods). As a control we included in this experiment the whole-field motion stimulus as presented in Figure 40. The results show that this whole-field motion stimulus again elicited the most swimming (Figure 42). Notably, all other conditions exhibited similar behavioral profiles with fewer bouts and again earlier than expected (Figure 42). This was even the case for the stimulus that combined the filter replay locally and whole-field forward moving gratings in the caudal visual field, suggesting a strong dependence of the behavioral profile on the local luminance transitions, although the whole-field component yielded a higher amount of bouts close to the whole-field motion levels (Figure 42).

We analyzed these local luminance transitions for the stimuli we presented and noticed that the luminance gradient of the whole-field
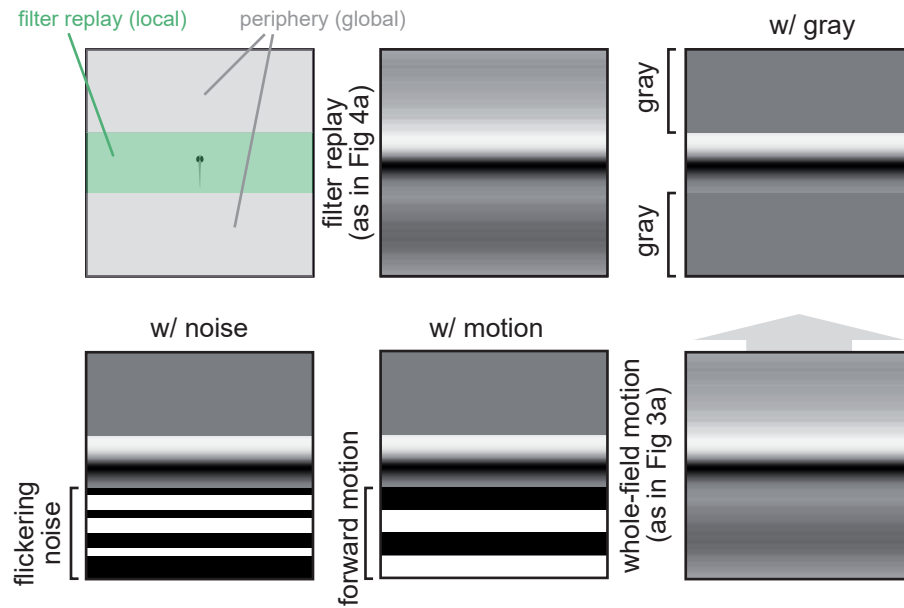
Figure 41: Visual stimuli that are presented in two zones: zone 1 (gray) either part of the filter replay, i.e. morphing of the filter, it is replaced with uniform gray, random flickering bars that induce peripheral noise, or forward moving bars. Zone 2 (green) stays constant as being the filter replay. As a control, we are using the whole-field moving filter.

motion stimulus was more pronounced than that of the filter replay. Interestingly, the onset of bouts was mostly concentrated during this light dark gradient, with a steeper gradient resulting in a shorter time window over which swimming would start (Figure 43a).

To probe the role of the gradient on the behavioral profile we introduced a version of the filter replay, which we call temporally-squeezed filter replay (filter replay*), which consists of the filter replay squeezed in time to yield a steeper temporal luminance gradient as similar as possible to the whole-field motion stimulus (Figure 43b-d). This stimulus elicited a behavioral profile with similar total number of bouts as the filter replay, but their onset was aligned to the expected bout start time just as was the case for the whole-field motion stimulus (Figure 43b,e). This confirms the importance of the light-dark luminance gradient in shaping the timing of the behavioral profile, while the missing whole-field motion features leads to reduced number of swimming events.

Finally, to investigate the relationship between this luminance gradient and whole-field motion, we presented larvae with visual stimuli that incorporated whole-field motion (similar to the whole field motion stimulus) and differed only in the local luminance gradient (Figure 44). As expected, swim bouts occurred throughout the light-dark transition. Steeper gradients resulted in sharper behavioral profiles, although
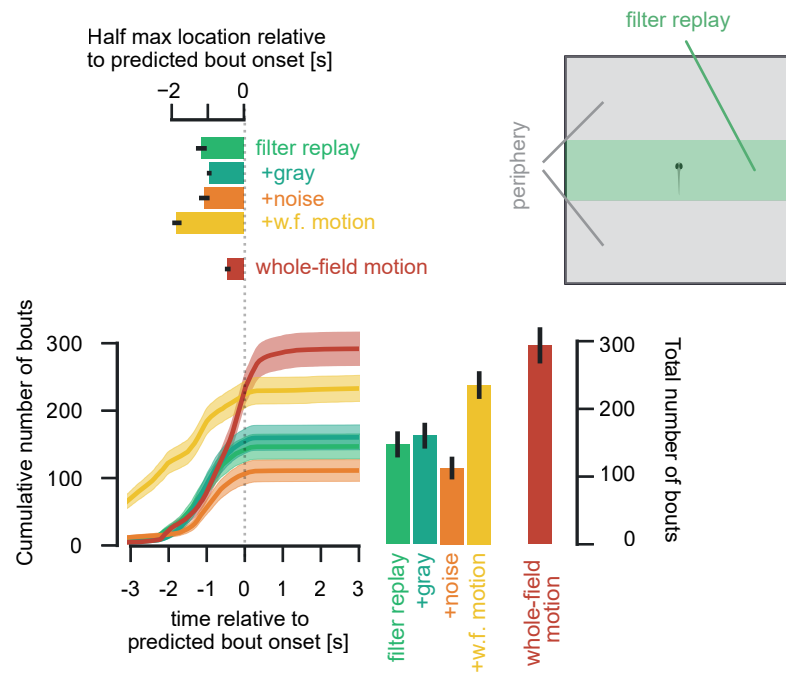
Figure 42: Whole-field motion improves behavioral response, but does not change behavioral onset timing. Top right: Schematic of experimental design. Filter replay is shown locally, close to the fish in an 8 mm window (rostral to caudal, complete stimulus window lateral to the fish) and in the periphery the stimulus is altered (global). Graph shows cumulative sums of bouts in time depending on stimulus. Either, filter replay (green), filter replay with gray in the periphery (turquoise), filter replay with noise (orange), filter replay with whole-field motion (yellow) or the whole-field motion filter as shown in b) were presented to the fish. Peak number of bouts and half maximum location of cumulative sum are derived from sigmoid fits of the data (see Methods). Shaded area indicate S.E.M.
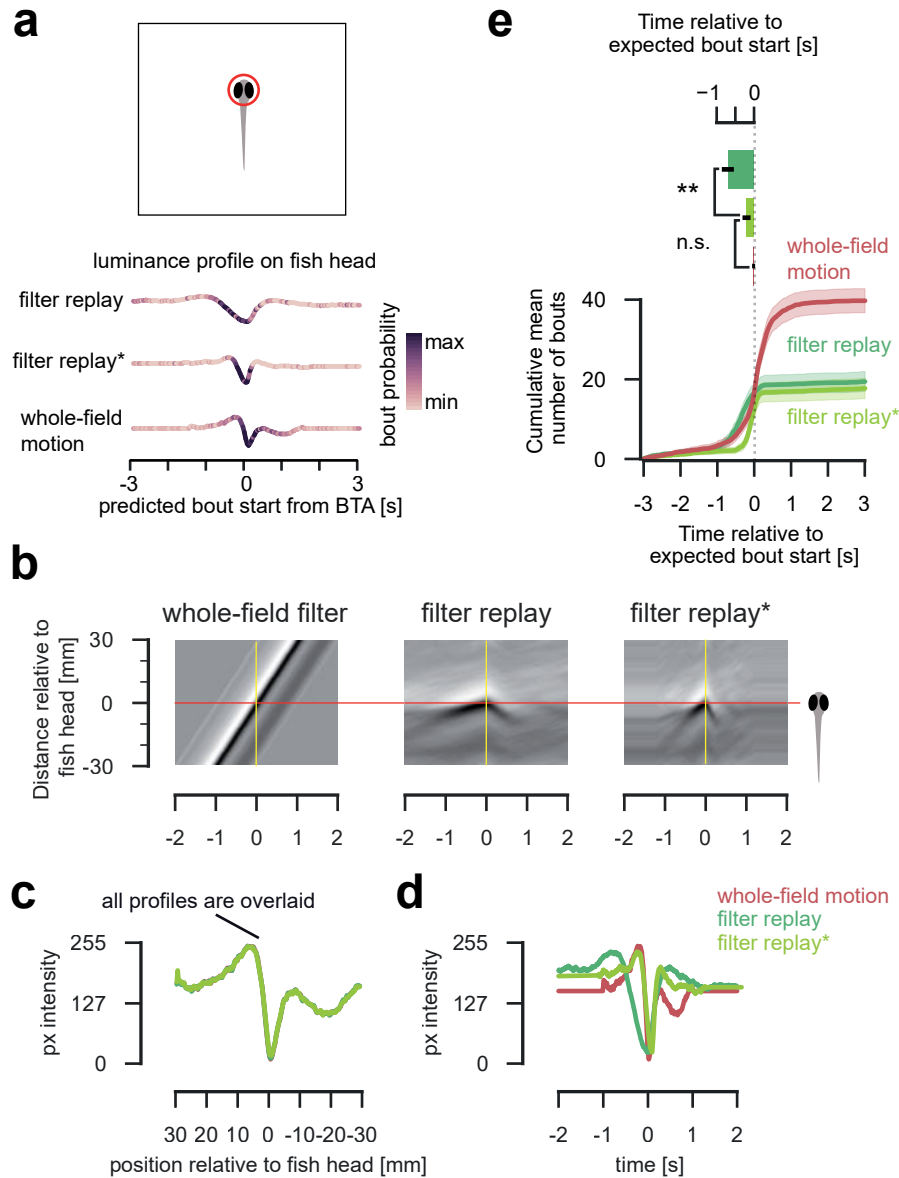
Figure 43: The light-dark gradient accumulates behavioral onsets. a) The luminance profile on the fish head over time during filter replay, whole-field motion filter and the temporally squeezed filter replay. b) The whole-field filter, filter replay and the temporally squeezed filter replay have different spatio-temporal luminance profiles. Heatmaps show luminance levels over time in relation to the fish's head position. c) On predicted bout onset (indicated as 0 in b), all of the three options of b) have the identical spatial luminance distribution. d) Over time, however, the luminance profiles are different. Note the same light-dark gradient in whole-field motion filter and the temporally squeezed filter replay. e) The temporally-squeezed filter replay has no significant different peak onset than the whole-field filter, and is shifted significantly compared to filter replay towards expected bout start, stressing the importance of the luminance gradient in evoking behavior. Shaded area indicates S.E.M.
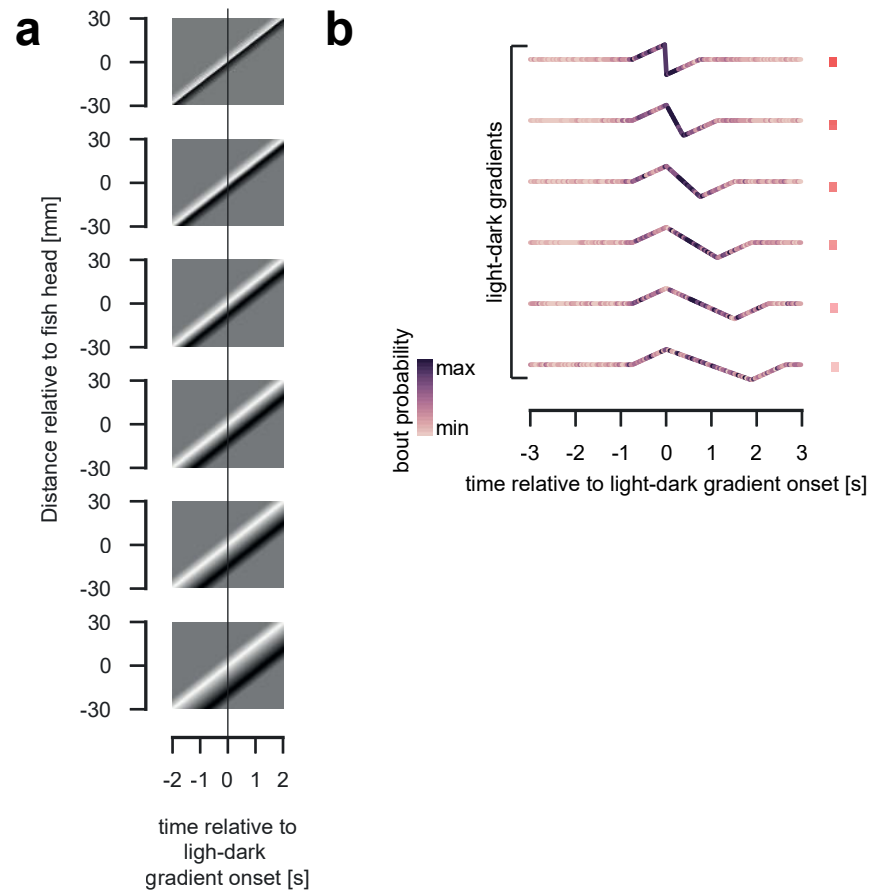
Figure 44: Different whole field moving, local light-dark gradients. a) different spatio-temporal luminance intensity heatmaps, similar to Figure 43. b) Different luminance profiles on fish head colored according to bout evoking probability. Steeper gradients show a stronger accumulation of bouts.
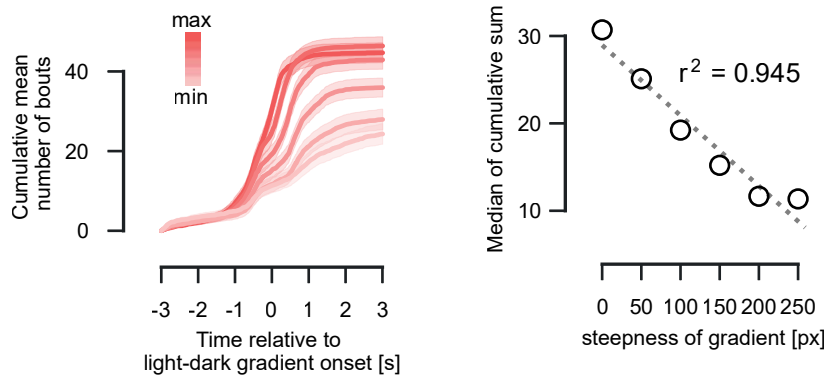
Figure 45: Gradient steepness modulates not only onset timing, but also number of bouts. Shown are cumulative sums of mean bout starts across 35 fish, color-coded depending on gradient slope (light colors shallow, dark colors steep gradient). Shaded area indicate S.E.M. Right panel shows the half maximum of cumulative sums against steepness of gradient (higher numbers produce shallower gradient).

surprisingly, stimuli with steeper gradients also elicited more bouts despite the fact that whole-field motion was still present (Figure 45).

Overall, the results presented in Figure 3 show that both the local luminance gradient and the presence of whole-field motion contributes to shaping the behavioral profile. In certain circumstances, whole-field motion is required to elicit a stronger behavioral response (Figure 40, 42 and 43e). The light-dark luminance gradient shapes the behavioral response distribution and its peak onset (Figure 40 and 45). However, this gradient may also affect the number of bouts elicited, suggesting a nuanced interplay between the local and global motion percept.

3.1.3 *Behaviorally relevant BTA whole-field motion causes tuned neural responses*

Having defined a visual filter that drives the OMR, we were interested if the visual filter causes specific neural activity. We therefore performed two-photon whole brain functional imaging in larvae pan-neuronally expressing the genetically encoded calcium indicator GCaMP6s. We presented the fish with five stimuli that incorporated whole-field motion and light-dark luminance transitions in diverse ways: a sharp light-dark transition (commonly known as off edge) moving forward across the visual scene, a smooth dark-to-light whole field luminance transition, a forward-moving sine grating, and finally the whole-field filter, first moving forwards and then the reversed filter moving backwards (Figure 46). This later stimulus was presented
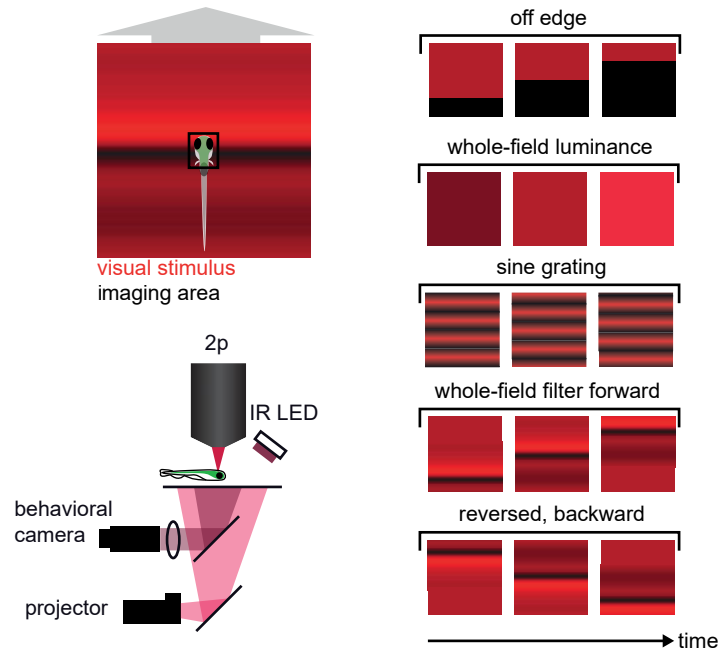
Figure 46: Visual stimuli for two-photon imaging experiment. We probed fish with a forward moving off edge, a whole-field luminance change (dark to bright), a forward moving sine grating, the whole-field motion filter forward, and the whole-field motion filter moving reversed, moving backward (same light-dark transition, opposite sign of motion).

because it has the opposite sign of motion by keeping the same light-to-dark transition.

Using pixel-wise correlations, we found 440,736 active regions of interests (ROIs) from nine fish that include cell somata and fibers (see Appendix for coverage). We grouped ROIs into clusters with distinct responses (Figures 47 and 48, see also Methods) and found five that were selectively responsive to the filter or its reverse (Figure 47). Clusters 1 and 5 showed luminance dependent responses corresponding to luminance on and off, respectively. Cluster 1 includes the medial cerebellum, as well as arborization fields (AFs), in particular AF9. Cluster 5 includes active units in the pretectum, dorsal thalamus and bilateral strata of the tectal neuropil. Cluster 3 responded specifically to the reversed filter that moves backward, and thus comprises a reverse motion cluster. ROIs in cluster 3 are mainly located in rhombomere 1 of the hindbrain and the tectal stratum periventriculare. Cluster 4 was active for all visual motion regardless of the direction (Figures 47 and 48). It includes the tectal neuropil, as well as other arborization fields and cells ventral to the tectum. Only cluster 2 had responses more specific to the forward moving filter. This cluster was also active when presented with the forward moving off edge, a feature shared with the forward filter, but not when the reversed filter is shown, which has the
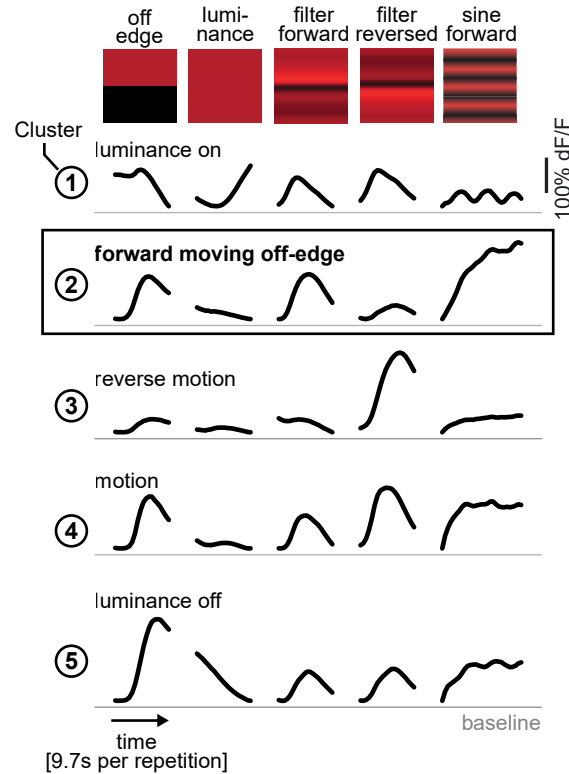
Figure 47: Cluster responses for the five clusters that have responses to either the forward moving whole-field motion filter or to its backward-moving reverse. Shown are calcium transients using the dF/F method relative to baseline (gray line).

same luminance transition but with the opposite sign of motion (Figure 47). These responses are spread out over the whole brain (Figure 48). They include the nucleus of the medio-lateral fasciculus (nMLF), the pretectum, the tectal neuropil (AF10) and AF6.

When looking at units that are active during swimming episodes, we identified a single cluster related to swimming (magenta cluster, Figure 48). Interestingly, the cluster that is closest specific to the forward filter (cluster 2) contained a very small overlap with this swimming cluster, mainly surrounding the nMLF neurons, indicating that the neurons in cluster 2 are either sensory or directly involved in the sensorimotor transformation that leads to behavior. Further, neurons in cluster 2 had only little correlation with swimming.

In summary, we show tuned responses to the forward moving filter that are located across the whole fish brain.

3.1.4 *A generalized linear model can capture more variance than chance*

Our results demonstrate that OMR swimming is triggered both by a light-dark transition and whole-field motion. We asked if a generalized
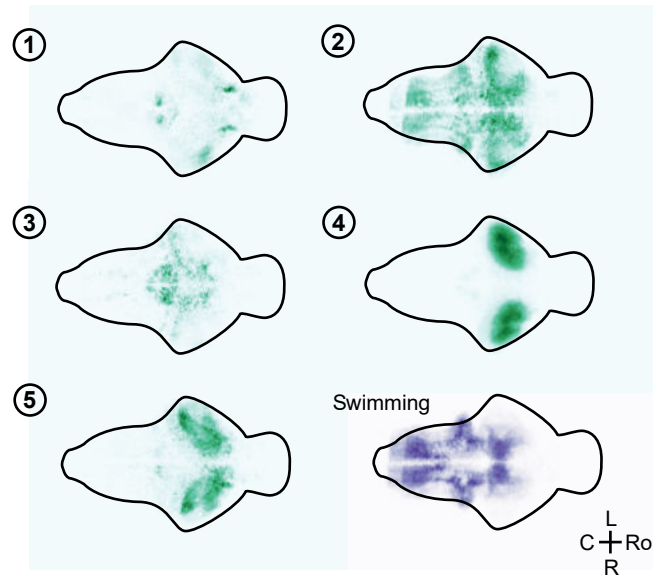
Figure 48: Anatomical localization of clusters shown in Figure 47. Green heatmaps show ROI locations in specific cluster gained from clustering analysis of automatically found ROIs across nine fish. Purple are ROIs that correlate well with behavior (r >= 0.8, N=9 fish).

linear model, a variant of the LNP model (Figure 5), can predict the fish's behavior as shown for a heat-induced swimming (Haesemeyer et al. 2015). At every instance in time, we fed the grating history computed over a one second window together with the bout starts as labels to the GLM fitting algorithm that finds the ideal filter using log-likelihood (Figure 49 and Methods). In agreement with our analysis, the GLM filter looks highly similar to the BTA (Figure 49, bottom left heatmaps). The GLM returns rates that should coincide with bouts (Figure 49, bottom right panel). We assessed model specificity and sensitivity, as well as false-positive and false-negative rates (Figure 50). For every given threshold and model (Figure 49, bottom right panel), we computed the percentage of peaks that are accompanied by a bout (i.e. true predictive value, Figure 50, top panel) and the percentage of bouts that are accompanied by a peak (i.e. true positive rate, Figure 50, bottom panel). The GLM is capable of explaining a higher amount of variance compared to bootstrap controls. Up to 13.2% of the detected peaks above threshold are accompanied by a bout, whereas 48.0% of the bouts are accompanied by a peak (compared to 8.6% and 21.0% in bootstrap controls, respectively, Figure 50). When determining the false negative and false positive rates for our model, we observe that the model outperforms the bootstrap control (Figure 51).
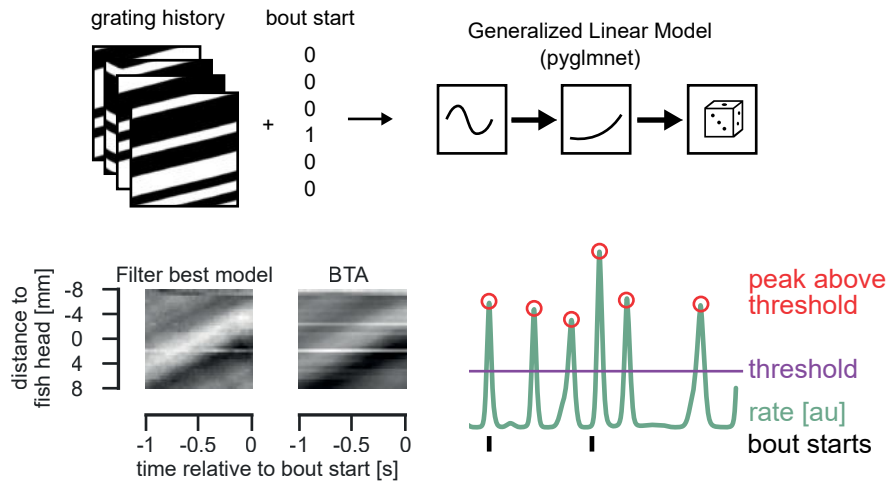
Figure 49: Fitting a generalized linear model (GLM). Using the grating history as features and bout start (binary, yes and no) as labels, we fitted a GLM using pyglmnet (see Methods). The filter gained by the fitting is shown next to the behavioral triggered average of the training data (bottom left). The GLM returns probability rates of a fish to swim (green). We used a variable threshold (purple) to determine which peaks above threshold (red circles) are accompanied by a bout (black dashes) in a given window.

Overall, the simple GLM succeeds in explaining the data better than chance, though we expect more complex models to be able to improve this significantly.

How many peaks above threshold are accompanied by a bout?
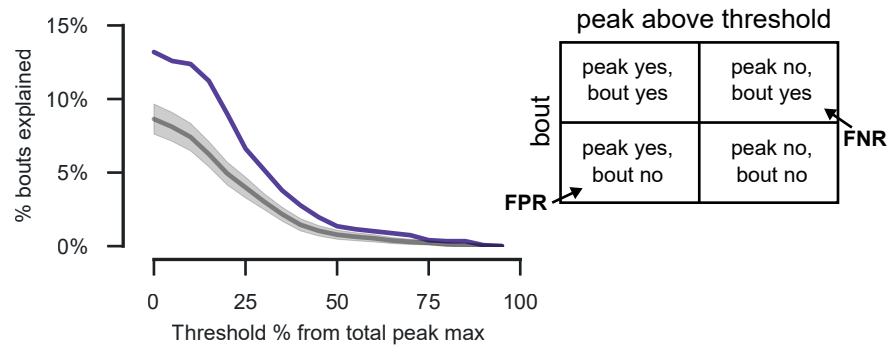
How many bouts are accompanied by a peak above threshold?
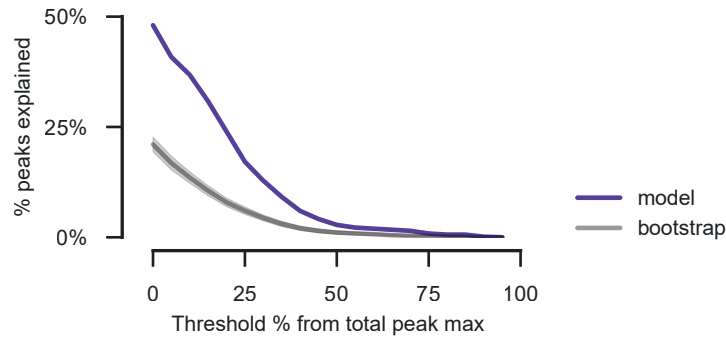
Figure 50: A GLM explains more variance than chance. On the top right, the matrix indicates the four conditions. False positive and false negative rates (FPR and FNR, respectively) are indicated. Top left: probability that peaks above threshold are accompanied by a bout (positive predictive value). Model in magenta, bootstrap (100 iterations) in gray with shaded error (standard deviation). Bottom left: probability that a bout is accompanied by a peak above threshold (True positive rate).
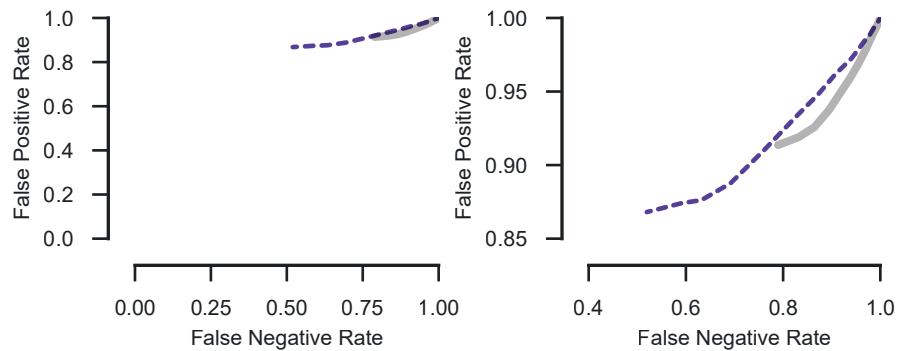
Figure 51: Quality and limitations of the GLM. Shown is the false negative rate versus the false positive rate. Color scheme as in Figure 50. To highlight that the bootstrap control does not achieve lower FPR and FNR rates we changed the line-style of the model.
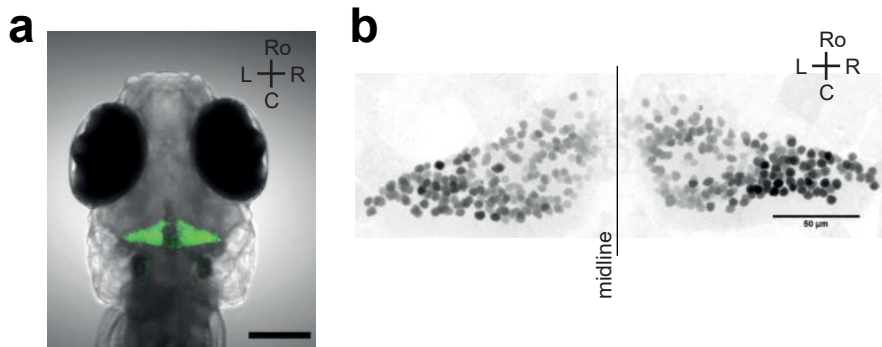
Figure 52: Transgenic fish lines labelling specifically Purkinje cells with different reporters. Left: PC:GCaMP6s maximum intensity projection (used in Knogler et al., 2018), Right: Zoom-in of PC:NLS-GCaMP6s, shown as maximum intensity projection.

3.2 STUDY II:
ROLE OF PURKINJE CELLS IN SENSORIMOTOR CONTROL

3.2.1 *Purkinje cell transgenic lines*

Effort has been made to create a toolbox to dissect cerebellar circuits. We developed transgenic lines that allow imaging of Purkinje cells (PC:GCaMP6s, Fyn-tagRFP:PC:NLS-GCaMP6f, PC:NLS-GCaMP6s), as well as ablation of Purkinje cells (PC:epNtr-tagRFP) based on the enhanced Nitroreductase (Tabor et al. 2014). For acute manipulation, we created transgenic lines that express channelrhodopsin (PC:ChR2-tagRFP) or ReaChR (a red-shifted channelrhodopsin variant, PC:ReaChR-tagRFP) in Purkinje cells. ReaChR was shown previously to be efficient in holographic activation (I.-W. Chen et al. 2018), thus, this line can be potentially used to map circuits using optogenetics. To gain high-quality anatomy stains, we generated transient and stable lines using the construct Fyn-mClover3:PC (Figure 52). Using the last line, one can easily see fine processes of Purkinje cells using a fluorescent stereoscope.

Further lines, that are part of this study include the ones summarized in table 1.

3.2.2 *Purkinje cell anatomy*

Earlier studies reported that around 180 to 300 Purkinje cells exist in a 7 dpf larval zebrafish (Hamling et al. 2015). However, by labelling the nuclei of Purkinje cells using a special transgenic line (PC:NLS-GCaMP6s), we were able to perform 3D template matching using a 3D gaussian as template. The 3D gaussian closely resembles the 3D anatomy of a Purkinje cell nucleus that appears to be almost spherical.

3D template matching

LINE	DESCRIPTION	REF
Fyn-mClover3:PC	Labels Purkinje cell dendrite and axon, used for high-quality single cell labelling.	Knogler et al. 2019
PC:GCaMP6s	GECI to image Purkinje cell activity.	Knogler et al. 2019
PC:NLS-GCaMP6s	Same as PC:GCaMP6s, with the GECI restricted to the nucleus. Used for Purkinje cell number estimation. Also available with GCaMP6f.	Knogler et al. 2019
PC:epNtr-tagRFP	Selectively ablates Purkinje cells using Nitroreductase upon Metronidazole treatment.	not published.
PC:Phobos^{CA}-tagRFP	A constant optogenetical activation of Purkinje cells that should lead to a functional silencing.	not published.
PC:ChR2(H134R)-tagRFP	Allows optogenetical activation of Purkinje cells with blue light. Sparse expressing fish were used for optogenetics experiments together with electrophysiology.	not published.
PC:ReaChR-tagRFP	Same as above, however, peak excitation in the red spectrum.	not published.
Fyn-tagRFP:PC:Cre	Expresses Cre in Purkinje cells for conditional expression of floxed genes.	not published.

Table 1: Available transgenic fish lines to label selectively Purkinje cells. A full list of all transgenic fish lines (not only restricted to Purkinje cells) is available in the Appendix.
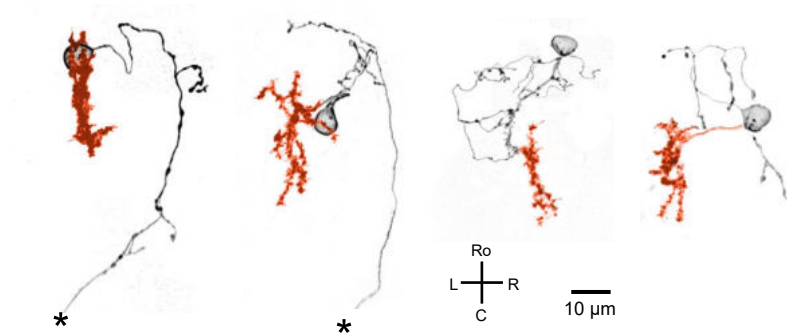
Figure 53: Purkinje cells come in two flavors: those with axon projecting outside of the cerebellum (left two) and those with axon remaining in the cerebellum (right two). The asterix indicates a cropped axon. The dendritic tree is colored in orange. Reprinted from Knogler et al. 2019 with permission.

We used a custom written software in Python to perform 3D template matching. The algorithm returns a heatmap of correlation values of a given voxel and its neighbours with the template (here, a 3D gaussian). We found peaks in this correlation map and labelled these points as center of mass of potential Purkinje cell nuclei. We then went manually through the stack and removed false positives and added missed Purkinje cells. Using this method, we found that there are around 433 ± 19 Purkinje cells labelled in this transgenic line (mean $\pm$ std, N=3 fish, 7 dpf), remarkably higher than previously reported (Hamling et al. 2015).

433 Purkinje cells

We acquired around 50 high-resolution and high-quality confocal stacks of individual Purkinje cells at 6 to 8 dpf. Confocal stacks were cleaned manually, deconvolved and interpolated to 200 nm per px (see Methods). A complete overview of all cells imaged is located in the Appendix. We found that Purkinje cells come in two flavors: 1) Purkinje cells whose axons remain in the cerebellar hemisphere and 2) Purkinje cells whose axons leave the cerebellum and projects to the vestibular nucleus (Figure 53). It is important to note, that we observed two times Purkinje cells that cross the hemispheres, however, all other fish screened (in the order of thousands) did not show this.

Further, we could verify that the Purkinje cell dendrite in larval zebrafish is planar, similarly to those found in mammals (see also introduction). For this, we used a novel metric based on principal axis. We assumed that a spherical or cubic data has three orthogonal axis, where the variance is equally distributed. Thus, when performing principal component analysis, would yield three components with equal weight. However, using planar data, only the first and the second component have large contributions to the data, whereas the third one only contributes very little. We therefore seeked a metric that can indicate non-planar and planar data, and propose that the third
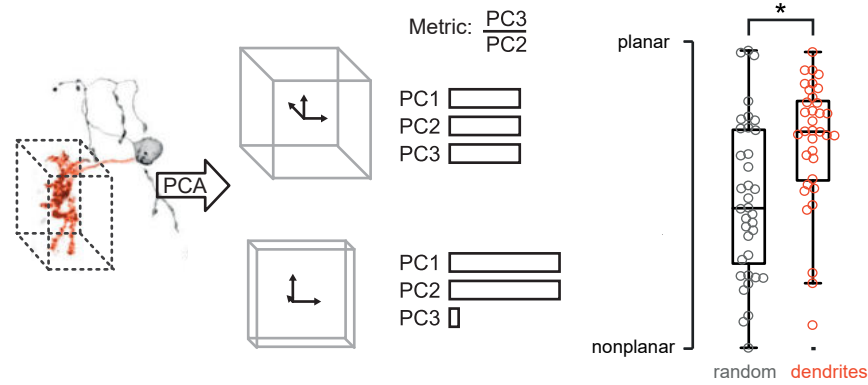
Figure 54: Purkinje cell dendrites are more planar than chance. We performed principal component analysis on binarized dendritic tress to determine principal axes. If the dendrite is planar, most variance is explained by the first two components, in contrast to spherical or cubic dendrites, where all three components contribute rather equally. Using our metric (component 3 over component 2), we found that Purkinje cell dendrites are rather planar compared to random data. Adapted from Knogler et al. 2019 with permission.

over the second principal component would yield 0 if planar and 1 if non-planar (see Figure 54). We selected manually the dendrite, thresholded it into fore- and background and performed principal component analysis. Using the aforementioned metric, we show that larval zebrafish Purkinje cells are indeed more planar than chance.

We further investigated, if Purkinje cells with the same axonal projection pattern cluster across the cerebellar hemisphere. We morphed traced neurons to a reference brain using the reference stack acquired simultaneously with the single Purkinje cell labelled channel. Assuming symmetry across cerebellar hemispheres, we flipped all cells to the right hemisphere. We found that Purkinje cells that project outside of the cerebellum cluster in the caudal-lateral edge (Figure 55). Interestingly, Purkinje cells with an axon remaining in the cerebellum spread across the whole cerebellum.

Figure 55: Purkinje cells with an axon leaving the cerebellum cluster at the caudal-lateral edge. 52 morphed individual Purkinje cells. Adapted from Knogler et al. 2019 with permission.
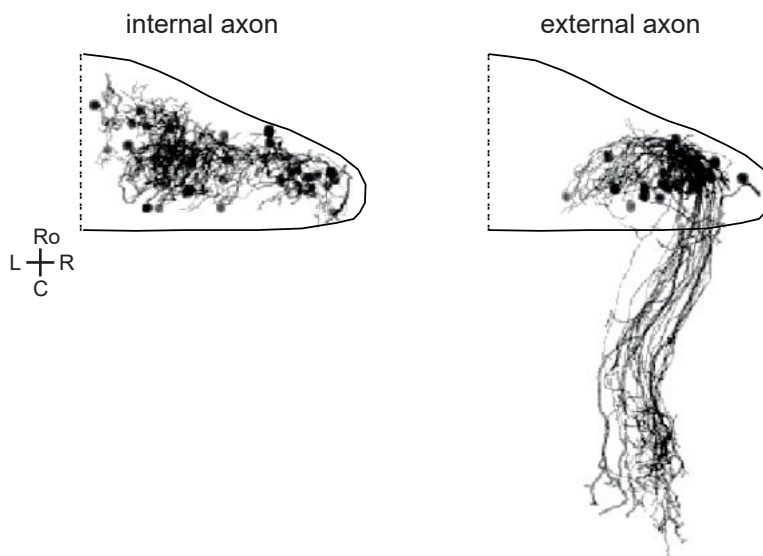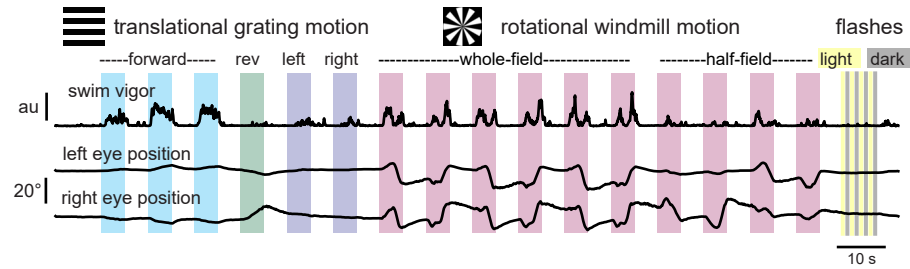
Figure 56: Stimuli presented and average behavior recorded for an example fish. We probed translational grating motion, i.e. forward at three different speeds (3, 10 and 30 mm/s), reverse, left and right translational motion at 10 mm/s. Rotational motion was clockwise-counterclockwise and counterclockwise-clockwise alternating, provided in one or both halves of the visual field. Alternating dark-light flashes probed luminance responses. Tail and eyes were tracked as described in Methods. Adapted from Knogler et al. 2019 with permission.

3.2.3   Purkinje cell response types and topography

Max. intensity across planes

A single plane

multilinear regression

The cerebellum is thought to be a key area for sensorimotor integration. To unravel underlying cerebellar internal models, we aimed to characterize the different input streams, i.e. from granule cells via parallel fibres and the inferior olive via climbing fibres (see Figure 10). We performed two-photon calcium imaging using fish expressing GCaMP6s in nearly all Purkinje cells (Figure 52). To get a better understanding about the coding properties of Purkinje cells, we probed the fish with a variety of different stimuli to evoke different behaviors, such as OMR and OKR (Figure 56). Movies showing a maximum z-projection of the Purkinje cell activity and a single plane during behavior is available online (use marginal QR codes).

Using multilinear regression (see Methods), we could infer which feature vectors contribute to the fluorescence trace. In Figure 57, we show the coefficient weights for all regressors used in multilinear regression. Interestingly, we found that sensory signals cluster spatially across the cerebellum (Figure 57, top panels), indicating a special context topography. However, motor information is presented throughout the cerebellum (Figure 57, lower panels).

We next asked if the source of these signals are granule cell or inferior olive dependent, and if they already show the same topographic organization. We repeated the experiment as presented above in Figure 56, this time with a line labelling granule cells (Knogler et al. 2017; Takeuchi et al. 2015). We imaged seven fish and morphed all fish to a reference stack of the same line. On the reference stack, we draw manually masks to split somatic and parallel fibre layers. We show that granule cell have in both, somatic and parallel fibre layer, a broad activation for motor-related signals (Figure 58, top panels). As
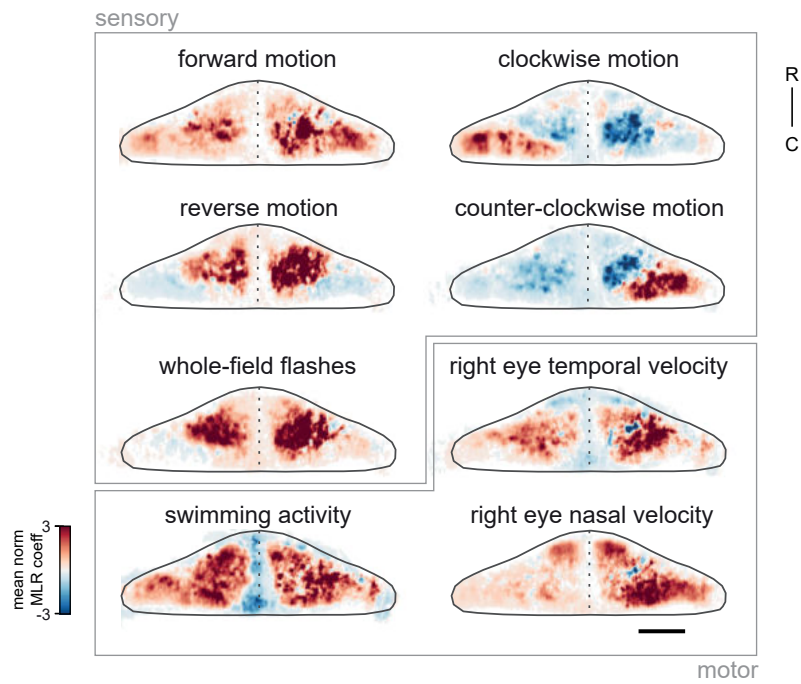
Figure 57: Mean *z* projection coefficient maps gained from voxel-wise multilinear regression across the whole Purkinje cell layer. 8 of 14 total regressors are shown. Note the topography for sensory stimuli and the broad coding for motor information. Adapted from Knogler et al. 2019 with permission.
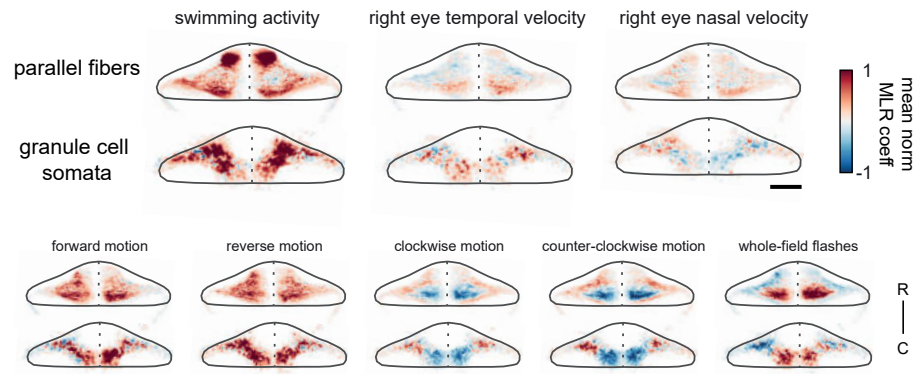
Figure 58: Mean z projection maps for somatic and parallel fibres for granule cell experiments. Note the differences to the Purkinje cell maps. Adapted from Knogler et al. 2019 with permission.

expected (Knogler et al. 2017), granule cells show also activity when probed with sensory information. However, compared to our Purkinje cell imaging study, sensory information is differently spatially organized. For example, responses for clockwise and counter-clockwise motion is symmetrically organized across the cerebellum. In Purkinje cells, we observed a distinct asymmetry for the stimuli, indicating that this sensory information is likely to be delivered by climbing fibre activity.

Recently, a study described that different kind of spikes, i.e. simple and complex spikes, are observable in different cellular compartments during functional calcium imaging: simple spikes in the soma, complex spikes in the dendrite (Ramirez and Stell 2016). To verify if this holds true in larval zebrafish, we sparsely labelled Purkinje cells with PC:GCaMP6s and performed two-photon imaging. On a total of 5 nicely separated cells that have their soma and significant parts of the dendrite in the same optical section, we could show, that larval zebrafish Purkinje cells have the same calcium response in the soma and different parts of the dendrite (Figure 59). This leads to the assumption that the source of the observed calcium response is ambiguous.

We were next interested if Purkinje cell signals are derived from granule cells or the inferior olive. Thus, we performed electrophysiological experiments. This part of the study was performed by Laura Knogler and further details are available in our publication attached to this thesis (Knogler et al. 2019). Briefly, we could show that indeed granule cells are providing the motor context in Purkinje cells, and the inferior olive provide a stereotypic topographic sensory context.

3.2.4 *Purkinje cell optogenetic responses*

As the cerebellum is known to be involved in sensorimotor transformation, we asked what is the functional role of Purkinje cells in
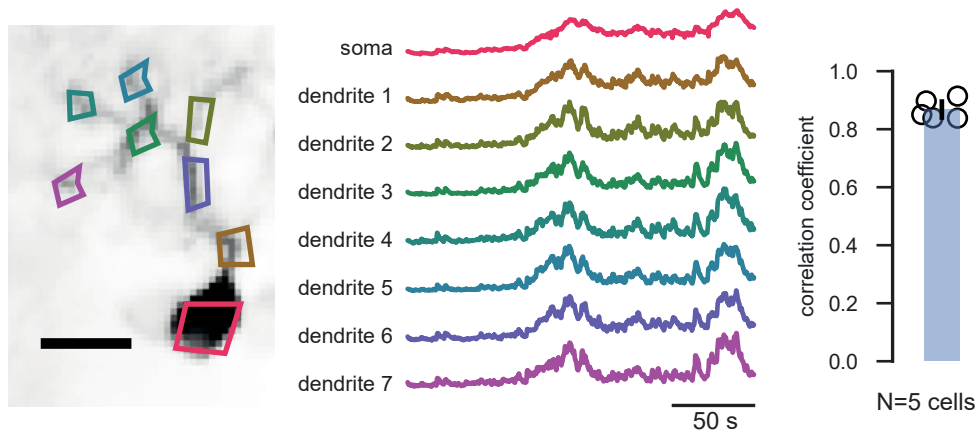
Figure 59: Calcium signals are the same in soma and dendrites of larval zebrafish Purkinje cells. Left, an example single Purkinje cell is shown. Different ROIs across the cell are indicated by colored polygons. The same color code is used for the calcium trace extracted from the ROIs. Interestingly, almost the same calcium signal is available across the different cell compartments. We compared the correlation for different Purkinje cells (N=5) and show that the somatic and distal dendritic signal are highly correlated.

sensorimotor control. For this, we utilized optogenetics to manipulate the firing rate of Purkinje cells to potentially observe differences in behavior.

As described in the Methods section, we used a DMD-based optogenetics behavior setup to dynamically select spatially constrained ROIs to specifically activate a subset of neurons. In the experiments presented, we stimulated the two cerebellar hemispheres simultaneously (Figures 19 and 60).

The behavioral paradigm is presented in Figure 60. We moved a binary grating with regular spaced white and black bars with a period of 10 mm at a speed of 10 mm/s forward relative to the fish. We tested fish that express or do not express channelrhodopsin in Purkinje cells. In half of the trials, we turned on the light stimulation. Trials without light and with light were alternated.

Interestingly, we observed that fish expressing ChR in Purkinje cells have a longer latency to initiate swimming after the grating started moving forward (Figure 61). This latency has not a fixed width, but rather follows a stochastically length. In Figure 61, the trials are sorted for latency, indicating that there are huge differences across individual trials. This is not only true for these two example fish, but also on a population level (Figure 62).

When analysis other behavioral parameters, such as mean bout duration and mean interbout duration, we observed no difference across light conditions and ChR expressing fish. This indicates that
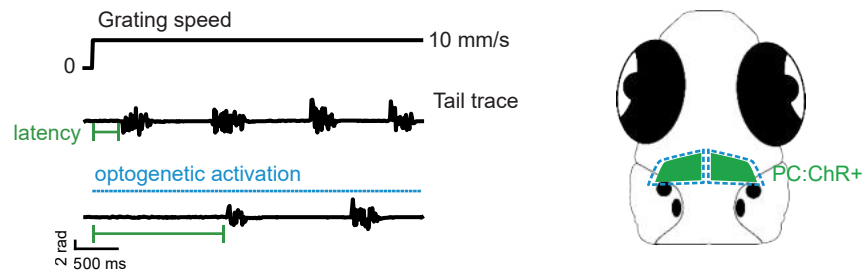
Figure 60: Behavioral paradigm optogenetics. A grating alternates between stationary or moving forward at 10 mm/s. This evokes the OMR, making the fish swim (see tail trace). When optogenetically stimulating cerebellar Purkinje cells (see schema on the right) during a forward moving grating, we observe that fish have an increased latency (green bar).
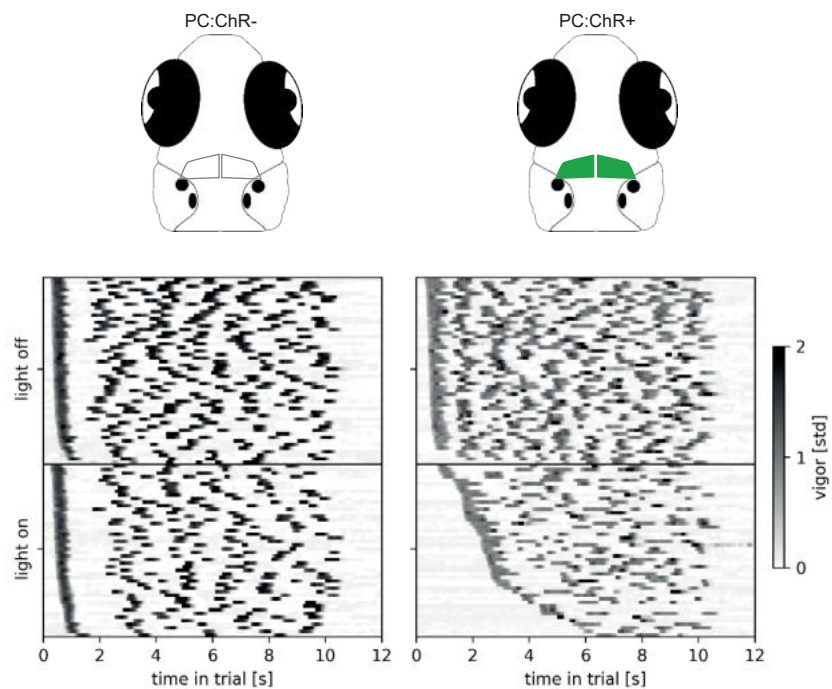
Figure 61: Vigor, i.e. swimming, heatmaps for two individual, representative fish (ChR negative and positive, respectively) are shown. Each row is a single trial. Trials are sorted by light on/off and latency. Note, that both fish have similar latency distributions for the light off trials, however, ChR positive fish have increased latencies to initiate swimming.
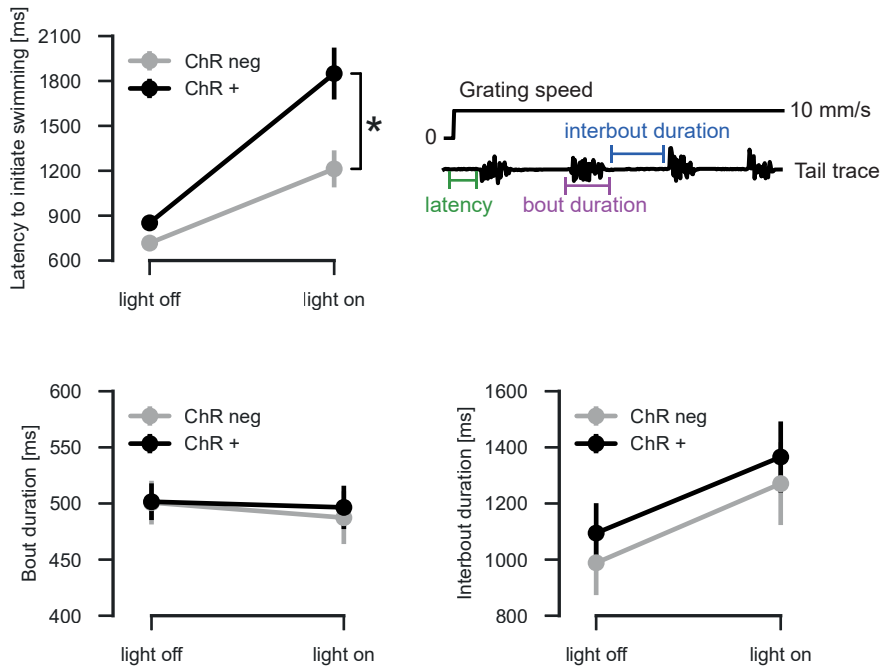
Figure 62: Activity perturbance of Purkinje cells lead to a higher latency to initiate swimming on a population level (p < 0.05), however, no other assessed behavioral parameters are altered, such as mean bout duration or mean interbout duration. Error bars represent S.E.M.

Purkinje cells have here a role in modulating the motor initiation, but have little role in motor execution, at least in this given experimental paradigm.

3.3   STUDY III:
in vivo APPLICATION OF A NEW FAR-RED PROTEIN.

Labelling proteins or cells have revolutionized biology research. However, we still lack appropriate fluorescent proteins in the far-red to overcome limitations of blue-excited fluorophores. Here, we show a joint collaboration with the lab of Oliver Griesbeck that focuses on the development of a new robot-aided platform to enhance screening fluorescent proteins.

During this study, our collaborators developed a new fluorescent protein resulting of multiple mutagenisis rounds of mNeptune684 termed mCarmine. We contributed in cloning the fluorescent protein in a vector enabling us to express mCarmine in zebrafish. To evaluate its performance, we fused it to mTFP1, a cyan fluorescence protein, with known characteristics (Day et al. 2008).

3.3.1   *Unraveling the* elavl3 *promotor*

We aimed to clone mTFP1-mCarmine in a vector containing the *elavl3* promotor to allow pan-neuronal expression of mTFP1-mCarmine (Park et al. 2000). However, we had problems to express our fusion protein: transient injected fish had only weak detectable fluorescence. We therefore mined the poorly annotated vector map and discovered, that the *elavl3* promotor already has the translation start way upstream the multiple cloning site. Further, we discovered that the multiple cloning site induces a frame-shift by one basepair (Figure 63). We assured using proper oligonucleotide primers and SLiCE cloning to excise hetereologous fragments and clone directly adjacent to the intron.

We decided to leave these three leading amino acids, as they are N-terminal and should not interfer with the fluorophore expression. Indeed, when we injected the improved construct, we observed decent expression levels. To further improve expression levels, we cloned the mTFP-mCarmine construct downstream of an upstream activation sequence (UAS) sequence. We injected the UAS:mTFP1-mCarmine construct in a fish expressing Gal4 (a protein that drives expression of genes downstream of UAS) pan-neuronally (*elavl3*:Gal4).

3.3.2   *mCarmine performs better than mTFP1*

We observed across multiple transient fish, that mCarmine performs a little bit worse on dorsal planes than mTFP1, however, largely outperforms mTFP1 in deeper layers due to far-red shifted excitation and emission spectra. We imaged a ventral-to-dorsal column from the top dorsal layer of the fish down to the very ventral located IPN.

We adjusted the laser power dorsally as such, that the histograms of the mTFP1 and mCarmine channel look highly similar (Figure 64i).
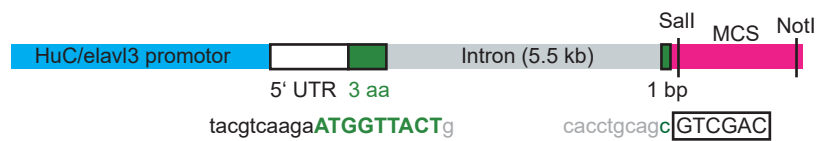
Figure 63: Cloning mTFP1-mCarmine in *elavl3* and UAS expression vectors. Cloning in elavl3 promotor should be performed by cutting the backbone using SalI and NotI. When using seemless cloning, one should remove the 1 bp 5' to SalI to avoid a frameshift due to the translation start before the large intron and multiple cloning site (MCS).

Then, we went to deeper layers and used the exact same settings. We observed that the mTFP1 signal almost completely vanished at deeper layers, however, the mCarmine signal was still present at -243 μm (Figure 64ii). When adjusting the mCarmin signal to a decent signal-to-noise ratio (Figure 64iii), we had to use a very high amount of laser power for mTFP1 excitation, despite the fact that mTFP1 is multiple times brighter than mCarmine. In both cases, we could resolve the IPN, however, even using deconvolution, the fine details in the mTFP1 channel are lost compared to the mCarmine channel (inset in Figure 64iii).

We calculated an performance index based on the biophysical properties of the fluorophore, the laser power and the photons collected (see Methods). Although mCarmine is multiple times dimmer than mTFP1, it outperforms mTFP1 in deeper layers (Figure 64, top right panel) 22.5 fold.
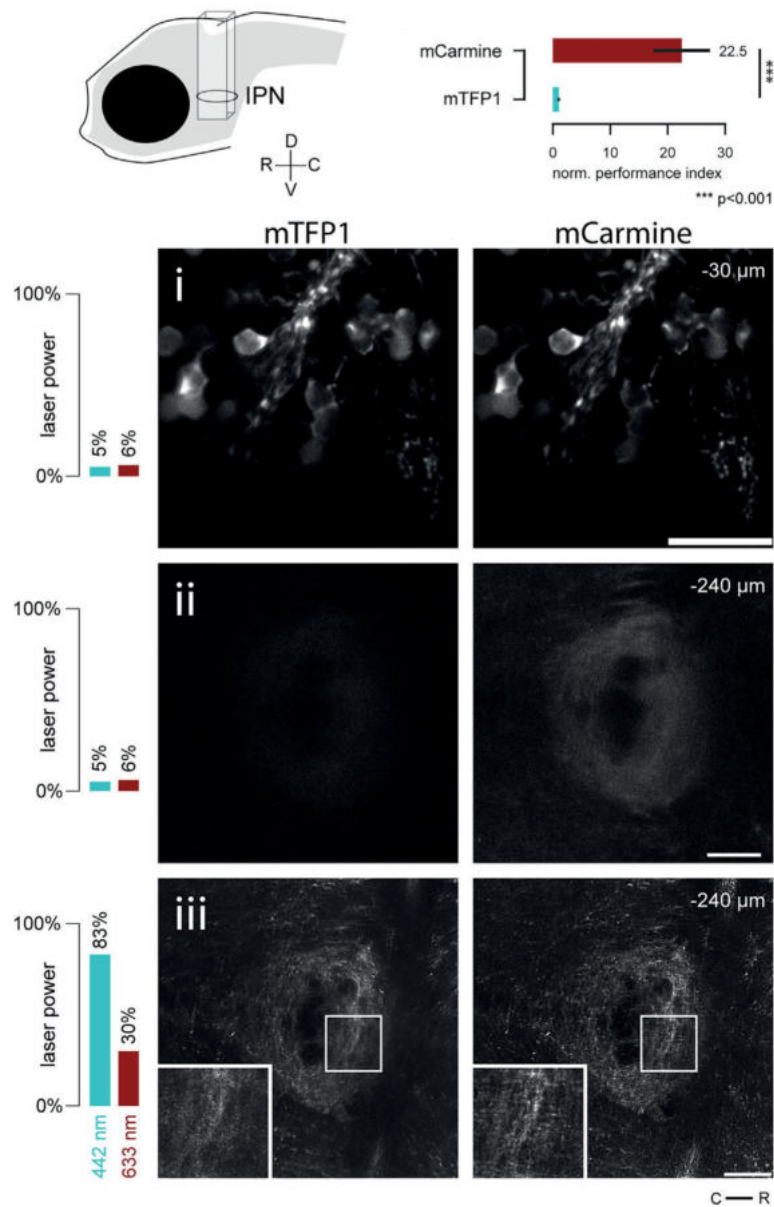
Figure 64: mCarmine outperforms mTFP1. We imaged a dorsal to ventral column of a seven dpf larval zebrafish expressing the fusion protein mTFP1-mCarmine pan-neuronally. We ensured to have the same fluorescence across channels in dorsal planes. We used the same settings and went ventrally. There, mTFP1 shows almost no fluorescence, however, mCarmine produces still some fluorescence. When adjusting laser powers, mCarmine needs less laser power to produce the same amount of fluorescence as mTFP1 and also shows a greater SNR. When computing a performance index (see paper in Appendix), we could show that mCarmine performs on average 22 times better than mTFP1. Adapted from Fabritius et al. 2018 with permission.

DISCUSSION

These three studies show how to utilize the larval zebrafish modelsystem to answer questions across different disciplines in neuroscience. In the following, open questions and potential answers are elaborated.

4.1 THE OPTOMOTOR RESPONSE

In this study we used a reverse-correlation approach to identify the stimulus that is optimal in eliciting the forward optomotor response. We found that this stimulus consists of two features: spatially symmetric global whole-field motion and an asymmetric light-dark transition occurring locally at the larva's head. The luminance gradient of this transition influences the swimming rate and timing of the bouts, with steeper gradients eliciting more bouts whose onsets are closer temporally aligned with the stimulus. Whereas a contribution of whole-field motion was expected from previous OMR studies, the importance of a local light-dark transition has not been described in this context before.

Different features of whole-field motion that lead to behavioral modulation have been probed before in the context of the OMR such as contrast, temporal and spatial frequency in flies (Haag et al. 2004) and speed in zebrafish larvae (Portugues et al. 2015; Severi et al. 2014). Asymmetries in the processing of light and dark stimuli in zebrafish have been shown to exist in zebrafish but always relating to behaviors that involve local or object-related motion, such as prey capture, looming stimuli or visually-evoked responses (Bianco and Engert 2015; Burgess and Granato 2007; Burgess et al. 2010; Dunn et al. 2016a; Semmelhack et al. 2014; Temizer et al. 2015). In the context of the OMR, experiments in flies, dragonflies and primates (D. A. Clark et al. 2014; Leonhardt et al. 2016; Nitzany et al. 2017) have shown asymmetries in the processing of light and dark in the ON and OFF pathways using two and three point correlation glider stimuli (Hu and Victor 2010). The asymmetries in processing have never been shown to be spatio-temporally confined like we show here. It is interesting to note that this light-dark transition is independent of color, as equal luminance red/green transitions elicit no optomotor swimming (Michael B. Orger and Baier 2005). In zebrafish, axons from RGCs are known to project to ten AFs (Burrill and S. S. Easter 1994; Robles et al. 2014). It is likely that the two features that we describe in this study, namely on/off-independent whole-field motion and a
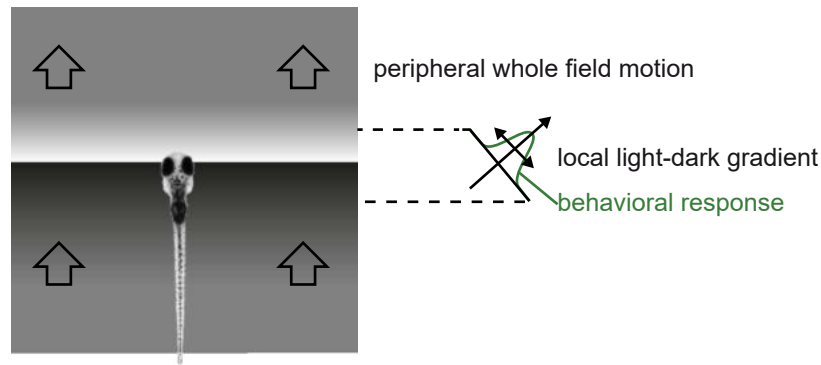
Figure 65: Our current working model for the optomotor response.

local light-dark transition, are conveyed by different RGCs, possibly to different AFs.

Our simple generalized linear model showed moderate success in explaining the observed behavior. However, it performs not worse than studies with similar constraints on the data (Haesemeyer et al. 2015). Further behavioral experiments accompanied by modeling studies need to be performed to understand the interaction between the two visual features that contribute to the OMR. If indeed different RGCs convey these features to different AFs, these models could provide a means to create hypotheses about the convergence of different visual streams and the neuronal mechanisms which could mediate this interaction, such as neuromodulation, gating or gain control.

Our preliminary imaging study was able to identify units tuned specifically to visual stimuli known to drive the OMR. Interestingly, we observe that units that respond to behavior-inducing stimuli occur throughout the brain but are enriched in the pretectum and AF6, areas that were recently suggested to contribute to OMR and behavior (Kubo et al. 2014; Naumann et al. 2016).

Here, we provide further evidence that these areas are indeed important for the OMR as they also respond to the light-dark transition feature we describe. To summarize, we propose a working model (Figure 65) in which the OMR is strongly induced by a whole-field motion percept together with a newly-described light-dark transition. The behavioral response to the OMR is further modulated by the steepness of the light-dark gradient, which may explain the known dependence of this behavior on visual features such as contrast, temporal and spatial frequency. This study shows that the OMR, a paradigm that has been used for decades, is still under-characterized and its comprehensive characterization is of great interest for further studies dissecting behavior-related neural circuits.

4.2 SENSORY INFORMATION IS SPATIALLY CLUSTERED ACROSS PURKINJE CELLS

Several studies found, that the cerebellum has a spatially patterned organization, for example using molecular markers, such as Zebrin II (Hawkes and Herrup 1995). Here, we can also show using for the first time single cell resolution (compared to Matsui et al. 2014) that sensory information is spatially clustered across Purkinje cells. The cerebellar organization in stripes is a common phenotype across common signal source, biomarker and species (Apps and Hawkes 2009; Hawkes 2014; Larouche and Hawkes 2006; Pakan et al. 2007; Sawada et al. 2008). We found that signals correlated with translational motion are clustered in the medial cerebellum, whereas signals correlated with rotational motion are clustered in the lateral cerebellum (Figure 57). These Purkinje cells that are tuned to rotional motion have long axons that leave the cerebellum and terminate at the vestibular nucleus (Knogler et al. 2019). With this, we believe that we found the zebrafish homologue of the mammalian flocculus, an important cerebellar structure for vestibular information processing and vestibulo-ocular coordination (Ito 1972; Simpson and Alley 1974). Complementary functional imaging studies looking at whole brain activity found activity in similar regions, i.e. in the lateral cerebellum (Favre-Bulle et al. 2018; Migault et al. 2018).

These results are very interesting in the sense of what signals the inferior olive conveys. Classically, the inferior olive is thought to be an error detector (Albus 1971; Ito 1972, 2013; Marr David 1969), thus, providing kind of a beacon, when signals conveyed by granule cells are not expected. However, by repeating the stimuli pattern over and over again, and we observed the same response, we do not think that climbing fiber activity is error related, but rather of sensory nature. We can also see that granule cells do exhibit sensory context as shown previously in fish (Knogler et al. 2017), but also provide a general motor context to presumably all Purkinje cells, as these signals were found homogenously across in the cerebellum. We therefore think, that these findings are in line with a forward model, one potential cerebellar internal model to perform sensorimotor control (Wolpert et al. 1995, 1998; Yavari et al. 2015). A forward model provides sensory expectations, that can be compared with the actual sensory information provided by granule cells.

In the literature, there is evidence for forward and inverse models Ishikawa et al. 2016; Miall and Wolpert 1996; Ohyama et al. 2003; Porrill et al. 2013; Wolpert et al. 1998; Yavari et al. 2015. Our study supports the forward model hypothesis, however, it is very likely that the cerebellum implements multiple models via different mechanisms. Thus, experiments aiming directly on the functional dissection of potential internal models are needed to investigate this further.

Additionally, eurydendroid cells (ECs) are the homologue of deep cerebellar nuclei because they are contacted by Purkinje cells (Bae et al. 2009; Takeuchi et al. 2015). However, ECs also send dendrites in the molecular layer, potentially connecting to granule cells via parallel fibers. This opens a new computational dimension, complicating the classical microcircuitry and internal model hypotheses, as these connections are not reported in the mammalian system.

We showed that it is likely that the inferior olive provides the sensory context for the spatial topography in the Purkinje layer. Indeed, when performing electrophysiological studies, we confirmed that sensory contexts driven complex spikes are clustered spatially (data shown in Knogler et al. 2018). However, imaging inferior olive neurons in the context of the same experimental paradigm (Figure 56) would reveal if there is already a topography in the inferior olive, or only climbing fibres provide that spatial organization. Further, probing all cerebellar cells with the same experimental paradigm would open the possibility to look for coding hypotheses and would provide further evidence for or against the existence of internal models.

Another interesting observation is the monocularity of the OKR response. Using only half-field rotational stimuli, we observed that the cerebellum shows monocular sensory signals and only for one direction of rotational motion. Interestingly, this is also observed in the inferior olive (D. Markov, personal communication), suggesting that already the inferior olive either receives only monocular input or filters the signal.

Using optogenetics, we were able to alter Purkinje cell activity and modulate the latency to initiate swimming. This provides new insights how the cerebellum can interact with pre-motor centers. The cerebellum is thought to actively modulate a given behavioral syllable and thus behavior as it goes, but not in the initiation of movement. Interestingly, we did not observe a change in the assessed behavioral parameters, suggesting that Purkinje cells only modulate mildly swimming behavior, if at all. With preliminary studies combining optogenetics and electrophysiology (together with L. Knogler), we observed that Purkinje cells are activated with already very low light intensities, but are easily blocked when providing too much light. However, it is hard to dose the light and read out the average Purkinje cell activity for each individual fish in the DMD-based optogenetics behavior rig. We used very low light intensities and assume that we activated Purkinje cells on average.

To understand the role of Purkinje cells in sensorimotor control, an obvious way to dissect the circuit is to ablate Purkinje cells. Previous studies suggested, that a loss of Purkinje cells can lead to spinocerebellar ataxia (Xia et al. 2013). Together with D. Markov, we could not observe a behavioral phenotype in larva with ablated Purkinje cells (OMR and OKR). Only when larvae were challenged enough,

we could observe that Purkinje cells mediate plasticity for long term adaptation (data not shown and not published).

Taken together, Purkinje cells share common hallmarks of mammalian Purkinje cells and exhibit a spatial, sensory related organization. However, there are still many open questions unresolved, to unravel the role of Purkinje cells in sensorimotor control. We provide evidence, that Purkinje cells are rather involved in motor initiation than in motor execution. Recent studies provide also a promising outlook for larval zebrafish cerebellar research, as other hallmarks, such as the potential to acquire an conditioned stimulus, has been shown to exist in larval zebrafish (Harmon et al. 2017).

4.3 MCARMINE IS A USEFUL FAR-RED FLUORESCENT PROTEIN

The lack of proper far-red fluorescent proteins constrains the possibilities of researches for multicolor imaging. With mCarmine, we provide a well in vivo performing fluorescent protein, that allows simultaneous acquisition of a blue excitable fluorescent protein with literally no cross-talk.

Despite the advantages of far-red proteins, we realized that screening for mCarmine expression is not possible with the human eye. Either with camera assisted microscopy or a fusion protein (here with mTFP1) was needed to allow easy sorting of positive transgenic fish. We suggest to use transgenesis marker, such as a bleeding heart (*cmlc2*:mCherry) to select transgene carrier.

mCarmine is with its brightness of 8.6 relatively dim compared to best performing green fluorescent proteins (e.g. mNeonGreen with 92.8 and EGFP with 33.6). However, after multiple mutagenesis rounds, no brighter variants could be found, indicating that the current structural arrangement does not allow modifications leading to brighter variants. Thus, new fluorescent protein sources that offer more structural possibilities are desired. This strategy led also to the first monomeric red fluorescent protein family (Shaner et al. 2004), and could potentially overcome physical limitations constraining the performance of far-red shifted fluorescence proteins.

CONCLUSION

In this thesis, we followed a comprehensive approach to investigate sensorimotor circuits in larval zebrafish. New transgenic lines were developed to allow imaging and optogenetics experiments and novel optical and behavioral setups were built to perform imaging, optogenetics and behavioral experiments.

To understand which visual stimulus features contribute to evoking OMR, we could show that an approach to map receptive fields can be applied to characterize the particular stimulus features that drive behavior in our first study. Notably, we extend the classical thought that the optomotor response is elicited by pure whole-field directional motion. We now know that a local light-dark transition plays also an important role in combination with the contribution from whole-field motion.

In the last decades, there has been an ongoing debate about how the cerebellum works. With our second study, we provide a rich dataset of the activity of the whole Purkinje cell population in a visually driven, behavior evoking paradigm. We showed that Purkinje cells cluster spatially depending on their encoding of visual information in complex spikes, while motor information is highly enriched in simple spike activity across the cerebellum. Also, we provide evidence that the inferior olive may not act as an error detector, but rather as a sensory information source.

Visualizing innately unlabelled structure using fluorescent proteins revolutionized biology. In the third study, we provide a novel fluorescent protein, that will be useful for researchers that desire a well performing, far-red fluorescent protein, that works well in deep tissue.

Taken together, my doctoral research provided novel insights in the biology of larval zebrafish and how their cerebellum works. Given the conservation of brain structure across vertebrates, this data that can be potentially extrapolated to mammals, including us humans.

BIBLIOGRAPHY

Ahrens, Misha B., Jennifer M. Li, Michael B. Orger, Drew N. Robson, Alexander F. Schier, Florian Engert, and Ruben Portugues (May 2012). "Brain-Wide Neuronal Dynamics during Motor Adaptation in Zebrafish." en. In: *Nature* 485.7399, pp. 471–477. DOI: `10.1038/nature11057` (cit. on pp. 2, 4).

Akerboom, Jasper et al. (Oct. 2012). "Optimization of a GCaMP Calcium Indicator for Neural Activity Imaging." In: *The Journal of neuroscience : the official journal of the Society for Neuroscience* 32.40, pp. 13819–13840. DOI: `10.1523/JNEUROSCI.2601-12.2012` (cit. on pp. 8, 41).

Albus, James S. (Feb. 1971). "A Theory of Cerebellar Function." In: *Mathematical Biosciences* 10.1, pp. 25–61. DOI: `10.1016/0025-5564(71)90051-4` (cit. on pp. 12, 83).

Alonso, J. R., R. Arèvalo, J. G. Briñòn, J. Lara, E. Weruaga, and J. Aijòn (Mar. 1992). "Parvalbumin Immunoreactive Neurons and Fibres in the Teleost Cerebellum." en. In: *Anatomy and Embryology* 185.4, pp. 355–361. DOI: `10.1007/BF00188547` (cit. on p. 12).

Apps, Richard and Richard Hawkes (Sept. 2009). "Cerebellar Cortical Organization: A One-Map Hypothesis." eng. In: *Nature Reviews. Neuroscience* 10.9, pp. 670–681. DOI: `10.1038/nrn2698` (cit. on p. 83).

Asakawa, Kazuhide, Maximiliano L. Suster, Kanta Mizusawa, Saori Nagayoshi, Tomoya Kotani, Akihiro Urasaki, Yasuyuki Kishimoto, Masahiko Hibi, and Koichi Kawakami (Jan. 2008). "Genetic Dissection of Neural Circuits by Tol2 Transposon-Mediated Gal4 Gene and Enhancer Trapping in Zebrafish." en. In: *Proceedings of the National Academy of Sciences* 105.4, pp. 1255–1260. DOI: `10.1073/pnas.0704963105` (cit. on p. 2).

Bae, Young-Ki, Shuichi Kani, Takashi Shimizu, Koji Tanabe, Hideaki Nojima, Yukiko Kimura, Shin-ichi Higashijima, and Masahiko Hibi (June 2009). "Anatomy of Zebrafish Cerebellum and Screen for Mutations Affecting Its Development." In: *Developmental Biology* 330.2, pp. 406–426. DOI: `10.1016/j.ydbio.2009.04.013` (cit. on pp. 12, 14, 17, 18, 84).

Bianco, Isaac H. and Florian Engert (Mar. 2015). "Visuomotor Transformations Underlying Hunting Behavior in Zebrafish." In: *Current Biology* 25.7, pp. 831–846. DOI: `10.1016/j.cub.2015.01.042` (cit. on p. 81).

Biechl, Daniela, Alessandro Dorigo, Reinhard W. Köster, Benedikt Grothe, and Mario F. Wullimann (2016). "Eppur Si Muove: Evidence for an External Granular Layer and Possibly Transit Amplification in the Teleostean Cerebellum." In: *Frontiers in Neuroanatomy*, p. 49. DOI: `10.3389/fnana.2016.00049` (cit. on p. 17).

Borst, Alexander, Juergen Haag, and Dierk F. Reiff (2010). "Fly Motion Vision." eng. In: *Annual Review of Neuroscience* 33, pp. 49–70. DOI: 10.1146/annurev-neuro-060909-153155 (cit. on p. 3).

Bosch, Marie K., Yarimar Carrasquillo, Joseph L. Ransdell, Ajay Kanakamedala, David M. Ornitz, and Jeanne M. Nerbonne (Apr. 2015). "Intracellular FGF14 (iFGF14) Is Required for Spontaneous and Evoked Firing in Cerebellar Purkinje Neurons and for Motor Coordination and Balance." en. In: *The Journal of Neuroscience* 35.17, pp. 6752–6769. DOI: 10.1523/JNEUROSCI.2663-14.2015 (cit. on p. 14).

Bresenham, J. E. (1965). "Algorithm for Computer Control of a Digital Plotter." In: *IBM Systems Journal* 4.1, pp. 25–30. DOI: 10.1147/sj.41.0025 (cit. on p. 43).

Brockerhoff, S. E., J. B. Hurley, U. Janssen-Bienhold, S. C. Neuhauss, W. Driever, and J. E. Dowling (Nov. 1995). "A Behavioral Screen for Isolating Zebrafish Mutants with Visual System Defects." eng. In: *Proceedings of the National Academy of Sciences of the United States of America* 92.23, pp. 10545–10549 (cit. on p. 3).

Burgess, Harold A. and Michael Granato (May 2007). "Sensorimotor Gating in Larval Zebrafish." eng. In: *The Journal of Neuroscience: The Official Journal of the Society for Neuroscience* 27.18, pp. 4984–4994. DOI: 10.1523/JNEUROSCI.0615-07.2007 (cit. on p. 81).

Burgess, Harold A., Hannah Schoch, and Michael Granato (Feb. 2010). "Distinct Retinal Pathways Drive Spatial Orientation Behaviors in Zebrafish Navigation." eng. In: *Current biology: CB* 20.4, pp. 381–386. DOI: 10.1016/j.cub.2010.01.022 (cit. on pp. 4, 81).

Burrill, John D. and Stephen S. Easter (1994). "Development of the Retinofugal Projections in the Embryonic and Larval Zebrafish (Brachydanio Rerio)." en. In: *Journal of Comparative Neurology* 346.4, pp. 583–600. DOI: 10.1002/cne.903460410 (cit. on pp. 4, 81).

Cannon, R. C, D. A Turner, G. K Pyapali, and H. V Wheal (Oct. 1998). "An On-Line Archive of Reconstructed Hippocampal Neurons." In: *Journal of Neuroscience Methods* 84.1, pp. 49–54. DOI: 10.1016/S0165-0270(98)00091-0 (cit. on p. 43).

Chen, I.-Wen, Emiliano Ronzitti, Brian R. Lee, Tanya L. Daigle, Hongkui Zeng, Eirini Papagiakoumou, and Valentina Emiliani (Jan. 2018). "Parallel Holographic Illumination Enables Sub-Millisecond Two-Photon Optogenetic Activation in Mouse Visual Cortex in Vivo." en. In: *bioRxiv*, p. 250795. DOI: 10.1101/250795 (cit. on p. 67).

Chen, Tsai-Wen et al. (July 2013). "Ultrasensitive Fluorescent Proteins for Imaging Neuronal Activity." en. In: *Nature* 499.7458, pp. 295–300. DOI: 10.1038/nature12354 (cit. on pp. 2, 8, 41).

Chung, C. T., S. L. Niemela, and R. H. Miller (Apr. 1989). "One-Step Preparation of Competent Escherichia Coli: Transformation and Storage of Bacterial Cells in the Same Solution." en. In: *Proceedings of the National Academy of Sciences* 86.7, pp. 2172–2175. DOI: 10.1073/pnas.86.7.2172 (cit. on p. 22).

Clark, Damon A., James E. Fitzgerald, Justin M. Ales, Daryl M. Gohl, Marion A. Silies, Anthony M. Norcia, and Thomas R. Clandinin (Feb. 2014). "Flies and Humans Share a Motion Estimation Strategy That Exploits Natural Scene Statistics." eng. In: *Nature Neuroscience* 17.2, pp. 296–303. DOI: `10.1038/nn.3600` (cit. on p. 81).

Clark, DT (1981). *Visual Responses in Developing Zebrafish (Brachydanio Rerio), Ph. D. Thesis* (cit. on p. 3).

Coco, Marinella and Vincenzo Perciavalle (Aug. 2015). "Where Did the Motor Function of the Cerebellum Come From?" In: *Cerebellum & Ataxias* 2. DOI: `10.1186/s40673-015-0029-8` (cit. on p. 11).

Dawid, Igor B. (Dec. 2004). "Developmental Biology of Zebrafish." eng. In: *Annals of the New York Academy of Sciences* 1038, pp. 88–93. DOI: `10.1196/annals.1315.015` (cit. on p. 2).

Day, Richard N., Cynthia F. Booker, and Ammasi Periasamy (2008). "Characterization of an Improved Donor Fluorescent Protein for Förster Resonance Energy Transfer Microscopy." In: *Journal of biomedical optics* 13.3, p. 031203. DOI: `10.1117/1.2939094` (cit. on p. 78).

del Toro, Daniel, Tobias Ruff, Erik Cederfjäll, Ana Villalba, Gönül Seyit-Bremer, Víctor Borrell, and Rüdiger Klein (May 2017). "Regulation of Cerebral Cortex Folding by Controlling Neuronal Migration via FLRT Adhesion Molecules." en. In: *Cell* 169.4, 621–635.e16. DOI: `10.1016/j.cell.2017.04.012` (cit. on p. 2).

Denk, W., J. H. Strickler, and W. W. Webb (Apr. 1990). "Two-Photon Laser Scanning Fluorescence Microscopy." eng. In: *Science (New York, N.Y.)* 248.4951, pp. 73–76 (cit. on p. 34).

Dieringer, N., W. Precht, and A. R. Blight (1982). "Resetting Fast Phases of Head and Eye and Their Linkage in the Frog." eng. In: *Experimental Brain Research* 47.3, pp. 407–416 (cit. on p. 3).

Dunn, Timothy W., Christoph Gebhardt, Eva A. Naumann, Clemens Riegler, Misha B. Ahrens, Florian Engert, and Filippo Del Bene (Feb. 2016a). "Neural Circuits Underlying Visually Evoked Escapes in Larval Zebrafish." In: *Neuron* 89.3, pp. 613–628. DOI: `10.1016/j.neuron.2015.12.021` (cit. on p. 81).

Dunn, Timothy W. et al. (Mar. 2016b). "Brain-Wide Mapping of Neural Activity Controlling Zebrafish Exploratory Locomotion." en. In: *eLife* 5, e12741. DOI: `10.7554/eLife.12741` (cit. on p. 41).

Easter Stephen S., Jr. and Gregory N. Nicola (Dec. 1996). "The Development of Vision in the Zebrafish (Danio Rerio)." In: *Developmental Biology* 180.2, pp. 646–663. DOI: `10.1006/dbio.1996.0335` (cit. on p. 3).

Easter, Stephen S. and Gregory N. Nicola (1997). "The Development of Eye Movements in the Zebrafish (Danio Rerio)." en. In: *Developmental Psychobiology* 31.4, pp. 267–276. DOI: `10.1002/(SICI)1098-2302(199712)31:4<267::AID-DEV4>3.0.CO;2-P` (cit. on p. 3).

Fabritius, Arne, David Ng, **Andreas M. Kist**, Mutlu Erdogan, Ruben Portugues, and Oliver Griesbeck (Sept. 2018). "Imaging-Based Screen-

ing Platform Assists Protein Engineering." English. In: *Cell Chemical Biology* 0.0. DOI: `10.1016/j.chembiol.2018.08.008` (cit. on p. 80).

Favre-Bulle, Itia A., Gilles Vanwalleghem, Michael A. Taylor, Halina Rubinsztein-Dunlop, and Ethan K. Scott (Dec. 2018). "Cellular-Resolution Imaging of Vestibular Processing across the Larval Zebrafish Brain." English. In: *Current Biology* 28.23, 3711–3722.e3. DOI: `10.1016/j.cub.2018.09.060` (cit. on p. 83).

Feng, Linqing, Ting Zhao, and Jinhyun Kim (Jan. 2015). "neuTube 1.0: A New Design for Efficient Neuron Reconstruction Software Based on the SWC Format." en. In: *eNeuro* 2.1, ENEURO.0049–14.2014. DOI: `10.1523/ENEURO.0049-14.2014` (cit. on p. 43).

Gallimore, Andrew R., Taegon Kim, Keiko Tanaka-Yamamoto, and Erik De Schutter (Jan. 2018). "Switching On Depression and Potentiation in the Cerebellum." eng. In: *Cell Reports* 22.3, pp. 722–733. DOI: `10.1016/j.celrep.2017.12.084` (cit. on p. 14).

Gibson, Daniel G., Lei Young, Ray-Yuan Chuang, J. Craig Venter, Clyde A. Hutchison, and Hamilton O. Smith (May 2009). "Enzymatic Assembly of DNA Molecules up to Several Hundred Kilobases." eng. In: *Nature Methods* 6.5, pp. 343–345. DOI: `10.1038/nmeth.1318` (cit. on p. 22).

Guggiana-Nilo, Drago A. and Florian Engert (2016). "Properties of the Visible Light Phototaxis and UV Avoidance Behaviors in the Larval Zebrafish." English. In: *Frontiers in Behavioral Neuroscience* 10. DOI: `10.3389/fnbeh.2016.00160` (cit. on p. 34).

Guizar-Sicairos, Manuel, Samuel T. Thurman, and James R. Fienup (Jan. 2008). "Efficient Subpixel Image Registration Algorithms." EN. In: *Optics Letters* 33.2, pp. 156–158. DOI: `10.1364/OL.33.000156` (cit. on p. 39).

Haag, J., W. Denk, and A. Borst (Nov. 2004). "Fly Motion Vision Is Based on Reichardt Detectors Regardless of the Signal-to-Noise Ratio." en. In: *Proceedings of the National Academy of Sciences* 101.46, pp. 16333–16338. DOI: `10.1073/pnas.0407368101` (cit. on p. 81).

Haesemeyer, Martin, Drew N. Robson, Jennifer M. Li, Alexander F. Schier, and Florian Engert (Nov. 2015). "The Structure and Timescales of Heat Perception in Larval Zebrafish." In: *Cell Systems* 1.5, pp. 338–348. DOI: `10.1016/j.cels.2015.10.010` (cit. on pp. 6, 37, 64, 82).

Hamling, Kyla R., Zachary J.C. Tobias, and Tamily A. Weissman (Nov. 2015). "Mapping the Development of Cerebellar Purkinje Cells in Zebrafish." en. In: *Developmental Neurobiology* 75.11, pp. 1174–1188. DOI: `10.1002/dneu.22275` (cit. on pp. 14, 16, 67, 69).

Harmon, Thomas C, Uri Magaram, David L McLean, and Indira M Raman (2017). "Distinct Responses of Purkinje Neurons and Roles of Simple Spikes during Associative Motor Learning in Larval Zebrafish." In: *eLife* 6. DOI: `10.7554/eLife.22537` (cit. on p. 85).

Hawkes, Richard (2014). "Purkinje Cell Stripes and Long-Term Depression at the Parallel Fiber-Purkinje Cell Synapse." eng. In: *Frontiers*

in Systems Neuroscience 8, p. 41. DOI: `10.3389/fnsys.2014.00041` (cit. on p. 83).

Hawkes, Richard and Karl Herrup (Sept. 1995). "Aldolase C/Zebrin II and the Regionalization of the Cerebellum." en. In: *Journal of Molecular Neuroscience* 6.3, pp. 147–158. DOI: `10.1007/BF02736761` (cit. on pp. 15, 83).

Heap, Lucy A., Chi Ching Goh, Karin S. Kassahn, and Ethan K. Scott (Apr. 2013). "Cerebellar Output in Zebrafish: An Analysis of Spatial Patterns and Topography in Eurydendroid Cell Projections." In: *Frontiers in Neural Circuits* 7. DOI: `10.3389/fncir.2013.00053` (cit. on p. 17).

Hruscha, Alexander, Peter Krawitz, Alexandra Rechenberg, Verena Heinrich, Jochen Hecht, Christian Haass, and Bettina Schmid (Dec. 2013). "Efficient CRISPR/Cas9 Genome Editing with Low off-Target Effects in Zebrafish." en. In: *Development* 140.24, pp. 4982–4987. DOI: `10.1242/dev.099085` (cit. on p. 24).

Hsieh, Jui-Yi, Brittany Ulrich, Fadi A. Issa, Jijun Wan, and Diane M. Papazian (2014). "Rapid Development of Purkinje Cell Excitability, Functional Cerebellar Circuit, and Afferent Sensory Input to Cerebellum in Zebrafish." In: *Frontiers in Neural Circuits* 8, p. 147. DOI: `10.3389/fncir.2014.00147` (cit. on p. 16).

Hu, Qin and Jonathan D. Victor (Mar. 2010). "A Set of High-Order Spatiotemporal Stimuli That Elicit Motion and Reverse-Phi Percepts." eng. In: *Journal of Vision* 10.3, pp. 9.1–16. DOI: `10.1167/10.3.9` (cit. on p. 81).

Ikenaga, Takanori, Masayuki Yoshida, and Kazumasa Uematsu (July 2005). "Morphology and Immunohistochemistry of Efferent Neurons of the Goldfish Corpus Cerebelli." eng. In: *The Journal of Comparative Neurology* 487.3, pp. 300–311. DOI: `10.1002/cne.20553` (cit. on p. 17).

– (Dec. 2006). "Cerebellar Efferent Neurons in Teleost Fish." en. In: *The Cerebellum* 5.4, pp. 268–274. DOI: `10.1080/14734220600930588` (cit. on p. 17).

Ishikawa, Takahiro, Saeka Tomatsu, Jun Izawa, and Shinji Kakei (Mar. 2016). "The Cerebro-Cerebellum: Could It Be Loci of Forward Models?" eng. In: *Neuroscience Research* 104, pp. 72–79. DOI: `10.1016/j.neures.2015.12.003` (cit. on p. 83).

Ito, Masao (May 1972). "Neural Design of the Cerebellar Motor Control System." In: *Brain Research* 40.1, pp. 81–84. DOI: `10.1016/0006-8993(72)90110-2` (cit. on p. 83).

– (Feb. 2013). "Error Detection and Representation in the Olivo-Cerebellar System." In: *Frontiers in Neural Circuits* 7. DOI: `10.3389/fncir.2013.00001` (cit. on pp. 17, 83).

Kim, Dal Hyung, Jungsoo Kim, João C. Marques, Abhinav Grama, David G. C. Hildebrand, Wenchao Gu, Jennifer M. Li, and Drew N. Robson (Sept. 2017). "Pan-Neuronal Calcium Imaging with Cellular

Resolution in Freely Swimming Zebrafish." en. In: *Nature Methods* advance online publication. DOI: `10.1038/nmeth.4429` (cit. on p. 21).

Kimmel, C. B., W. W. Ballard, S. R. Kimmel, B. Ullmann, and T. F. Schilling (July 1995). "Stages of Embryonic Development of the Zebrafish." eng. In: *Developmental Dynamics: An Official Publication of the American Association of Anatomists* 203.3, pp. 253–310. DOI: `10.1002/aja.1002030302` (cit. on p. 2).

Kimura, Yukiko, Chie Satou, and Shin-ichi Higashijima (Sept. 2008). "V2a and V2b Neurons Are Generated by the Final Divisions of Pair-Producing Progenitors in the Zebrafish Spinal Cord." en. In: *Development* 135.18, pp. 3001–3005. DOI: `10.1242/dev.024802` (cit. on p. 21).

Kirshner, H., F. Aguet, D. Sage, and M. Unser (Jan. 2013). "3-D PSF Fitting for Fluorescence Microscopy: Implementation and Localization Application." eng. In: *Journal of Microscopy* 249.1, pp. 13–25. DOI: `10.1111/j.1365-2818.2012.03675.x` (cit. on p. 43).

Kist, Andreas M., Laura D. Knogler, Daniil A. Markov, Tugce Yildizoglu, and Ruben Portugues (2017). "Whole-Brain Imaging Using Genetically Encoded Activity Sensors in Vertebrates." en. In: *Decoding Neural Circuit Structure and Function*. Springer, Cham, pp. 321–341. DOI: `10.1007/978-3-319-57363-2_13` (cit. on pp. 21, 34).

Knogler, Laura D., **Andreas M. Kist**, and Ruben Portugues (Oct. 2018). "Motor Context Dominates Output from Purkinje Cell Functional Regions during Reflexive Visuomotor Behaviors." en. In: *bioRxiv*, p. 432153. DOI: `10.1101/432153` (cit. on p. 84).

– (Jan. 2019). "Motor Context Dominates Output from Purkinje Cell Functional Regions during Reflexive Visuomotor Behaviours." In: *eLife* 8. Ed. by Indira M. Raman, e42138. DOI: `10.7554/eLife.42138` (cit. on pp. 15, 19, 40, 68–74, 83).

Knogler, Laura D., Daniil A. Markov, Elena I. Dragomir, Vilim Štih, and Ruben Portugues (May 2017). "Sensorimotor Representations in Cerebellar Granule Cells in Larval Zebrafish Are Dense, Spatially Organized, and Non-Temporally Patterned." In: *Current Biology* 27.9, pp. 1288–1302. DOI: `10.1016/j.cub.2017.03.029` (cit. on pp. 12, 13, 41, 43, 72, 74, 83).

Kono, Maya, Wataru Kakegawa, Kazunari Yoshida, and Michisuke Yuzaki (Nov. 2018). "Interneuronal NMDA Receptors Regulate Long-Term Depression and Motor Learning in the Cerebellum." eng. In: *The Journal of Physiology*. DOI: `10.1113/JP276794` (cit. on p. 14).

Kubo, Fumi, Bastian Hablitzel, Marco Dal Maschio, Wolfgang Driever, Herwig Baier, and Aristides B. Arrenberg (Mar. 2014). "Functional Architecture of an Optic Flow-Responsive Area That Drives Horizontal Eye Movements in Zebrafish." In: *Neuron* 81.6, pp. 1344–1359. DOI: `10.1016/j.neuron.2014.02.043` (cit. on pp. 4, 82).

Larouche, Matt and Richard Hawkes (2006). "From Clusters to Stripes: The Developmental Origins of Adult Cerebellar Compartmentation."

eng. In: *Cerebellum (London, England)* 5.2, pp. 77–88. DOI: `10.1080/14734220600804668` (cit. on p. 83).

Leonhardt, Aljoscha, Georg Ammer, Matthias Meier, Etienne Serbe, Armin Bahl, and Alexander Borst (May 2016). "Asymmetry of Drosophila ON and OFF Motion Detectors Enhances Real-World Velocity Estimation." eng. In: *Nature Neuroscience* 19.5, pp. 706–715. DOI: `10.1038/nn.4262` (cit. on p. 81).

Lin, John Y., Per Magne Knutsen, Arnaud Muller, David Kleinfeld, and Roger Y. Tsien (Oct. 2013). "ReaChR: A Red-Shifted Variant of Channelrhodopsin Enables Deep Transcranial Optogenetic Excitation." en. In: *Nature neuroscience* 16.10, p. 1499. DOI: `10.1038/nn.3502` (cit. on p. 14).

Lister, J.A., C.P. Robertson, T. Lepage, S.L. Johnson, and D.W. Raible (1999). "Nacre Encodes a Zebrafish Microphthalmia-Related Protein That Regulates Neural-Crest-Derived Pigment Cell Fate." In: *Development* 126.17, pp. 3757–3767 (cit. on pp. 2, 21).

Looger, Loren L and Oliver Griesbeck (Feb. 2012). "Genetically Encoded Neural Activity Indicators." In: *Current Opinion in Neurobiology*. Neurotechnology 22.1, pp. 18–23. DOI: `10.1016/j.conb.2011.10.024` (cit. on p. 8).

Lucy, L. B. (June 1974). "An Iterative Technique for the Rectification of Observed Distributions." In: *The Astronomical Journal* 79, p. 745. DOI: `10.1086/111605` (cit. on p. 42).

Margulis, Lynn and Michael J Chapman (Jan. 2009). "Chapter Three - ANIMALIA." In: *Kingdoms and Domains (Fourth Edition)*. Ed. by Lynn Margulis and Michael J Chapman. London: Academic Press, pp. 231–377. DOI: `10.1016/B978-0-12-373621-5.00003-9` (cit. on p. 1).

Marques, João C., Simone Lackner, Rita Félix, and Michael B. Orger (Jan. 2018). "Structure of the Zebrafish Locomotor Repertoire Revealed with Unsupervised Behavioral Clustering." eng. In: *Current biology: CB* 28.2, 181–195.e5. DOI: `10.1016/j.cub.2017.12.002` (cit. on p. 4).

Marr David (June 1969). "A Theory of Cerebellar Cortex." In: *The Journal of Physiology* 202.2, pp. 437–470. DOI: `10.1113/jphysiol.1969.sp008820` (cit. on pp. 12, 83).

Matilla-Dueñas, A. et al. (Apr. 2014). "Consensus Paper: Pathological Mechanisms Underlying Neurodegeneration in Spinocerebellar Ataxias." In: *Cerebellum (London, England)* 13.2, pp. 269–302. DOI: `10.1007/s12311-013-0539-y` (cit. on p. 16).

Matsui, Hideaki, Kazuhiko Namikawa, Andreas Babaryka, and Reinhard W. Köster (Dec. 2014). "Functional Regionalization of the Teleost Cerebellum Analyzed in Vivo." en. In: *Proceedings of the National Academy of Sciences* 111.32, pp. 11846–11851. DOI: `10.1073/pnas.1403105111` (cit. on pp. 3, 10, 12, 14, 16, 21, 83).

Matsuo, Megumi, Yoriko Ando, Yasuhiro Kamei, and Shoji Fukamachi (June 2018). "A Semi-Automatic and Quantitative Method to Evaluate Behavioral Photosensitivity in Animals Based on the Optomotor Response (OMR)." eng. In: *Biology Open* 7.6. DOI: 10.1242/bio.033175 (cit. on p. 3).

McFarland, Karen A., Jolanta M. Topczewska, Gilbert Weidinger, Richard I. Dorsky, and Bruce Appel (June 2008). "Hh and Wnt Signaling Regulate Formation of Olig2+ Neurons in the Zebrafish Cerebellum." In: *Developmental Biology* 318.1, pp. 162–171. DOI: 10.1016/j.ydbio.2008.03.016 (cit. on p. 17).

Meek, J. (May 1992). "Why Run Parallel Fibers Parallel? Teleostean Purkinje Cells as Possible Coincidence Detectors, in a Timing Device Subserving Spatial Coding of Temporal Differences." In: *Neuroscience* 48.2, pp. 249–283. DOI: 10.1016/0306-4522(92)90489-0 (cit. on p. 13).

Meek, J., T. G. M. Hafmans, L. Maler, and R. Hawkes (Feb. 1992). "Distribution of Zebrin II in the Gigantocerebellum of the Mormyrid Fish Gnathonemus Petersii Compared with Other Teleosts." In: *Journal of Comparative Neurology* 316.1, pp. 17–31. DOI: 10.1002/cne.903160103 (cit. on pp. 12, 14).

Meera, Pratap, Stefan M. Pulst, and Thomas S. Otis (Aug. 2016). "Cellular and Circuit Mechanisms Underlying Spinocerebellar Ataxias." In: *The Journal of Physiology* 594.16, pp. 4653–4660. DOI: 10.1113/JP271897 (cit. on p. 16).

Miall, R. C. and D. M. Wolpert (Nov. 1996). "Forward Models for Physiological Motor Control." In: *Neural Networks*. Four Major Hypotheses in Neuroscience 9.8, pp. 1265–1279. DOI: 10.1016/S0893-6080(96)00035-4 (cit. on p. 83).

Migault, Geoffrey, Thijs L. van der Plas, Hugo Trentesaux, Thomas Panier, Raphaël Candelier, Rémi Proville, Bernhard Englitz, Georges Debrégeas, and Volker Bormuth (Dec. 2018). "Whole-Brain Calcium Imaging during Physiological Vestibular Stimulation in Larval Zebrafish." English. In: *Current Biology* 28.23, 3723–3735.e6. DOI: 10.1016/j.cub.2018.10.017 (cit. on p. 83).

Müller, Thomas and Mario F. Wullimann (Dec. 2015). *Atlas of Early Zebrafish Brain Development - 2nd Edition*. English. Elsevier (cit. on p. 2).

Muto, Akira et al. (Nov. 2005). "Forward Genetic Analysis of Visual Behavior in Zebrafish." en. In: *PLOS Genetics* 1.5, e66. DOI: 10.1371/journal.pgen.0010066 (cit. on p. 4).

Nakai, J., M. Ohkura, and K. Imoto (Feb. 2001). "A High Signal-to-Noise Ca(2+) Probe Composed of a Single Green Fluorescent Protein." eng. In: *Nature Biotechnology* 19.2, pp. 137–141. DOI: 10.1038/84397 (cit. on p. 8).

Namikawa, Kazuhiko, Alessandro Dorigo, Marta Zagrebelsky, Giulio Russo, Toni Kirmann, Wieland Fahr, Stefan Dübel, Martin Korte,

and Reinhard W. Köster (May 2019). "Modeling Neurodegenerative Spinocerebellar Ataxia Type 13 in Zebrafish Using a Purkinje Neuron Specific Tunable Coexpression System." en. In: *Journal of Neuroscience* 39.20, pp. 3948–3969. DOI: 10.1523/JNEUROSCI.1862-18.2019 (cit. on p. 14).

Naumann, Eva A., James E. Fitzgerald, Timothy W. Dunn, Jason Rihel, Haim Sompolinsky, and Florian Engert (Nov. 2016). "From Whole-Brain Data to Functional Circuit Models: The Zebrafish Optomotor Response." English. In: *Cell* 167.4, 947–960.e20. DOI: 10.1016/j.cell.2016.10.019 (cit. on pp. 4, 82).

Neuhauss, Stephan C. F., Oliver Biehlmaier, Mathias W. Seeliger, Tilak Das, Konrad Kohler, William A. Harris, and Herwig Baier (Oct. 1999). "Genetic Disorders of Vision Revealed by a Behavioral Screen of 400 Essential Loci in Zebrafish." en. In: *Journal of Neuroscience* 19.19, pp. 8603–8615 (cit. on pp. 3, 4).

Nikolaou, Nikolas, Andrew S. Lowe, Alison S. Walker, Fatima Abbas, Paul R. Hunter, Ian D. Thompson, and Martin P. Meyer (Oct. 2012). "Parametric Functional Maps of Visual Inputs to the Tectum." eng. In: *Neuron* 76.2, pp. 317–324. DOI: 10.1016/j.neuron.2012.08.040 (cit. on p. 4).

Nitzany, Eyal, Gil Menda, Paul S. Shamble, James R. Golden, Qin Hu, Ron R. Hoy, and Jonathan Victor (Dec. 2017). "Neural Computations Combine Low- and High-Order Motion Cues Similarly, in Dragonfly and Monkey." en. In: *bioRxiv*, p. 240101. DOI: 10.1101/240101 (cit. on p. 81).

Ohyama, Tatsuya, William L. Nores, Matthew Murphy, and Michael D. Mauk (Apr. 2003). "What the Cerebellum Computes." In: *Trends in Neurosciences* 26.4, pp. 222–227. DOI: 10.1016/S0166-2236(03)00054-7 (cit. on p. 83).

Okamoto, Hitoshi (Dec. 2014). "Minicerebellum, Now Available for Reductionists' Functional Study." en. In: *Proceedings of the National Academy of Sciences* 111.32, pp. 11580–11581. DOI: 10.1073/pnas.1411821111 (cit. on p. 12).

Orger, M. B., M. C. Smear, S. M. Anstis, and H. Baier (Nov. 2000). "Perception of Fourier and Non-Fourier Motion by Larval Zebrafish." eng. In: *Nature Neuroscience* 3.11, pp. 1128–1133. DOI: 10.1038/80649 (cit. on p. 4).

Orger, Michael B. and Herwig Baier (May 2005). "Channeling of Red and Green Cone Inputs to the Zebrafish Optomotor Response." en. In: *Visual Neuroscience* 22.3, pp. 275–281. DOI: 10.1017/S0952523805223039 (cit. on pp. 4, 81).

Orger, Michael B. and Gonzalo G. de Polavieja (July 2017). "Zebrafish Behavior: Opportunities and Challenges." In: *Annual Review of Neuroscience* 40.1, pp. 125–147. DOI: 10.1146/annurev-neuro-071714-033857 (cit. on p. 3).

Orger, Michael B. and Ruben Portugues (2016). "Correlating Whole Brain Neural Activity with Behavior in Head-Fixed Larval Zebrafish." en. In: *Zebrafish: Methods and Protocols*. Ed. by Koichi Kawakami, E. Elizabeth Patton, and Michael Orger. Methods in Molecular Biology. New York, NY: Springer New York, pp. 307–320. DOI: `10.1007/978-1-4939-3771-4_21` (cit. on p. 40).

Pakan, Janelle M. P., Andrew N. Iwaniuk, Douglas R. W. Wylie, Richard Hawkes, and Hassan Marzban (Apr. 2007). "Purkinje Cell Compartmentation as Revealed by Zebrin II Expression in the Cerebellar Cortex of Pigeons (Columba Livia)." eng. In: *The Journal of Comparative Neurology* 501.4, pp. 619–630. DOI: `10.1002/cne.21266` (cit. on p. 83).

Park, Hae-Chul et al. (Nov. 2000). "Analysis of Upstream Elements in the HuC Promoter Leads to the Establishment of Transgenic Zebrafish with Fluorescent Neurons." In: *Developmental Biology* 227.2, pp. 279–293. DOI: `10.1006/dbio.2000.9898` (cit. on pp. 3, 10, 78).

Piersol, George A. (George Arthur) and Thomas Dwight (1916). *Human Anatomy, Including Structure and Development and Practical Considerations*. eng. Philadelphia & London : Lippincott company (cit. on p. 15).

Pillow, Jonathan W., Jonathon Shlens, Liam Paninski, Alexander Sher, Alan M. Litke, E. J. Chichilnisky, and Eero P. Simoncelli (Aug. 2008). "Spatio-Temporal Correlations and Visual Signalling in a Complete Neuronal Population." eng. In: *Nature* 454.7207, pp. 995–999. DOI: `10.1038/nature07140` (cit. on p. 5).

Porrill, John, Paul Dean, and Sean R. Anderson (Nov. 2013). "Adaptive Filters and Internal Models: Multilevel Description of Cerebellar Function." In: *Neural Networks*. Computation in the Cerebellum 47, pp. 134–149. DOI: `10.1016/j.neunet.2012.12.005` (cit. on p. 83).

Portugues, Ruben and Florian Engert (2011). "Adaptive Locomotor Behavior in Larval Zebrafish." In: *Frontiers in Systems Neuroscience* 5, p. 72. DOI: `10.3389/fnsys.2011.00072` (cit. on pp. 3, 4, 29, 30).

Portugues, Ruben, Claudia E. Feierstein, Florian Engert, and Michael B. Orger (Mar. 2014). "Whole-Brain Activity Maps Reveal Stereotyped, Distributed Networks for Visuomotor Behavior." English. In: *Neuron* 81.6, pp. 1328–1343. DOI: `10.1016/j.neuron.2014.01.019` (cit. on p. 40).

Portugues, Ruben, Martin Haesemeyer, Mirella L. Blum, and Florian Engert (May 2015). "Whole-Field Visual Motion Drives Swimming in Larval Zebrafish via a Stochastic Process." en. In: *Journal of Experimental Biology* 218.9, pp. 1433–1443. DOI: `10.1242/jeb.118299` (cit. on pp. 4, 81).

Ramirez, Jorge E. and Brandon M. Stell (Dec. 2016). "Calcium Imaging Reveals Coordinated Simple Spike Pauses in Populations of Cerebellar Purkinje Cells." English. In: *Cell Reports* 17.12, pp. 3125–3132. DOI: `10.1016/j.celrep.2016.11.075` (cit. on pp. 14, 15, 74).

Randlett, Owen et al. (Sept. 2015). "Whole-Brain Activity Mapping onto a Zebrafish Brain Atlas." en. In: *Nature Methods* advance online publication. DOI: 10.1038/nmeth.3581 (cit. on p. 41).

Ransdell, Joseph L., Edward Dranoff, Brandon Lau, Wan-Lin Lo, David L. Donermeyer, Paul M. Allen, and Jeanne M. Nerbonne (Apr. 2017). "Loss of Navβ4-Mediated Regulation of Sodium Currents in Adult Purkinje Neurons Disrupts Firing and Impairs Motor Coordination and Balance." eng. In: *Cell Reports* 19.3, pp. 532–544. DOI: 10.1016/j.celrep.2017.03.068 (cit. on p. 14).

Richardson, William Hadley (Jan. 1972). "Bayesian-Based Iterative Method of Image Restoration*." EN. In: *JOSA* 62.1, pp. 55–59. DOI: 10.1364/JOSA.62.000055 (cit. on p. 42).

Robles, Estuardo, Eva Laurell, and Herwig Baier (Sept. 2014). "The Retinal Projectome Reveals Brain-Area-Specific Visual Representations Generated by Ganglion Cell Diversity." eng. In: *Current biology: CB* 24.18, pp. 2085–2096. DOI: 10.1016/j.cub.2014.07.080 (cit. on pp. 4, 81).

Roeser, Tobias and Herwig Baier (May 2003). "Visuomotor Behaviors in Larval Zebrafish after GFP-Guided Laser Ablation of the Optic Tectum." eng. In: *The Journal of Neuroscience: The Official Journal of the Society for Neuroscience* 23.9, pp. 3726–3734 (cit. on p. 4).

Rohlfing, Torsten and Calvin R. Maurer (Mar. 2003). "Nonrigid Image Registration in Shared-Memory Multiprocessor Environments with Application to Brains, Breasts, and Bees." eng. In: *IEEE transactions on information technology in biomedicine: a publication of the IEEE Engineering in Medicine and Biology Society* 7.1, pp. 16–25 (cit. on p. 43).

Rose, Tobias, Pieter M. Goltstein, Ruben Portugues, and Oliver Griesbeck (2014). "Putting a Finishing Touch on GECIs." English. In: *Frontiers in Molecular Neuroscience* 7. DOI: 10.3389/fnmol.2014.00088 (cit. on pp. 2, 8).

Rosenblatt, Frank (Mar. 1961). *Principles of Neurodynamics. Perceptrons and the Theory of Brain Mechanisms.* en. Tech. rep. VG-1196-G-8. CORNELL AERONAUTICAL LAB INC BUFFALO NY (cit. on p. 30).

Sage, Daniel, Lauréne Donati, Ferréol Soulez, Denis Fortun, Guillaume Schmit, Arne Seitz, Romain Guiet, Cédric Vonesch, and Michael Unser (Feb. 2017). "DeconvolutionLab2: An Open-Source Software for Deconvolution Microscopy." eng. In: *Methods (San Diego, Calif.)* 115, pp. 28–41. DOI: 10.1016/j.ymeth.2016.12.015 (cit. on p. 43).

Sawada, Kazuhiko, Yoshihiro Fukui, and Richard Hawkes (July 2008). "Spatial Distribution of Corticotropin-Releasing Factor Immunopositive Climbing Fibers in the Mouse Cerebellum: Analysis by Whole Mount Immunohistochemistry." eng. In: *Brain Research* 1222, pp. 106–117. DOI: 10.1016/j.brainres.2008.05.029 (cit. on p. 83).

Scalise, Karina, Takashi Shimizu, Masahiko Hibi, and Nathaniel B. Sawtell (Nov. 2016). "Responses of Cerebellar Purkinje Cells during

Fictive Optomotor Behavior in Larval Zebrafish." en. In: *Journal of Neurophysiology* 116.5, pp. 2067–2080. DOI: `10.1152/jn.00042.2016` (cit. on p. 16).

Scholz, Judith, Hüseyin Besir, Claudia Strasser, and Sabine Suppmann (Feb. 2013). "A New Method to Customize Protein Expression Vectors for Fast, Efficient and Background Free Parallel Cloning." In: *BMC Biotechnology* 13, p. 12. DOI: `10.1186/1472-6750-13-12` (cit. on p. 24).

Schwartz, Odelia, Jonathan W. Pillow, Nicole C. Rust, and Eero P. Simoncelli (Feb. 2006). "Spike-Triggered Neural Characterization." In: *Journal of Vision* 6.4, pp. 13–13. DOI: `10.1167/6.4.13` (cit. on pp. 5, 37, 47, 50).

Scott, Ethan K., Herwig Baier, Ethan K. Scott, and Herwig Baier (2009). "The Cellular Architecture of the Larval Zebrafish Tectum, as Revealed by Gal4 Enhancer Trap Lines." In: *Frontiers in Neural Circuits* 3, p. 13. DOI: `10.3389/neuro.04.013.2009` (cit. on p. 3).

Scott, Ethan K. et al. (Apr. 2007). "Targeting Neural Circuitry in Zebrafish Using GAL4 Enhancer Trapping." eng. In: *Nature Methods* 4.4, pp. 323–326. DOI: `10.1038/nmeth1033` (cit. on p. 3).

Semmelhack, Julia L., Joseph C. Donovan, Tod R. Thiele, Enrico Kuehn, Eva Laurell, and Herwig Baier (Dec. 2014). "A Dedicated Visual Pathway for Prey Detection in Larval Zebrafish." en. In: *eLife* 3, e04878. DOI: `10.7554/eLife.04878` (cit. on p. 81).

Sengupta, Mohini and Vatsala Thirumalai (Sept. 2015). "AMPA Receptor Mediated Synaptic Excitation Drives State-Dependent Bursting in Purkinje Neurons of Zebrafish Larvae." en. In: *eLife* 4, e09158. DOI: `10.7554/eLife.09158` (cit. on p. 16).

Severi, Kristen E., Ruben Portugues, João C. Marques, Donald M. O'Malley, Michael B. Orger, and Florian Engert (Aug. 2014). "Neural Control and Modulation of Swimming Speed in the Larval Zebrafish." eng. In: *Neuron* 83.3, pp. 692–707. DOI: `10.1016/j.neuron.2014.06.032` (cit. on pp. 4, 50, 81).

Shaner, Nathan C., Robert E. Campbell, Paul A. Steinbach, Ben N. G. Giepmans, Amy E. Palmer, and Roger Y. Tsien (Dec. 2004). "Improved Monomeric Red, Orange and Yellow Fluorescent Proteins Derived from *Discosoma* Sp. Red Fluorescent Protein." en. In: *Nature Biotechnology* 22.12, pp. 1567–1572. DOI: `10.1038/nbt1037` (cit. on pp. 9, 85).

Shi, Cong, Xuedong Yuan, Karen Chang, Kin-Sang Cho, Xinmin Simon Xie, Dong Feng Chen, and Gang Luo (June 2018). "Optimization of Optomotor Response-Based Visual Function Assessment in Mice." eng. In: *Scientific Reports* 8.1, p. 9708. DOI: `10.1038/s41598-018-27329-w` (cit. on p. 3).

Simpson, John I. and Keith E. Alley (Dec. 1974). "Visual Climbing Fiber Input to Rabbit Vestibulo-Cerebellum: A Source of Direction-

Specific Information." In: *Brain Research* 82.2, pp. 302–308. DOI: 10. 1016/0006-8993(74)90610-6 (cit. on p. 83).

Štih, Vilim, Luigi Petrucco, **Andreas M. Kist**, and Ruben Portugues (Dec. 2018). "Stytra: An Open-Source, Integrated System for Stimulation, Tracking and Closed-Loop Behavioral Experiments." en. In: *bioRxiv*, p. 492553. DOI: 10.1101/492553 (cit. on p. 33).

Streng, Martha L., Laurentiu S. Popa, and Timothy J. Ebner (Dec. 2018). "Complex Spike Wars: A New Hope." eng. In: *Cerebellum (London, England)* 17.6, pp. 735–746. DOI: 10.1007/s12311-018-0960-3 (cit. on p. 19).

Suvrathan, Aparna and Jennifer L. Raymond (Aug. 2018). "Depressed by Learning—Heterogeneity of the Plasticity Rules at Parallel Fiber Synapses onto Purkinje Cells." en. In: *The Cerebellum*, pp. 1–9. DOI: 10.1007/s12311-018-0968-8 (cit. on pp. 12, 14).

Tabor, Kathryn M., Sadie A. Bergeron, Eric J. Horstick, Diana C. Jordan, Vilma Aho, Tarja Porkka-Heiskanen, Gal Haspel, and Harold A. Burgess (May 2014). "Direct Activation of the Mauthner Cell by Electric Field Pulses Drives Ultra-Rapid Escape Responses." en. In: *Journal of Neurophysiology*, jn.00228.2014. DOI: 10.1152/jn.00228. 2014 (cit. on p. 67).

Takeuchi, Miki et al. (Jan. 2015). "Establishment of Gal4 Transgenic Zebrafish Lines for Analysis of Development of Cerebellar Neural Circuitry." In: *Developmental Biology* 397.1, pp. 1–17. DOI: 10.1016/j. ydbio.2014.09.030 (cit. on pp. 10, 12, 14, 17, 18, 21, 72, 84).

Temizer, Incinur, Joseph C. Donovan, Herwig Baier, and Julia L. Semmelhack (July 2015). "A Visual Pathway for Looming-Evoked Escape in Larval Zebrafish." In: *Current Biology* 25.14, pp. 1823–1834. DOI: 10.1016/j.cub.2015.06.002 (cit. on pp. 4, 81).

Thestrup, Thomas et al. (Feb. 2014). "Optimized Ratiometric Calcium Sensors for Functional *in Vivo* Imaging of Neurons and T Lymphocytes." en. In: *Nature Methods* 11.2, pp. 175–182. DOI: 10.1038/nmeth. 2773 (cit. on p. 8).

Thompson, R. F. (Aug. 1986). "The Neurobiology of Learning and Memory." en. In: *Science* 233.4767, pp. 941–947. DOI: 10.1126/ science.3738519 (cit. on p. 11).

Thompson, R. F. and J. E. Steinmetz (Sept. 2009). "The Role of the Cerebellum in Classical Conditioning of Discrete Behavioral Responses." eng. In: *Neuroscience* 162.3, pp. 732–755. DOI: 10.1016/j. neuroscience.2009.01.041 (cit. on p. 11).

Tsai, Philbert S. and David Kleinfeld (2009). "In Vivo Two-Photon Laser Scanning Microscopy with Concurrent Plasma-Mediated Ablation Principles and Hardware Realization." eng. In: *In Vivo Optical Imaging of Brain Function*. Ed. by Ron D. Frostig. 2nd. Frontiers in Neuroscience. Boca Raton (FL): CRC Press/Taylor & Francis (cit. on p. 34).

Tsien, R. Y. (Apr. 1981). "A Non-Disruptive Technique for Loading Calcium Buffers and Indicators into Cells." eng. In: *Nature* 290.5806, pp. 527–528 (cit. on p. 6).

Villamizar, Natalia, Luisa María Vera, Nicholas Simon Foulkes, and Francisco Javier Sánchez-Vázquez (Apr. 2014). "Effect of Lighting Conditions on Zebrafish Growth and Development." In: *Zebrafish* 11.2, pp. 173–181. DOI: 10.1089/zeb.2013.0926 (cit. on p. 34).

Voogd, Jan and Neal H. Barmack (2006). "Oculomotor Cerebellum." eng. In: *Progress in Brain Research* 151, pp. 231–268. DOI: 10.1016/S0079-6123(05)51008-2 (cit. on p. 16).

White, Richard Mark et al. (Feb. 2008). "Transparent Adult Zebrafish as a Tool for in Vivo Transplantation Analysis." eng. In: *Cell Stem Cell* 2.2, pp. 183–189. DOI: 10.1016/j.stem.2007.11.002 (cit. on p. 42).

Williams, D. A., K. E. Fogarty, R. Y. Tsien, and F. S. Fay (Dec. 1985). "Calcium Gradients in Single Smooth Muscle Cells Revealed by the Digital Imaging Microscope Using Fura-2." eng. In: *Nature* 318.6046, pp. 558–561 (cit. on p. 6).

Wolpert, D. M., Z. Ghahramani, and M. I. Jordan (Sept. 1995). "An Internal Model for Sensorimotor Integration." en. In: *Science* 269.5232, pp. 1880–1882. DOI: 10.1126/science.7569931 (cit. on pp. 16, 83).

Wolpert, D. M., R. Chris Miall, and Mitsuo Kawato (Sept. 1998). "Internal Models in the Cerebellum." In: *Trends in Cognitive Sciences* 2.9, pp. 338–347. DOI: 10.1016/S1364-6613(98)01221-2 (cit. on pp. 16, 83).

Xia, Guangbin, Karen N. McFarland, Kang Wang, Partha S. Sarkar, Anthony T. Yachnis, and Tetsuo Ashizawa (Dec. 2013). "Purkinje Cell Loss Is the Major Brain Pathology of Spinocerebellar Ataxia Type 10." en. In: *J Neurol Neurosurg Psychiatry* 84.12, pp. 1409–1411. DOI: 10.1136/jnnp-2013-305080 (cit. on p. 84).

Yavari, Fatemeh, Shirin Mahdavi, Farzad Towhidkhah, Mohammad-Ali Ahmadi-Pajouh, Hamed Ekhtiari, and Mohammad Darainy (Dec. 2015). "Cerebellum as a Forward but Not Inverse Model in Visuomotor Adaptation Task: A tDCS-Based and Modeling Study." en. In: *Experimental Brain Research* 234.4, pp. 997–1012. DOI: 10.1007/s00221-015-4523-2 (cit. on p. 83).

Zhang, Yongwei, Uwe Werling, and Winfried Edelmann (Jan. 2012). "SLiCE: A Novel Bacterial Cell Extract-Based DNA Cloning Method." en. In: *Nucleic Acids Research* 40.8, e55–e55. DOI: 10.1093/nar/gkr1288 (cit. on p. 22).

Zhu, Peixin, Otto Fajardo, Jennifer Shum, Yan-Ping Zhang Schärer, and Rainer W. Friedrich (July 2012). "High-Resolution Optical Control of Spatiotemporal Neuronal Activity Patterns in Zebrafish Using a Digital Micromirror Device." en. In: *Nature Protocols* 7.7, pp. 1410–1425. DOI: 10.1038/nprot.2012.072 (cit. on p. 28).

ACKNOWLEDGMENTS

Little fish movie

am so proud of you. My life and family would be nothing without my wife Janina. I know that you have had to cut back yourself so much, in order to give me the freedom and possibility to do my PhD. You ensure that our family holds together, I am so grateful every day that I can be with you.

APPENDIX

A
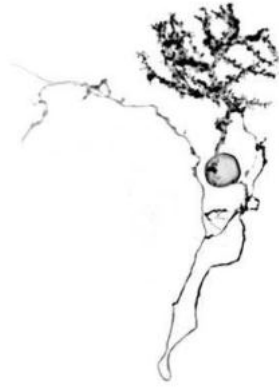
APPENDIX

In this appendix are important methodological notes and protocols, such as molecular biology techniques and Python code used in this thesis.

In particular, you will find

- Licensing and reuse of published material in this thesis

- List of generated transgenic fish lines

- Github and bitbucket repositories with short description

- Light-sheet chamber

- Jupyter notebook explaining LNP, STA and STC

- Jupyter notebook using artificial neural network to find features

- Tail track code

- Eye track code

- Cloning protocol for PC enhancer plasmid

- Colony PCR protocol

- *Tol2* mRNA precipitation

- Danieau recipe

- Preparing chemical competent cells protocol

- BTA for different visual stimulus parameters

- All imaged single Purkinje cells

- The stimuli presented in the imaging study in Knogler et al., 2019

- Manuscript: Fabritius et al., Cell Chemical Biology 2018

- Manuscript: Knogler et al., eLife 2019

Licensing and permission for reuse in the thesis
Andreas Kist (2019): "Cerebellar and sensory contributions to the optomotor response in larval zebrafish"

Paper	What	Where	License?
Akerboom et al 2012	Part of Figure 1	Figure 6	J Neurosci Open Access
Chen et al 2013	Part of Figure 3	Figure 6	Rightslink
Kurt Thorn and Talley Lambert	Fluorescent protein data	Figure 8	MIT
Knogler et al. 2017	Parts of Figure 1	Figure 11	CC BY NC ND
Ramirez and Stell 2016	Parts of Figure 2	Figure 12	CC BY
Hawkes and Herrup 1995	Figure 1	Figure 12	Rightslink
Matsui et al 2014	Part of Figure 1A and Figure 4A	Figure 13	PNAS requires no permission for non-commercial use.
Hamling et al 2015	Figure 4A	Figure 13	Rightslink
Hsieh et al 2014	Figure 1G	Figure 13	CC BY
Bae et al 2009	Figure 5B,C	Figure 14	Rightslink
Takeuchi et al 2015	Figure 5C, D, F, S	Figure 14	Rightslink

Transgenic fish lines generated

Purkinje cells

Name	Purpose	Comment	Status
Fyn-tagRFP:PC:Cre	Intersectional expression	Cre works perfectly, shown with Huc:flox-RFP-flox-GFP	F4
Fyn-tagRFP:PC:Ace2N-2aa-mNeonGreen	Voltage imaging	No signals	Discontinued
Fyn-tagRFP:PC:Ace2N-2aa-mVenus	Voltage imaging	Some signals	Discontinued
PC:epNtr-tagRFP	Ablations	Works well, strong expression	F3
Fyn-tagRFP:PC:NLS-GCaMP6f	Calcium imaging	Works, example data acquired on light-sheet	F3
Fyn-tagRFP:PC:NLS-GCaMP6s	Calcium imaging	Good SNR, behavioral data for open and closed loop	F4
PC:GCaMP6s	Calcium imaging	Good SNR, nice signals, used for exp022 and exp027	F3
PC:ReaChR-tagRFP	Optogenetics	Red-shifted ChR	F2
Fyn-mClover3:PC	Cell marker	Membrane tagged, very bright fish	F2
loxP-Fyn-mClover3-loxP:PC	Intersectional suppression of expression, sparse labelling	As Fyn-mClover3, but with the option to label only few cells	F1
Fyn-tagRFP:PC: miniSOG2-2A-Venus	Single cell directed ablations	Did not work so far	F1
PC:Marina-2A-H2B-mCherry	Voltage indicator	No real signals observed	F2 (discontinued)
PC:ChR2(H134R)-tagRFP	Optogenetics	Works well also in electrophysiology	F1

Eurydendroid cells

Name	Purpose	Comment	Status
UAS:GCaMP6s	Calcium imaging	Two very bright founder with nice signals	F1, F2 (Luigi)
Olig2:KalTA4	Driver	Very good expression in RGCs, but less in ECs…	F3

Reporter lines

Name	Purpose	Comment	Status
tetO:GFP	Reporter line	Bleeding Heart+	Discontinued
tetO:ChR2-tagRFP	Reporter line	Bleeding heart+	Discontinued
UAS:mTFP1-mCarmine	Reporter line	Bleeding heart+	F0
Huc:H2B-mCherry	Reporter line		F0
Huc:H2B-mCherry(mir124)	Reporter line	Mir124 from Eduardo, dubious	F1
UAS:H2B-GFP	Reporter line		F0
Huc:H2B-GFP	Reporter line		F0
Huc:H2B-GFP(mir124)	Reporter line	With real mir124, designed by me	F0
Huc:H2B-GFP(mir181a)	Reporter line	With real mir181a, designed by me	F0

Github repositories - contributions

DMD-based optogenetics
https://github.com/portugueslab/dmd

Code for calibration of DMD with camera (calib.py), to interact with the DMD (dlpc350.py) and a graphical user interface to control the DMD, draw and save ROIs, show checkerboard patterns and brightfield mode (main.py).

Offline tail tracking
https://github.com/portugueslab/offline_tail_tracking

Minimal graphical user interface to open a video (codec should be supported by OpenCV) and track the tail of a larval zebrafish. One has to select tail base and tail tip, the fish should face to the right. Creates csv file with the cumulative sum of tail segments (N=10, adjustable).

H5viewer
https://github.com/portugueslab/h5viewer

Program to open h5 (with data in "stack" key), nrrd and TIF files, shows a z-stack using a custom pyqtgraph ImageWindow. Z-stacks can be easily converted to z-sum and maximum projections using shortcuts. Further, images from the clipboard can be imported via Ctrl+V and immediately saved as pngs, jpgs or tif. Easily inverts 2D images using Ctrl+I.

Regionfinder
https://github.com/portugueslab/regionfinder

Regionfinder is a program used in the BRF paper to find anatomical regions in cluster maps. For this, the cluster map should be morphed to the lab reference brain. Then, it is re-sized to fit the internal size and compared with all annotated maps from the Z-brain atlas. It shows coverage and region power.

Hardware
https://github.com/portugueslab/hardware

All hardware I custom designed is available in this repository. This includes the light-sheet chambers, the illumination ring for the light-sheet, two-photon and minimal behavior setup, as well as the preparation chamber used in Gema's and Daniil's experiments.

Volumetric drawing
https://github.com/portugueslab/volumetric_drawing

Adds two functions to draw easily in 3D lines and spheres (used to convert swc files to binarized z-stacks).

Marean
https://bitbucket.org/mpin_sensorimotor_control/marean/src/master/

Flexible tool to label different regions in a reference stack, based on pyqtgraph ROIs. Capable of copying ROIs from previous plane. Alpha status, however, worked well for granule cell reference stack (parallel fibres, somatic layer, third unknown region).

The following repositories are either publicly available or on request:

Zebrafish_NN
https://github.com/anki-xyz/zebrafish_nn

Here I trained a multilayer perceptron and a convolutional neural network to identify specific regions in the larval zebrafish, such as head, tail base and tail tip.

LNP
https://github.com/anki-xyz/LNP

All functions to create an artificial neuron following a linear-nonlinear Poisson process model. Based on the functions given in Schwartz et al., 2006. It provides functions for spike-triggered average, spike-triggered covariance and a simulated Poisson process.

Image_analysis
https://github.com/anki-xyz/image_analysis

This repository carries a lot of functions related to image processing, such as confocal and two-photon microscopy.

- SWC_magic
  Opens a SWC file and a reference file and creates a binarized line stack, and draws a sphere of given diameter on the first node. Used for single cell Purkinje cell study.
- Confocal
  - planarityEvaluator: Used to binarize the dendritic tree of high-res stacks and perform PCA and exports the principal axes.
  - Czi_to_cell_and_reference: Uses a Zeiss CZI file and exports the cell z-stack for tracing and the reference z-stack for morphing.
  - Czi_to_nrrd_for_morphing: Uses the meta data in CZI file and creates an NRRD file for morphing (also able to register stack in 3D)
- Twophoton
  - Copy_and_compress: Copies TIF Files to folder and compresses them as HDF5 files with BLOSC compression.
  - Deinterlace: Deinterlaces images
  - Register: Provides different functions for 2D and 3D registration
  - Repair_tiff_files: Repairs broken TIF files from 2p experiments (due to LabVIEW bug with larger TIF files).
  - Roi_select_and_extract: Used to label custom ROIs in soma vs. dendritic signal study.
  - select_ROI_mask: Selects arbitrary ROI masks per plane (only 1 mask per plane), with matplotlib implementation. Quick and dirty.

Light sheet chamber

The light sheet chamber is assembled using different parts (as shown in figure below):

a) 3D printed chamber
b) Laser cut acrylic bottom
c) Coverslip glass sides

The chamber is designed in 3D using OpenSCAD and parametrized to adjust the width and height of the chamber, as well as the windows. The illumination source (e.g. a blue laser forming a light sheet) enters through the sides. Glass coverslips with a low scatter effect were chosen to allow the light to pass freely. We use standard coverslips from Menzel (#1.5). The coverslips are mounted using grease (glisseal®). The grease is water tight, but allows the removal of broken or dirty parts. The bottom is made of laser cut acrylic (2-3 mm thickness) and also sealed with grease. The standard width of the chamber is 29.6 mm, the chamber rim is 1 mm, the bottom is around 27.5 mm wide. Hint: test different sizes (e.g. 27 to 27.6 mm) to see which version fits best to the chamber.

The chamber are normally printed using a Formlabs Form2 3D printer using translucent resin. Medium quality is fine, the standard printing orientation is slightly tilted. Hint: check the supports that they are not close to the outer windows, i.e. the coverslip mounting surface.

The chamber is part of the Portugues' lab hardware repository.
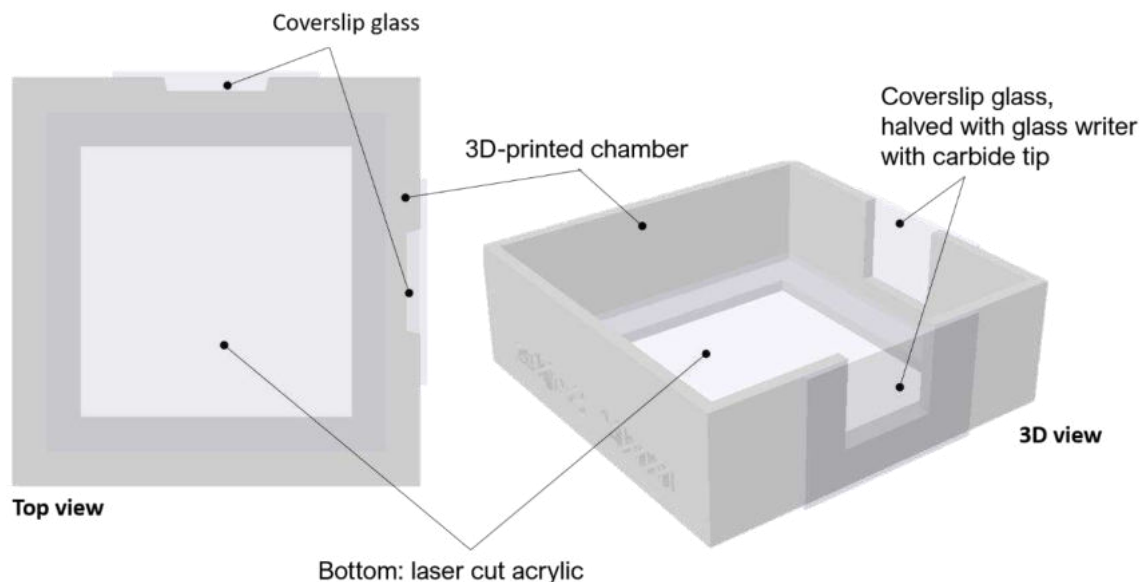
Artificial LNP model with STA and STC

December 4, 2018

1 STA and STC

Here, I probe some fake data using an LNP (Linear-Nonlinear-Poisson cascade) model.

$$LNP = Poisson(N(\sum_i k_i \cdot x))$$

where k_i is a linear filter, x the stimulus, $N[\cdot]$ a non-linearity, such as exp or $[\cdot]^2$.

1.1 Strategy for STA

1. I generate a random stimulus in time (gaussian, mean 0, std 1)
2. I generate a nice linear filter k
3. The linear filter is multiplied with the stimulus $stim$
4. A non-linear transformation is applied (half-square rectification)
5. Everything is fed to a Poisson process
6. Reverse correlate to find STA, which should be close to filter k

```
In [1]: import numpy as np
        import matplotlib.pyplot as plt
        %matplotlib inline
        from IPython.display import set_matplotlib_formats
        set_matplotlib_formats('png', 'pdf')
        plt.plot()
        plt.close()

In [2]: plt.rcParams['figure.figsize'] = (4.0, 2.0)

In [3]: def dot(stim, k):
            """dot product of spatiotemporal stimulus with filter k"""
            dot_product = np.zeros(stim.shape[0])
            history = k.shape[0]

            # iterate over time
            for i in range(history, stim.shape[0]):
                dot_product[i] = stim[i-history:i] @ k

            return dot_product
```

```python
def hsr(x):
    """half-square rectifier
    if x is below 0, return 0, otherwise square the result."""
    return 0 if x < 0 else x**2

def STA(stim, spikes, history=20):
    """Calculates spike-triggered average of stimulus using a spike train"""
    # Introduce safety margin hack
    spikes[:history] = 0
    spikes[-history:] = 0

    sta = []

    #np.zeros((spikes.astype(np.bool).sum(), history))

    # Iterate over spikes
    for i, sp in enumerate(np.where(spikes)[0]):
        # Multiply each spatiotemporal stimulus
        #  by the amount of spikes elicited
        sta.extend([stim[sp-history+1:sp+1]]*spikes[sp])

    return np.array(sta).mean(0)
```

```
In [4]: # Time
        N = 10000
        history = 7

        #  Seed random for reproducability
        np.random.seed(1)

        # Generate gaussian stim with 0 mean and 1 std
        stim = np.random.randn(N)

        # Linear filter
        k = np.array([0]*2 + list(np.sin(np.arange(history-4)/np.pi*8)) + [0]*2)
```

```
In [5]: plt.plot(k)
        plt.title('linear filter $k$')
```

```
Out[5]: Text(0.5,1,'linear filter $k$')
```

linear filter k
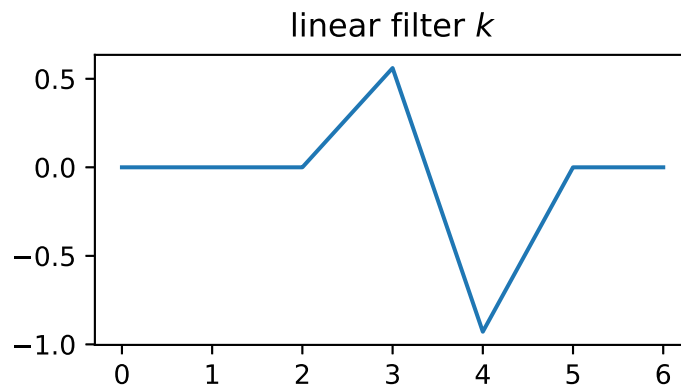

```
In [6]: plt.plot(dot(stim,k)[:100])
        plt.title('dot product of stimulus and $k$')

Out[6]: Text(0.5,1,'dot product of stimulus and $k$')
```

dot product of stimulus and k
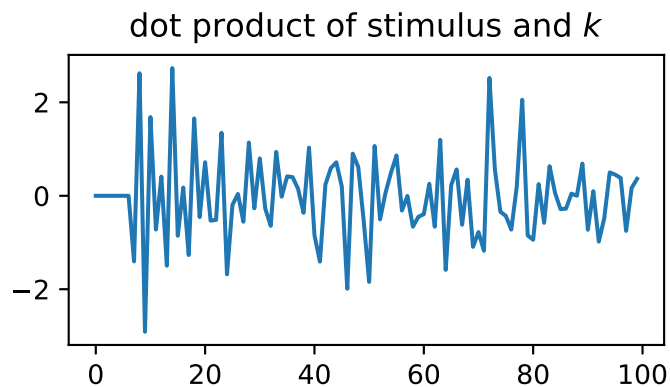

```
In [7]: plt.plot([hsr(i) for i in dot(stim,k)][:100])
        plt.title('raw Linear-Nonlinear relationship as entry for poisson process')

Out[7]: Text(0.5,1,'raw Linear-Nonlinear relationship as entry for poisson process')
```

3

raw Linear-Nonlinear relationship as entry for poisson process
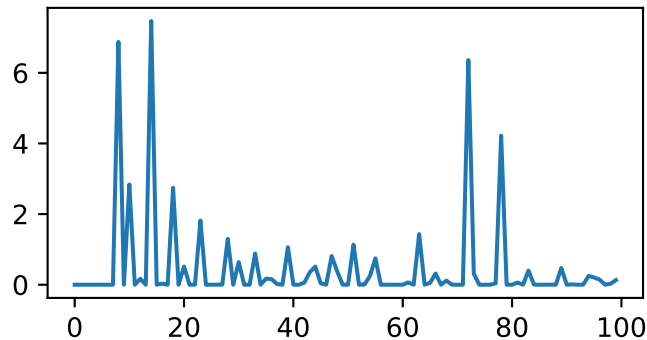
In [8]: # Linear-Nonlinear relationship for each time bin
LN = [hsr(i) for i in dot(stim,k)]

In [9]: # Create poisson process
limit = np.percentile(LN, 99) # set the frequency limit
LNP = np.array([np.random.poisson(i/limit) for i in LN])

In [10]: plt.plot(LNP[:100])
plt.title('spikes from Poisson process')

Out[10]: Text(0.5,1,'spikes from Poisson process')

spikes from Poisson process
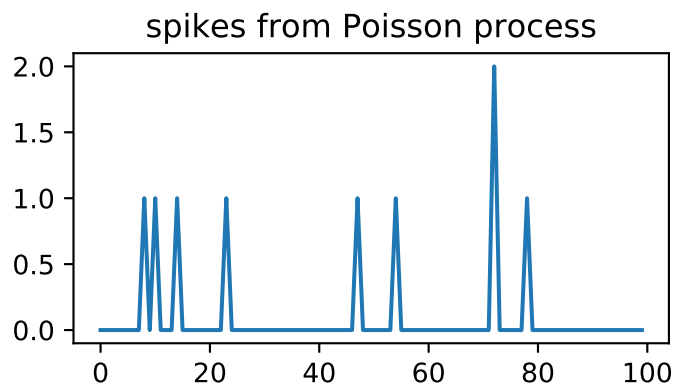
Calculates STA.

$$\text{STA} = \frac{1}{n_{sp}} \sum_{i=1}^{T} y_i \mathbf{x_i},$$

(from wiki)

In [11]: plt.plot(STA(stim, LNP))
plt.title('spike-triggered average over last 20 time bins')

4

`Text(0.5,1,'spike-triggered average over last 20 time bins')`

spike-triggered average over last 20 time bins
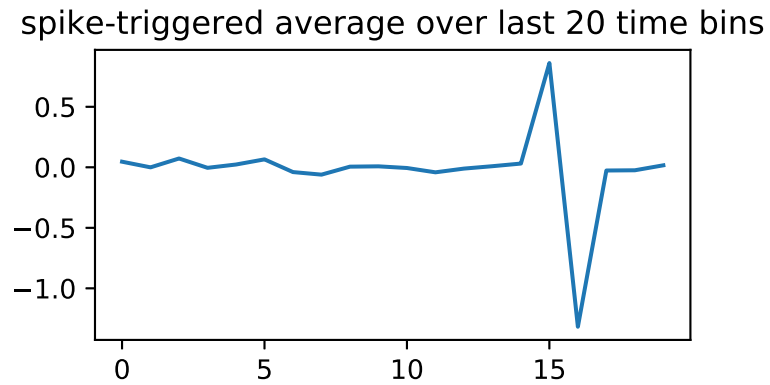
In [12]:
```python
plt.figure(figsize=(9,3))
plt.subplot(121)
plt.plot(k)
plt.title('real filter (7 time points)')
plt.subplot(122)
plt.plot(STA(stim, LNP), color=(0,0,0,.5))
plt.plot(np.arange(20-7, 20), STA(stim, LNP)[-7:], color='r')
plt.title('retrieved filter (20 time points)')
plt.tight_layout()
```
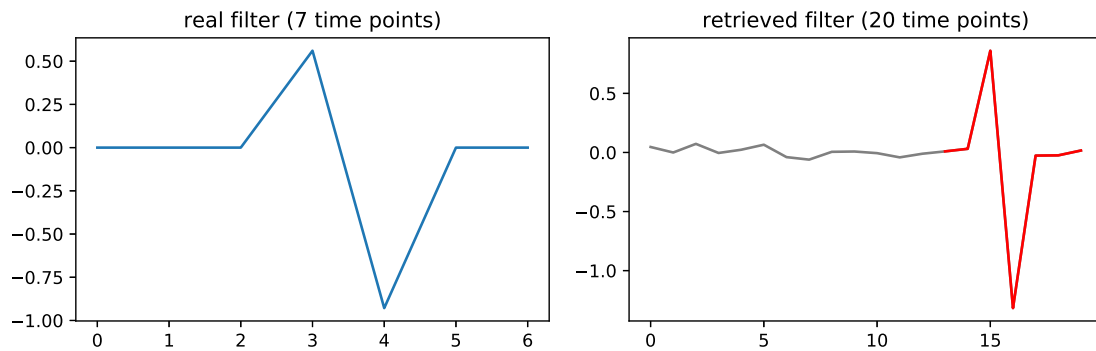

1.2   and now STC...

In [13]:
```python
# Time
np.random.seed(1)

N = 10000
history = 7
```

```
          stim = np.random.randn(N)

          # Create two filters, one should be roughly the inverse of the other
          k1 = np.array([0]*2 + list(np.sin(np.arange(history-4)/np.pi*8)) + [0]*2)+np.random.
          k2 = -np.array([0]*2 + list(np.sin(np.arange(history-4)/np.pi*8)) + [0]*2)+np.random
```

In [14]:
```
plt.plot(k1, label='filter 1')
plt.plot(k2, label='filter 2')
plt.legend(loc='best')
```

Out[14]: <matplotlib.legend.Legend at 0x20ce37db710>
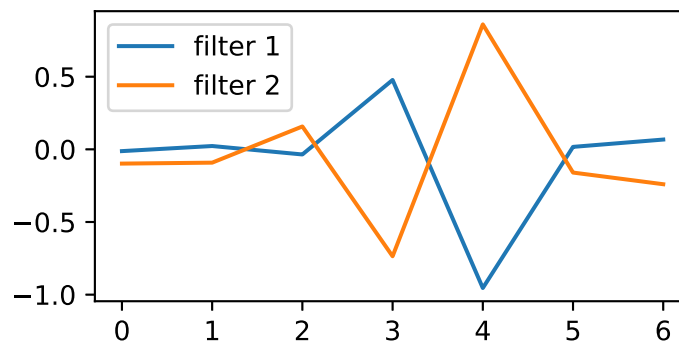
In [15]:
```
# Perform LN operation (dot product and squared)
#   over each filter, then sum both, see equation in the beginning,
#   hsr is N
LN_2filters = np.sum((dot(stim, k1)**2,
                      dot(stim, k2)**2), 0)
```

In [16]:
```
# Poisson process
limit = np.percentile(LN_2filters, 99.9) # limit frequency
LNP_2filters = np.array([np.random.poisson(i/limit) for i in LN_2filters])
```

In [17]:
```
plt.plot(LNP_2filters[:100])
plt.title('spikes from poisson process')
```

Out[17]: Text(0.5,1,'spikes from poisson process')

spikes from poisson process
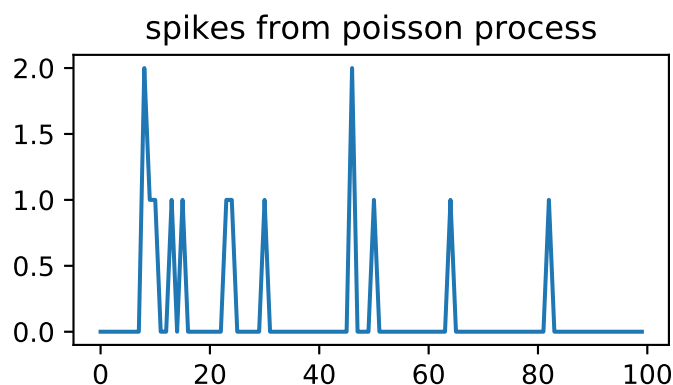
In [18]: `# Set history to 20 to see effects beyond the generated filter`
`history = 20`

In [19]: `sta = STA(stim, LNP_2filters, history)`

In [20]: `plt.plot(sta)`
`plt.title('spike-triggered average for 2 filters, \nshould be unstructured')`

Out[20]: `Text(0.5,1,'spike-triggered average for 2 filters, \nshould be unstructured')`

spike-triggered average for 2 filters, should be unstructured
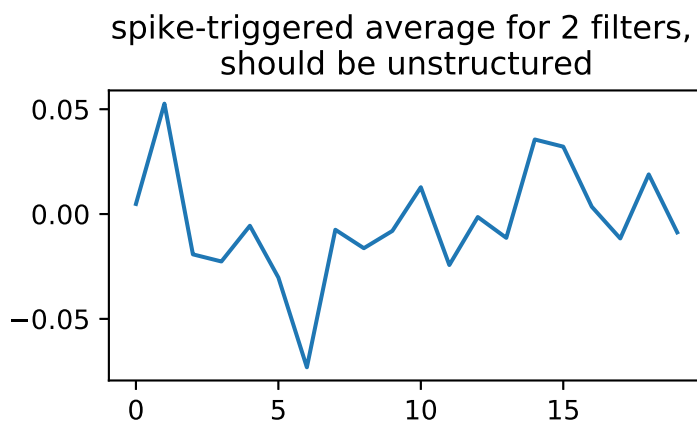
1.3 STC formula

$$STC = \frac{1}{n_s - 1} \sum_{i=1}^{T} y_i (\mathbf{x_i} - STA)(\mathbf{x_i} - STA)^T,$$

with y_i the number of spikes, x_i the spatio-temporal stimulus as *column vector*, *STA* the spike-triggered average, and n_s the number of spikes. The covariance of the stimulus is given by

$$\mathbf{C} = \frac{1}{n_p - 1} \sum_{i=1}^{T} \mathbf{x_i} \mathbf{x_i^T},$$

7

with n_p the number of stimuli. The sum $\sum$ is over complete stimulus time T. Also from wiki and from Schwartz et al.

```
In [21]: S = []  # Sum

         # Iterate over time
         for i in range(history, stim.shape[0]):
             xi = stim[i-history+1:i+1][None].T # x, as column vector, at time point i
             yi = LNP_2filters[i] # spike at time point i

             # Sum y_i * (x_i-st)
             S.append(yi * (xi-sta[None].T) * (xi-sta[None].T).T)

         S = np.array(S)

         print('S shape is stimuli x history x history: ', S.shape)

         # STC is 1 / the number of spikes * sum summed over axis 0 (i.e. stimuli)
         stc = 1 / (LNP_2filters.sum()-1) * S.sum(0)

         # for the covariance of the stimulus itself, let Sx be
         Sx = []

         for i in range(history, stim.shape[0]):
             xi = stim[i-history+1:i+1][None].T # see above
             Sx.append(xi*xi.T)

         Sx = np.array(Sx)

         C = 1 / (Sx.shape[0]-1) * Sx.sum(0)

         print('shape of stc:', stc.shape)
         print('shape of C:  ', C.shape)
S shape is stimuli x history x history:  (9980, 20, 20)
shape of stc: (20, 20)
shape of C:   (20, 20)
```

Singular-value decomposition (SVD) to compute eigenvalues and eigenvectors

```
In [22]: from scipy.linalg import svd
```

```
In [23]: %timeit svd(stc-C)
```

```
342 ţs ś 32 ţs per loop (mean ś std. dev. of 7 runs, 1000 loops each)
```

```
In [24]: U, e_val, e_vec = svd(stc-C)
```

8

```
In [25]: plt.figure(figsize=(3,9))
         for i in range(history):
             plt.plot(e_vec[i]-i, color=(1-i/history, 0, 1-i/history))

         plt.yticks(np.arange(-history, 0)+1, np.arange(history)[::-1]+1)
         plt.ylabel('eigenvector #')
         plt.xticks(np.arange(-1, history)[::5], np.arange(-history, 1)[::5])
         plt.xlabel('Time to spike [au]');
```

The y-axis is labeled "eigenvector #" with values 1 through 20. The x-axis is labeled "Time to spike [au]" with values -20, -15, -10, -5, 0.
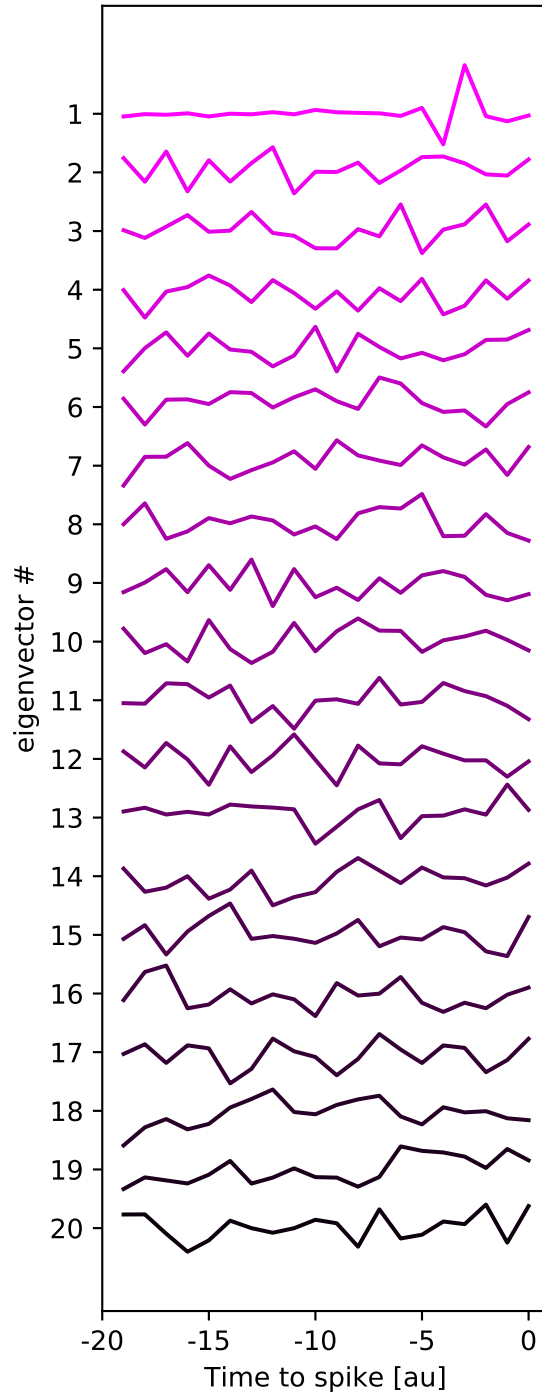
```
In [26]: plt.plot(e_val, 'o')
         plt.title('eigenvalues, sorted')
         plt.xlabel('eigenval #')
         plt.xticks(np.arange(history+1)[::5]);
```

eigenvalues, sorted
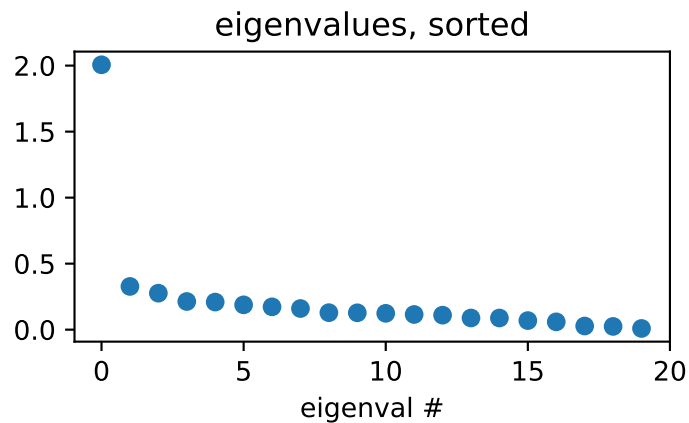
See how PCA performs compared to SVD

```
In [27]: from sklearn.decomposition import PCA

In [28]: pca = PCA()

In [29]: %timeit pca.fit(stc-C)

628 ţs ś 33.6 ţs per loop (mean ś std. dev. of 7 runs, 1000 loops each)
```

Shows similar result...

```
In [30]: plt.figure(figsize=(3,9))
         for i in range(history):
             plt.plot(pca.components_[i]-i, color=(1-i/history, 0, 1-i/history))

         plt.yticks(np.arange(-history, 0)+1, np.arange(history)[::-1]+1)
         plt.ylabel('principal component #')
         plt.xticks(np.arange(-1, history)[::5], np.arange(-history, 1)[::5])
         plt.xlabel('Time to spike [au]')

Out[30]: Text(0.5,0,'Time to spike [au]')
```
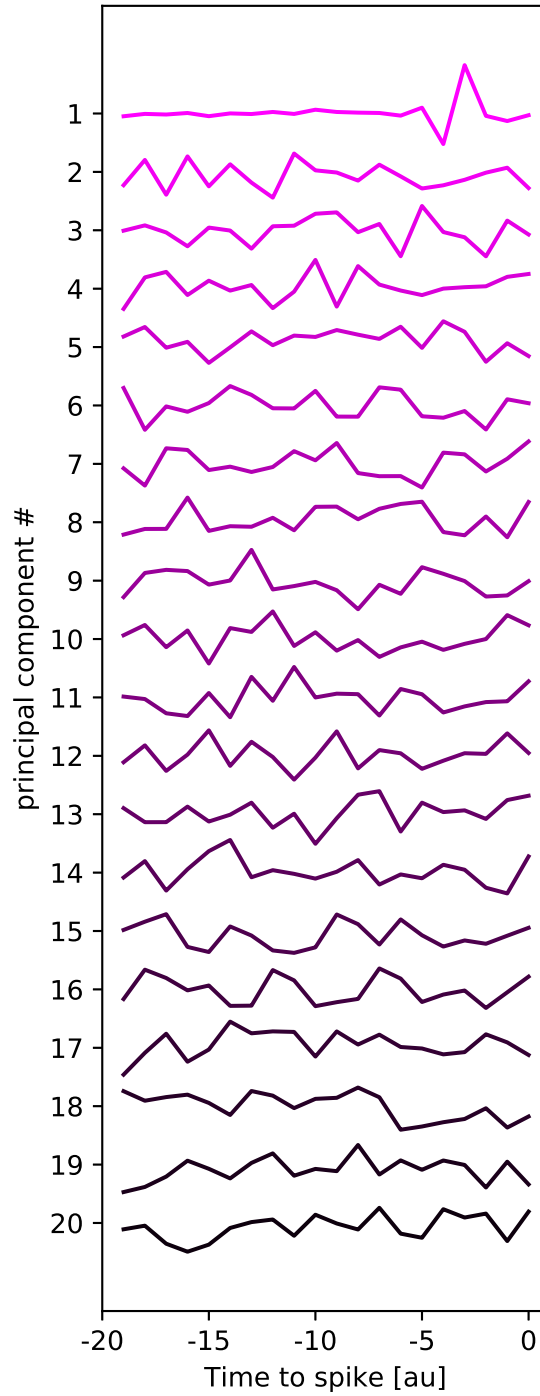
```
In [31]: plt.plot(pca.explained_variance_, 'o')
         plt.title('explained variance for each PC, sorted')
         plt.xlabel('principal component #')
         plt.ylabel('explained variance')
         plt.xticks(np.arange(history+1)[::5]);
```

explained variance for each PC, sorted
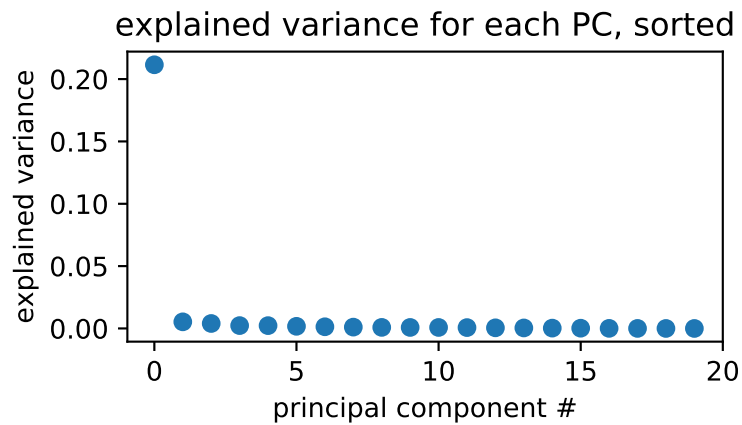

```
In [ ]: plt.title('Explained variance ratio')
        plt.plot(pca.explained_variance_ratio_, 'o')

Out[ ]: [<matplotlib.lines.Line2D at 0x20ceb3ea6d8>]
```

Explained variance ratio
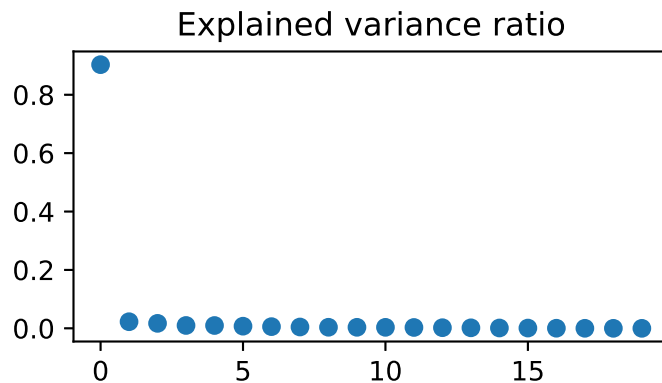
Comparison of SVD eigenvector 1 and first principal component:

```
In [ ]: plt.plot(e_vec[0], color=(1,0,0,.5)) # red
        plt.plot(pca.components_[0], color=(0,0,1,.5)) # blue, inverse
        # Overlap ==> magenta

        plt.title('1st Eigenvector and 1st Principal Component overlap')

Out[ ]: Text(0.5,1,'1st Eigenvector and 1st Principal Component overlap')
```

13

Find Larval Zebrafish Features Using Artificial Neural Networks

February 24, 2019

1 Machine learning approaches to find features in zebrafish images

Here, I train a Multi-Layer Perceptron (MLP) to classify image tiles.

Load modules

```
In [ ]: import cv2
        from glob import glob
        import numpy as np
        import matplotlib.pyplot as plt
        %matplotlib inline
        from numba import jit
        # ML
        from sklearn.model_selection import train_test_split
        from keras.models import Sequential
        from keras.layers import Dense, Conv2D, Flatten, MaxPooling2D
        from keras.utils import to_categorical
        import pandas as pd
```

Load plotting related stylesheets

```
In [2]: import seaborn as sns
        sns.set_style('white')
        sns.set_style('ticks')
        plt.rcParams['figure.figsize'] = (3, 2)
        plt.rcParams['figure.dpi'] = 300
```

Load and prepare data for NN

```
In [3]: folder = r'C:\Users\me\Documents\MPIN\fish_images'
        path_to_a_fish = r"C:\Users\me\Documents\MPIN\fish_images\20150513_142329_image.png"

        heads = np.array([cv2.imread(i,0) for i in glob(folder+'\\head\\*.png')])
        tip = np.array([cv2.imread(i,0) for i in glob(folder+'\\tailtip\\*.png')])
        base = np.array([cv2.imread(i,0) for i in glob(folder+'\\tailbase\\*.png')])
        bg = np.array([cv2.imread(i,0) for i in glob(folder+'\\background\\*.png')])
        labels = ['head','tail tip', 'tail base', 'background']
```

```
        input_shape = heads.shape[1]

        X = np.vstack([heads, tip, base, bg])
        X = X / X.max(0)[None] # convert to float and normalize image from 0 to 1.
        Y = np.repeat([0, 1, 2, 3],450,0)
```

Split train and test dataset

```
In [4]: X_train, X_test, y_train, y_test = train_test_split(X,
                                                            Y,
                                                            test_size=0.2,
                                                            random_state=42)
```

Train a neuron network that consist of

- a full connected layer
- a dense, hidden layer with 32 neurons
- an output layer with 4 neurons comprising the four categories *head, tail base, tail tip* and *background*

```
In [5]: model = Sequential()
        n_epochs = 10 # Train for N epochs

        model.add(Dense(units=32, activation='relu', input_dim=80*80))
        model.add(Dense(units=4, activation='softmax'))

        model.compile(loss='categorical_crossentropy',
                      optimizer='adam',
                      metrics=['accuracy'])

        r = model.fit(X_train.reshape(X_train.shape[0],-1),
                      to_categorical(y_train,4),
                      batch_size=32,
                      epochs=n_epochs,
                      validation_split=0.05)
```

```
Train on 1368 samples, validate on 72 samples
Epoch 1/10
1368/1368 [==============================] - 3s 2ms/step - loss: 0.9451 - acc: 0.6520 - val_l
Epoch 2/10
1368/1368 [==============================] - 0s 338us/step - loss: 0.3567 - acc: 0.8246 - val
Epoch 3/10
1368/1368 [==============================] - 1s 496us/step - loss: 0.2401 - acc: 0.9539 - val
Epoch 4/10
1368/1368 [==============================] - 1s 453us/step - loss: 0.2089 - acc: 0.9569 - val
Epoch 5/10
1368/1368 [==============================] - 1s 473us/step - loss: 0.1720 - acc: 0.9642 - val
Epoch 6/10
```

```
1368/1368 [==============================] - 1s 474us/step - loss: 0.1488 - acc: 0.9744 - val
Epoch 7/10
1368/1368 [==============================] - 1s 517us/step - loss: 0.1240 - acc: 0.9788 - val
Epoch 8/10
1368/1368 [==============================] - 1s 515us/step - loss: 0.1215 - acc: 0.9766 - val
Epoch 9/10
1368/1368 [==============================] - 0s 340us/step - loss: 0.1272 - acc: 0.9598 - val
Epoch 10/10
1368/1368 [==============================] - 1s 532us/step - loss: 0.1200 - acc: 0.9686 - val
```

Plot the accuracy of the neural network evolved per epoch

```
In [6]: plt.plot(r.history['acc'], label='accuracy')
        plt.plot(r.history['loss'], label='loss')
        plt.xlabel('epoch')
        plt.xticks(np.arange(n_epochs)[1::2], np.arange(n_epochs)[1::2]+1)
        plt.legend(loc='best')
        plt.ylim([-.1, 1.1])
        sns.despine(trim=True, offset=10)
```
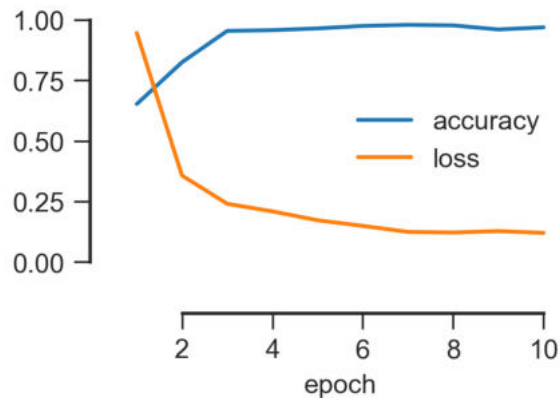

Plot the probability of each test image per category

```
In [7]: plt.plot(model.predict(X_test.reshape(X_test.shape[0],-1))[np.argsort(y_test)])
        sns.despine(trim=True, offset=10)
        plt.xlabel('image# (sorted by class)')
        plt.ylabel('class probability')
        plt.legend(labels, loc=[1, 0])
```

```
Out[7]: <matplotlib.legend.Legend at 0x1e05a168c88>
```

3
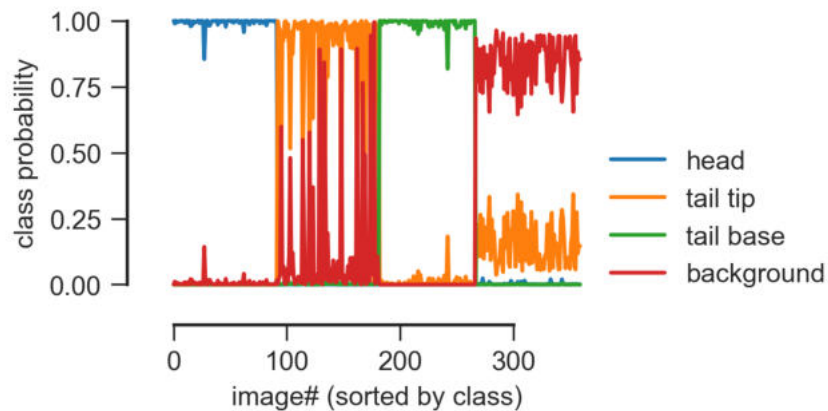
Predict the class of each test image (ordered by category).

Note the spikes that indicate that some images are misclassified as background being actual tail tips.

```
In [8]: plt.plot(model.predict_classes(X_test.reshape(X_test.shape[0],-1)[np.argsort(y_test)]
        sns.despine(trim=True, offset=10)
        plt.yticks(range(4), labels)
        plt.xlabel('image# (sorted by class)')
```

```
Out[8]: Text(0.5,0,'image# (sorted by class)')
```
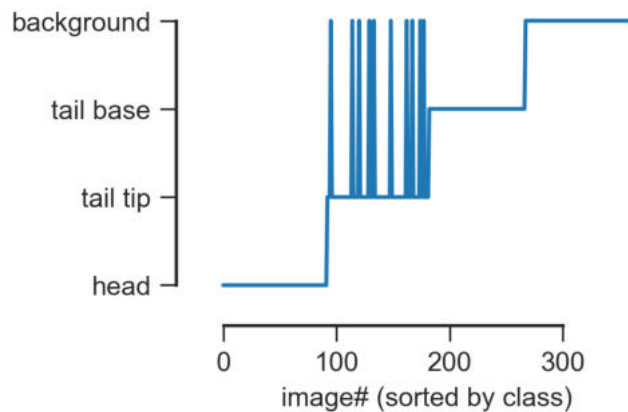

Predict the NN response px-wise in a zebrafish image

```
In [9]: fish = cv2.imread(path_to_a_fish, 0)
```

Downsample the image by a given factor

```
In [10]: sample_step = 2
```

```
In [13]: @jit
         def subsample_px_from_im(im, input_shape=80, step=2):
             range_x = np.arange(input_shape//2, im.shape[0]-input_shape//2, step)
             range_y = np.arange(input_shape//2, im.shape[1]-input_shape//2, step)
             pred_im = np.zeros((range_x.shape[0], range_y.shape[0], input_shape*input_shape)
                               dtype=np.float16)

             for i, x in enumerate(range_x):
                 for j, y in enumerate(range_y):
                     pred_im[i,j] = im[x-input_shape//2:x+input_shape//2,
                                       y-input_shape//2:y+input_shape//2].flatten()

             return pred_im
```

Subsample image and prepare data for NN. Predict for each px the NN response.

```
In [14]: %time subim = subsample_px_from_im(fish/255, step=sample_step)
         %time pred = model.predict(subim.reshape((-1, input_shape*input_shape)))

Wall time: 2.67 s
Wall time: 2.82 s
```

Plot the predicted class probabilty per class

```
In [15]: peaks = []

         plt.figure(figsize=(12,3))
         for i in range(4):
             plt.subplot(1,4,i+1)
             plt.imshow(pred.reshape((*subim.shape[:2], -1))[...,i], vmin=0, vmax=1)
             plt.axis('off')
             #plt.colorbar(fraction=.03)
             plt.title(labels[i])

             # Show peaks for the three foreground features
             if i < 3:
                 peak = np.unravel_index(np.argmax(pred[...,i]), subim.shape[:2])
                 plt.scatter(*peak[::-1], s=100, alpha=1, color='b',
                             lw=2, marker='o', facecolor='none')
                 peaks.append(np.array(peak)*sample_step+input_shape//2)

         plt.tight_layout()
```
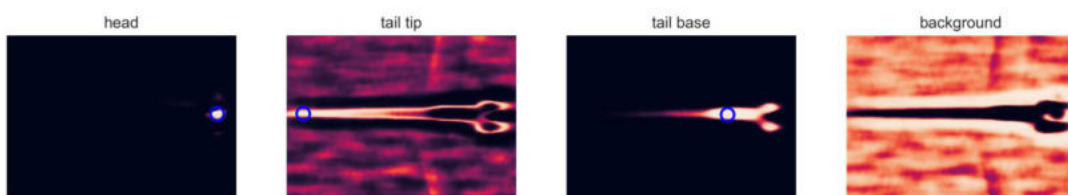
1.1 Display features at fish

```
In [23]: plt.figure(figsize=(5,3))
         plt.imshow(fish, cmap='gray') #[4:-4, 4:-4]

         plt.scatter(*peaks[0][::-1], s=1000, alpha=.7)
         plt.text(*(peaks[0][::-1]-60), 'head')

         plt.scatter(*peaks[1][::-1], s=20, alpha=.7)
         plt.text(*(peaks[1][::-1]+25), 'tail tip')

         plt.scatter(*peaks[2][::-1], s=20, alpha=.7)
         plt.text(*(peaks[2][::-1]-35), 'tail base')

         plt.axis('off')

Out[23]: (-0.5, 647.5, 487.5, -0.5)
```
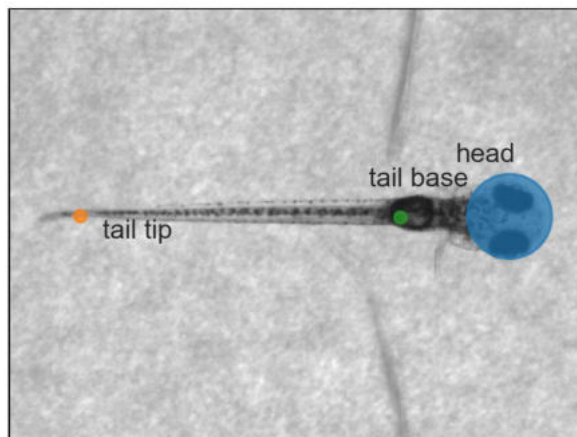

1.2 Show effect of neurons in first hidden layer on accuracy

```
In [ ]: all_acc = []
        acc_course = []
        n_neurons_1st_layer = [4, 8, 12, 16, 32, 48, 64, 128]
        n_epochs = [5, 10, 20, 40]

        for _n_epochs in n_epochs:
            acc = []
```

```
for _n_neurons_1st_layer in n_neurons_1st_layer:
    model = Sequential()

    model.add(Dense(units=_n_neurons_1st_layer,
                    activation='relu', input_dim=80*80))
    model.add(Dense(units=4, activation='softmax'))

    model.compile(loss='categorical_crossentropy',
                  optimizer='adam',
                  metrics=['accuracy'])

    r = model.fit(X_train.reshape(X_train.shape[0],-1),
                  to_categorical(y_train,4),
                  batch_size=32,
                  epochs=_n_epochs,
                  validation_split=0.05)

    acc.append(r.history['acc'])

all_acc.append([i[-1] for i in acc])
acc_course.append(acc)
```

```
In [25]: plt.figure(figsize=(3,2))
         for e in range(len(n_epochs)):
             plt.plot(n_neurons_1st_layer, all_acc[e], label='{} epochs'.format(n_epochs[e]))
         plt.ylim([0,1.1])
         plt.legend(loc=[1,0])
         plt.xlabel('#neurons in 1st hidden layer')
         plt.ylabel('accuracy')

         sns.despine(trim=True, offset=10)
```
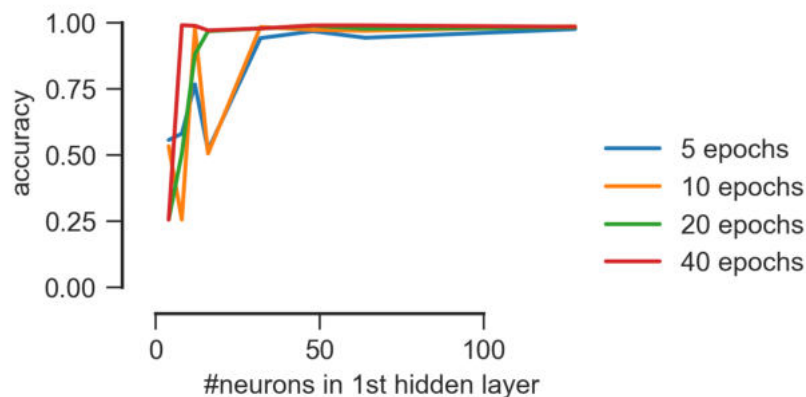
1.3   Show the effect of # of neurons and epochs on accuracy

```
In [26]: df = pd.DataFrame([pd.Series(v) for v in acc_course[2]]).T
```

```
In [27]: plt.figure(figsize=(9, 3.5))

         for ni, neurons in enumerate(n_neurons_1st_layer):
             if ni == 0:
                 ax = plt.subplot(2,4,ni+1)
             else:
                 plt.subplot(2,4,ni+1, sharey=ax)

             for i in range(len(acc_course)):
                 df = pd.DataFrame([pd.Series(v) for v in acc_course[i]]).T
                 plt.plot(df[ni])

             plt.title('{} neurons'.format(neurons), y=1.2)
             plt.ylim([-.1,1.1])
             plt.ylabel('Accuracy')
             plt.xlabel('epoch')

         plt.legend(['{} epochs'.format(i) for i in [5,10,20,40]], loc=[1,0])
         plt.tight_layout()
         sns.despine(trim=True, offset=10)
```
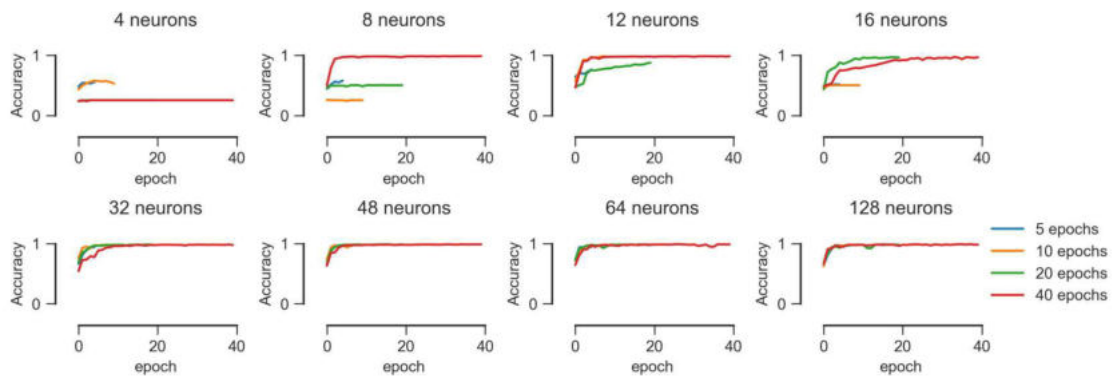

1.4   Use the data in convolutional neural network

```
In [28]: n_epochs = 10

         conv_model = Sequential()
         conv_model.add(Conv2D(32, kernel_size=(4, 4),
                               input_shape=(80,80,1), activation='relu'))
         conv_model.add(MaxPooling2D(pool_size=(2, 2)))
         conv_model.add(Flatten())
```

```python
conv_model.add(Dense(32, activation='relu'))
conv_model.add(Dense(units=4, activation='softmax'))

conv_model.compile(loss='categorical_crossentropy',
                   optimizer='adam',
                   metrics=['accuracy'])

r = conv_model.fit(X_train[...,None],
                   to_categorical(y_train,4),
                   batch_size=32,
                   epochs=n_epochs,
                   validation_split=0.05)
```

```
Train on 1368 samples, validate on 72 samples
Epoch 1/10
1368/1368 [==============================] - 3s 2ms/step - loss: 0.6459 - acc: 0.7193 - val_l
Epoch 2/10
1368/1368 [==============================] - 1s 908us/step - loss: 0.2240 - acc: 0.8984 - val
Epoch 3/10
1368/1368 [==============================] - 1s 911us/step - loss: 0.1358 - acc: 0.9620 - val
Epoch 4/10
1368/1368 [==============================] - 1s 1ms/step - loss: 0.0926 - acc: 0.9715 - val_l
Epoch 5/10
1368/1368 [==============================] - 1s 1000us/step - loss: 0.1061 - acc: 0.9656 - va
Epoch 6/10
1368/1368 [==============================] - 1s 928us/step - loss: 0.1271 - acc: 0.9503 - val
Epoch 7/10
1368/1368 [==============================] - 1s 923us/step - loss: 0.0690 - acc: 0.9854 - val
Epoch 8/10
1368/1368 [==============================] - 1s 957us/step - loss: 0.0634 - acc: 0.9832 - val
Epoch 9/10
1368/1368 [==============================] - 1s 931us/step - loss: 0.0595 - acc: 0.9868 - val
Epoch 10/10
1368/1368 [==============================] - 1s 917us/step - loss: 0.0819 - acc: 0.9788 - val
```

```python
In [29]: plt.plot(conv_model.predict(X_test[np.argsort(y_test)][...,None]))
         sns.despine(trim=True, offset=10)
         plt.xlabel('image# (sorted by class)')
         plt.ylabel('class probability')
         plt.legend(['head','tail tip', 'tail base', 'background'], loc=[1, 0])
```

```
Out[29]: <matplotlib.legend.Legend at 0x1e0ba3094e0>
```
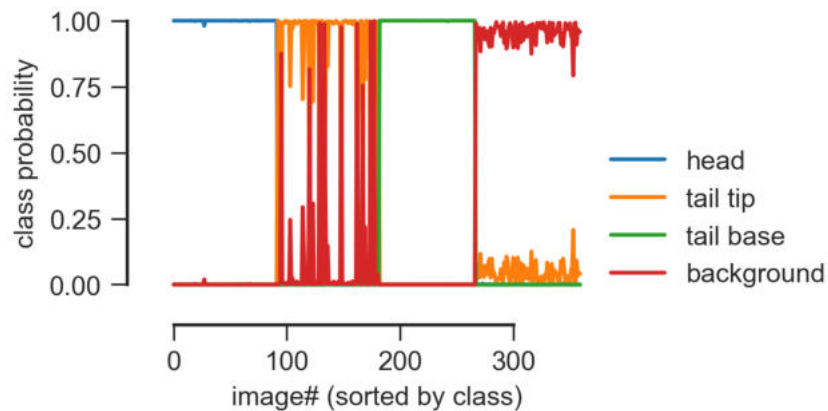
```
In [30]: plt.plot(conv_model.predict_classes(X_test[np.argsort(y_test)][...,None]))
         sns.despine(trim=True, offset=10)
         plt.xlabel('image# (sorted by class)')
         plt.ylabel('class probability')
         plt.legend(['head','tail tip', 'tail base', 'background'], loc=[1, 0])
```

```
Out[30]: <matplotlib.legend.Legend at 0x1e0ba33fa90>
```
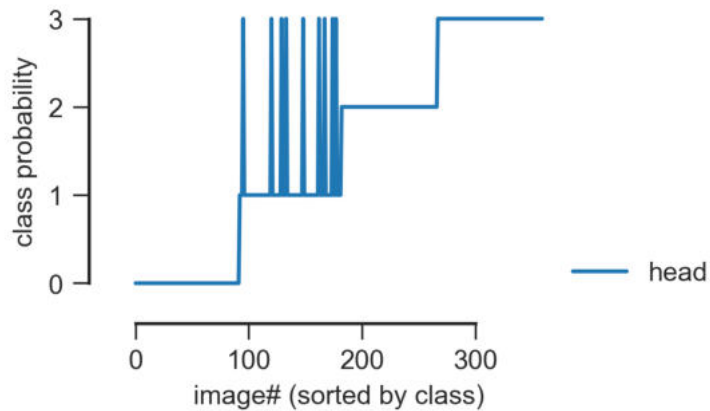


```
In [31]: %time subim = subsample_px_from_im(fish/255, step=sample_step)
         %time pred = conv_model.predict(subim.reshape(-1, 80, 80, 1))
```

```
Wall time: 2.42 s
Wall time: 16 s
```

```
In [32]: peaks = []
```

```python
plt.figure(figsize=(12,3))
for i in range(4):
    plt.subplot(1,4,i+1)
    plt.imshow(pred.reshape((*subim.shape[:2], -1))[...,i], vmin=0, vmax=1)
    plt.axis('off')
    #plt.colorbar(fraction=.03)
    plt.title(labels[i])

    # Show peaks for the three foreground features
    if i < 3:
        peak = np.unravel_index(np.argmax(pred[...,i]), subim.shape[:2])
        plt.scatter(*peak[::-1], s=100, alpha=1, color='b',
                    lw=2, marker='o', facecolor='none')
        peaks.append(np.array(peak)*sample_step+input_shape//2)

plt.tight_layout()
```
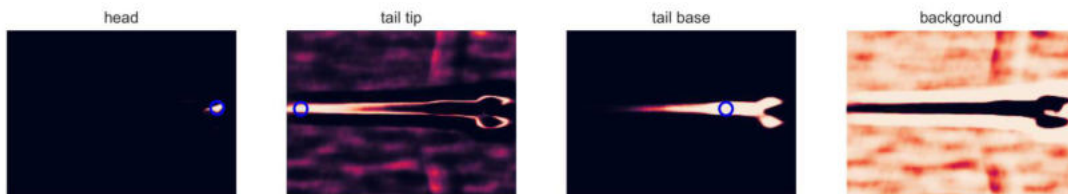
```python
def tail_trace(img, tailbase, taillength, num_points = 10):
    """
    Traces the tail, fish should face right, tail to the left
    :param img: the image with the fish (and obviously the tail)
    :param tailbase: the tail base coordinates as tuple
    :param taillength: The length of the tail in px
    :param num_points: Number of tail segments to be traced
    :return: tail angle sum
    """
    # X/Y position on tail base
    x = tailbase[0]
    y = tailbase[1]

    # Create an arc of 180 deg
    lin = np.linspace(0, np.pi, 20)

    # Initiate tail_points
    tail_points = [(x, y)]
    tail_angles = []
    tail_sum = 0

    # Filter image slighty to enhance tracking
    img_filt = np.zeros(img.shape)
    img_filt = cv2.boxFilter(img, -1, (7, 7), img_filt)

    # Iterate for number of segments times.
    for j in range(num_points):
        xs = x-taillength / num_points * np.sin(lin)
        ys = y-taillength / num_points * np.cos(lin)

        # Convert them to integer, because of definite pixels
        xs, ys = xs.astype(int), ys.astype(int)

        # Remove points out of the scene
        xs = xs[xs < img.shape[1] - 1]
        ys = ys[ys < img.shape[0] - 1]

        # Draws all points of the arc on the image
        for a in zip(xs, ys):
            cv2.circle(img, a, 1, (255, 0, 0), 1)

        if len(xs) != len(ys):
            return False

        # Find the darkest point
        ident = np.where(img_filt[ys, xs] == min(img_filt[ys, xs]))[0][0]

        # The minimum is the starting point of the next arc
        x = xs[ident]
        y = ys[ident]
```

```python
        # Add the angle to a total tail sum!
        tail_sum += lin[ident]

        tail_angles.append(lin[ident])

        # Create an 180 deg angle depending on the previous one
        lin = np.linspace(lin[ident] - np.pi / 2, lin[ident] + np.pi / 2, 20)

        # Add point to list
        tail_points.append((x, y))

    # draw the found tail points onto the fish's tail
    for i in tail_points:
        cv2.circle(img, i, 2, (255, 0, 0), 1)

    return tail_sum
```

```python
"""
    Eye tracking code based on OpenCV
"""
import cv2
import numpy as np

def find_eyes (im, show_eyes=True, show_mask=False):
    """
    Find eyes in image and returns the bounding box positions

    Returns:
    axis 0 from,
    axis 0 to,
    axis 1 from,
    axis 1 to,
    mask array with the same size as input image (dtype=np.bool)

    """

    # Use the SimpleBlobDetector from OpenCV to detect automatically the eyes
    p = cv2.SimpleBlobDetector_Params()

    # Find best threshold (around 20 for eyes without noise)
    p.minThreshold = 20
    p.maxThreshold = 25
    p.thresholdStep  = 1

    # Only find BLACK blobs == eyes
    p.filterByColor = True
    p.blobColor = 0

    # Eyes are not round, but ellipsoid, thus, enable Inertia
    p.filterByInertia = True

    # Detect eyes and save them as KeyPoints
    d = cv2.SimpleBlobDetector_create(p)
    kp = d.detect(im)

    # Draw the keypoints on the image and show it
    im_w_kp = cv2.drawKeypoints(im, kp, np.array([]),
                                (0,0,255),
                                cv2.DRAW_MATCHES_FLAGS_DRAW_RICH_KEYPOINTS)

    # Determine centers and radius to create bounding box
    y1 = int(max([i.pt[1] for i in kp]))
    y0 = int(min([i.pt[1] for i in kp]))
    x = int(min([i.pt[0] for i in kp]))
    r = int(max([i.size for i in kp]))
```

```python
        # Show bounding box
        cv2.rectangle(im_w_kp,(x-r,y0-r),(x+r,y1+r),(0,255,0),1)

        #Create mask to subindex only the eyes for eye tracking
        mask = np.zeros_like(im, dtype=np.bool)
        mask[y0-r:y1+r,x-r:x+r] = True

        if show_eyes:
            cv2.imshow("Im with Keypoints",im_w_kp)
            cv2.waitKey(0)

        if show_mask:
            cv2.imshow("Mask",mask.astype(np.uint8)*255)
            cv2.waitKey(0)

        return y0-r, y1+r, x-r, x+r, mask



def eye_track (e, show_eyes = False, t = 90):
    """

        Basic and fast eye tracking algorithm
        @author anki

        returns left and right eye angle
    """
    thres = (e > t).astype(np.uint8)*255

    # Fit two largest contours and sort them left/right
    _, contours, _ = cv2.findContours(thres.copy(), cv2.RETR_TREE, cv2.CHAIN_APPROX_SIMPLE)
    contours = sorted(contours, key=lambda c: c.shape[0],  reverse=True)[:2]
    contours = sorted(contours, key=np.max)

    # Fit an ellipse and add angle to result array
    eye_pos = [cv2.fitEllipse(contours[i])[2] for i in range(2)]

    if show_eyes:
        e_det = cv2.cvtColor(thres.copy(), cv2.COLOR_GRAY2BGR)
        e_det = cv2.ellipse(e_det,cv2.fitEllipse(contours[0]), (0,0,199),1)
        e_det = cv2.ellipse(e_det,cv2.fitEllipse(contours[1]), (127,0,127),1)

        e_det = cv2.resize(e_det, (0,0), fx=5, fy=5)

        cv2.imshow("Tracked Eye", e_det)
        cv2.waitKey(1)

    return eye_pos[0], eye_pos[1], contours
```

Example Protocol cloning into PC enhancer

Options:
The PC enhancer plasmid has two (!) cassettes, one can clone into either one. For convenience, I am using Fyn-tagRFP:PC:empty (1) if I need an independent red tag or Fyn-mClover3:PC:empty (2) if I need an independent green tag. If one opts for not an independent tag, one can either remove the e.g. red tag afterwards using restriction digest and re-ligation (MscI and EcoRV, both blunt end) or use PC:epNtr-tagRFP (3) or PC:ChR2-tagRFP (3) as basis and release the insert.

Equipment

- PC backbone (1), (2) or (3)
- Insert (here EGFP as example)
- Forward primer insert with homology to E1b promotor and EcoRI restriction site, plus ideally a kozak sequence (see Figure)
- Reverse primer insert with homology to T7 and XbaI restriction site. As stop codon I suggest the use of UAAA (shown previously to be the most efficient one with expression boost, see Horstick et al.)
- T4 Ligase buffer (there are 10 µl aliquots @-20°C, NEB #B0202S)
- SLiCE extract (@-20°C, ask Griesbeck lab or make yourself, see Zhang et al., 2015)
- *as alternative*: Gibson Assembly or NEBuilder HiFi, follow manufacturer's instructions
- 5x Hot FIREPol Blend Master Mix Ready to Load 7.5 mM $MgCl_2$.
- EcoRI and XbaI restriction enzymes, either from NEB or ThermoScientific.
  I have the latter around and use them normally with 10x red Anza buffer to directly load on gel for gel purification (PCR purification sufficient for backbone (1) and (2))

Backbone preparation

1) Use around ~ 5 µg of DNA in a 50 µl reaction:
    5 µl 10x Anza buffer red
    1 µl EcoRI (#11)
    1 µl XbaI (#12)
    x µl DNA
ad 50 µl H_2O, @37°C at least 15-30 min, normally as long as PCR

2) Gel purify if you release insert (e.g. from (3)), otherwise PCR purify.
anki tipp: bring the elution buffer to 50°C, elute in 15 µl, leave column w/ buffer on shaker @50°C for around 5 min. Then centrifuge. Increases yield dramatically.

3) Nanodrop it

Insert preparation
You can assembly even complex inserts if they have also some common homology!.

1) Setup PCR, use 50 µl reactions with Hot FIREPol, I usually do 20 µl with Q5 or Phusion
10   µl 5x Hot FIREPol MM
 2.5 µl forward primer
 2.5 µl reverse primer
<0.5 µl DNA template (is mostly a plasmid, so use a very low amount!)
ad 50 µl H_2O.

2) Cycling parameters (maybe have to be optimized!, here for Hot FIREPol, check manual!)

95°C ~ 5 min (maybe longer)
95°C 15 s |
Ta°C 20-30 s | 35x ← check primer Tm, run maybe gradient and use the NEB tm calculator
72°C 1 min | ← polymerase speed is around 1 kb/min
72°C 2 min
10°C inf.

3) Resolving PCR product on gel to see if band is specific

4) Ideally gel purify PCR product
anki tipp: Don't use UV when doing SLiCE, it won't work anymore!! Use only blue light.

5) Nanodrop it.

Assembly

1) Use my small program to find the right volumes, briefly, there should be 50-100 ng of vector
and 1:3 **molar** (!) excess of inserts (totally easy are 1-2 inserts)

2) Prepare SLiCE reaction

 1 µl T4 Ligase buffer
 x µl Insert (e.g. EGFP)
 y µl backbone (e.g. gel purified, EcoRI-XbaI digested (1))
 1 µl SLiCE
ad 10 µl H2O
@37°C 30 min to 60 min (the more fragments, the longer).

Transformation

1) Thaw homebrew chemical competent bacteria on ice (100 µl per trafo)
2) Add 1-10 µl (normally transform 2 µl and then the rest in a second batch of bacteria)
3) incubate on ice for 30 min
4) heatshock @42°C for 30-60 s
5) keep them on ice for around 2 min
6) plate them on pre-warmed LB plates with appropriate antibiotic (PC enhancer has ampR)
7) overnight @37°C.

You should expect around 10 – 50 colonies in a good reaction.

Problems:
- low DNA yields → do PCR or digestion again, change amount or cycling parameters
- no colonies → try NEBuilder or Gibson Assembly if DNA yields are low
→ use larger homology arms (best around 30-40 bp for SLiCE)
→ maybe SLiCE extract is bad (get fresh one, -80°C), always use fresh T4 ligase buffer.
→ use decent concentrations and amounts of DNA and molar ratios
→ check antibiotic of LB plates

Cloning into PC enhancer plasmid
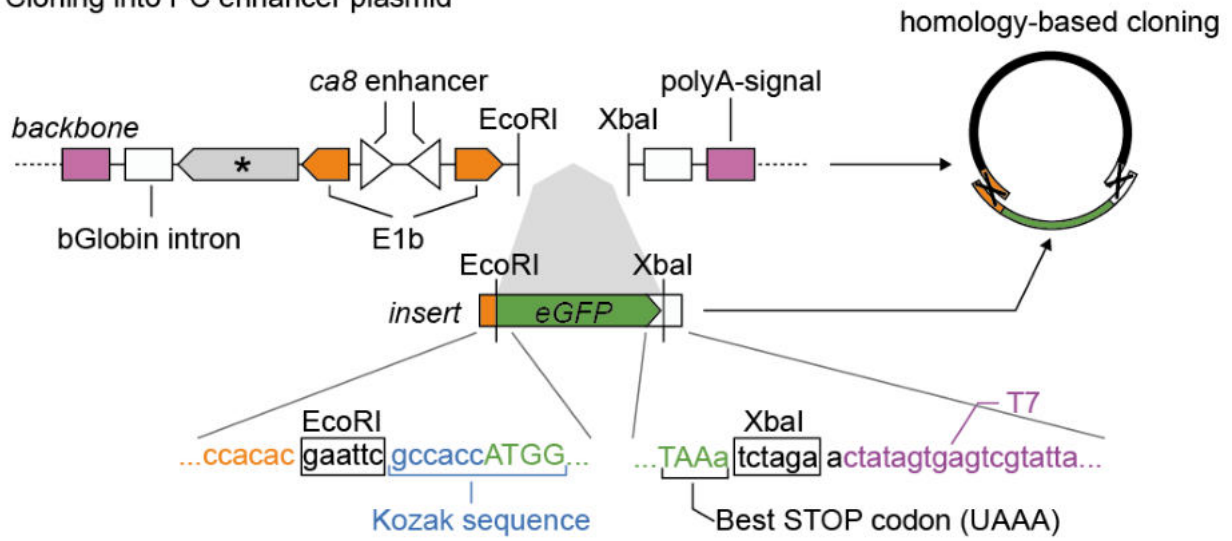
See also thesis.

T4 ligase buffer
https://bit.ly/2OWaxKy

5x Hot FIREPol MM
https://bit.ly/2PtymdT

Colony PCR Protocol

Equipment
- A fresh LB plate (pre-warmed) with appropriate antibiotic (e.g. Ampicillin)
- LB plate with colonies
- 2x OneTaq Mastermix with Standard buffer (NEB #M0482L)
- forward and reverse colony PCR primer (e.g. E1b_f and Seq_T7_PCenh)
- 0.1 – 10 µl filter tips
- P2 or P10 pipette
- Gel electrophoresis equipment (see extra protocol)
- Racks

Steps

1) Label fresh plate, draw areas to indicate colony#

2) Prepare 1x Mastermix

	10 rxn, for 8 colonies	20 rxn, for ~16 colonies
2x OneTaq	75 µl	150 µl
Primer forward (10 µM)	3 µl	6 µl
Primer reverse (10 µM)	3 µl	6 µl
Water	69 µl	138 µl
	150 µl (15 µl each)	300 µl (15 µl each)
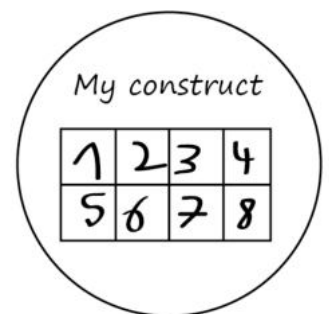
3) Pipette 1x mastermix in tubes

4) take a fresh filter tip, briefly touch the colony, spread it on the corresponding colony# area on the new LB plate and put it directly to the prepared PCR reaction

5) Perform 4) for each colony, close the lid and go to the thermocycler

6) Use the following cycling parameters:

94°C 3 min
94°C 30 s |
52°C 30 s | 35 x   ← adjust for primers, my sequencing primers are optimized for this
68°C 1 min | ← adjust for fragment length, 1 kb/min
68°C 2 min
4-10°C inf.

Resolve ~8 µl on a 1% - 1.5% agarose gel (in 1x TAE buffer).
Run for around 20-30 min at ~120 V.
Use the 1 kb NEB ladder to identify fragments of correct size.

2x OneTaq MM

anki phd thesis 2018
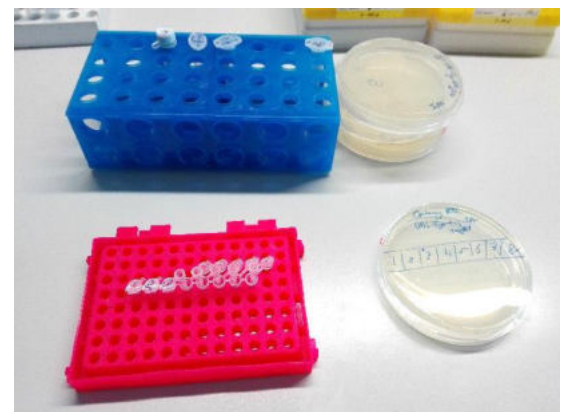
Tol2 mRNA preparation

Reagents

- Tol2 transposase plasmid (pCS-zT2TP)
- CutSmart NotI-HF or Anza NotI with respective buffer
- Ambion mMESSAGE mMACHINE (SP6) kit
- DNase- and RNase-free water
- LiCl (shipped with Ambion kit, but make sure it's there)
- 70 % Ethanol (stored at -20 °C)
- Nanodrop
- Filter tips and high grade microfuge tubes
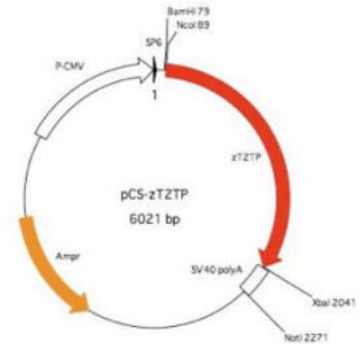
Digest plasmid

Use a 50 ul reaction

5 ul	10x Anza or CutSmart buffer
x ul	5 ug plasmid
1 ul	NotI enzyme (depending on buffer system)
ad 50 ul	ddH$_2$O

@ 37°C, **3-5 h** (to ensure highly complete digestion)

Recover DNA by PCR purification kit
(e.g. NucleoSpin, Machery-Nagel, follow manufacturer's protocol, elute in RNase-free H$_2$O).

In vitro transcription (taken from kit manual)

Capped transcription reaction assembly

1. Thaw the frozen reagents

   Place the RNA Polymerase Enzyme Mix on ice, it is stored in glycerol and will not be frozen at –20°C.

   Vortex the 10X Reaction Buffer and the 2X NTP/CAP until they are completely in solution. Once thawed, store the ribonucleotides (2X NTP/CAP) on ice, but *keep the 10X Reaction Buffer at room temperature while assembling the reaction*.

   All reagents should be microfuged briefly before opening to prevent loss and/or contamination of material that may be present around the rim of the tube.

2. Assemble transcription reaction at room temp

   The spermidine in the 10X Reaction Buffer can coprecipitate the template DNA if the reaction is assembled on ice.

   Add the 10X Reaction Buffer after the water and the ribonucleotides are already in the tube.

   The following amounts are for a single 20 μL reaction. Reactions may be scaled up or down if desired.

   IMPORTANT! The following reaction setup is recommended when the RNA produced will be 300 bases to 5 kb in length. For transcripts longer or shorter than this, consider the suggestions in sections "Optimizing yield of long transcripts" on page 20 and "Optimizing yield of short transcripts" on page 21, respectively.

Amount	Component
to 20 µL	Nuclease-free Water
10 µL	2X NTP/CAP
2 µL	10X Reaction Buffer
(1 µL)	(optional) [α-32P]UTP as a tracer
0.1-1 µg	linear template DNA†
2 µL	Enzyme Mix

† Use 0.1–0.2 µg PCR-product template or ~1 µg linearized plasmid template.

3. **Mix thoroughly**

Gently flick the tube or pipette the mixture up and down gently, and then microfuge tube briefly to collect the reaction mixture at the bottom of the tube.

4. **Incubate at 37°C, 1 hr**

Typically, 80% yield is achieved after a 1 hr incubation. For maximum yield, we recommend a 2 hr incubation. Since SP6 reactions are somewhat slower than T3 and T7 reactions, they especially may benefit from the second hour of incubation.

A second hour of incubation is recommended for synthesis of <300 base transcripts and for inefficiently transcribed templates. (See sections "Optimizing yield of long transcripts" on page 20 and "Optimizing yield of short transcripts" on page 21 for optimizing yield from templates coding RNA outside the 0.3–5 kb range.

Incubate at least 2 h

5. **(optional) Add 1 µL TURBO DNase, mix well and incubate 15 min at 37°C**

This DNase treatment removes the template DNA. For many applications it may not be necessary because the template DNA will be present at a very low concentration relative to the RNA.

   a. Add 1 µL TURBO DNase, and mix well.
   b. Incubate at 37°C for 15 min.

2. **Lithium chloride precipitation**

Lithium Chloride (LiCl) precipitation is a convenient and effective way to remove unincorporated nucleotides and most proteins. Lithium chloride precipitation, however, does not precipitate transfer RNA and may not efficiently precipitate RNAs smaller than 300 nucleotides. Also, the concentration of RNA should be at least 0.1 µg/µL to assure efficient precipitation. To precipitate from mMESSAGE mMACHINE® reactions that are thought to have relatively low yields of RNA, do not dilute the transcription reaction with water prior to adding the LiCl Precipitation Solution the first substep below.

   a. Stop the reaction and precipitate the RNA by adding 30 µL Nuclease-free Water and 30 µL LiCl Precipitation Solution.
   b. Mix thoroughly. Chill for ≥30 min at –20°C.
   c. Centrifuge at 4°C for 15 min at maximum speed to pellet the RNA.
   d. Carefully remove the supernatant. Wash the pellet once with ~1 mL 70% ethanol, and re-centrifuge to maximize removal of unincorporated nucleotides.
   e. Carefully remove the 70% ethanol, and resuspend the RNA in a solution or buffer† appropriate for your application. Determine the RNA concentration and store frozen at –20°C or –70°C.

Dilute RNA to 175 ng/ul concentration and store **4 ul aliquots** in PCR tubes at -20°C.

Use 1 ul of tol2 mRNA in a 10 ul injection reaction (final concentration: around 18 ng/ul, can be increased, embryos are very tolerant to high RNA concentrations, but not DNA!!)

Danieau solution

Recipe for 1 l of 30x Danieau solution

Reagent	Amount	Concentration
NaCl	101.7 g	1740 mM
KCl	1.56 g	21 mM
$MgSO_4 * 7 H_2O$	2.96 g	12 mM
$Ca(NO_3)_2$	4.25 g	18 mM
HEPES	35.75 g	150 mM

Use a beaker of 1 L size.
Add around 600 mL of ddH2O.
Add an magnetic stir bar to the water.

Add salts one after another while stirring.
Check pH with pH meter (wash electrode extensively with water beforehand).

Adjust pH with NaOH (you will need A LOT!) to 7.6
Store at 4°C.

Note: Don't check pH with pH paper, the massive amount of salt affects the indicator!
        Will work for 1x Danieau solution.

For 6 L of 1x Danieau solution

Add 200 mL of 30x Danieau stock to 10 L bottle.
Add ddH2O to 6 L.
Check pH with pH paper (should be 7.6).

Add 3-4 drops of methylene blue

Prepare chemical competent cells

Prepare TSS Buffer (Chung et al., P.N.A.S. 1989)

5g	PEG 8000 (or 3350)
1.5 mL	1 M $MgCl_2$ (or 0.30 g $MgCl_2 * 6 H_2O$)
2.5 mL	DMSO
To 50 mL	LB

Sterile filter, store at 4°C for around 3-6 months.
Check pH, should be slightly acidic, around ~ 6.5

1. Grow 1 µl E.coli in 50 mL LB or SOB medium overnight
   DON'T USE ANY ANTIBIOTICS!!

2. Dilute 1:100 starter culture in 50 mL fresh LB or SOB medium

3. Grow until OD_{600} = 0.2 – 0.5

4. Put everything, TSS, culture and plenty 1.5 mL Eppendorf tubes, on ice.
   Use dry ice to cool down the storage box.

5. Centrifuge for 10 min at around 3,000 rpm at 4°C (big centrifuge!)

6. Remove supernatant carefully and completely!!

7. Resuspend pellet in around 10% TSS of original culture (i.e. 5 mL for 50 mL final culture)

8. Aliquot in 100 µl (use 1.5 mL Eppendorf tubes)

9. Freeze immediately in the storage box (dry ice) and then → -80°C.

10. Next day: Test performance using a random plasmid and compare it to previous batch

Use 100 µl for transformations.

Original recipe

Scheme 1. Transformation procedure

1. A fresh overnight culture of bacteria is diluted 1:100 into prewarmed LB broth and the cells are incubated at 37°C with shaking (225 rpm) to an OD_{600} of 0.3–0.4.
2. An equal volume of ice-cold 2× TSS is added and the cell suspension is mixed gently. [TSS is LB broth with 10% PEG (molecular weight 3350 or 8000), 5% DMSO, and 20–50 mM Mg^{2+} ($MgSO_4$ or $MgCl_2$) at a final pH of 6.5.]
3a. For long-term storage, cells are frozen immediately in a dry ice/ethanol bath and stored at −70°C.
3b. For transformation, a 0.1-ml aliquot of cells is pipetted into a cold polypropylene tube containing 1 µl (100 pg) of plasmid DNA, and the cell/DNA suspension is mixed gently. (When frozen cells are used, cells are thawed slowly on ice and used immediately.)
4. The cell/DNA mixture is incubated for 5–60 min at 4°C.
5. A 0.9-ml aliquot of TSS (or LB broth) plus 20 mM glucose is added, and the cells are incubated at 37°C with shaking (225 rpm) for 1 hr to allow expression of the antibiotic-resistance gene.
6. Transformants are selected by standard methods.

a Behavioral triggered average for different bar sizes

b Behavioral triggered average for different grating speeds

c Behavioral triggered average for different white-to-black bar ratios
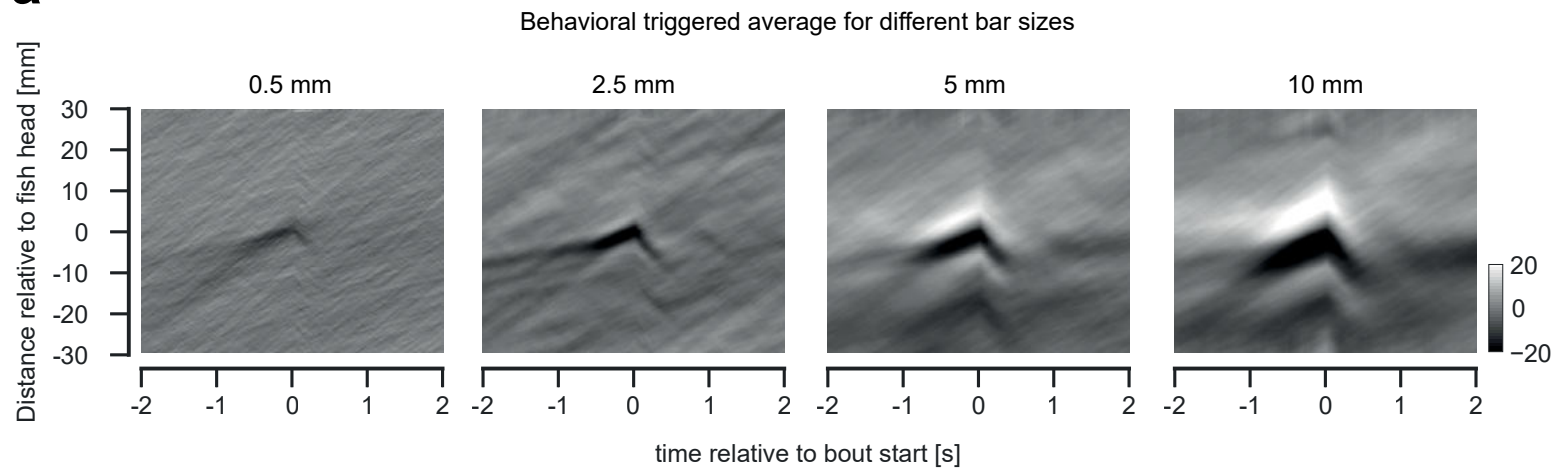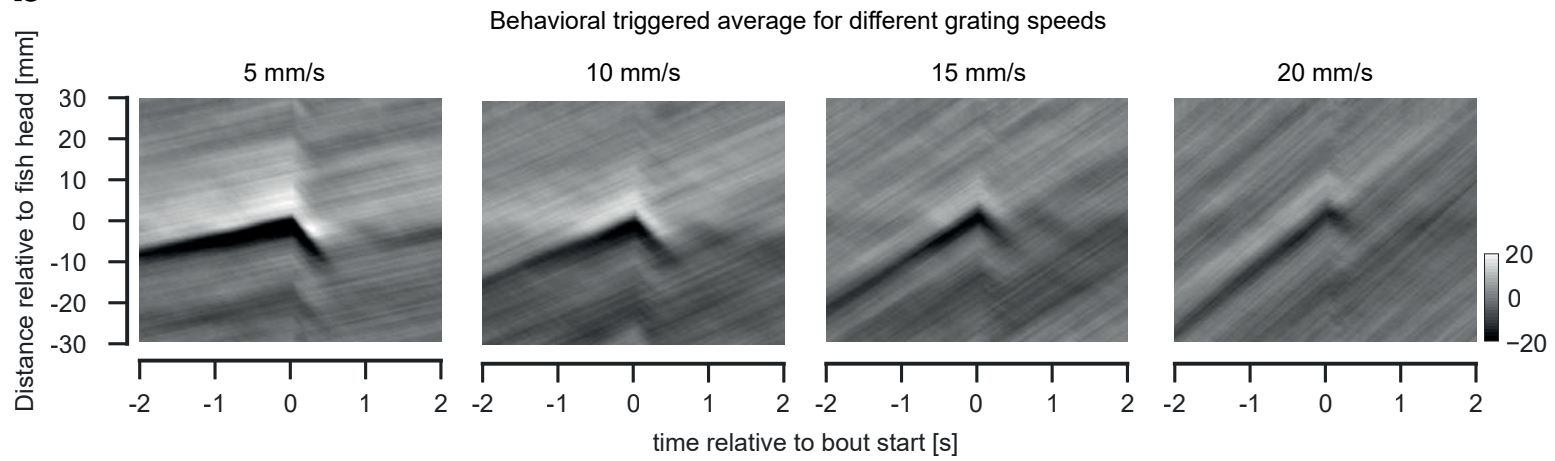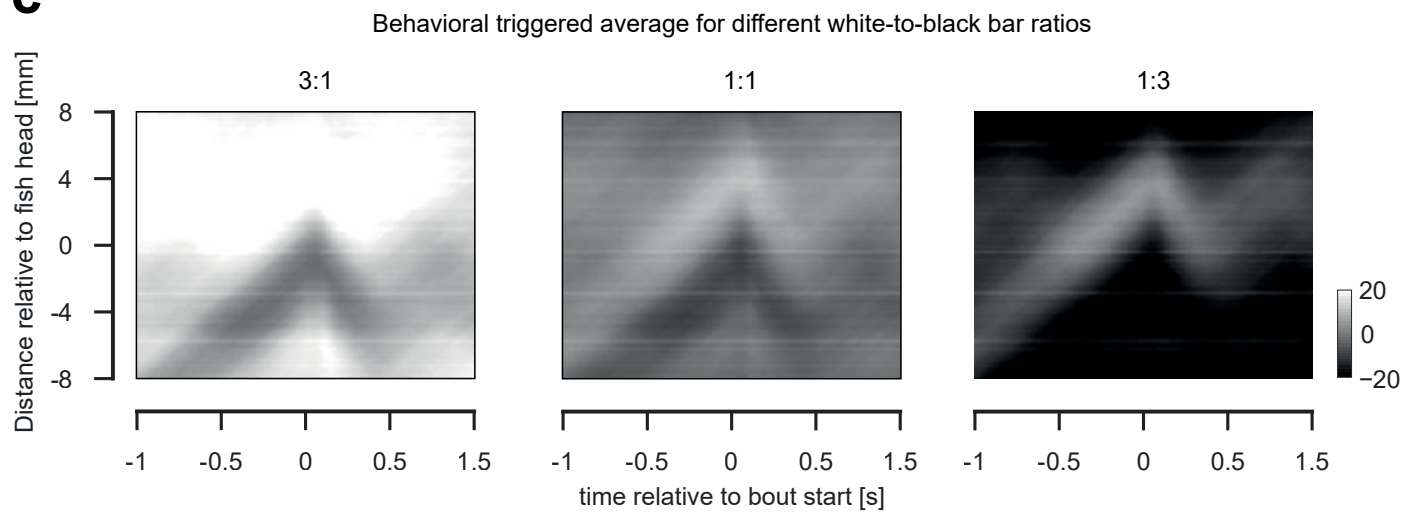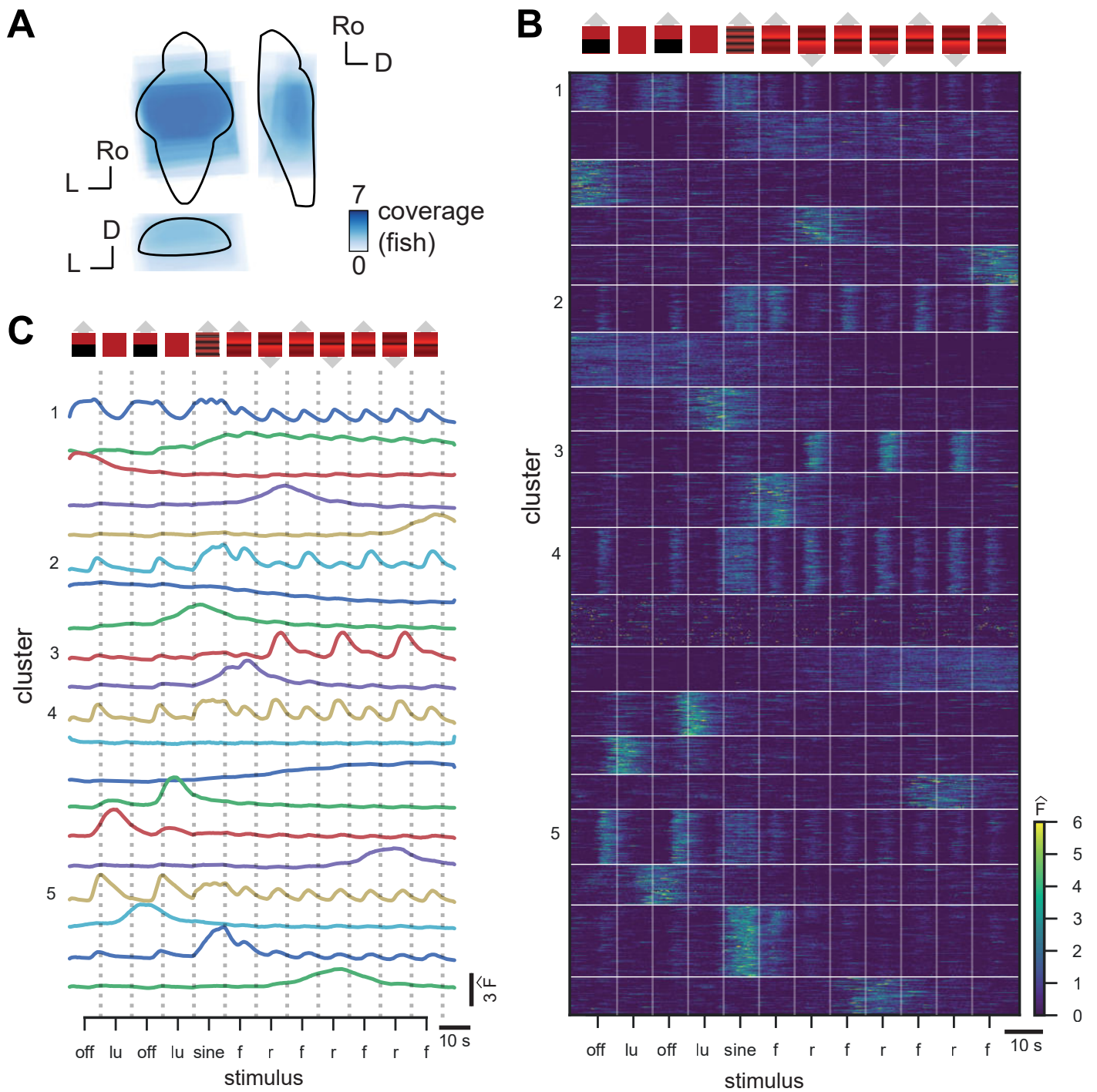
Grouping of distinct responses reveal five clusters tuned to the whole-field moving filter. A) Sampling coverage of functional imaging experiments. Colormaps indicate the number of fish sampled. **B)** Heatmap of all ROIs with z-scored fluorescence. Stimuli are indicated by off for off edge, lu for luminance transition, sine for a forward moving sine grating and f for the forward filter and r for the reverse filter (see Methods). X-ticks indicate when stimuli are on the fish head, different stimuli are separated by light gray lines. **C)** Average activity profile of each cluster with same stimuli presented as in A).
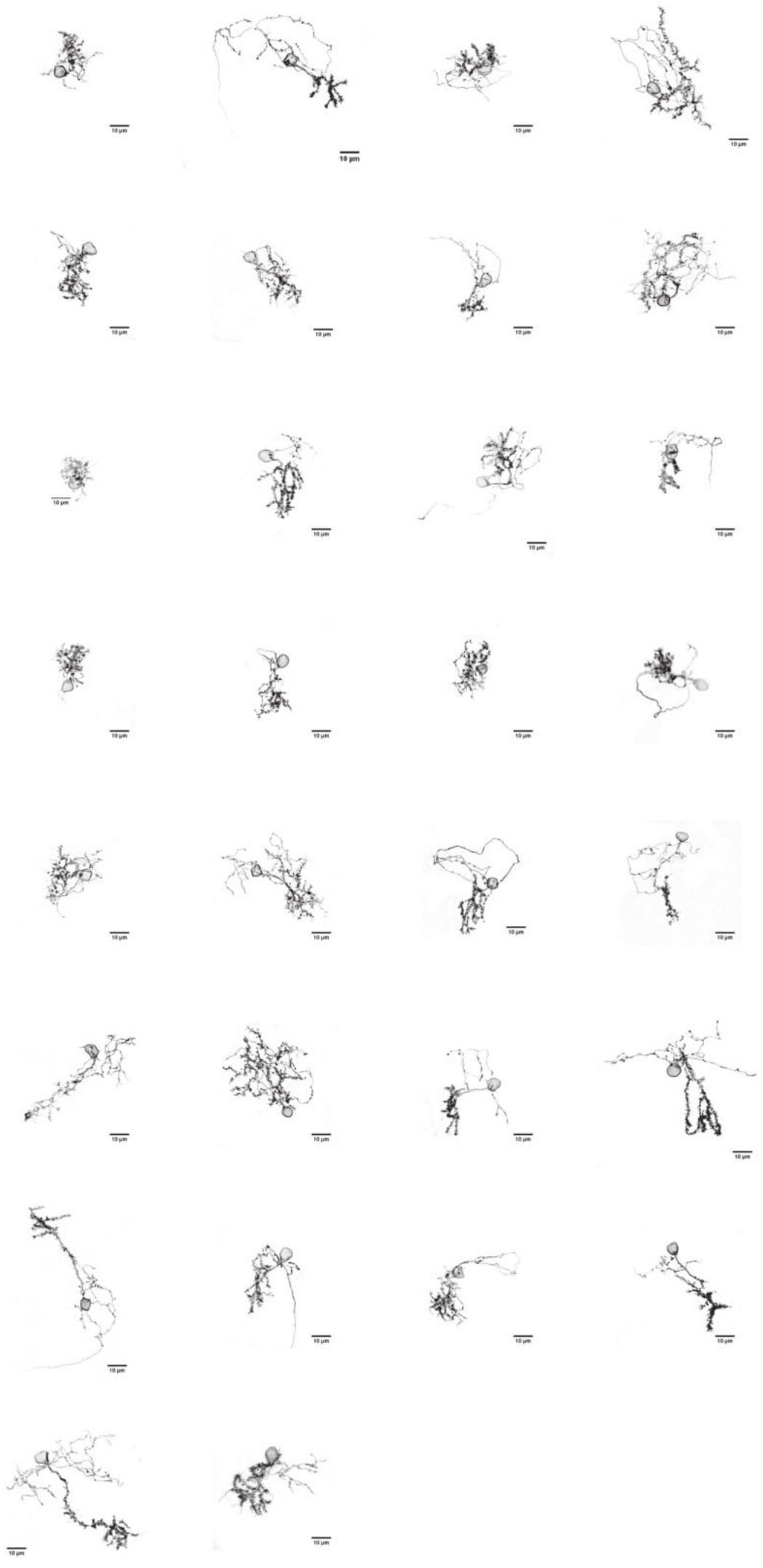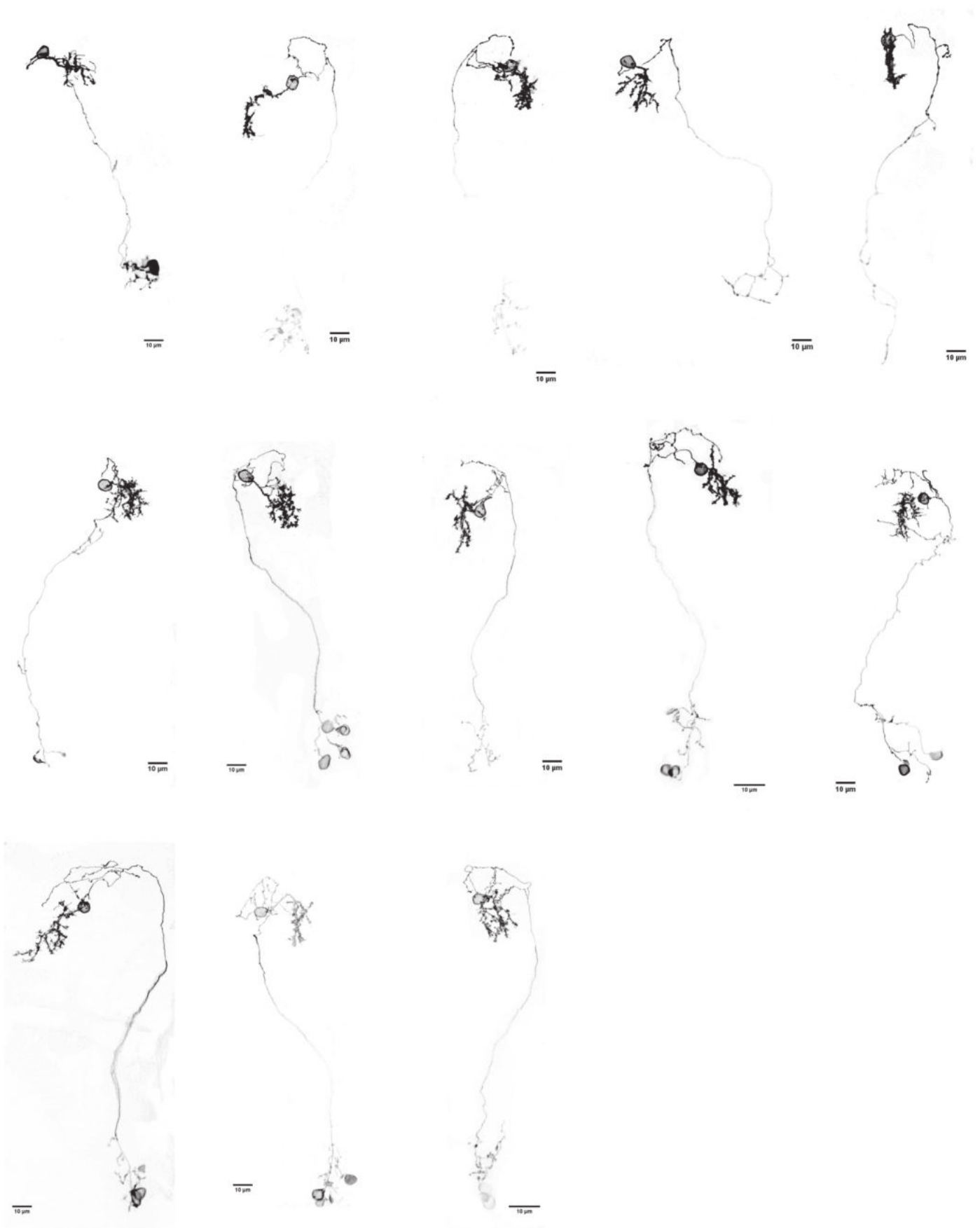
frame id	time	stim id	stim	stim duration	associated parameter
0	0,216432	0	dark	5	0
22	4,977936	0	dark	5	0
23	5,194368	1	forward	5	0
45	9,955872	1	forward	5	0
46	10,172304	2	forward	5	3
68	14,933808	2	forward	5	3
69	15,15024	3	forward	5	0
91	19,911744	3	forward	5	0
92	20,128176	4	forward	5	10
114	24,88968	4	forward	5	10
115	25,106112	5	forward	5	0
137	29,867616	5	forward	5	0
138	30,084048	6	forward	5	30
160	34,845552	6	forward	5	30
161	35,061984	7	forward	5	0
183	39,823488	7	forward	5	0
184	40,03992	8	reverse	5	10
206	44,801424	8	reverse	5	10
207	45,017856	9	reverse	2,5	0
218	47,398608	9	reverse	2,5	0
219	47,61504	10	left	2,5	0
230	49,995792	10	left	2,5	0
231	50,212224	11	left	5	10
253	54,973728	11	left	5	10
254	55,19016	12	left	5	0
276	59,951664	12	left	5	0
277	60,168096	13	right	5	10
299	64,9296	13	right	5	10
300	65,146032	14	left	2,5	0
310	67,310352	14	left	2,5	0
311	67,526784	15	OKR	2,5	0
322	69,907536	15	OKR	2,5	0
323	70,123968	16	OKR	5	1
345	74,885472	16	OKR	5	1
346	75,101904	17	OKR	5	0
368	79,863408	17	OKR	5	0
369	80,07984	18	OKR	5	-1
391	84,841344	18	OKR	5	-1
392	85,057776	19	OKR	5	0
414	89,81928	19	OKR	5	0
415	90,035712	20	OKR	5	1
437	94,797216	20	OKR	5	1
438	95,013648	21	OKR	5	0
461	99,991584	21	OKR	5	0
462	100,208016	22	OKR	5	-1
484	104,96952	22	OKR	5	-1
485	105,185952	23	OKR	5	0
507	109,947456	23	OKR	5	0
508	110,163888	24	OKR	5	1
530	114,925392	24	OKR	5	1
531	115,141824	25	OKR	5	0
553	119,903328	25	OKR	5	0
554	120,11976	26	OKR	5	-1
576	124,881264	26	OKR	5	-1
577	125,097696	27	OKR	2,5	0
588	127,478448	27	OKR	2,5	0
589	127,69488	28	OKR_left	2,5	0
599	129,8592	28	OKR_left	2,5	0
600	130,075632	29	OKR_left	5	1
622	134,837136	29	OKR_left	5	1
623	135,053568	30	OKR_left	5	0
645	139,815072	30	OKR_left	5	0
646	140,031504	31	OKR_left	5	-1
668	144,793008	31	OKR_left	5	-1
669	145,00944	32	OKR_left	2,5	0
680	147,390192	32	OKR_left	2,5	0
681	147,606624	33	OKR_right	2,5	0
692	149,987376	33	OKR_right	2,5	0
693	150,203808	34	OKR_right	5	1
715	154,965312	34	OKR_right	5	1
716	155,181744	35	OKR_right	5	0
738	159,943248	35	OKR_right	5	0
739	160,15968	36	OKR_right	5	-1
761	164,921184	36	OKR_right	5	-1
772	167,301936	37	OKR_right	2,5	0
773	167,518368	38	dark	2,5	0
784	169,89912	38	dark	2,5	0
785	170,115552	39	flash	1	190
789	170,98128	39	flash	1	190
790	171,197712	40	dark	1	0
793	171,847008	40	dark	1	0
794	172,06344	41	flash	1	190
798	172,929168	41	flash	1	190
799	173,1456	42	dark	1	0
802	173,794896	42	dark	1	0
803	174,011328	43	flash	1	190
807	174,877056	43	flash	1	190
808	175,093488	44	dark	1	0
812	175,959216	44	dark	1	0
813	176,175648	45	flash	1	190
816	176,824944	45	flash	1	190
817	177,041376	46	dark	5	0
859	186,13152	46	dark	5	0

Cell Chemical Biology

Imaging-Based Screening Platform Assists Protein Engineering

Highlights

- Low-cost screening platform for image analysis and picking of bacterial colonies

- Tracks each colony in a population expressing diversified protein libraries

- Adaptable for many protein engineering projects

- Platform was used to engineer mCarmine, a far-red-emitting fluorescent protein

Authors

Arne Fabritius, David Ng,
Andreas Michael Kist, Mutlu Erdogan,
Ruben Portugues, Oliver Griesbeck

Correspondence

griesbeck@neuro.mpg.de

In Brief

Protein evolution requires generation and screening of large numbers of variants. To expedite screening, Fabritius et al. built a platform that integrates fluorescence-based image analysis and picking of bacterial colonies. They engineered mCarmine, a far-red-emitting fluorescent protein for tagging and deep tissue imaging.

CellPress

Resource

CellPress

Imaging-Based Screening Platform Assists Protein Engineering

Arne Fabritius,[1] David Ng,[1] Andreas Michael Kist,[2] Mutlu Erdogan,[1] Ruben Portugues,[2] and Oliver Griesbeck[1,3,*]

[1]Tools for Bio-Imaging, Max-Planck-Institut für Neurobiologie, Am Klopferspitz 18, Martinsried 82152, Germany
[2]Sensorimotor Control, Max-Planck-Institut für Neurobiologie, Am Klopferspitz 18, Martinsried 82152, Germany
[3]Lead Contact
*Correspondence: griesbeck@neuro.mpg.de
https://doi.org/10.1016/j.chembiol.2018.08.008

SUMMARY

Protein engineering involves generating and screening large numbers of variants for desired properties. While modern DNA technology has made it easy to create protein diversity on the DNA level, the selection and validation of candidate proteins from large libraries remains a challenge. We built a screening platform that integrates high-quality fluorescence-based image analysis and robotic picking of bacterial colonies. It allows tracking each individual colony in a large population and collecting quantitative information on library composition during the protein evolution process. We demonstrate the power of the screening platform by optimizing a dim far-red-emitting fluorescent protein whose brightness increased several fold using iterative cycles of mutagenesis and platform-based screening. The resulting protein variant mCarmine is useful for imaging cells and structures within live tissue as well as for molecular tagging. Overall, the platform presented provides powerful, flexible, and low-cost instrumentation to accelerate many fluorescence-based protein optimization projects.

INTRODUCTION

Directed protein evolution involves generating and screening large numbers of diversified variants (Jäckel et al., 2008; Packer and Liu, 2015). While diversification of proteins on the DNA level is straightforward, the analysis of generated mutants can be time consuming and laborious. Fluorescent proteins, biosensors, and other proteins whose functions can be coupled to fluorescence readout are particularly favorable classes of proteins for imaging-based screening (Heim and Tsien, 1996; Miyawaki et al., 2005; Goedhart et al., 2010; Rodriguez et al., 2017). Due to the ease of transforming libraries and retrieving selected DNAs, *Escherichia coli* has been a preferred vehicle to express and screen diversified proteins (Chen et al., 2001; Castle et al., 2004; Packer and Liu, 2015). Critical steps are the image analysis to identify improved protein variants and the retrieval of identified bacterial colonies from an agar plate. When performed manually, colony picking is a slow, laborious, and error-prone process.

Automated colony pickers have been built (Jones et al., 1992), and there are high-end commercial versions available for the many facets of genomics. However, they are expensive, not well suited to protein engineering applications, typically do not have the necessary flexibility in fluorescence image analysis, and do not allow collecting information on library composition during the different steps of a protein evolution process. To remove this bottleneck, we constructed a low-cost, customizable bacterial colony screening station that combines flexible online fluorescence image analysis with a robotic colony-picking component. This integrated approach increases throughput for directed evolution applications, while reducing human error. Furthermore, a focus was put on improving data quality, by enhancing wide-field fluorescence imaging capability and analysis of this setup. To demonstrate one possible use of the screening platform, we set out to improve a far-red-emitting fluorescent protein. There is a continuing drive to engineer brighter and more red-shifted fluorescent proteins due to the favorable mammalian tissue penetration above 600 nm (Tromberg et al., 2000). We chose to improve the far-red-emitting fluorescent protein mNeptune684 (Li et al., 2016), a protein with the most red-shifted emission maximum of current fluorescent proteins apart from the co-factor-dependent bacterial phytochromes.

RESULTS

An Imaging-Based Bacterial Colony Screening Platform

The platform was built around a camera system imaging bacterial colonies on agar plates or blotted onto filter membranes (Figures 1 and S1, Data S1). For the three-dimensional (3D) manipulation of the picking arm, we used a delta robot configuration (Clavel, 1988; Merlet, 2006) adapted from an open-source 3D printer design (Figure 1A). This manipulator setup allowed 3D movement of the picking head within a cylindrical volume with a diameter of 210 mm and a height of 200 mm, with a resolution of 0.05 mm in X/Y/Z. We also designed a picking head (Figure 1B) consisting of a ferromagnetic metal rod at the core of a copper coil. When put under load, the induced magnetic field lifted the rod and magnetized it, which allowed for the attachment of a small disposable steel sphere. The picking head was then maneuvered to dip the sphere briefly into a bacterial colony of interest. Subsequently, the picking head was directed to a selected well of a 96-well plate for inoculating liquid medium into which the steel sphere was dropped by turning off the electromagnet. For each colony a fresh sterilized steel sphere was
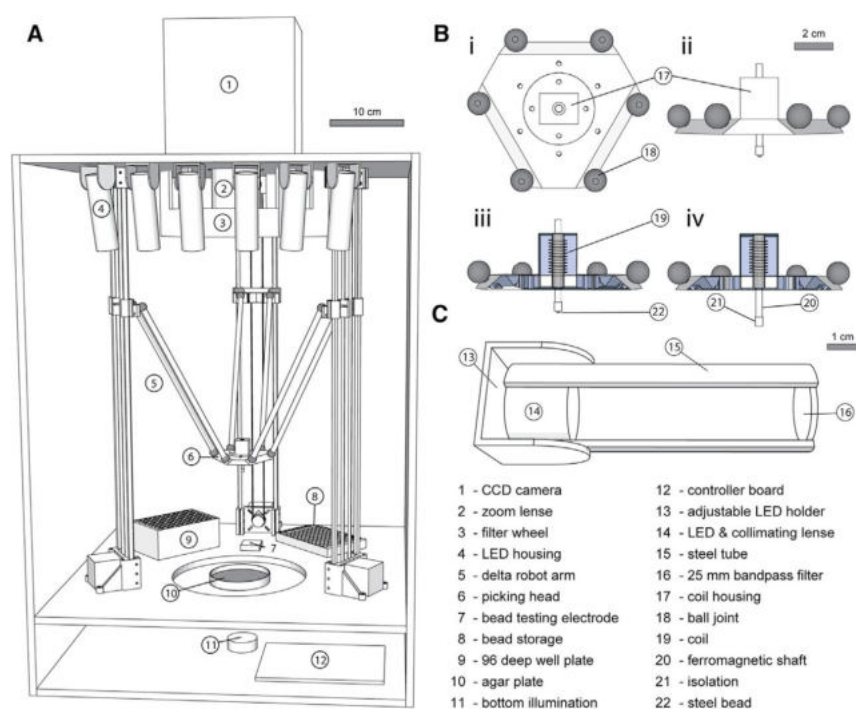
Figure 1. An Imaging-Based Screening Platform to Assist Protein Engineering

(A) Scheme of the analysis and picking station. Wide-field CCD camera imaging (1) is used to analyze performance of library variants expressed in *E. coli* on agar plates (10). Up to 800 colonies can be assayed simultaneously and can be picked by the robotic arm (6) for further analysis. Scale bar, 10 cm.

(B) Picking head design. A steel rod (20) inside a copper coil (19) with corresponding insulation (21) is magnetized. It can be used to engage and trap a small-diameter steel sphere (22). The steel sphere can then be transported throughout the 3D volume by the robotic arm, be dipped into a bacterial colony, and then dropped into a well of a multi-well plate filed with liquid medium for inoculation. (i) Top view; (ii) side view; (iii) cut side view with electromagnet engaged and a steel sphere attached; (iv) cut side view with electromagnet disengaged. Scale bar, 2 cm.

(C) Scheme of illumination device with internal LEDs. Scale bar, 1 cm.

1 - CCD camera
2 - zoom lense
3 - filter wheel
4 - LED housing
5 - delta robot arm
6 - picking head
7 - bead testing electrode
8 - bead storage
9 - 96 deep well plate
10 - agar plate
11 - bottom illumination
12 - controller board
13 - adjustable LED holder
14 - LED & collimating lense
15 - steel tube
16 - 25 mm bandpass filter
17 - coil housing
18 - ball joint
19 - coil
20 - ferromagnetic shaft
21 - isolation
22 - steel bead

used, omitting the need for sterilization between picks. For fluorescence excitation we used single-color light-emitting diodes (LEDs) fitted with collimating lens assemblies and fluorescence filters and placed them at the end of a 100 mm steel tube (Figure 1C). To detect non-fluorescent colonies, the platform was also fitted with bottom-up illumination using a white LED array. The complete screening setup was housed in a 50 cm × 50 cm × 60 cm box made from medium-density fiber plates to exclude ambient light. A charge-coupled device (CCD) camera was mounted on top of the platform and fitted with a zoom lens to capture the plate at high resolution. To allow fluorescence imaging, a custom-made filter wheel for large-diameter emission filters was placed in front of the camera assembly (Figure 1). Integrated control of the platform was achieved with a standard microcontroller board and custom software for hardware control. For image analysis (Figure 2), automatic plate detection and bacterial colony detection algorithms were implemented. Within a single screening session, 50,000–100,000 clones could be conveniently tracked and analyzed and colonies expressing proteins with desirable properties identified for picking. No special precautions for sterility were necessary, apart from autoclaving steel spheres and medium before use.

Platform-Based Engineering of mCarmine

Our optimization started with mNeptune684 (Li et al., 2016), a fluorescent protein with large Stoke shift and an emission maximum at 684 nm. mNeptune684 and randomized libraries thereof were fused to the bright cyan- to green-emitting fluorescent protein mTFP1 (Ai et al., 2006), which served as a reference fluorophore (Figure 2C). Fusions were assayed using ratiometric image processing to account for variations in protein expression levels seen between *E. coli* colonies after transformation or between different libraries assayed over weeks. We executed

several modes of mutagenesis and variant selection using the screening platform. Briefly, in small-scale selections the robotic arm was used to pick identified variants with higher relative brightness per plate for further analysis. For large scale screens of up to 100,000 bacterial colonies, several hundred plates were screened and analyzed using the station, and final pick suggestions were made by the software post analysis for individual plates and colonies according to customized performance criteria. Overall, screening time per plate depended on a number of factors: image acquisition, image processing, and eventually picking of colonies. The time required varied depending on brightness of the fluorescent proteins; the number of channels to be acquired; and, in the case of biosensor screening (data not shown), the time it takes to obtain F_{min} and F_{max} (or R_{min} and R_{max}) in successive images. In most cases, image acquisition (~3 min) and processing (~20 s–1.5 min/plate) required the major time in a particular screening step. Density of colonies was typically 500–800 per plate. Higher densities of 800–1,000 colonies per plate are technically possible, but in our experience densities exceeding 800 colonies per plate often resulted in fusion of colonies and double colonies, which would not be picked because of colony border mixing.

Summaries of the outcomes of several mutagenesis steps on the brightness distribution of variants are shown in Figure 3 and are discussed in Method Details. Notably, during the evolution process, after each mutagenesis step the effects on the total library composition could be monitored. The software kept track of each individual colony, its relevant property of interest, and coordinates. Parental mNeptune684 expressed and matured poorly in *E. coli*. We first subjected mNeptune684 to random mutagenesis by error-prone PCR. Dimeric or tetrameric revertants (R126I,S,T,G) initially dominated the pool of brighter variants in error-prone PCR mutagenesis of mNeptune684. Only one variant, mNeptune684 H161Y/P163T, was found that was
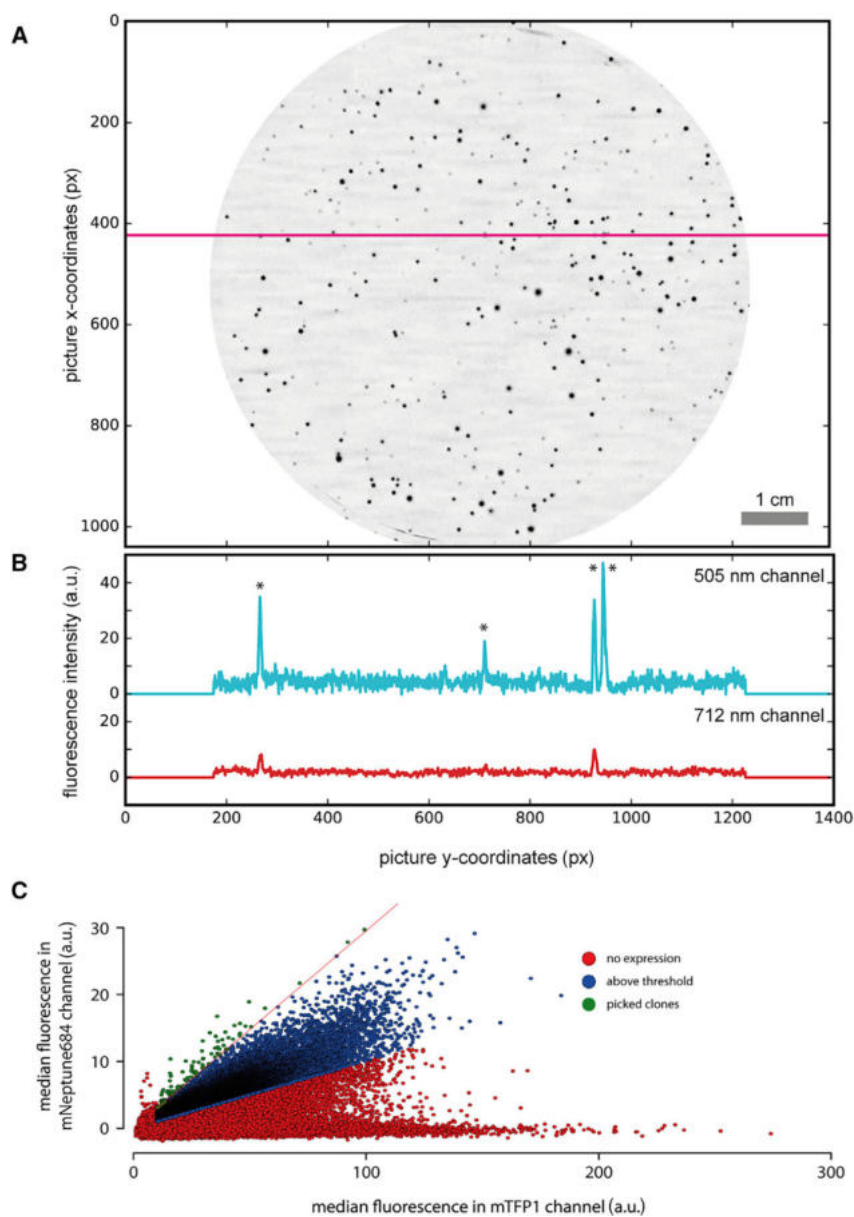
Figure 2. Image Analysis and Colony Selection

(A) Inverse greyscale presentation of a fluorescence image of an agar plate with bacterial colonies expressing a fusion protein consisting of the reference protein mTFP1 and a variant of mNeptune684. The pink line shows the position of a line plot.

(B) Line plot along the x axis of the plate as shown in (A). The blue/cyan line displays values of the mTFP1 reference channel. The red line reports values within the mNeptune684 measurement channel. Identified colonies along the line are highlighted with an asterisk. 1 pixel (px): 76 μm.

(C) Example of analysis of variants after diversification. Bacterial colonies are plotted according to their fluorescence values in the mNeptune684 channel and an mTFP1 reference channel. Diversified mNeptune684 variants had been fused to reference protein mTFP1. Red clones were classified as "no expression", indicating no functional fluorescent mNeptune684 variant, and excluded from further evaluation. Blue clones were above performance threshold, green clones were eventually selected for further analysis.

acids. We focused on regions with high levels of variability in alignments of far-red fluorescent proteins derived from the closely related precursors eqFP578/611 (Figures 3B and S2). Randomizations in several regions were screened (Figure 3). Cassette mutagenesis of region 175–178 yielded a distinctively brighter variant by introducing the mutations I175Q, C176T, and N177F. Cassette mutagenesis was furthermore used to probe several other regions for enhancement of brightness using this background but did not reveal any additive effects. Finally, an extensive round of error PCR mutagenesis was performed in which about 100,000 variants were scanned and processed using the station (Figure 3). Interestingly, all picked variants from this round had one of four possible mutations: C65S, N75K, T77P, and I125V, all of which have occurred either in mMaroon1 (Bajar et al., 2016) or in mGarnet2 (Matela et al., 2017) before. Some variants carried one of these four mutations and one or more other mutations. Most double mutations proved to be worse than the related single-mutation variant. Saturated screening that targeted only residues 65 and 125 in unison did not yield further improvements.

In Vitro Characterization of mCarmine

The final selected variant was named mCarmine. On the background of parental mNeptune684 it harbored mutations C65S, T107K, A108V, T109K, H161Y, P163T, I175Q, C176T, and N177F. mCarmine had an extinction coefficient of 83,000 and a quantum yield of 7%, bringing its brightness close to that of

brighter and did not show a reverting mutation in position 126. In order to further disfavor dimerization, we engineered a library randomizing residues 107–109 within the AC interface using cassette mutagenesis (Reidhaar-Olson and Sauer, 1988) and seamless phage recombinase–based ligation cloning (Zhang et al., 2012). The oligonucleotides used here contained biased diversity favoring charged residues in position 107 and 109 to break hydrophobic interactions within the interface (Figure 3B). We performed a small-scale screen of 2,500 clones to cover all 72 possible variants within the spectrum of the biased library. The mutations T107K, A108V, and T109K emerged, maintaining brightness and providing additional stabilization of the monomeric state. We next performed cassette mutagenesis on stretches of 3–5 neighboring amino acids in selected regions for a more exhaustive and focused diversification of amino

CellPress

Figure 3. Evolution of mCarmine

(A) The effects of successive rounds of mutagenesis on the brightness distribution of the resulting library expressed in *E. coli* are depicted. Only colonies with set fluorescence values over background in both recorded channels were included. Brightness is calculated as relative performance index (PI). The median of the distribution is marked as black horizontal line. Within each population the PI, identity and coordinates of every bacterial colony are kept track of. Blue signature lines mark the median of the parental mNeptune684 brightness and its multiples. The lower graph indicates the total number of colonies per library. F_λ = fluorescence intensity at wavelength, P = performance, $\tilde{P}_{WT}$ = median performance of mNeptune684.

(B) Crystal structure of the eqFP578 (PDB: 3PIB) precursor of mNeptune684 with highlighted regions for cassette mutagenesis. Dotted lines show the A/C dimer interface, where residue 126 (yellow) interacts with region 107–109 (turquoise).

$$PI = P - \tilde{P}_{WT}$$

$$P = \ln\left(\frac{F_{712nm}}{F_{505nm}}\right)$$

Performance of mCarmine in Tissue Labeling

Due to its long emission wavelengths, mCarmine should have advantages for imaging deeper into tissue than more blue-shifted fluorescent proteins. We tested its performance in a live larval zebrafish preparation (Figures 4B–4D). We cloned an mTFP1-mCarmine fusion protein downstream of a UAS cassette (UAS:mTFP1-mCarmine) and injected this construct in an HuC (*elavl3*) Gal4 driver line that allows strong pan-neuronal labelling (Park et al., 2000; Halpern et al., 2008; Asakawa and Kawakami, 2008). In anesthetized 6–7-day-old zebrafish larvae, we used confocal microscopy to image mTFP1 and mCarmine channels (442 nm and a 633 nm laser excitation, respectively) simultaneously. To compare performance in terms of scattering and signal-to-noise ratio, we acquired z stacks that covered around 300 μm dorsal to ventral (Figure 4B). In a very dorsal plane, we adjusted both laser powers to achieve comparable fluorescence signals in both channels. We used these exact laser settings to acquire the whole z stack. In addition, to generate Figure 4D-iii, in a very ventral plane (here at the interpeduncular nucleus [IPN]), we re-adjusted the laser power to cover as much of the dynamic range of the hybrid detector as possible to again obtain comparable fluorescence signals in both channels. To compare mTFP1 and mCarmine quantitatively, we determined a performance index (PI) in a deconvolved z stack with a theoretical point spread function for mTFP1 and mCarmine (Kirshner et al., 2013; Sage et al., 2017) that covers the IPN (around 240 ± 28 μm deep) with re-adjusted laser

bacterial phytochromes (Shcherbakova et al., 2015) with and ahead of other fluorescent proteins with emission maxima beyond 670 nm (Table S1). Its excitation and emission maxima were 603 nm and 675 nm, respectively (Figure 4A, Table S1). The pKa was determined to be 5.6, which renders it very favorable for cell applications because, under physiological pH, essentially all of the protein is in the fluorescent anionic state, in contrast to the parental mNeptune684 with a pKa of 6.5 (Table S1). mCarmine was found to be strictly monomeric, as determined with analytical size exclusion chromatography (Figure S3), while parental mNeptune684 and revertants incorporating R126I remained in a dimeric or tetrameric state, respectively.
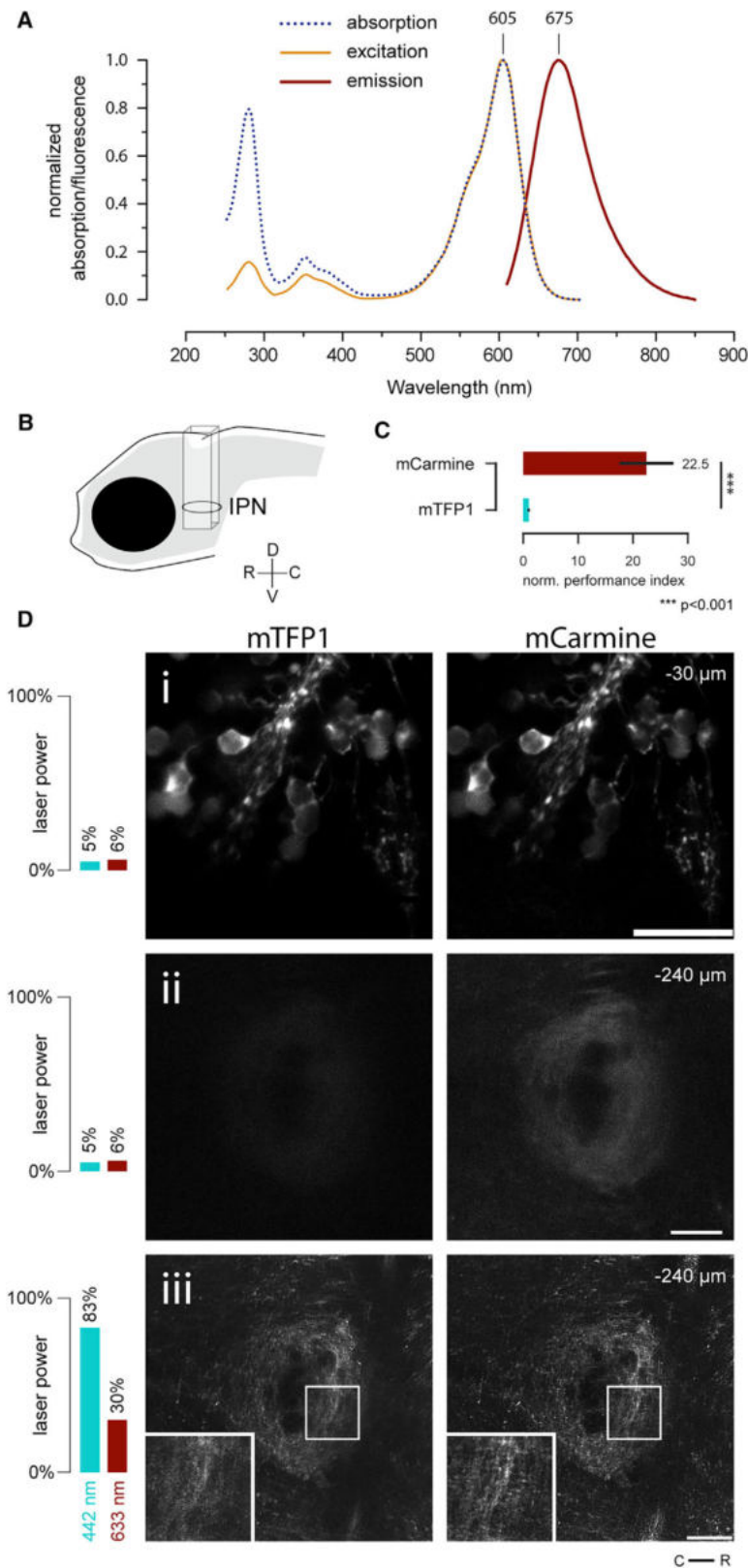
Figure 4. Characterization of mCarmine

(A) Excitation and emission spectra of purified recombinant mCarmine.

(B) A 6-day old zebrafish larva pan-neuronally expressing mTFP1 fused to mCarmine was imaged in a column dorsal to ventral, including the ventrally located interpeduncular nucleus (IPN).

(C) Performance index (PI) normalized to mTFP1. PI is calculated for each plane in the z stack of panel D (iii), and based on mean fluorescence per plane divided by properties of the fluorophore (see STAR Methods). Error bars represent SD; n = 2.

(D) Confocal images from cross-sections of the columns as shown in (B) with corresponding laser power used (percentage of maximal available power, turquoise and magenta for 442 and 633 nm laser lines, respectively. (i) Cross-section of a dorsal plane, used to calibrate laser powers across channels. (ii) Cross-section at the IPN with same laser powers as in (i). (iii) Deconvolved maximum intensity projection of a z stack spanning the whole IPN (~50 μm), using re-calibrated laser powers. Note the much higher laser power needed for the brighter mTFP1 fluorophore. Inset shows differences in fine structures between channels. Scale bar, 20 μm.

CellPress
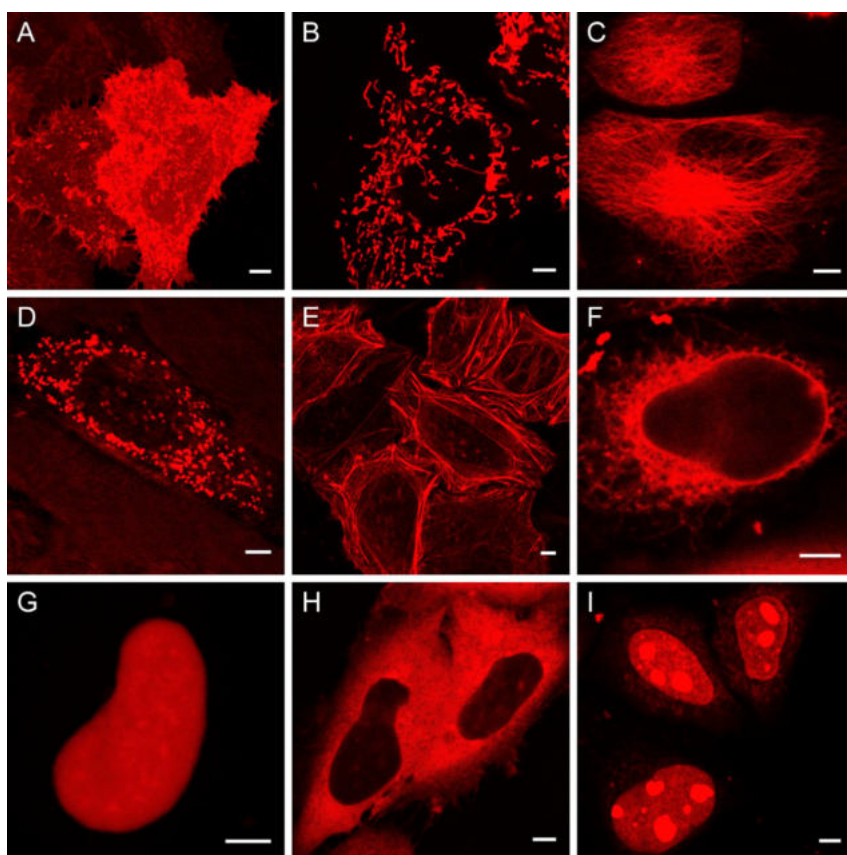
Figure 5. Subcellular targeting of mCarmine in HeLa cells

HeLa cells were transfected with mammalian expression vectors expressing the following mCarmine fusions: (A) Gap43-mCarmine, targeting to plasma membrane; (B) mito-mCarmine, targeting mitochondria; (C) mCarmine-α-tubulin, targeting cytoskeleton; (D) mCarmine-SKL, targeting peroxisomes; (E) Lifeact-mCarmine, targeting actin filaments; (F) ER-mCarmine, targeting ER; (G) mCarmine-NLS, nuclear import; (H) mCarmine-NES, nuclear export; (I) H2B-mCarmine, histone fusion. Scale bars: 5 μm.

DISCUSSION

We here present a bacterial colony screening platform that facilitates protein engineering projects using microbial expression systems. It does so by integrating image processing and online data analysis with classification and picking of colonies with desirable properties. Both plate segmentation and colony segmentation are fully automated, which allows fast screening through large numbers of bacterial colonies on agar plates or filter paper with minimal intervention by an experimenter. The picking function is optional, but in typical engineering cycles it mitigates an error-prone bottleneck in the optimization. Computer screen images may have to be aligned with the actual agar plate, which is time consuming, and the actual manual picking lends itself to numerous kinds of error. To this end, we also developed an electromagnetic picking head that uses small disposable steel spheres that are dipped into the bacterial colony of interest and subsequently used for inoculation of liquid medium. This turned out to be efficient, cheap, and of practical usefulness. Industrial colony pickers, in contrast, either use more expensive disposable plastic tips or high-resistance wire tips that are sterilized between each pick by heating through current injection, leading to build-up of burnt material on the tip over time. The comprehensive analysis of each expressed library gives a good overview of a given mutagenesis step on the overall composition of the population over iterative rounds of diversification and screening and allows comparing multiple libraries assayed over weeks. Naturally, microbial expression systems, in spite of all advantages, have limitations in the range of proteins that can be expressed and engineered.

To give an example of what can be done with the platform, we took on an engineering project that aimed at improving brightness of a fluorescent protein variant. The parental protein we chose was the far-red-emitting mNeptune684 (Li et al., 2016). Over a number of documented and illustrated steps of mutagenesis and screening, we substantially improved the brightness of the protein by 4–5-fold, demonstrating the power of the screening platform for such an optimization task. At the same time, we also engineered the protein to improve monomeric

settings. The greatly enhanced performance of mCarmine in deeper tissue sections was evident. Notably also, auto-fluorescence in the mTFP1 channel generated by the skin and other structures was barely visible in the mCarmine channel (Figure S4).

Subcellular Protein Fusions Using mCarmine

The increase in brightness of mCarmine obtained by screening using our microbial expression system was maintained in mammalian cells, as verified by fluorescence-activated cell sorting (FACS) analysis (Figure S5). We subsequently tested the use of mCarmine as a molecular tag by generating a number of fusions with subcellular targeting motifs to either the N or C terminus of mCarmine. These fusions were finally examined in HeLa cells (Figure 5). Overall, they showed the expected localization when targeted to organelles and subcellular structures. These included targeting to the plasma membrane via fusion of an N-terminal targeting motif derived from GAP-43 (Figure 5A), to mitochondria (Figure 5B), mCarmine-α-tubulin fusions (Figure 5C), targeting to peroxisomes (Figure 5D), labeling of actin filaments via lifeact peptide fusion (Figure 5E), localization to the ER (Figure 5F), targeting to the nucleus via a nuclear localization sequence (Figure 5G), nuclear export (Figure 5H), or fusions of mCarmine to histone2B (Figure 5I). Performance of the sensitive visual OSER (organized smooth ER) assay (Constantini et al., 2012; Cranfill et al., 2016) for strictly monomeric state yielded a value of 56% of correctly appearing cells for mCarmine (Table S2).

state and to ensure favorable pKa and good expression properties. The final variant, mCarmine, has great usefulness for tissue labeling and subcellular targeting. In some applications in the far-red to near-infrared regime, it may rival bacterial phytochromes, whose fluorescence is dependent on the availability of co-factors.

Finally, the screening station developed here can be constructed with a small budget (overall costs ∼€1500 without camera), affordable for most laboratories. If required, it can be downgraded for simpler colony-picking tasks, such as blue-white screening of colonies in cloning projects. It can be easily adapted for further optimizing selected genetically encoded biosensors (Belal et al., 2014; Thestrup et al., 2014) (our unpublished data), switchable proteins (Brakemann et al., 2011), for optimizing photostability (Wiens et al., 2018), and for the improvement of many other proteins for which functional fluorescence readout is feasible. It could also accommodate high-end laser excitation light sources for two-photon optimization of fluorescent proteins and biosensors (Stoltzfus et al., 2017). Thus, we believe it provides valuable instrumentation for many protein engineering projects.

SIGNIFICANCE

Protein engineering involves screening large libraries of diversified variants, but often the instrumentation used is not matched to the task. We here developed a fluorescence-based platform for screening proteins that integrates image analysis and instructed robotic picking of bacterial colonies expressing variants with desirable properties. It allows tracking each individual colony in a population and collecting quantitative information on library composition during each individual step of the protein evolution process. We used it to engineer mCarmine, a far-red-emitting monomeric fluorescent protein with peak emission at 675 nm and substantial emission beyond 700 nm. Starting from a dim parental protein, we could boost brightness several fold, combining mutagenesis protocols and screening using the platform. As its fluorescence is not dependent on co-factors, mCarmine may rival bacterial phytochromes in protein fusions and tissue imaging applications in the far-red to near-infrared emission range. The low-cost platform described here can be used to expedite numerous protein engineering projects.

STAR★METHODS

Detailed methods are provided in the online version of this paper and include the following:

- KEY RESOURCES TABLE
- CONTACT FOR REAGENT AND RESOURCE SHARING
- EXPERIMENTAL MODEL AND SUBJECT DETAILS
  - Bacterial Strains
  - Cell line
  - Zebrafish
- METHOD DETAILS
  - Screening Platform: 3D Manipulator
  - Screening Platform: Picking Head
  - Screening Platform: Illumination and Image Acquisition
  - Screening Platform: Image Analysis
  - Screening Platform: Controls and Software
  - Protein Purification and Spectroscopy
  - Chromatography
  - Screening Vector and Error Prone PCR
  - Cassette Mutagenesis
  - Evolution of mNeptune684
  - Cell Lines and Tissue Culture
  - Flow Cytometry
  - OSER Assay
  - Imaging Larval Zebrafish
- QUANTIFICATION AND STATISTICAL ANALYSIS
- DATA AND SOFTWARE AVAILABILITY

SUPPLEMENTAL INFORMATION

Supplemental Information includes five figures, three tables, and one data file and can be found with this article online at https://doi.org/10.1016/j.chembiol.2018.08.008.

AUTHOR CONTRIBUTIONS

A.F. and D.N. built the station and performed programming for hardware control and image processing. A.F. performed mutagenesis of mNeptune684 and in vitro characterization of mCarmine. A.F., A.M.K., and R.P. performed in vivo characterization of mCarmine in fish. A.F. and M.E. performed FACS analysis and mammalian cell culture work. A.F., D.N., and O.G. conceived the study. All authors participated in writing the manuscript.

DECLARATION OF INTERESTS

The authors declare no competing financial interest.

SUPPORTING CITATION

The following reference appears in the Supplemental Information: Piatkevich et al., 2013.

REFERENCES

Ai, H.W., Henderson, J.N., Remington, S.J., and Campbell, R.E. (2006). Directed evolution of a monomeric, bright and photostable version of Clavularia cyan fluorescent protein: structural characterization and applications in fluorescence imaging. Biochem. J. 400, 531–540.

Asakawa, K., and Kawakami, K. (2008). Targeted gene expression by the Gal4-UAS system in zebrafish. Dev. Growth Differ. 50, 391–399.

Bajar, B.T., Lam, A.J., Badiee, R.K., Oh, Y.H., Chu, J., Zhou, X.X., Kim, N., Kim, B.B., Chung, M., Yablonovitch, A.L., et al. (2016). Fluorescent indicators for simultaneous reporting of all four cell cycle phases. Nat. Methods 13, 993–996.

Belal, A.S., Sell, B.R., Hoi, H., Davidson, M.W., and Campbell, R.E. (2014). Optimization of a genetically encoded biosensor for cyclin B1-cyclin dependent kinase 1. Mol. Biosyst. 10, 191–195.

CellPress

Brakemann, T., Stiel, A.C., Weber, G., Andresen, M., Testa, I., Grotjohann, T., Leutenegger, M., Plessmann, U., Urlaub, H., Eggeling, C., et al. (2011). A reversibly photoswitchable GFP-like protein with fluorescence excitation decoupled from switching. Nat. Biotechnol. *29*, 942–947.

Canny, J. (1986). A computational approach to edge detection. IEEE Trans. Pattern Anal. Mach. Intell. *8*, 679–698.

Castle, L.A., Siehl, D.L., Gorton, R., Patten, P.A., Chen, Y.H., Bertain, S., Cho, H.J., Duck, N., Wong, J., Liu, D., and Lassner, M.W. (2004). Discovery and directed evolution of a glyphosate tolerance gene. Science *304*, 1151–1154.

Chen, G., Hayhurst, A., Thomas, J.G., Harvey, B.R., Iverson, B.L., and Georgiou, G. (2001). Isolation of high-affinity ligand-binding proteins by periplasmic expression with cytometric screening (PECS). Nat. Biotechnol. *19*, 537–542.

Clavel, R. (1988). Delta, a fast robot with parallel geometry. Proceedings of the 18th International Symposium on Industrial Robots, Lausanne.

Constantini, L.M., Fossati, M., Fancolini, M., and Snapp, E.L. (2012). Assessing the tendency of fluorescent proteins to oligomerize under physiological conditions. Traffic *13*, 643–649.

Cranfill, P.J., Sell, B.R., Baird, M.A., Allen, J.R., Lavagnino, Z., de Gruiter, H.M., Kremers, G.J., Davidson, M.W., Ustione, A., and Piston, D.W. (2016). Quantitative assessment of fluorescent proteins. Nat. Methods *13*, 557–562.

Eilers, H.C., and Boelens, H.F.M. (2005). Baseline Correction with Asymmetric Least Squares Smoothing (Leiden University Medical Centre).

Goedhart, J., van Weeren, L., Hink, M.A., Vischer, N.O., Jalink, K., and Gadella, T.W., Jr. (2010). Bright cyan fluorescent protein variants identified by fluorescence lifetime screening. Nat. Methods *7*, 137–139.

Gross, L.A., Baird, G.S., Hoffman, R.C., Baldridge, K.K., and Tsien, R.Y. (2000). The structure of the chromophore within DsRed, a red fluorescent protein from coral. Proc. Natl. Acad. Sci. USA *97*, 11990–11995.

Halpern, M.E., Rhee, J., Goll, M.G., Akitake, C.M., Parsons, M., and Leach, S.D. (2008). Gal4/UAS transgenic tools and their application to zebrafish. Zebrafish *5*, 97–110.

Heim, R., and Tsien, R.Y. (1996). Engineering green fluorescent protein for improved brightness, longer wavelengths and fluorescence resonance energy transfer. Curr. Biol. *6*, 178–182.

Jäckel, C., Kast, P., and Hilvert, D. (2008). Protein design by directed evolution. Annu. Rev. Biophys. *37*, 153–173.

Jones, P., Watson, A., Davies, M., and Stubbings, S. (1992). Integration of image analysis and robotics into a fully automated colony picking and plate handling system. Nucleic Acids Res. *20*, 4599–4606.

Kimura, Y., Satou, C., and Higashijima, S. (2008). V2a and V2b neurons are generated by the final divisions of pair-producing progenitors in the zebrafish spinal cord. Development *135*, 3001–3005.

Kirshner, H., Aguet, F., Sage, D., and Unser, M. (2013). 3-D PSF fitting for fluorescence microscopy: implementation and localization application. J. Microsc. *249*, 13–25.

Li, Z., Cui, Z., Deng, J., Wang, D., and Zhang, X.E. (2016). Mutagenesis of mNeptune red-shifts emission spectrum to 681-685 nm. PLoS One *11*, e0148749.

Matela, G., Gao, P., Guigas, G., Eckert, A.F., Nienhaus, K., and Nienhaus, G.U. (2017). A far-red emitting fluorescent marker protein, mGarnet2, for microscopy and STED nanoscopy. Chem. Commun. (Camb.) *53*, 979–982.

Merlet, J.P. (2006). Parallel Robots, *Vol. 128* (Springer Science & Business Media).

Merzlyak, E., Goedhart, J., Shcherbo, D., Bulina, M.E., Shcheglov, A.S., Fradkov, A.F., Gaintzeva, A., Lukyanov, K.A., Lukyanov, S., Gadella, T.W., and Chudakov, D.M. (2007). Bright monomeric red fluorescent protein with an extended fluorescence lifetime. Nat. Methods *4*, 555–557.

Miyawaki, A., Nagai, T., and Mizuno, H. (2005). Engineering fluorescent proteins. Adv. Biochem. Eng. Biotechnol. *95*, u1–15.

Packer, M.S., and Liu, D.R. (2015). Methods for the directed evolution of proteins. Nat. Rev. Genet. *16*, 379–394.

Park, H.C., Kim, C.H., Bae, Y.K., Yeo, S.Y., Kim, S.H., Hong, S.K., Shin, J., Yoo, K.W., Hibi, M., Hirano, T., et al. (2000). Analysis of upstream elements in the HuC promoter leads to the establishment of transgenic zebrafish with fluorescent neurons. Dev. Biol. *227*, 279–293.

Piatkevich, K.D., Malashkevich, V.N., Kateryna, V., Morozova, S., Nemkovich, N.A., Almo, S.C., and Verkhusha, V.V. (2013). Extended stokes shift in fluorescent proteins: chromophore–protein interactions in a near-infrared TagRFP675 variant. Sci. Rep. *13*, 1847.

Reidhaar-Olson, J.F., and Sauer, R.T. (1988). Combinatorial cassette mutagenesis as a probe of the informational content of protein sequences. Science *241*, 53–57.

Rodriguez, E.A., Campbell, R.E., Lin, J.Y., Lin, M.Z., Miyawaki, A., Palmer, A.E., Shu, X., Zhang, J., and Tsien, R.Y. (2017). The growing and glowing toolbox of fluorescent and photoactive proteins. Trends Biochem. Sci. *42*, 111–129.

Sage, D., Donati, L., Soulez, F., Fortun, D., Schmit, G., Seitz, A., Guiet, R., Vonesch, C., and Unser, M. (2017). DeconvolutionLab2: an open-source software for deconvolution microscopy. Methods *115*, 28–41.

Scholz, J., Besir, H., Strasser, C., and Suppmann, S. (2013). A new method to customize protein expression vectors for fast, efficient and background free parallel cloning. BMC Biotechnol. *13*, 12.

Shcherbakova, D., Baloban, M., and Verkhusha, V. (2015). Near-infrared fluorescent proteins engineered from bacterial phytochromes. Curr. Opin. Chem. Biol. *27*, 52–63.

Stoltzfus, C., Mikhailov, A., Rebane, A. (2017). Optimizing ultrafast wide field-of-view illumination for high throughput multi-photon imaging and screening of mutant fluorescent proteins. Proc. SPIE 10069, Multiphoton Microscopy in the Biomedical Sciences XVII, 1006924. https://doi.org/10.1117/12.2250048.

Thestrup, T., Litzlbauer, J., Bartholomäus, I., Mues, M., Russo, L., Dana, H., Kovalchuk, Y., Liang, Y., Kalamakis, G., Laukat, Y., et al. (2014). Optimized ratiometric calcium sensors for functional in vivo imaging of neurons and T lymphocytes. Nat. Methods *11*, 175–182.

Tromberg, B.J., Shah, N., Lanning, R., Cerussi, A., Espinoza, J., Pham, T., Svaasand, L., and Butler, J. (2000). Non-invasive in vivo characterization of breast tumors using photon migration spectroscopy. Neoplasia *2*, 26–40.

Van der Walt, S., Schönberger, J.L., Nunez-Iglesias, J., Boulogne, F., Warner, J.D., Yager, N., Gouillart, E., and Yu, T.; scikit-image contributors (2014). scikit-image: image processing in Python. PeerJ *2*, e453.

Wiens, M.D., Hoffmann, F., Chen, Y., and Campbell, R.E. (2018). Enhancing fluorescent protein photostability through robot-assisted photobleaching. Integr. Biol. https://doi.org/10.1039/c8ib00063h.

Zhang, Y., Werling, U., and Edelmann, W. (2012). SLiCE: a novel bacterial cell extract-based DNA cloning method. Nucleic Acids Res. *40*, e55.

CellPress

STAR★METHODS

KEY RESOURCES TABLE

REAGENT or RESOURCE	SOURCE	IDENTIFIER
Bacterial and Virus Strains		
E. coli XL1 blue *recA1 endA1 gyrA96 thi-1 hsdR17 supE44 relA1 lac* [F′ *proAB lacIqZΔM15* Tn*10* (Tetr)]	Invitrogen	Cat#200249
E. coli Bl21 (DE3) gold *E. coli* B F– *ompT hsdS*(rB– mB–) *dcm*+ Tetr *gal* λ(DE3) *endA* Hte	Invitrogen	Cat#230132
E. coli PPY F– *end*A1 *rec*A1 *gal*E15 *gal*K16 *nup*G *rps*LΔ*lac*X74 Φ*80lac*ZΔM15 *ara*D139Δ(*ara,leu*)7697 *mcr*A Δ(*mrr-hsd*RMS-*mcr*BC) *cyn*X::[*ara*C pBAD- *red*α EM7- *red*β Tn5-*gam*]λ–	Zhang et al., 2012	N/A
Chemicals, Peptides, and Recombinant Proteins		
NcoI-HF®	New England Biolabs	Cat#R3193S
DpnI	New England Biolabs	Cat#R0176L
PvuI	New England Biolabs	Cat#R0150S
EcoRV-HF®	New England Biolabs	Cat#R3195L
T4 DNA Ligase Reaction Buffer	New England Biolabs	Cat#B0202S
Herculase II Fusion DNA Polymerase	Agilent Technologies	Cat#600679
GeneMorph II Random Mutagenesis Kit	Agilent Technologies	Cat#200550
Phenylmethanesulfonyl fluoride	Sigma Aldrich	Cat#P7626
Pepstatin A	Sigma Aldrich	Cat#P5318
Leupeptin	Sigma Aldrich	Cat#L0649
G418 disulfat salt	Sigma Aldrich	Cat#A1720
Lipofectamine 3000 transfection reagent	Invitrogen	Cat#L3000015
Penicillin-Strepomycin-Glutamine (100X)	Thermo Fisher	Cat#10378016
DMEM, high glucose, pyruvate, no glutamine	Thermo Fisher	Cat#21969035
Fetal Bovine Serum, qualified, heat inactivated, E.U.-approved, South America Origin	Thermo Fisher	Cat#10500064
Opti-MEM I Reduced Serum Medium, no phenol red	Thermo Fisher	Cat#11058021
Hoechst 33342 Solution	Thermo Fisher	Cat#62249
Experimental Models: Cell Lines		
HELA Gender: female	DSMZ GmbH	Cat#ACC 57
Experimental Models: Organisms/Strains		
Danio rerio TL strain with mitfa-/- knockout (Nacre) HuC:Gal4	Kimura et al., 2008	N/A
UAS:mTFP1-mCarmine	This work	N/A
Oligonucleotides		
Primers See Table S3	This work	N/A
mNeptune684 de novo synthesis	This work	N/A
Recombinant DNA		
pRSET-B	Thermo Fisher Scientific (Invitrogen)	Cat#V35120
pcDNA3	Invitrogen	N/A
mTFP1-pBAD	Addgene	Cat#54553
UAs:mTFP1-mCarmine	This work	N/A
mCarmine	This work	https://www.ncbi.nlm.nih.gov/nuccore/MH062789

CellPress

Continued		
REAGENT or RESOURCE	SOURCE	IDENTIFIER
mCarmine in pRSETB	This work	https://www.addgene.org/109484/
mCarmine in pcDNA3	This work	https://www.addgene.org/109486/
Software and Algorithms		
Marlin firmware (adapted)	http://marlinfw.org/	https://github.com/GriesbeckLab
Colony picker operation software	This work	https://github.com/GriesbeckLab
Colony analysis software	This work	https://github.com/GriesbeckLab
Other		
LUXEON Rebel Royal Blue	Philips	Part#LXML-PR01
LUXEON Rebel Blue	Philips	Part#LXML-PB01
LUXEON Rebel Cyan	Philips	Part#LXML-PE01
LUXEON Rebel Green	Philips	Part#LXML-PM01
LUXEON Rebel Amber	Philips	Part#LXML-PL01
LUXEON Rebel Deep Red	Philips	Part#LXM3-PD01
LUXEON Neutral White	Philips	Part#LXML-PWN1
Star Board Luxeon Rebel	LED-tech.de	Cat#LT-1103
Carclo 20 mm Collimating lense	LED-tech.de	Cat#LT-0770
Carclo lense holder for Rebel	LED-tech.de	Cat#LT-1158
LT3080ET#PBF	Farnell	Cat#2102611
capacitor 1 100nF	Farnell	Cat#2112751
capacitor 2 1uF	Farnell	Cat#2112910
R1 0.1 ohms	Farnell	Cat#2330244
R2 7k ohms	Farnell	Cat#1128743
reed relais	Farnell	Cat#1079435
Hall effect sensor	Farnell	Cat#9783806
A4988 Stepper Motor Driver Carrier	Pololu	Cat#1182
Nema 17 Stepper Motor	Gunda Automation GmbH	Cat#SM17H1.3O0L
Sanguinololu 1.3b	Joem	https://reprap.org/wiki/Sanguinololu

CONTACT FOR REAGENT AND RESOURCE SHARING

Further information and requests for resources and reagents should be directed to and will be fulfilled by the Lead Contact Oliver Griesbeck (griesbeck@neuro.mpg.de).

EXPERIMENTAL MODEL AND SUBJECT DETAILS

Bacterial Strains
Bacterial strains E. coli XL1Blue1 (for screening) (Stratagene) and E.coli BL21 (DE) (for protein purification) (Invitrogen) were grown over night at 37°C in 50 mL auto-inductive LB (LB supplemented with 0.05% D-(+)- glucose (w/v), 0.2% lactose (w/v), 0.6% glycerol (v/v).

Cell line
Hela cells (Human, female) were cultured in Dulbecco's Modified Eagle Medium supplemented with 10% fetal bovine serum.

Zebrafish
All zebrafish procedures were approved by the Regierung von Oberbayern via the TVA 55-2-1-54-2532-82-2016.

METHOD DETAILS

Screening Platform: 3D Manipulator
The colony picking unit of the integrated screening system had to be rapid, precise and accurate to be able to pick individual colonies, selected from analyzed image files. It also had to be flexible to allow for multiple configurations, e.g. inoculating liquid media or re-plating on solid media. It was built to execute all essential functions of a colony picker as commonly used in cloning and genomics, e.g

re-plating, or colony picking according to blue-white selection schemes. With these criteria in mind, the choice for the 3D manipulator fell on a delta robot design. The delta robot is a type of parallel robot and was envisioned by Clavel (1988) for pick and place applications. It has three degrees of freedom in translation and allows for rapid movements. Recently, delta robot designs have become very popular in the 3D printing community for the use in fused deposition modeling printers (FDM). Because FDM printers have similar requirements as the envisioned picking system (3D manipulator with high resolution, precision and speed), its design was adapted from an existing open source 3D printer design. Specifically, a 3D printer developed by Johann Rocholl in 2012, the "Rostock", was used as the base for a colony picking system (http://reprap.org/wiki/Rostock).

The colony picking system consisted of a triangular platform, harboring the pick head, which was held in place by three pairs of parallel arms made of light-weight carbon fiber tubes. The parallel arms in turn were mounted to three carriages, which were seated on vertical linear motion systems. The arms were connected with the platform and the carriages via custom built, magnetic, universal ball-joints, to ensure smooth motion in all directions with minimum tolerances. The linear motion systems, consisted of three pairs of 600 mm hardened steel rods fitted with linear bearings. They were positioned at $120°$ intervals on the edge of a circle with a radius of 210 mm, encompassing a cylindrical volume. The carriages seated with linear bearings on these rails were driven vertically by geared belts through the action of three NEMA 17 stepper motors (GUNDA, Germany), mounted at the base of each individual column. Because of the fixed length of the arms and their parallel configuration, vertical movement of the three carriages could be converted into 3 degrees of translation movement of the platform harboring the pick head. This manipulator set-up allowed three-dimensional movement of the pick head within a cylindrical volume with a radius of 210 mm and a height of 200 mm, with a resolution of 0.05 mm in X/Y/Z.

Screening Platform: Picking Head

For the picking-head, several important aspects had to be addressed. To avoid cross-contamination, tips had to be sterilized in between colonies in a fast manner. Colonies had to be picked from agar plates with varying heights and from blotting paper, rendering hard coding of height coordinates impractical. Furthermore, it was desirable to be able to inoculate small liquid cultures in deep multi-well plates and to re-streak clones onto selective agar plates.

In order to address these issues, we designed a unique picking head. Usually picking tips are sterilized either by heat or by dipping them into sterilization solutions. This procedure is speed limiting and causes build-up of burnt material residues over time. Therefore, we opted for a disposable tip, which is brought into contact with the bacterial colony, used for inoculation and then discarded. Steel spheres (Schulz Stanztechnik GmbH, Germany) were used, each with a diameter of 2 mm and which were kept as reservoir in 96 well-plates with V-bottoms. To ensure that only a single sphere is picked up by the electromagnet single spheres were pre-sorted into individual wells of the 96-well plate. The picking head itself consisted of a steel rod resting inside a copper coil. When put charged, the coil induced a magnetic field inside the steel rod, lifting it vertically by around 5 mm. The magnetized rod then was used to lift the steel spheres and transport them inside the volume of the 3D manipulator. When the electromagnet was turned off, the rod would drop into its initial position, ejecting the steel sphere downward in the process. This simple system allowed the quick picking-up of sterilized steel spheres from a 96-well plate, dipping them into a colony and finally transferring the sphere into a deep-well plate, inoculating liquid medium. For each colony, a fresh sterilized steel sphere was used, avoiding cross-contamination.

Because of the varying heights of surfaces which were picked from, a responsive system was built to detect when the steel sphere touched the surface of the colonies. For detection, an electrode was connected to the agar plate. The other side of the detection circuit was connected to the steel rod. For picking, a fresh steel sphere was picked up, positioned over a colony, and then continuously lowered towards the agar plate. As soon as the sphere touched the agar plate, the circuit was closed, triggering the halt of the pick head. This same system was used to verify a steel sphere had been successfully picked up correctly. This was achieved by first picking up a steel sphere and then lowering it over a test-electrode with a fixed height. The detection circuit could only be triggered if a sphere was present, if no sphere was detected, the pick head would return and try to pick up another sphere. To prevent the steel rod from triggering the detection circuit accidently, its end was isolated using a silicone sleeve.

The standard picking routine was as follows: A fresh sphere was picked up by the pick head and then transferred to the testing electrode, to test whether a sphere was present. If no sphere was detected the head was sent to pick up another sphere. Successful sphere detection would cause the pick head to move above the selected colony. Then the head was lowered until the detection circuit was triggered, bringing the sphere in contact with bacterial material. The head was then lifted and moved above well of a 96-deep-well plate filled with selective liquid medium. For inoculation, the electromagnet was turned off, depositing the sphere into the well. The inoculation rate was 99.5%. If colonies were re-plated, the head was moved above a selective agar plate and lowered until the detection circuit was triggered. Then the head moved in a square pattern to streak out the bacteria. These squares were placed in a grid to allow easy identification. After plating, the steel sphere was moved over a beaker glass filled with sterilization solution and discarded.

Screening Platform: Illumination and Image Acquisition

Bright single color and rapidly switching LEDs (Luxeon® Rebel, Phillips) were used as a light source. They were fitted with collimation lens assemblies and placed at the end of a 100 mm steel tubes. To define the excitation bandwidth, 25 mm bandpass filters (Chroma) were fitted into the other end of the steel tubes and held in place by set-screws. The combinations of LEDs and bandpass filters initially put in place were: Luxeon® Rebel royal blue + 440/20; Luxeon® Rebel blue + 472/30; Luxeon® Rebel cyan + 500/20; Luxeon® Rebel green + 535/25; Luxeon® Rebel amber + 575/50; Luxeon® Rebel deep red + 620/60. The tubes were then fixed

to the roof of the screening set-up and pointed towards the plate area. The assembly focused homogenous light towards the plate, whilst reducing scattering in other directions. Their emission spectrum could be adjusted by using different bandpass filters. To increase the flexibility of the automated screening set-up, it was of use to be able to detect non-fluorescent colonies on agar plates. To achieve that, the plate area was fitted with a translucent, opaque bottom and lit with a white LED array (Luxeon® Rebel cool white, Phillips, Germany) from underneath. With this bottom illumination, colonies could be identified as dark silhouettes against a white background.

For imaging a CoolSNAP–HQ (Visitron Systems, Germany) CCD camera was used. In order to capture as much light as possible and to maximize the plate area on the camera sensor, the camera was fitted with a 50 mm manual zoom lens (NavitarZoom 7000E). This non-standard arrangement required a custom built filter-wheel which was placed in front of the zoom lens. The filter wheel contained seven 50 mm long pass or bandpass filters (485/20 nm, 505LP nm, 535/40 nm, 570/30 nm, 600/20 nm, 630/30nm, 712/30 nm) and was housed in a hexagonal box made from black acrylic. The wheel was turned by a NEMA 17 stepper motor (GUNDA, Germany) and fitted with a 5 mm cube neodymium magnet. This magnet could be detected by a Hall-effect sensor in the housing and served as fixed homing point for the filter wheel. The measured illumination density on plate was 23.0 μW/cm^2 for the mTFP1 (LED 472/30 nm) channels and 16.2 μW/cm^2 for the mCarmine channel (LED 620/60nm). When screening for mCarmine, exposure times were 300 ms for the mTFP1 reference protein and 6 s for the mCarmine channel.

Screening Platform: Image Analysis

The image processing software implemented contained several features for rapid analysis and extraction of relevant information. It is custom written in Python 2.7 and uses in many aspects the scikit-image library (Van der Walt et al., 2014)

Reference Channel

For all image processing an aligned reference channel was used. The reference channel was a channel in which all colonies were visible. This could be the bottom white light illumination image which visualized all colonies, or, in case of mNeptune684 optimization, it was the channel to detect the fused reference fluorescent protein mTFP1. *E. coli* auto-fluorescence could also be used for this purpose (e.g. excitation at 440/20 nm, emission 535/40 nm).

Plate Detection

To eliminate the influence of objects outside of the plate area (dust particles, plate rim etc.) and to reduce processing time (as only a fraction of the total image is processed), the plate was automatically detected and the none-plate area masked out (set to zero).The reference channel (mTFP1; 505/5 nm) was first converted from 12 to 8 bit. Canny edge detection (Canny, 1986) was applied with empirical values for sigma of Gaussian blur filter and high and low threshold for hysteresis (scikit-image implementation). Contour images were then fitted with circles in size range of the bacterial plates or filter papers used. Accordingly, the best fit defined center position and plate radius. For masking out-of-plate areas two masks were created from plate position and plate radius: an outer mask that included plate rim and an inner mask that excluded the plate rim and rim area. First the outer mask was applied to all measurement channels, the inner mask was applied after background correction to eliminate rim artefacts.

Bacterial Colony Detection

Colonies were detected in the reference channel by template matching based on normalized cross-correlation, and a labeled colony mask was created for measurements in all channels. We used a 2D Gaussian (17x17 px) as a template, as this approximates the typical shape of a colony. We determined individual colony coordinates by computing peaks of local maxima with a correlation cut-off of 0.65. We created a binary mask that we dilated four times to increase measurement area. This colony area mask is subsequently used for measurements in all channels.

Background Correction

Background correction is a computationally costly step and the limiting factor for online image processing and therefore required a lot of optimization. The background in each picture was calculated on a horizontal line-by-line basis using iterative reweighted asymmetric least square smoothing (Eilers and Boelens, 2005). Since the background fluorescence of agar plates and blotting paper is relatively homogeneous with only gradual changes and the imaging set-up allows for relatively high resolution (76 μm/px), this calculation could be significantly sped up by performing it only for every 9th horizontal line, linearly interpolating all in-between lines. Furthermore, to improve accuracy and speed, all zero values were first stripped of both ends of each line, removing non-plate area form the background calculations, and afterwards re-added. Background images were created for each individual picture for each channel and then subtracted from the original picture. Finally, the inner mask from the aforementioned plate detection algorithm was applied, to remove rim artifacts.

Measurements and Noise Level Correction

A labeled colony mask was used to measure colony intensity in every relevant background-corrected channel. Median colony intensity within the colony area was determined. Because the main estimator of variant performance was a ratio of channel intensities, it was susceptible to small values introduced by noise on low expressing variants, as these ratios can get arbitrarily high when dominated by noise. The noise level was calculated by median + MAD (median absolute deviation) of all non-zero plate pixels (this approximation assumes that the area in each plate covered by colonies is much smaller than the total plate area, this assumption does not hold true for very densely populated plates >1500 colonies). The noise level was subsequently subtracted from the median colony intensity. For each individual colony the plate number, location (x, y coordinates) and intensity of each channel with and without noise and the ratio between channels was saved.

Screening Platform: Controls and Software

All mechanical components of the screening set-up (3D manipulator, pick head, filter wheel) and the LEDS were controlled by a Sanguinololu 1.3b microcontroller board. This controller board is Arduino based and was developed by the 3D printing community for the use in 3D printers and CNC machines. The firmware used, was Marlin 1.0.0.0. The board was connected via USB to the screening computer and operated through G-Code, a low-level programming language for machine tools. The Sanguinololu was fitted with 4 Polulu stepper driver boards (website: Reprap.me) to control the four NEMA 17 stepper motors (GUNDA, Germany) (three for the 3D manipulator, one for the filter wheel). The LEDs and the plate detection circuit were controlled using digital pins, provided by the board. The board was powered using a 15 V DC power supply.

On the software side, the screening set-up was controlled by a Python program. This program provided high-level functions (e.g. pick next colony, take picture etc.) and translated these functions into G-Code to communicate with the microcontroller board. The camera was controlled through the python application programming interface (API) of μManager, version 1.4.15, which also offered high-level camera control functions.

Protein Purification and Spectroscopy

His-tagged proteins were expressed in *E.coli* BL21 (DE) (Invitrogen) over night at 37°C in 50 mL auto-inductive LB (LB supplemented with 0.05% D-(+)- glucose (w/v), 0.2% lactose (w/v), 0.6% glycerol (v/v). Cells were harvested by centrifugation (4°C, 10 min, 6000 x g) and re-suspended in 10 mL Resuspension buffer (20 mM Na_2PO_4, 300 mM NaCl, 20 mM imidazole, Sigma Aldrich, Germany) supplemented with protease inhibitors (4 mM PMSF, 20 μg/mL Pepstatin A, 4 μg/mL Leupeptin, Sigma Aldrich, Germany) and 5 μg/mL DNase and 10 μg/mL RNAse (Sigma Aldrich, Germany). Cells were first lysed physically, through 3 freeze thaw cycles, then enzymatically, by adding 1 mg of lysozyme (Sigma Aldrich, Germany) and incubating for 1 h at 37°C. Finally, the cell suspension was supplemented with 0.4 % Triton-X-100 (v/v) and sheered in an ultrasonic water bath (ONOREX SUPER RK 510, Bandelin, Germany) at 4°C for 1 h. Insoluble components were pelleted through centrifugation (4°C, 30 min at 20000 x g). For purification, the supernatant was incubated with 150 μL 6% (v/v) Nickel-IDA agarose bead suspension (Jena Bioscience, Germany) over night at 4°C under light agitation. Agarose beads were collected in 1 mL propylene gravity flow columns (Qiagen, Germany) and washed with 10 mL wash buffer (20 mM Na_2PO_4, 300 mM NaCl, 55 mM imidazole, Sigma Aldrich, Germany). Finally, purified protein was eluted in 600 μL elution buffer (20 mM Na_2PO_4, 300 mM NaCl, 300 mM imidazole, Sigma Aldrich, Germany).

Spectroscopic measurements were acquired with 1/10 diluted protein solutions in protein buffer (25 mM TRIS-HCl, 200 mM NaCl, pH 7.5). Absorption spectra were acquired using a Varian Cary 100 Scan spectrophotometer (Agilent, Germany). Fluorescence spectra were acquired using a Varian Cary Eclipse fluorescent spectrophotometer (Agilent, Germany) or an Infinite M200 PRO plate reader (Tecan, Germany).

Molar extinction coefficients for mTFP1-mNeptune684 fusion proteins were determined ratio-metrically directly from the absorption spectrum, assuming an extinction coefficient of 64000 $M^{-1}cm^{-1}$ for mTFP1 at 462 nm (Ai et al., 2006). For single fluorescent proteins the molar extinction coefficient was determined through the absorption of the denatured chromophore at 452 nm (extinction coefficient 44000 $M^{-1}cm^{-1}$) (Gross et al., 2000). Proteins were denatured using 0.5 M NaOH.

The quantum yield of new variants was determined relative to mNeptune 684 by using the slope method. First, the absorption and emission spectra of three serial 1:2 dilutions were acquired in the same cuvette. Then, the integrated emission spectrum was plotted against the maximum absorption and the slope was determined. For mNeptune684 a quantum yield of 0.03 was assumed (Li et al., 2016).

Chromatography

Size exclusion chromatography was performed on an Äkta basic (GE Healthcare Life Science, USA) chromatography system using a Superdex PC 3.2/30 column (GE Healthcare Life Science, USA) with a flow rate of 0.1 mL/min. The sample volume was 50 μL with a protein concentration of 40 μM (2 nmol protein). PBS was used as the mobile phase in the chromatography.

Screening Vector and Error Prone PCR

For screening libraries generated through error prone PCR a screening vector with counter-selection was used to reduce background. The screening vector contained the gene for the reference protein mTFP1 and a C-terminal linker sequence (7 amino acid TEV protease site) under the control of the T7 inducible promotor. In place of the future insert was the counter selection gene sacB under the control of the lpp5 promotor, flanked by EcoRV sites. The sacB gene encodes the lavansucrase of *B.subtilis* which is toxic in media containing sucrose (Scholz et al., 2013).

Error prone PCR mutagenesis was performed using the GeneMorph II Random mutagenesis kit (Agilent, Germany) with primers introducing 20 base pair overhangs homologous to the screening vector. The mutated insert DNA was cloned with SLiCE cloning (Zhang et al., 2012) into EcoRV linearized screening vector. Libraries were then transformed into chemically competent *E. coli* XL1 blue (Invitrogen) and plated onto YTS agar plates (Yeast extract 5 g/L tryptone 10 g/L D-(+)-saccharose 100 g/L agar-agar 10 g/L, 100 μg/ml ampicillin)

Cassette Mutagenesis

Cassette mutagenesis (Reidhaar-Olson and Sauer, 1988) was performed by amplifying the full parental vector encoding a mTFP1-mNeptune684 fusion protein through PCR with primers binding adjacent to the region of interest. One of these primers

had a degenerated overhang, introducing random codons and a 3' 20 base pair homology towards the downstream side of the region of interest. The amplified vector DNA was then circularized using SLiCE cloning and transformed into chemically competent *E.coli* XL1 blue cells and plated on selective agar plates.

Evolution of mNeptune684

As a first strategy to improve the brightness and expression of mNeptune684 we applied error prone PCR mutagenesis. The brightest clones picked from this library were dominated by mutations of the residue R126 (to either I, S or T), which reverted the former monomeric protein to a dimer (/tetramer), by removing a positive charge that was introduced to break the A/C interface into TagRFP, a precursor of mNeptune684 (Merzlyak et al., 2007). In fact, only one clone (mNeptune 684 H162Y P163T) picked from this first library did not display this type of mutation. This variant displayed a much-improved expression at 37°C and was slightly brighter. mNeptune 684 H162Y P163T was used as the parental base for the next round of error prone PCR, which was similarly dominated by the mutation of R126 (to I, S, T and G). We concluded that the dimerization improved the brightness through stabilization of the protein, and performed much better than any other possible single point mutation and therefore dominated the brightest variants. To not confound oligomerization into future constructs, we devised two mitigation strategies. First, we screened specific region of interests via cassette mutagenesis, which avoids the possibility of mutations in position 126 entirely. For a second strategy we introduced two further positive residues on the other side of the A/C interface (region 107-109, TAT), which means 3 residues have to be mutated in order to allow dimerization, which is very unlikely. This was achieved by cassette mutagenesis, introducing three biased codons (MRNGYNMRN) having a 50% chance for a positively charged residue in position 107 and 109 and either alanine or valine in position 108. The best performing clone from this library displayed the substitutions T107K A108V and T109K, similarly to mTFP1 in the same region. This variant in turn was slightly brighter and was used as the parental construct for further optimization.

Cassette mutagenesis was performed initially in two regions of interest 144-149 and 159-163. The rational for region 144-149 was, that it directly covers the chromophore and therefore had several chromophore interacting residues. It was mutated using the degenerated library NNBNNBNNBAACNNBNNB starting from position 144.The library deliberately kept the residue N147 in place, as it was one of the main residues introducing the red shift into mNeptune684. Screening this library proved not fruitful, as most clones (>100000 screened) were non-fluorescent. Because with a 5-amino acid library only about 2.5 % of all possibilities could be covered with the typical screening scale, we concluded that several critical interdependent residues lay within this stretch and therefore most observed variants were non-fluorescent.

In parallel, we screened region 159-164, which seemed interesting because the variant arising from the first error prone PCR round mNeptune684 H162Y P163T had mutations there. Furthermore, alignments of far red fluorescent proteins showed a high variance of possible amino acids in this region. We addressed this region with a 4 amino acid library (NNBGGCNNBNNBNNB) keeping the glycine in position 160 constant as it was conserved in all far red fluorescent proteins. This library led to several interesting insights. Specifically residue 162 seemed to be very important. Variants with an asparagine in this position displayed similar spectral characteristics to mNeptune684. If residue 162 was mutated to serine, the absorption and emission spectrum were blue shifted (to 555 nm and 600 nm respectively) mimicking mRuby. If mutated to a cysteine only the emission spectrum was blue shifted (towards 650 nm) mimicking the spectral characteristics of mNeptune. Several variants were more than twice as bright as the original mNeptune684. Taking these results into account, we reduced the size of the library to 3 amino acids (using NNBGGCNNBAAYNNB), keeping N162 constant to avoid blue shifting. This approach had the advantage that significantly higher percentage of all possibilities could be covered in the scope of a typical screening volume (17 % of a 4-amino acid library and 75 % with a 3-amino acid library covered by 50000 clones).

This shrunken library was screened on the variant mNeptune684 T197K A108V T109K. Interestingly many resulting variants were picked multiple times in different codon variations, demonstrating the robustness of the screening procedure. Most of the brightest variants had an isoleucine in position 161 and in position 163, with position 159 being relatively flexible. The best variants were 2.5 x brighter than mNeptune684 (6A1, mNeptune684 T107K A108V T109K R159T H161I P163I)

Following the rational of regions with high variance in the alignment of far red fluorescent proteins a third region was selected (region 175-178), which is the adjacent beta sheet to region 159-163. Screening a 4-amino acid library (NNBNNBNNBNNB) on the variant mNeptune684 T107K A108V T109K H161Y P163T let to the variant 8A1 (mNeptune684 T107K A108V T109K H161Y P163T I175Q C176T N177F), which was 3.4x brighter than mNeptune684. Next, we tried to combine the results from both of these regions by applying the 3 amino acid library for region 159-163 on variant 8A1 and similarly the 4 amino acid library of region 175-178 on variant 6A1. Both screenings did not yield brighter variants. In fact, both optimizations seemed to be incompatible with one another.

We then performed another round error prone PCR mutagenesis. As predicted, no mutation of residue R126 was observed within all picked variants. Interestingly, all picked variants had one of four possible mutations: C65S, N75K T77P and I125V all of which have occurred either in mMaroon1 or in mGarnet2 before. Some variants carried one of these 4 mutations and one or more other mutations. Most double mutations proved to be worse than the related single variant. Out of these 4 mutations C65S proved to be the brightest and was late incorporated into mCarmine.

Structurally, these sets of mutations were very interesting. While C65 and I125 were relatively far apart in the sequence, they pointed directly at each other within the beta barrel. N75, T77 and G79 formed a second cluster of very close mutations, all situated on a loop following the central alpha helix. We screened opposing residues 65 and residue 125 in unison with a small library consisting

CellPress

of only 2 variable amino acids, testing all combinations. However, no further improvements were detected using this approach. Combining all 4 beneficial mutations (C65S, N75K, T77P and I125V) from the error prone screening did not improve its brightness, but lead to a variant that was more resistant to denaturation with sodium hydroxide, which could indicate an overall improved stability.

During the first round of error-prone mutagenesis the mutation P163T arose, which lead to a 6 – 8 nm blue shift compared to mNeptune684. Yang et.al extensively characterized various mutations in this position and their effect on the maximum emission (ref mNeptune684 paper). After finalizing mCarmine we sought to red-shift its emission maximum by reintroducing various amino acids in this position (A, C, G, N, W, P), which were described as red-shifting. This residue seemed to be very critical for various adverse characteristics of mNeptune684. All of these mutations reduced the expression of the resulting protein, with T163G, T163W and T163P not expressing at all. Of the remaining 3 variants T163A had the largest red-shift (Em_{max} at 681 nm) and best expression. This came at the cost of a 40% reduced brightness and a shift of the pKa to 6.3.

Cell Lines and Tissue Culture

All cell lines were derivatives of HeLa and were grown in high glucose Dulbecco's Modified Eagle Medium with high glucose, pyruvate (Gibco) supplemented with 10% fetal bovine serum (FBS), 29.2 mg/ml of L-glutamine, 10,000 units of penicillin and 10,000 μg streptomycin at 37°C with 5% CO2. Imaging experiments were carried out in Opti-MEM Reduced Serum Medium, no phenol red (Gibco). The plasmid constructs used for stable cell line generation were linearized with PvuI restriction enzyme (NEB) before transfection and 2 μg linearized plasmid was used per transfection. G418 selection for stable cell line generation was carried out at a concentration of 600 μg/mL for 10 days. For subcellular labelling, transient transfections were performed in 3 cm diameter dishes with 2 μg circular plasmid per transfection, and for OSER assay, transient transfections were performed in 6 cm diameter dishes with 3 μg circular plasmid per transfection. Hoechst staining was performed immediately before imaging with 1 μg/mL for 20 minutes. Fluorescence microscopy was performed 20 h post transfection using a Leica SP8.

Flow Cytometry

Cells were collected from 10 cm dishes and diluted in 1 mL PBS inside Falcon test tubes with cell strainer snap cap (Corning). 50,000 – 100,000 events were acquired using a BD FACSAria III cytometer and data were processed using FlowJo (FlowJo, LLC). Events were gated by forward and side scatter in parallel to exclusion of the doublet cells, and median fluorescence values were then calculated. The FITC channel (488-530/30) was used to measure mTFP1 fluorescence, and APC channel (633-660/20) was used to measure mCarmine or mNeptune fluorescence.

OSER Assay

For each construct (CytERM-mCarmine, CytERM-mCardinal, CytERM-Cherry) a 3 mm² area of transfected HeLa cells was automatically imaged using a 63x water immersion objective (272 individual frames, automatically stitched). Cells were identified by nuclear stain using image processing in ImageJ (automatic thresh holding: Triangle, 4x binary erosion, 4x binary dilation, particle analyzer) and saved as individual 200 px x 200 px images, containing an individual cell in the center. Images from all three groups were randomized into a single database and presented to 3 people for manual classification (positive control: mCherry, negative control, mCardinal, test group: mCarmine). This ensured that the person performing classification did not know which protein was currently presented and therefor eliminated potential bias.

Imaging Larval Zebrafish

Zebrafish (*D. rerio*) Tüpfel-Longfin (TL) fish (female or male) carrying the *mitfa-/-* knockout mutation were incrossed and eggs were injected at the 1-cell-stage with tol2 mRNA (17.5 ng/μl) and DNA (25 ng/μl). We cloned mTFP1-mCarmine downstream to a UAS cassette using standard methods and injected the resulting construct (UAS:mTFP1-mCarmine) in fish carrying the HuC:Gal4 transgene to drive expression pan-neuronally (Kimura et al., 2008). Injected embryos were selected at one day post fertilization (1 dpf) for positive mTFP1 fluorescence. Fish were kept throughout at 28°C at a 14/10 h light cycle using standard protocols.

At 6-7 dpf, transient positive fish were embedded in 1.5% low melting point agarose, anesthetized and imaged *in vivo* using a Leica SP8 and 20x high-NA water immersion objective. We excited mTFP1 and mCarmine with a 442 and a 633 nm laser, respectively. To compare mTFP1 and mCarmine quantitatively, we determined a performance index (PI) in a deconvolved z-stack (Richardson-Lucy algorithm with a theoretical PSF for mTFP1 and mCarmine) (Kirshner et al., 2013; Sage et al., 2017) that covers the IPN (around 240 ± 28 μm deep) with re-adjusted laser settings. The PI shows the relation of signal (the higher the fluorescence, the better) to brightness (the brighter the fluorophore, the easier it is to emit photons and thus, cause fluorescence) and laser power (the less laser power is needed to emit photons, the better). Thus, the following equation describes the PI with $\overline{F}$ being the mean fluorescence in a given frame, b the brightness of the fluorophore (54.0 and 6.0 for mTFP1 and mCarmine, respectively) and β the laser power used in that frame (ranging from 0 to 1). The PI was normalized to the mean PI of mTFP1.

$$PI = \frac{\overline{F}}{b \cdot \beta}$$

CellPress

QUANTIFICATION AND STATISTICAL ANALYSIS

Details to descriptive statistical methods can be found in figures, their respective legends, tables, and their footnotes. The center and dispersion of populations are either presented as median and plots of population spread (violin plot, histogram) or mean and standard deviation (SD). For the performance index difference in the imaging experiments in zebra fish (Figure 4C) a two sided t-test was performed using the implementation of the python scipy.stats library. Significance was assumed if the p-value was below 0.001. For the randomization in the manual OSER assay evaluation the python library random was used to rearrange a database of pictures of all 3 constructs for each person performing classifications.

DATA AND SOFTWARE AVAILABILITY

Software, firmware, circuits diagrams and 3D models are available at the Github repository: https://github.com/GriesbeckLab.
    The accession numbers for the sequences and DNA samples are Genbank: MH062789 and Addgene: Plasmid #109484; Plasmid #109486.

Supplemental Information

Imaging-Based Screening Platform

Assists Protein Engineering

Arne Fabritius, David Ng, Andreas Michael Kist, Mutlu Erdogan, Ruben Portugues, and Oliver Griesbeck

Supplementary File 1: 3D Sketchup file of screening station.

Related to Figure 1

online

Supplementary Figure 1: Circuit diagram of screening platform
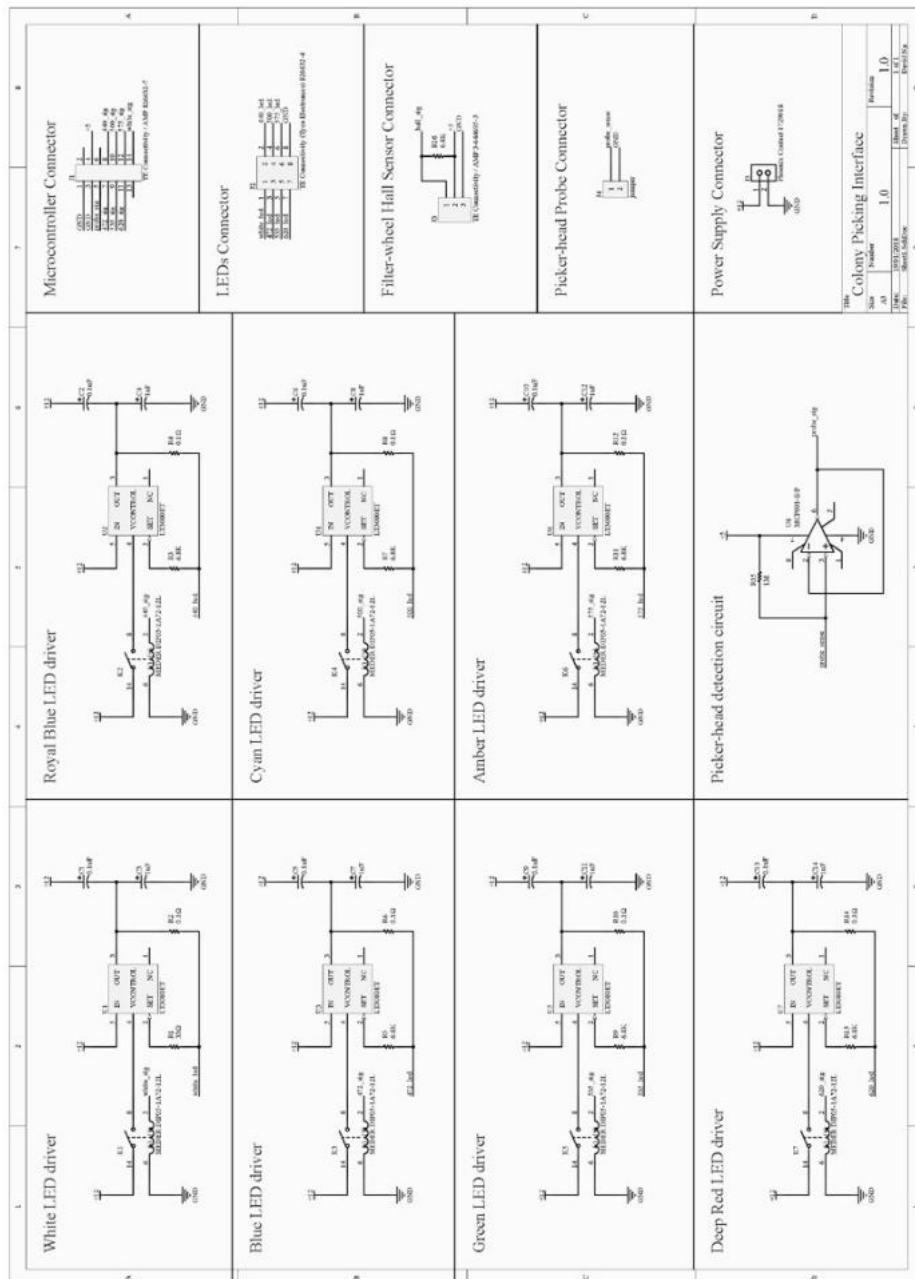
Related to Figure 1

The schematic for the interface between the Sanguinololu board and the Picking Robot. This diagram shows the required circuitry for the LED drivers, Hall effect sensor, probe sensor, and the pin-header interface to the microcontroller board using our customized firmware.

Supplementary Figure 2: Alignment of far-red emitting fluorescent proteins
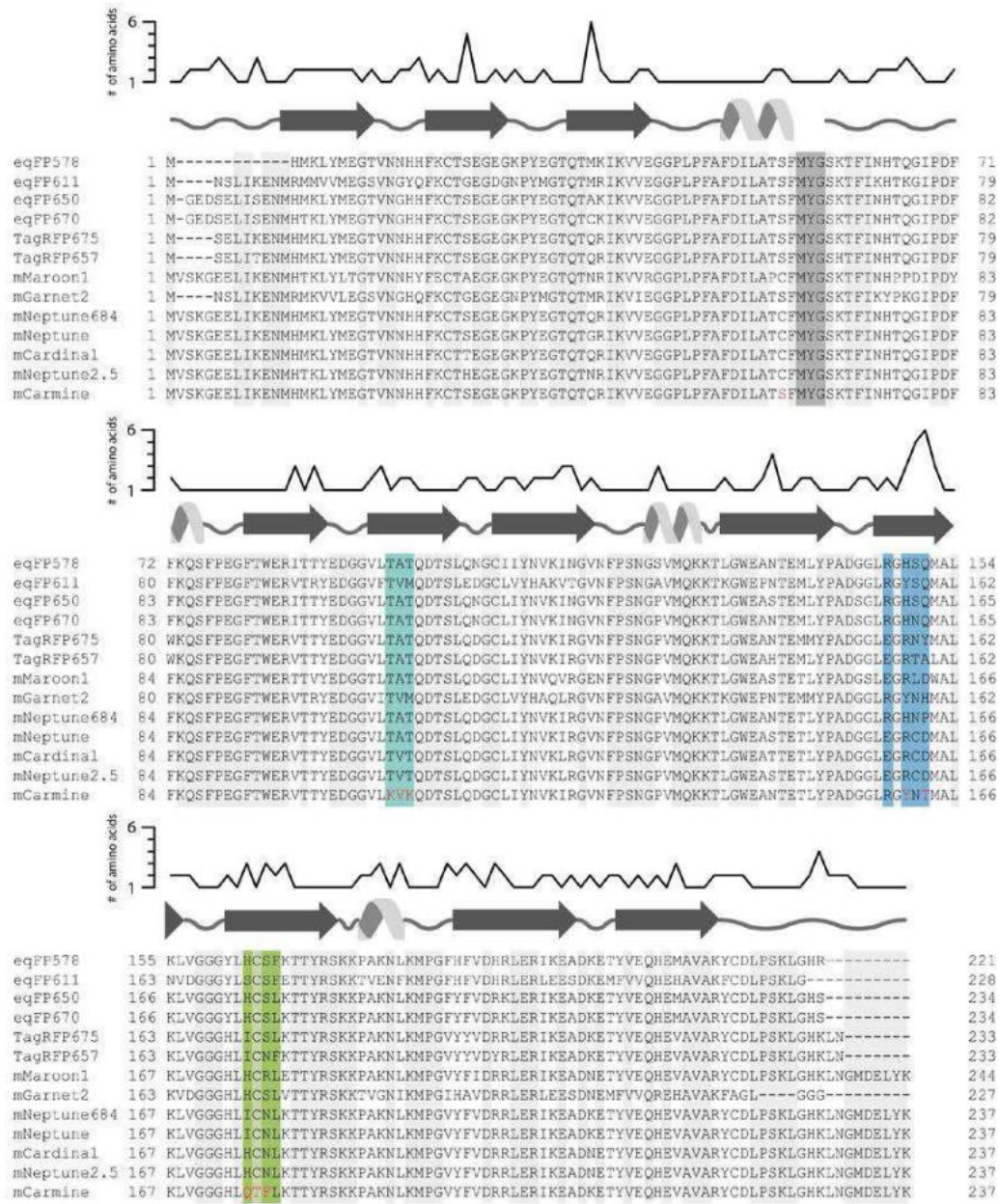
Related to Figure 3 B

Mutations from mNeptune684 to mCarmine are indicated in red. Regions subjected to cassette mutagenesis are shaded in color. Chromophore is shaded dark grey. The upper plot is an appreciation of variability at a given amino acid residue.

Supplementary Figure 3: Analytical size-exclusion chromatography of mCarmine variants and related fluorescent proteins.
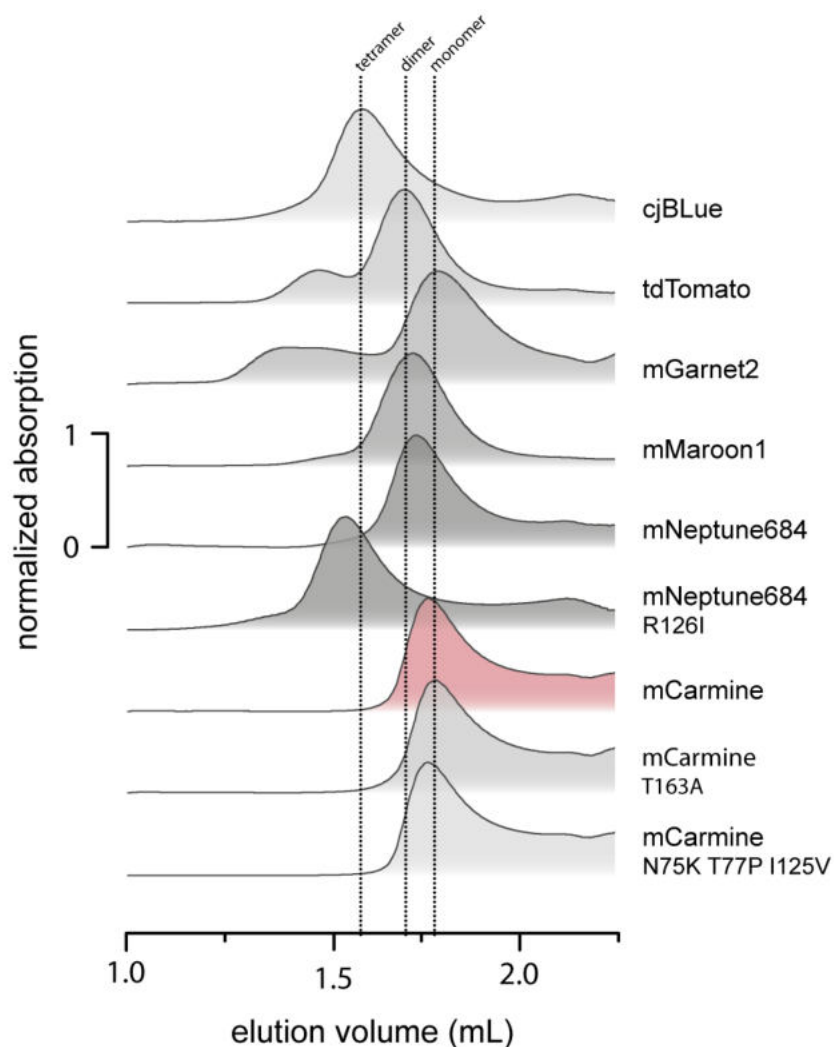
Related to STAR Methods section Chromatography

Elution profiles of far-red fluorescent proteins after size exclusion chromatography. The dotted lines denote monomer, dimer and tetramer peaks. As reference proteins cjBlue (tetrameric) tdTomato (pseudo-dimeric), mGarnet2 and mMaroon1 (monomeric) were used. mCarmine and its variants behaved as strict monomers, while mNeptune684 and mMaroon1 seemed to be in a mixture of monomer and dimer. While being mostly monomeric, mGarnet2 also displayed higher order oligomer states. Introduction of mutation R126I transforms mNeptune684 into a tetramer.

Supplementary Figure 4: Auto-fluorescence in mTFP1 channel in live zebrafish larvae
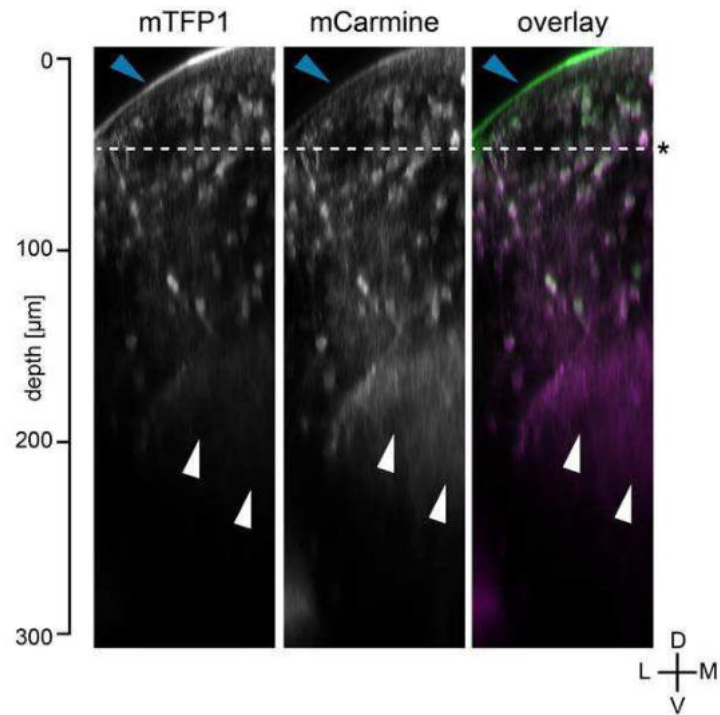
Related to Figure 4

We imaged a column in live anesthetized zebrafish larvae. Blue arrows indicate auto-fluorescence generated by the fish skin that is not related to cellular expression of a fluorescent protein. Note that this auto-fluorescence is prominent in the mTFP1 channel but only barely present in the mCarmine channel. White arrows indicate structural details of neuropil visible only in the mCarmine channel but not in the mTFP1 channel. Dotted line was reference plane for laser power adjustment. D, dorsal, V, ventral, L, lateral, M, medial.

Supplementary Figure 5: FACS analysis in HeLa cells
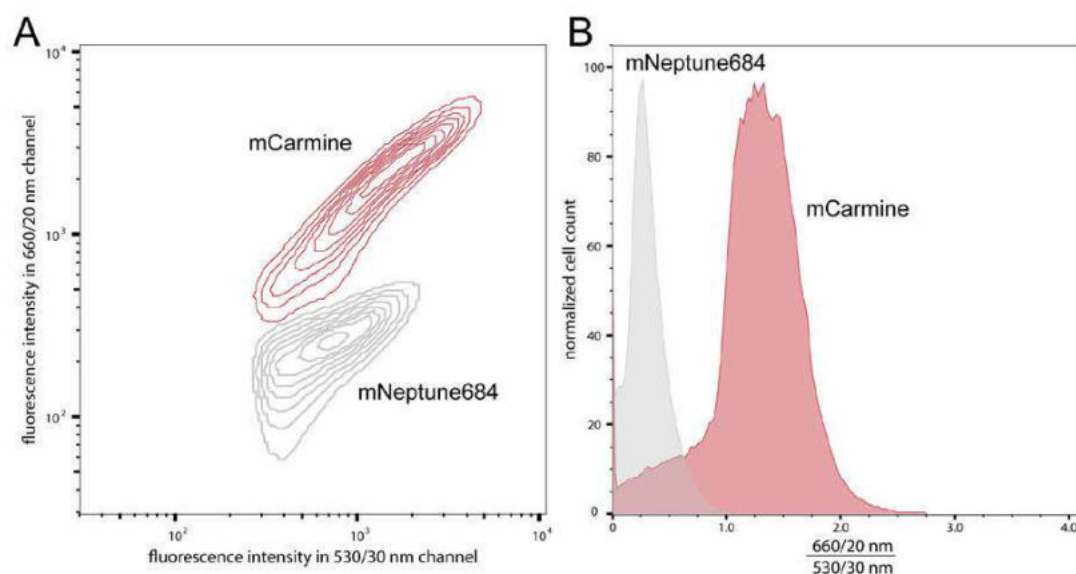
Related to STAR Methods section Flow cytometry

FACS analysis for HeLa cells expressing mTFP1-mCarmine and mTFP1-mNeptune684 fusion proteins. A: Contour plot of population fluorescent intensity in red channel vs. cyan channel (contours contain 90% of population) B: Ratio histogram of red/cyan channel

FACS brightness analysis in HeLa cells

Name	Cell count	Median 530/30 fluorescence intensity	Median 660/20n fluoresce intensity	Median ratio 630/660
mNeptune684	39568	575	202	0.28
mCarmine	55102	1010	1341	1.29

Table S1: Spectroscopic properties of far-red emitting fluorescent proteins

Related to Figure 4

Name	$Ex_{max,}$ [nm]	Em_{max} [nm]	ε [mM^{-1}cm^{-1}]	ϕ	$\varepsilon*\phi$	pKa
mCarmine	**603***	**675***	**83 ± 0.7***	**0.07 ± 0.002***	**5.73 ± 0.14***	**5.58 ± 0.03***
mCarmine T163A	608*	682*	66 ± 1.4*	0.05 ± 0.002*	3.35 ± 0.13*	6.29 ± 0.04*
mNeptune684[1]	604	684	39	0.03	1.17	6.50
	606*	684*	53±0.4*	0.03*	1.6*	6.6±0.1*
mMaroon1[2]	609	657	80	0.11	8.80	6.20
	608*	657*	98 ± 1.7*	0.17 ± 0.003*	16.68 ± 0.15*	6.17 ± 0.03*
mGarnet2[3]	598	671	105	0.087	9.14	6.80
	601*	668*	46 ± 0.4*	0.11 ± 0.002*	5.00 ± 0.17*	6.67 ± 0.07*
TagRFP675[4]	598	675	46	0.08	3.68	5.7

*values determined in our lab using our protocols
n=3, n represents independent protein purifications with 3 technical replicates for each measurements
(9 measurements total);
mean ± SD

Other values taken from
1 Li et al 2016
2 Bajar et al 2016
3 Matela et al. 2017
4 Piatkevich et al. 2013

Table S2: OSER (Organized Smooth Endoplasmic Reticulum) assay

Related to STAR Methods section OSER assay

Construct	#cells analyzed	% healthy cells	% healthy cells ref
CytERM-mCardinal	548	50 ± 9	41.3 ± 3.6[1]
CytERM-mCarmine	728	56 ± 16	
CytERM-mCherry	916	89 ± 9	95.0 ± 0.8[1]

n=3, mean ± SD

other values taken from

[1]Cranfill et al. 2016

Table S3: Primer table

See File Table S3

Related to Key Resource Table

RESEARCH ARTICLE

Motor context dominates output from purkinje cell functional regions during reflexive visuomotor behaviours

Laura D Knogler, Andreas M Kist, Ruben Portugues*

Max Planck Institute of Neurobiology, Sensorimotor Control Research Group, Martinsried, Germany

Abstract The cerebellum integrates sensory stimuli and motor actions to enable smooth coordination and motor learning. Here we harness the innate behavioral repertoire of the larval zebrafish to characterize the spatiotemporal dynamics of feature coding across the entire Purkinje cell population during visual stimuli and the reflexive behaviors that they elicit. Population imaging reveals three spatially-clustered regions of Purkinje cell activity along the rostrocaudal axis. Complementary single-cell electrophysiological recordings assign these Purkinje cells to one of three functional phenotypes that encode a specific visual, and not motor, signal via complex spikes. In contrast, simple spike output of most Purkinje cells is strongly driven by motor-related tail and eye signals. Interactions between complex and simple spikes show heterogeneous modulation patterns across different Purkinje cells, which become temporally restricted during swimming episodes. Our findings reveal how sensorimotor information is encoded by individual Purkinje cells and organized into behavioral modules across the entire cerebellum.
DOI: https://doi.org/10.7554/eLife.42138.001

Introduction

Decades of influential anatomical (*Eccles et al., 1967*; *Palay and Chan-Palay, 1974*), theoretical (*Marr, 1969*; *Albus, 1971*; *Ito, 1972*) and experimental work (see *Ito, 2006* for review) have led to our current knowledge highlighting the cerebellum as a major brain region for the control of motor behaviors. This ability to coordinate motor control and learning relies critically on the integration of sensory and motor-related signals in Purkinje cells, as these neurons constitute the main computational units and output of the cerebellum. In order to understand the detailed operations of the cerebellum, it is therefore of fundamental importance to characterize the physiology of cerebellar neurons, especially the Purkinje cells, during sensorimotor behaviors.

Purkinje cells receive two excitatory input streams, via parallel fibers from granule cells and a single climbing fiber from the inferior olive, that differentially modulate their spike output. Across vertebrate species, climbing fibers from inferior olivary neurons drive complex spikes in Purkinje cells at a spontaneous rate of ~0.5–2 Hz whereas parallel fiber inputs modulate intrinsic simple spike activity at much higher rates (from tens of Hz in larval zebrafish up to hundreds of Hz in mammals; *Hsieh et al., 2014*; *Eccles et al., 1967*; *Raman and Bean, 1997*). Simple spike output can furthermore be biased to burst or pause by the arrival of a complex spike (*Mathews et al., 2012*; *Badura et al., 2013*; *Sengupta and Thirumalai, 2015*), though the precise nature of this relationship varies across Purkinje cells (*Zhou et al., 2014*; *Zhou et al., 2015*; *Xiao et al., 2014*). In addition, inhibitory interneurons may also exert considerable control over simple spike rates (*Dizon and Khodakhah, 2011*; *ten Brinke et al., 2015*; *Jelitai et al., 2016*). Characterizing the type of information carried by these different input streams at the population level and disentangling their relative contributions to Purkinje cell output has been challenging due to the large number of Purkinje cells in

the mammalian cerebellum (>300,000 in the rat cerebellum) receiving convergent input from 100,000 to 200,000 parallel fibers (*Harvey and Napper, 1991*).

Due to this complicated physiology, the anatomy of climbing fiber projections onto Purkinje cells has primarily been used to characterize the organization of the mammalian cerebellum. Four transverse zones along the rostrocaudal axis have been described (*Ozol et al., 1999*) that can be further subdivided into longitudinal zones and microzones defined by additional anatomical, physiological and molecular features (see *Apps and Hawkes, 2009* for review). This organization is thought to produce functional modules that each participate in the control of a certain set of behaviors (*Cerminara and Apps, 2011*). However, since these regions have been largely defined in terms of anatomical rather than physiological properties, the behavioral relevance of cerebellar modules is not well understood. Purkinje cells are at the center of cerebellar circuits, integrating climbing fiber and parallel fiber input. A detailed description of the flow of sensory and motor information within both individual and groups of Purkinje cells is important to understand the functional significance of these proposed behavioral modules.

A fundamental first step is therefore a population-level investigation of Purkinje cell activity during a simple set of sensorimotor behaviors with single-cell resolution of simple and complex spikes. In this study, we took advantage of the larval zebrafish to study how sensorimotor variables are encoded in Purkinje cell output during reflexive, visually-driven motor behaviors. The larval zebrafish cerebellum is anatomically organized in a typical vertebrate tri-layered configuration, with a population of fewer than 500 Purkinje cells, each receiving inputs from many parallel fibers and likely just one climbing fiber (*Bae et al., 2009*; *Hashimoto and Hibi, 2012*; *Hsieh et al., 2014*; *Hamling et al., 2015*). Several studies have demonstrated a functional role for the cerebellum in the larval zebrafish relating to motor coordination, adaptation, and learning (*Aizenberg and Schuman, 2011*; *Ahrens et al., 2012*; *Matsui et al., 2014*; *Portugues et al., 2014*; *Harmon et al., 2017*). The behavioral repertoire of the larval zebrafish includes robust but variable swimming and eye movements to drifting gratings and rotating stimuli (the optomotor and optokinetic response, respectively). These visual stimuli are particularly useful because they elicit graded, episodic swim bouts and eye movements that vary across trials, allowing us to disambiguate clearly between sensory and motor responses. We are furthermore able to extract many different features from both the visual stimuli and motor behaviors (i.e. onset, direction, velocity) to pinpoint how Purkinje cell activity correlates with particular features of visual stimuli at a fine temporal scale.

Using this approach, in this study we investigated three main questions: (1) how motor and sensory information is encoded in individual Purkinje cells from different input pathways, (2) how the temporal dynamics of these different information streams are encoded in Purkinje cell output, and (3) how responses are spatially organized across the entire cerebellum. Calcium imaging across the whole cerebellum to the same set of visual stimuli in tandem with tail-free and eye-free behavior revealed considerable spatial segregation in Purkinje responses. We supplemented calcium imaging data with direct electrophysiological recordings in order to examine complex and simple spikes directly under conditions of fictive or eye-free behavior. In agreement with our imaging data, we uncovered a consistent and striking organization of the Purkinje cell population into three functional regions along the rostrocaudal axis that encode visual information with respect to either directional motion onset, rotational motion velocity, or changes in luminance. The fine temporal resolution of our electrophysiological recordings together with our ability to disentangle different sensorimotor variables revealed that these regions receive similar motor-related parallel fiber input but are strongly differentiated by sensory complex spike responses that encode distinct visual features with unique temporal dynamics. We relate these findings to other work in the field to propose an overarching organization of the larval zebrafish cerebellum into cerebellar modules underlying innate and flexible visually-driven behaviors.

Results

Activity in the cerebellum is arranged into functionally-defined and anatomically-clustered symmetrical regions of Purkinje cells

Anatomical, physiological, and genetic studies of the mammalian cerebellum across species show that the cerebellar cortex is organized into spatially-restricted regions of Purkinje cells, where a

given region has a specific set of inputs and outputs and is thought to control the coordination and adaptation of a different set of sensorimotor behaviors (*Apps and Hawkes, 2009*; *Witter and De Zeeuw, 2015*). In order to describe the organization of Purkinje cell responses across the entire cerebellum with high spatial resolution, we performed two-photon calcium imaging across the complete population of Purkinje cells while presenting a variety of visual stimuli that drive variable, reflexive sensorimotor behaviors (*Easter and Nicola, 1996*) to awake, head-embedded larval zebrafish whose eyes and tail were freed and could move (*Figure 1a,b*; see *Video 1* for an animation of visual stimuli as presented to the fish during two-photon imaging experiments).

Figure 1. Using population imaging and multilinear regression to describe feature responses across the Purkinje population during visuomotor behaviors. (a) Cartoon of the embedded zebrafish preparation under the two-photon microscope with freely-moving eyes and tail. (b) Overview of the visual stimuli presented to the awake, behaving zebrafish during volumetric two-photon calcium imaging. See Materials and methods for further details. The mean swimming activity and eye position for a representative fish across an entire experiment is shown (N = 100 trials). (c) Composite bright field image of a seven dpf zebrafish larva from a dorsal view showing Purkinje cells expressing GCaMP6s driven by a ca8 enhancer element. Scale bar = 100 microns. (d) Overview of the multilinear regression analysis. See Materials and methods for additional details and see *Figure 1—figure supplement 1* for full list of regressors. (e) Left panels, example calcium signal from a Purkinje cell across two planes (black trace) can be well recapitulated through multilinear regression (MLR, grey trace; R^2 = 0.77). The regressors with the seven largest coefficients (β) are shown below scaled in height and colored by their β value (blue = positive, red = negative). The asterisk for regressor four refers to a negative value of β which results in an inverted regressor. Right, a bar graph quantifying the normalized β values for all regressors for this cell with the regressors shown at left labelled. See also *Figure 1—figure supplements 1* and *2*.
DOI: https://doi.org/10.7554/eLife.42138.002

The following figure supplements are available for figure 1:

Figure supplement 1. Functional imaging anatomy and full regressor list.
DOI: https://doi.org/10.7554/eLife.42138.003

Figure supplement 2. Calcium signals report complex spikes reliably but can also report simple spike bursts.
DOI: https://doi.org/10.7554/eLife.42138.007

Video 1. Z-projection map of GCaMP6s responses (max dF/F) in Purkinje cells to visual stimuli. Related to *Figure 2*.
DOI: https://doi.org/10.7554/eLife.42138.004

We observed frequent eye and tail movements that varied across visual stimuli and across trials (*Figure 1b*). Whole-field gratings moving in the four cardinal directions elicited reflexive but variable optomotor swimming responses. Swimming episodes (bouts) were evoked in a probabilistic manner that was modulated by the direction and speed of the visual motion (i.e. no swim response to gratings in the reverse direction). A windmill pattern centered on the larva's head rotating with a sinusoidal velocity elicited a reflexive optokinetic response of the eyes that also showed some behavioral variability across trials. Moderate intensity whole-field flashes were included to provide stimuli that evoke no acute behavioral response (*Figure 1b*) but that could nonetheless contribute to ethological behaviors over longer timescales, for example relating to circadian rhythms (*Burgess and Granato, 2007*). The visual stimuli were presented in open loop (i.e. with no updating of the visual stimuli in response to behavior) in order to clearly dissociate the sensory stimuli and any behavioral response. It should be noted that visually-driven motor behaviors are robust on average but episodic and variable across trials, allowing us to clearly disambiguate sensory and motor contributions to neuronal activity when we examine the correlations between Purkinje cell activity and eye or tail motor activity on a trial by trial basis.

We used two-photon calcium imaging to image neural activity in 7 days-post fertilization (dpf) zebrafish larvae expressing GCaMP6s in all Purkinje cells (*Figure 1c*, *Figure 1—figure supplement 1a*). This strategy allowed us to measure the entire Purkinje cell population in response to this set of stimuli with high spatial resolution while tracking eye and tail movements. Neural responses to these

Figure 2. Purkinje cell activity is functionally clustered across the cerebellum. (**a**) Heatmaps of the z-projected mean voxelwise correlation coefficients from multilinear regression (MLR) with example sensory and motor regressors for a representative fish (see Materials and methods). Scale bar = 50 microns. (**b**) Voxels from the example fish in a) are colored according to whether the best regressor for correlated sensory stimuli and motor events (including i) swimming and ii) eye movement) are sensory (magenta), motor (green), or equal/uncorrelated (white). (**c**) Left, quantification of principal component analysis, clustering, and stereotypy of Purkinje cell responses. Left axis, index values across the first ten principal components with respect to the anatomical clustering of principal components within a fish (red line) and the stereotypy of these clusters across fish (blue line). Dotted black line shows an index value of 1 (equivalent to chance). Right axis, total variance explained across principal components. Right panel, mean spatial mapping of the four principal components with the highest index values for anatomical clustering and stereotypy as individual maps (above) and composite (below). Colors are arbitrarily chosen.
DOI: https://doi.org/10.7554/eLife.42138.006

stimuli showed considerable temporal and spatial structure across the cerebellum, as visualized by the z-projection map of average calcium responses (max dF/F) in the entire Purkinje cell population across the trial (*Video 1*) as well as in the activity from single imaging planes (*Video 2*). We estimated the number of Purkinje cells in the larval zebrafish to be 433 ± 19 (mean ± std, N = 3) by identifying spherical nuclei in confocal stacks of a transgenic line that expresses nuclear-localized GCaMP6s using 3D template matching (*Figure 1—figure supplement 1*; see Materials and methods). This number is higher than the previously reported range of 180–360 Purkinje cells at seven dpf (N = 6; *Hamling et al., 2015*).

In order to quantify how different features of the visual stimuli and the tail and eye behaviors contribute to Purkinje cell activity, we performed multilinear regression on voxelwise calcium signals obtained across the Purkinje cell population (*Figure 1d*, *Figure 1—figure supplement 1*; see Materials and methods for detailed description). Multilinear regression is advantageous for two reasons in particular. First, it allows the identification of multiple visual and/or motor features that may contribute to a single calcium signal. Second, we can distinguish between regressors that may be moderately correlated in our experiments, such as forward moving gratings and the variable swim bouts that these stimuli elicit. Zebrafish swim in episodic bursts of swimming that last just hundreds of milliseconds, separated by rest periods lasting seconds, whereas the visual stimuli driving these swim bouts were presented for many seconds. As a result, motor regressors for eye or tail movements look very different from visual sensory regressors (*Figure 1d,e*, *Figure 1—figure supplement 1*) and their respective contributions to calcium signals can be determined.

Our analysis showed that Purkinje cell activity is functionally segregated across the cerebellum with respect to different visual and motor features (*Figure 2a*, *Video 3*). Responses to whole-field flashes were enriched in a bilaterally symmetric central region of the cerebellar cortex, whereas responses to clockwise and counterclockwise rotational motion had an asymmetric localization within the left and right hemisphere of the caudolateral cerebellum, respectively. Purkinje cell responses to motor activity, including eye and tail motion, were generally broad and showed strong, uniform correlations across most of the cerebellar cortex.

Next, to disambiguate between visual and motor responses we explicitly visualized the sensory/motor preference across the Purkinje cell layer for two visuomotor behaviors: swimming driven by forward-moving gratings, and left/right eye movements driven by rotational windmill motion. *Figure 2b* shows a z-projection of the cerebellum for each of these visuomotor behaviors, with areas colored magenta or green based on whether the relevant visual or motor feature was significantly better in explaining the activity in that region (see Materials and methods). As *Figure 2bi* shows, the activity of Purkinje cells distributed across a broad region of the cerebellum correlated highly with tail movement during swimming and accounted for the modulation of calcium activity to a much greater extent that sensory grating motion. In contrast, *Figure 2bii* shows that a large dense bilateral area of the caudolateral cerebellum had activity that was more strongly related to sensory rotational motion while the remaining area of the rostral and medial cerebellum showed a stronger correlation with eye movements. These results indicate that locomotor activity of the tail and eyes is broadly encoded in Purkinje cell activity across the cerebellum whereas sensory responses to visual features are more anatomically clustered.

Finally, in order to identify groups of Purkinje cells whose activity was similarly modulated during the experiment, regardless of which feature

Video 2. Single plane at −35 microns depth from the dorsal surface showing GCaMP6s responses (max dF/F) in Purkinje cells to visual stimuli. Related to *Figure 2*.
DOI: https://doi.org/10.7554/eLife.42138.005
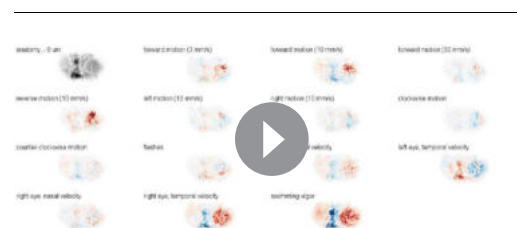
Video 3. Upper left, anatomical stack of Purkinje cell anatomy (upper left) showing the depth in microns of the plane from the dorsal surface. Other panels, the corresponding plane from the stack of regressor coefficient weights (labelled for regressor type) for all Purkinje cells as quantified with multilinear regression (see Materials and methods). Related to *Figure 2*.
DOI: https://doi.org/10.7554/eLife.42138.008

drove the response, we performed principal component analysis on the coefficient weights for all cells across all fish (N = 10; see Materials and methods). This analysis again revealed considerable spatial structure and stereotypy in Purkinje cell responses, with most functional clusters being also both anatomically clustered within fish and similarly located across fish (*Figure 2c*, *Figure 1—figure supplement 1d*). Four functional clusters emerged that were particularly spatially-clustered and tiled the cerebellum across the rostrocaudal axis of each hemisphere (*Figure 2c*). Together, these results suggest a clear spatial organization of Purkinje cells into functional regions along the rostrocaudal axis of the zebrafish cerebellum.

Calcium signals in Purkinje cells report complex spikes with high fidelity with lesser contributions from simple spikes

Since Purkinje cells receive excitatory inputs from both climbing fibers and parallel fibers that drive different types of spiking, it is critical to understand exactly what the calcium signals described above represent in terms of the underlying spike identity and structure. Climbing fiber inputs driving complex spikes have been shown to reliably produce large dendritic calcium signals in mammalian Purkinje cells with little to no signal in the soma (*Lev-Ram et al., 1992*). In contrast, parallel fiber inputs may contribute to small, local calcium signals at dendritic spines or branchlets (see *Kitamura and Kano, 2013* for review) while changes in sodium-dependent simple spike rates may be read out from somatic calcium signals (*Ramirez and Stell, 2016*). We performed in vivo cell-attached electrophysiological recordings of spontaneous activity from single Purkinje cells expressing GCaMP6s in order to show how the signals obtained during calcium imaging relate to complex and simple spike output in larval zebrafish Purkinje cells (*Figure 1—figure supplement 2*).

As expected, we found that every complex spike elicited a peak in the calcium signal of a Purkinje cell's dendrites (*Figure 1—figure supplement 2a,b*). However, we also found that isolated bursts of simple spikes correlated with widespread increases in the dendritic calcium signal. Aligning the calcium signal to the onset of simple spike bursts and single complex spike events showed consistent simple spike-triggered calcium transients that were of smaller amplitude but similar duration to complex spike-triggered transients (*Figure 1—figure supplement 2b,d*). We used multilinear regression methods to determine the relative contribution from the activity of complex and simple spikes to the calcium signals we measured in different Purkinje cells across fish. We find that although the majority of the signal is driven by the occurrence of a complex spike, simple spikes also contribute to a varying degree across cells and can account for up to half of the calcium signal (mean percentage contribution from complex spikes = 78.4 ± 6.8%, N = 8 cells from eight fish; *Figure 1—figure supplement 2e,f*).

These findings reveal that both complex spikes and simple spike bursts can contribute to the dendritic fluorescence signals obtained by calcium imaging in larval zebrafish Purkinje cells. The observation above that many visual and motor features can contribute to the calcium signal from a single Purkinje cell (*Figure 1e*) is therefore unsurprising if this signal represents not only complex spikes but also simple spike responses modulated by the convergent input from many parallel fibers. We furthermore observed that somatic signals and dendritic signals were highly correlated with each other (mean correlation = 0.87 ± 0.2, N = 5 cells from three fish; *Figure 1—figure supplement 2g, h*), suggesting that the contribution from these different input streams may not be as spatially segregated in these Purkinje cells as shown in other systems and therefore cannot be isolated by subcellular imaging. In summary, calcium signals across Purkinje cells report both complex spikes and high frequency simple spiking and care must therefore be taken when interpreting the underlying activity patterns of Purkinje cells measured with functional imaging.

Electrophysiological recordings from Purkinje cells reveal distinct complex spike responses that can be grouped into three primary visual response phenotypes

In order to overcome the mixed contribution of complex spikes and simple spike bursts to calcium signals and to record Purkinje cell spiking activity in greater detail, we turned to single-cell electrophysiology. We performed cell-attached Purkinje cell electrophysiological recordings at different locations across the cerebellum in the awake, paralyzed larval zebrafish while presenting visual stimuli as for the functional imaging experiments described above (N = 61 cells from 61 fish). Complex

spikes and simple spikes can be clearly distinguished in these recordings with automated thresholding by amplitude (*Figure 3a*) and converted to a spike rate (*Figure 3b*; see Materials and methods). Simultaneous fictive recordings of locomotor activity were obtained from a ventral root extracellular electrode (*Figure 3a*) as previously described (*Masino and Fetcho, 2005*) and used to extract information about fictive swim bouts (see Materiials and methods). The high temporal resolution of electrophysiological recordings further enhances our ability to separate feature components. For example, we find that swimming activity is only moderately correlated with forward visual motion on a trial by trial basis (mean correlation = 0.31 ± 0.2, *Figure 3c*, *Figure 3—figure supplement 2*).

In an approach similar to that used to analyze the functional imaging results presented above, we built regressors to capture the most salient features of the visual and motor stimuli (see *Figure 3d* for examples and *Figure 3—figure supplement 1* for the full regressor list). The high temporal resolution of electrophysiology allows us to resolve transient changes in simple spike firing rate as well as single complex spikes, therefore we added regressors for the visual and motor regressors that would capture spiking responses to a more specific set of visual stimulus and behavioral features such as visual motion onset, duration, velocity, swim onset, and graded swim strength. The window chosen for stimulus onset covered 500 milliseconds from actual stimulus onset (e.g. motion onset of forward gratings) in order to account for the inherent synaptic delays for visual information to arrive in the cerebellar input layer, on the order of 100–200 milliseconds (*Knogler et al., 2017*). Preliminary assessments of spike rates with visual and motor feature regressors further confirmed that these regressors appropriately captured the temporal dynamics of Purkinje cell spiking (*Figure 3d*, *Figure 3—figure supplement 2*). We employed a variant of multilinear regression with elastic net optimization that includes regularization terms to help sparsify the number of features that are used to reconstruct the signal, as well as variable selection and parameter optimization to overcome the minor degree of correlation between some regressors (*Figure 3e* and *Figure 3—figure supplement 1*; see Materials and methods).

Since the complex spikes and simple spikes of Purkinje cells are modulated by climbing fiber and parallel fiber input streams, respectively, we independently assessed these responses across the population of cells (*Figure 3e*). We will first address the complex spike responses, as these provided a useful classification of Purkinje cell groups within the population in line with the functional and spatial organization seen during functional imaging.

We observed that complex spikes were generally evoked by a narrow subset of stimuli. Only a few visual or motor features provided a significant contribution to each cell's complex spike rate (mean number of nonzero coefficients = 6.0 ± 0.4 out of 22, N = 61), and in many cases a single feature was very dominant (*Figure 3e*). Mixed complex spike responses to multiple stimuli are possible due to mixed selectivity in neurons of the inferior olive (*Ohmae and Medina, 2015*; *Ju et al., 2018*) or residual multiple climbing fiber input (*Crepel et al., 1976*). We found little evidence however that individual Purkinje cells encode multiple types of visual stimuli or both visual and motor features in their complex spike responses. The current results do not rule out the likely possibility that information from other sensory modalities than vision are also encoded in the complex spikes of these cells.

A survey of the best regressor category for each cell from this dataset revealed that Purkinje cell complex spike responses were strongly enriched for visual information (*Figure 3e*), specifically the onset of direction-specific translational motion (N = 31/61) and direction-specific rotational velocity (N = 14/61). The remaining Purkinje cells were categorized as having complex spikes that best responded to changes in whole-field luminance, to fictive motor activity, or to the duration of translational motion. Notably, sensory responses across visual features are far better represented than motor responses in the complex spike responses of Purkinje cells (*Figure 3e*). This was not due to a paucity of motor activity, as bouts of swimming behavior were consistently elicited across trials. Only 8/61 cells had the biggest contribution to complex spike rates from motor activity, and across the remaining cells the average contribution from motor regressors was less than 5% (3.7 ± 1%, N = 53). Of the eight cells whose best regressor was motor-related, there were nonetheless significant responses to visual features present as determined by non-zero sensory coefficient weights accounting for 10–40% of the complex spike activity (mean contribution = 20 ± 5%). As a result, we made the surprising observation that all but one of the Purkinje cells that we recorded from across the entire cerebellum could be unambiguously assigned to one of three visual complex spike 'phenotypes' corresponding to a response to directionally-selective translational motion onset, directionally-selective rotational velocity, or changes in luminance.

Figure 3. Electrophysiological recordings from Purkinje cells reveal distinct complex spike responses that can be grouped into four primary response types corresponding to sensory or motor features. (a) Cartoon of the embedded, paralyzed zebrafish preparation used for simultaneous Purkinje cell (PC) electrophysiology with fictive swimming patterns extracted from the ventral root (VR). (b) Example single trial from a cell-attached Purkinje cell (PC) recording (upper trace, black) with simultaneous ventral root recording (lower trace, gray, shown as a moving standard deviation). Complex spikes in the PC are indicated by orange dots above the trace and simple spikes are indicated by blue dots below the trace. Stimuli are color-coded as before (see *Figure 1* and Materials and methods for more details). (b) Left, the mean simple spike (SS) and complex spike (CS) rate for the cell shown in (a) across five trials. Right, the correlation coefficients of forward, left and rightward grating motion with the trial by trial fictive swim activity for all fish. (c) Plot of the correlation coefficient for each fish between the regressor for concatenated swimming activity during moving forward, left, and right gratings across all trials and the summed sensory regressor for forward, left, and right grating motion. The mean is indicated by the black bar. (d) Example mean complex spike rate extracts from three different Purkinje cells showing the temporal similarity of firing dynamics with visual feature regressors. (e) Above, heatmap of coefficient weights for the complex spike firing rates of 61 cells from z-scored least-squares multilinear regression (MLR) with a full set of 24 stimulus- and motor-related variables (see Materials and methods). Below, histogram showing the distribution of cells' highest regressor weight. (f) Location of these cells across all fish mapped onto a reference cerebellum (dorsal view). The color indicates the highest MLR coefficient weight for that cell while the size indicates the degree to which that coefficient contributes to the overall firing rate respective to the others, where the biggest circles = 100%. Scale bar = 50 microns. (g) Left, heatmap of complex spike rates for all 61 cells clustered according to the category of their

Figure 3 continued on next page

We hypothesized that these three different visual complex spike phenotypes could underlie the spatial clustering of Purkinje cell population activity that we observed with functional imaging (*Figure 2c*). Mapping the coordinates of all Purkinje cells onto a reference cerebellum revealed a spatial organization of complex spike sensory response phenotypes similar to our functional imaging data (*Figure 3f*). In particular, we observed a rostromedial cluster of cells responsive to the onset of directional motion in the visual stimulus and a caudolateral cluster of cells responsive to rotational stimulus velocity. Luminance responses were more scattered but generally occupied the central zone between these regions.

Together with our functional imaging data, these results suggest that zebrafish Purkinje cells contribute to the formation of three distinct spatial regions across each cerebellar hemisphere through visual complex spike profiles encoding either directionally-selective translational motion onset, directionally-selective rotational velocity, or changes in luminance. These regions b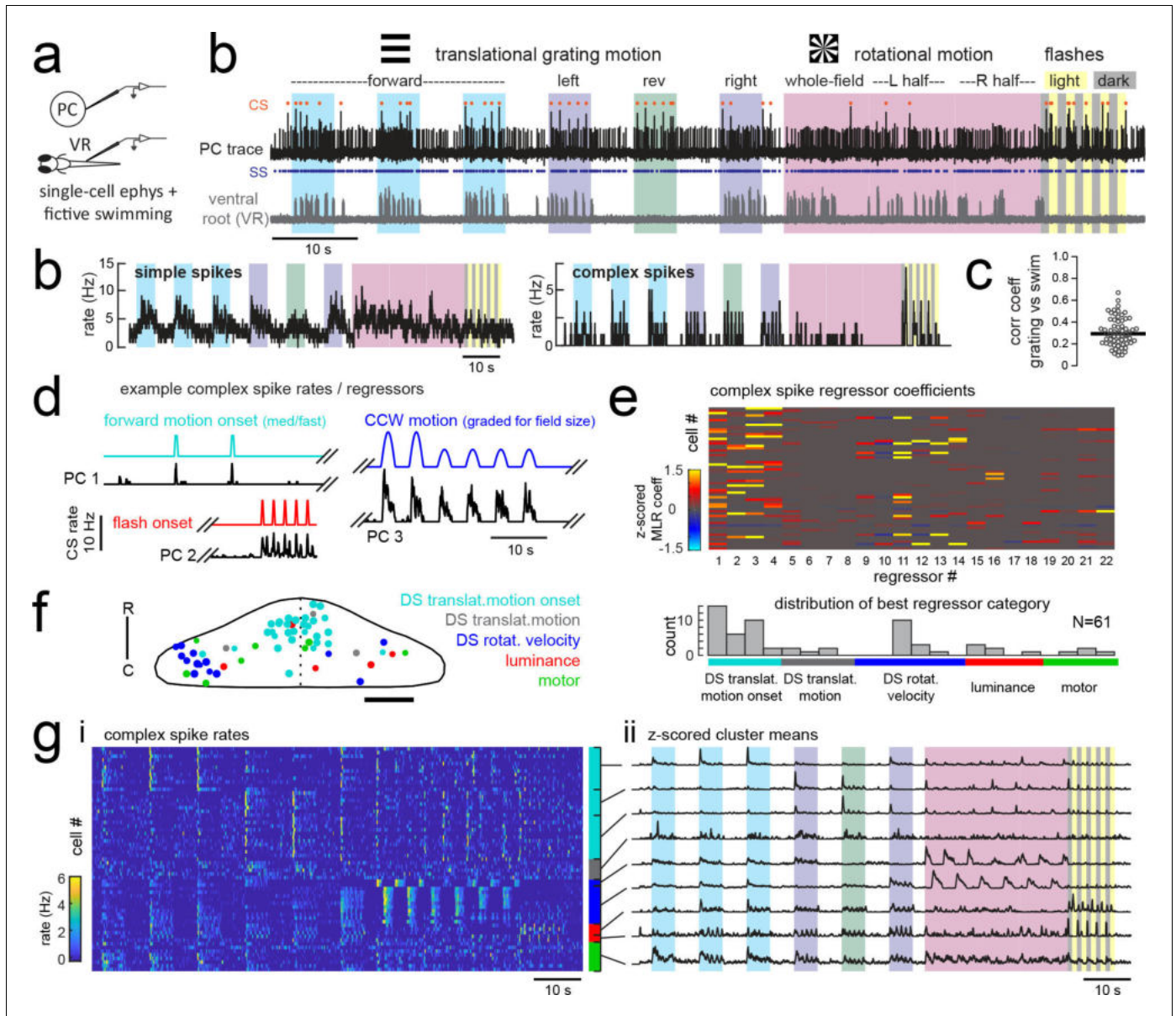ear a striking resemblance to the anatomically clustered activity patterns identified by principal component analysis in our imaging data (*Figure 2c*), suggesting that the visual complex spike response phenotype is an important parameter that can be used to understand the spatial and functional organization of Purkinje cells across the cerebellum.

Purkinje cells in different regions receive feature-specific climbing fiber input and project to different downstream regions

From the three major visual complex spike phenotypes we observed across the Purkinje cell population, we observed that further subdivisions could be made based on the specific type of response to a given visual stimulus. For example, direction-selective motion onset-responsive Purkinje cells differ in their directional tuning, and luminance-responsive cells can prefer either increases in luminance, or bidirectional changes (*Figure 3d,g*). Therefore, we next performed further detailed analyses of Purkinje cell complex spike activity in combination with additional anatomical experiments in order to quantify precisely how visual features such as directionality are encoded by different Purkinje cells with the same visual phenotype and to also identify the projection patterns of Purkinje cells across phenotypes.

The largest group of Purkinje cells showed a phenotype for strong, direction-selective responses to the onset of translational motion (N = 33/61 cells). These responses typically spanned two of the four cardinal directions tested, producing on average just one complex spike at the onset of motion in the preferred directions (1.2 ± 0.6 spikes/stimulus; *Figure 4a*). The occurrence of a complex spike was not dependent on the behavioral response since visually-evoked complex spikes occurred with equal probability whether there was a swimming response or not (*Figure 3—figure supplement 2*). In the clearest example, reverse visual motion evokes no swimming but is equally well-represented by a complex spike response at motion onset as the directions that do drive swimming (*Figures 3g* and *4a*, *Figure 3—figure supplement 2a*).

The direction selectivity index (see Materials and methods) of these cells ranged from 0.2 to 0.9 (*Figure 4—figure supplement 1a*), and cells typically responded to two of the four cardinal directions tested (*Figure 4a*). No cells were found that responded significantly to motion onset in opposing directions. Although the Purkinje cell somata displaying this complex spike phenotype were closely clustered in the most rostromedial part of the cerebellum (*Figure 3f*), the lateralization of Purkinje cells was biased such that cells in the left cerebellar hemisphere preferred either forward

Figure 4. Purkinje cells in different regions show complex spike responses that encode different visual features and one group sends outputs to a different downstream region. (a) Raster plot (upper left panels) and histogram (lower left panels, 500 ms bins) of complex spikes occurring across trials during translational whole-field motion of black and white bars in all four cardinal directions for two example Purkinje cells (PC). Numbers assigned to PCs for this and panels b-c are arbitrary. (b) Raster plot (upper left panels) and histogram (lower left panels, 100 ms bins) of complex spikes occurring across trials during whole- and half-field bidirectional rotational motion of a black and white windmill for an example cell. The dashed lines over the histogram show the velocity of the stimulus in each direction across the trial. (c) Raster plot (upper left panels) and histogram (lower left panels, 100 ms bins) of complex spikes occurring across trials during whole-field light/dark flashes for two example cells, (i) and ii). (d) A box plot of complex spike firing rates during blank trials (no visual stimuli) for cells grouped by their sensory or motor complex spike category (see *Figure 2*). N = 31, 14, 5, 8. Asterisks indicate significance (one-way ANOVA with Bonferroni post hoc correction, p<0.001). j (i) The location of cells colored by complex spike phenotype are plotted onto a flattened dorsal view of the cerebellum with all coordinates flipped to the right half of the cerebellum. e (ii) Three example maximum projection images of traced axonal morphology from stochastically-labelled, Fyn-mClover3-expressing Purkinje cells for which electrophysiological recordings were also obtained. Labels for each cell refer to the electrophysiological traces in panels a-c. The asterisk for cell a) indicates that these coordinates were flipped to the right half of the cerebellum. Scale bar = 50 microns. e (iii) Categorical grouping of complex spike phenotypes for internal versus caudal axonal projections. N = 17 cells from 17 fish. (f) Morphed Purkinje cell axonal morphologies from single-cell labelling across fish (N = 50 cells) can be grouped into two populations based on axonal projection (as for e iii). N = 27 cells with internal axons, N = 23 cells with caudal axons. See also *Figure 4—figure supplement 1*.

The following figure supplements are available for figure 4:

Figure supplement 1. Complex spike responses encode specific aspects of visual features.
Figure supplement 2. Purkinje cell dendrites show a mostly planar morphology.
Figure supplement 3. Motor-related complex spikes are rare.

motion to the right (0 to 90°, N = 7) or reverse motion to the left (−90 to −180°, N = 5; *Figure 4—figure supplement 1a*). Conversely, Purkinje cells in the right cerebellar hemisphere preferred either forward motion to the left (0 to −90°, N = 5) or reverse motion to the right (90 to 180°, N = 5; *Figure 4—figure supplement 1a*). The reliable, phasic nature of these complex spike responses suggests that these Purkinje cells encode acute, directional changes in the visual field.

The second group of Purkinje cells, located in the caudolateral cerebellum, showed a phenotype for large, directionally-selective increase in complex spikes during either clockwise or counter-clockwise rotational motion that unlike the previous group persisted throughout the duration of movement (*Figure 4b*; N = 12/61 cells). During rotational motion in the preferred direction, complex spike firing rates in these cells were two to five times higher than baseline (mean rate increase = 340 ± 40%, N = 12). In contrast, complex spike rates during motion in the non-preferred direction fell to nearly zero, well below the baseline rate (mean rate non-preferred direction = 0.32 ± 0.1 Hz versus 0.87 ± 0.1 Hz at baseline; *Figure 4—figure supplement 1b*). Consistent with our functional imaging data (*Figure 2*), these complex spike responses to rotational motion were highly lateralized such that all Purkinje cells (10/10) that preferred clockwise rotational motion were located in the caudolateral region of the left cerebellar hemisphere while the only two Purkinje cells that preferred counter-clockwise motion were located in the mirror symmetric region of the right cerebellar hemisphere (*Figure 4—figure supplement 1b*). Additional experiments in the semi-paralyzed animal (see 'Motor-related complex spikes are rare for tail and eye movements', below) confirmed this laterality (N = 11; *Figure 4—figure supplement 3h*).

These Purkinje cells also showed an increase in complex spiking for the duration of translational motion in a preferred lateral direction, determined to be rightwards motion for clockwise motion-preferring cells and vice versa (mean rate increase above baseline = 280 ± 20%; *Figure 4—figure supplement 1b*), suggesting that these cells respond to motion over a large area situated in the front half of the visual field. Finally, we observed an apparent homeostatic regulation firing in these cells where spontaneous complex spike rates were strongly depressed for several seconds following the robust complex spike responses elicited by rotational motion (normalized mean rate for one second following rotational stimuli = 37 ± 16% of spontaneous firing rates). Thus a high complex spike rate for the preferred direction of rotational motion may come at the expense of stochastic complex spikes. A homeostatic regulation of complex spike rates has also recently been observed in the mammalian cerebellum (*Ju et al., 2018*), though the underlying mechanism is not known.

The third prominent group of Purkinje cells had complex spike responses correlated with changes in whole-field luminance that were surprisingly heterogeneous in feature encoding compared to the notably stereotyped responses seen for the previous two groups (N = 25/61 cells; *Figure 4c* and *Figure 4—figure supplement 1c–e*; see Materials and methods). Purkinje cells with this luminance phenotype had complex spike responses that encoded either luminance increases (9/25) or decreases (11/25) or both (5/25; *Figure 4c* and *Figure 4—figure supplement 1d*) and the location of cells with different luminance response types was mixed across the central region of the cerebellum (*Figure 4—figure supplement 1e*). The latency from the onset of the preferred luminance transition to the first complex spike occurred for each cell with very little jitter, but the latency itself varied across cells (*Figure 4—figure supplement 1d*). Most whole-field luminance responses were transient such that cells fired just one complex spike for the preferred luminance change (mean = 0.80 ± 0.02 spikes). We did however observe, in two cells, different complex firing rates as a function of the ambient luminance presented that did not adapt over tens of minutes and therefore appear to encode ambient luminance through their complex spike rate (*Figure 4cii*, one-way ANOVA with Bonferroni post hoc correction, p<0.01; *Figure 4—figure supplement 1g,h*). Luminance-responsive Purkinje cells furthermore showed differing patterns of complex spike responses to local luminance changes during the translational motion of gratings (*Figure 4—figure supplement 1f*), suggesting that these cells have a wide range of receptive field sizes over which they integrate luminance.

In additional to having qualitative and quantitative differences in visual feature encoding, the three different types of Purkinje cell visual phenotypes described thus far also had notable differences in spontaneous complex spike rates (*Figure 4d*). Purkinje cells responding to rotational motion velocity had a significantly higher baseline firing rate than those with directionally selective motion onset responses (0.77 ± 0.1 Hz and 0.20 ± 0.02 Hz, respectively, p<0.001, Bonferroni post hoc correction). Purkinje cells responding most strongly to luminance or motor activity had intermediate baseline complex spike rates (0.28 ± 0.1 Hz and 0.34 ± 0.1 Hz, respectively).

Mapping the coordinates of Purkinje cell somata belonging to these three visual complex spike phenotypes supports a regional division of the cerebellum along the rostrocaudal axis where each of the three regions within the cerebellar hemisphere receives inputs from the same or similar inferior olive neurons carrying visual information (*Figure 4ei*). To examine the corresponding outputs of

Purkinje cells from these groups, we performed cell-attached electrophysiological recordings in combination with morphological reconstructions via stochastic single-cell labelling of Purkinje cells to visualize the axonal projections (N = 17 cells from 17 fish; *Figure 4eii*). Unlike the mammalian cerebellum, where all Purkinje cell axons project outside of the cerebellar cortex, zebrafish Purkinje cells can be divided into two anatomical populations - one with internally-projecting axons that contact eurydendroid cells (the equivalent of mammalian cerebellar nuclei neurons) and the other whose somata are more lateral and who have externally-projecting caudal axons that contact neurons in the vestibular nuclei (*Bae et al., 2009*; *Matsui et al., 2014*).

Strikingly, 6/7 Purkinje cells with caudally projecting axons exhibited a clear complex spike phenotype for directional rotational motion, whereas only 1/10 cells with an internal axon had this same phenotype (*Figure 4e*). We further reconstructed and aligned 50 singly-labelled Purkinje cell morphologies across fish to a reference brain. Although the somata of Purkinje cells with caudal (N = 23/50) and internal (N = 27/50) axons partially overlap (*Figure 4f*), the segregation of rotational motion responses with caudal axon anatomies in this dataset further support our definition of this functional region of Purkinje cells. We also found that Purkinje cell dendrites generally had a classic albeit simplified morphology with mostly planar dendrites (*Figure 4—figure supplement 2*) oriented orthogonally to the axis of parallel fiber extension across the cerebellum (*Knogler et al., 2017*), as seen in mammalian cerebellum (*Eccles et al., 1967*). Together, these results define three functional groups of Purkinje cells residing in different regions across the cerebellum. These groups operate with different complex spike frequencies and encode distinct visual features related to visuomotor behaviors, and one group also sends the majority of its projections to a different downstream area than the others.

Motor-related complex spikes are rare for tail and eye movements

As discussed above, motor regressors did not significantly contribute to complex spike activity in the majority of Purkinje cells (N = 49/61) despite an abundance of visually-evoked fictive behavior and the use of multiple motor regressors to capture different motor features. We nonetheless used this small group of Purkinje cells with motor-related complex spike responses to examine motor feature encoding (*Figure 4—figure supplement 3*).

We analyzed complex spike responses from Purkinje cells during spontaneously-evoked swimming in blank trials as well as in trials where visual stimuli elicited swimming and confirmed that some complex spikes were indeed correlated with swimming activity even in the absence of visual stimuli (*Figure 4—figure supplement 3a*). Swim-related responses were however unreliable such that a complex spike occurred on fewer than half of swim bouts on average for these cells (mean probability = 0.38 ± 0.07 for stimuli trials, N = 9 cells; mean probability for blank trials = 0.42 ± 0.07, N = 5 cells; p<0.05, Wilcoxon signed rank test). Aligning the subset of swim bouts that were positive for motor-related complex spikes showed that the latency from bout onset to the occurrence of a complex spike in blank trials varied considerably for an individual cell, in contrast to the fixed latencies for most visual-driven complex spikes (*Figure 4—figure supplement 3b*, compare with *Figure 4* and *Figure 3—figure supplement 2*). This is consistent with observations that complex spikes do not show phase-locking with stereotyped locomotor movements (*Apps, 1999*). Some Purkinje cells showed a decrease in complex spikes during swim bouts with a subsequent increase following bout offset (mean probability of a complex spike during bout <0.02, N = 3 cells; *Figure 4—figure supplement 3c*) however this was rarer than those with motor-related increases (*Figure 4—figure supplement 3d*). Unlike the spatial mapping seen for Purkinje cells with visual complex spike responses, Purkinje cells with motor-related complex signals were distributed across the cerebellum with no apparent clustering (*Figure 4—figure supplement 3e*).

We observed that both translational and rotational visual motion induced frequent bouts of fictive swimming in fish (*Figure 3b*); however the complex spike responses during these visual stimuli in most Purkinje cells did not correlate well on a trial-by-trial basis with swim bouts (*Figure 3b*, *Figure 3—figure supplement 2*) and were thus classified from multilinear regression analysis as sensory (visual), as described above. Rotational windmill stimuli are however known to evoke stereotyped eye movements known as the optokinetic reflex (*Easter and Nicola, 1996*), therefore complex spike responses to rotational visual motion could relate to the activation of eye rather than tail muscles. Studies of the cerebellar control of eye movements have shown evidence that climbing fibers provide eye motor error signals, which could account for the prominent complex spike signals observed

in Purkinje cells in the caudolateral cerebellum during rotational windmill motion. In order to examine the potential contribution of eye movements to complex spikes in this group of Purkinje cells, we performed cell-attached recordings from Purkinje cells in the caudolateral cerebellum in the semi-paralyzed zebrafish, where the eyes were free to move and were tracked with a high-speed camera (see Materials and methods). The independent movement of each eye was then used to build a set of twelve regressors corresponding to eye position and velocity in different directions (*Figure 4—figure supplement 3f*).

Least-squares multilinear regression was used to analyze the complex spike activity of all cells with the existing set of sensory regressors for visual features and the twelve new eye motor regressors. We once again observed a clear bias for a visual complex spike phenotypes across Purkinje cells (N = 11/13), with only two cells whose best regressor related to eye movement (*Figure 4—figure supplement 3g,h*). A further analysis of the complex spike phenotypes of these latter two cells showed that in one case, the eye movement was exceptionally well-correlated with one visual feature (directional rotational velocity) that it was hard to disambiguate the true sensory vs motor nature of the complex spike response (*Figure 4—figure supplement 3i*, cell 2). For the other cell (*Figure 4—figure supplement 3i*, cell 3), a strong luminance (sensory) complex spike phenotype was identified through additional autocorrelation analyses (p<0.001 from Ljung-Box Q-test; r = 0.67 for correlation with the luminance regressor) in addition to the moderate correlation with eye movement (r = 0.32 for correlation with eye motor regressor). Nonetheless, the majority of Purkinje cells in this region could be clearly assigned to a visual complex spike phenotype since these cells showed very stereotyped complex spike responses to directional rotational stimuli that did not correlate well with the variable eye movements observed across trials (*Figure 4—figure supplement 3j,k*). We conclude from these data that the complex spike responses during rotational visual motion are predominantly sensory rather than motor. It is furthermore important to note that these responses are equally prominent in electrophysiological recordings in the paralyzed fish, where the eyes cannot move, as in the electrophysiological and functional imaging experiments where the eyes are free and track the stimulus (compare *Figure 2*, *Figure 3f–g*, and *Figure 4—figure supplement 3*).

Simple spike responses across the Purkinje cell population are highly modulated by motor efference copies during fictive swimming

Having observed that Purkinje cells can be clustered into functional regions defined by their visual complex spike responses and anatomical features, we next wanted to understand how simple spike responses were organized across the cerebellum. Multilinear regression showed that many visual and motor features contributed to simple spike responses in individual Purkinje cells, such that response phenotypes were broader than those observed for complex spike activity (*Figure 5a* and *Figure 3e*), as expected in a circuit where many parallel fibers converge on a single Purkinje cell (*De Zeeuw et al., 2011*). Although simple spike rates were modulated to some extent by many of the visual stimuli presented, motor activity significantly modulated simple spike activity in nearly all Purkinje cells across the cerebellum (N = 60/61) and was in fact the main contributor to modulating simple spike activity in the majority of cells (N = 44/61; *Figure 5a*).

Different motor regressors accounted for various motor features including swim onset, offset, duration, and the continuous quantitative readout of swim strength, termed vigor (calculated from the standard deviation of the ventral root signal). Simple spike firing rates for these cells had consistently larger contributions to their activity from swim vigor than from bout duration or any other motor regressor, suggesting that fictive swimming activity is encoded in a graded manner by simple spike output. Mean simple spike firing rates across the population were on average twice as high during a bout as during the rest of the trial (mean rate during a bout = 14.5 ± 1.5 Hz vs 7.6 ± 0.8 Hz at rest; p<0.001, Wilcoxon signed rank test). Trial-averaged simple spike responses across the population appeared as a continuum rather than as clusters (*Figure 5b*), suggesting that the organization of parallel fiber inputs does not follow the same regional specificity as climbing fiber inputs across the cerebellum. Our analyses furthermore revealed that translational and rotational motion of visual stimuli, regardless of direction, was the most prominent sensory feature encoded by simple spike activity (*Figure 5a*). These findings suggest that Purkinje cells are integrating inputs from motion responsive granule cells with different directional tuning (*Knogler et al., 2017*).

In order to rule out potential sensory contributions to simple spike rates during visually-evoked behaviors, we analyzed simple spike activity during additional blank trials where no visual stimuli was
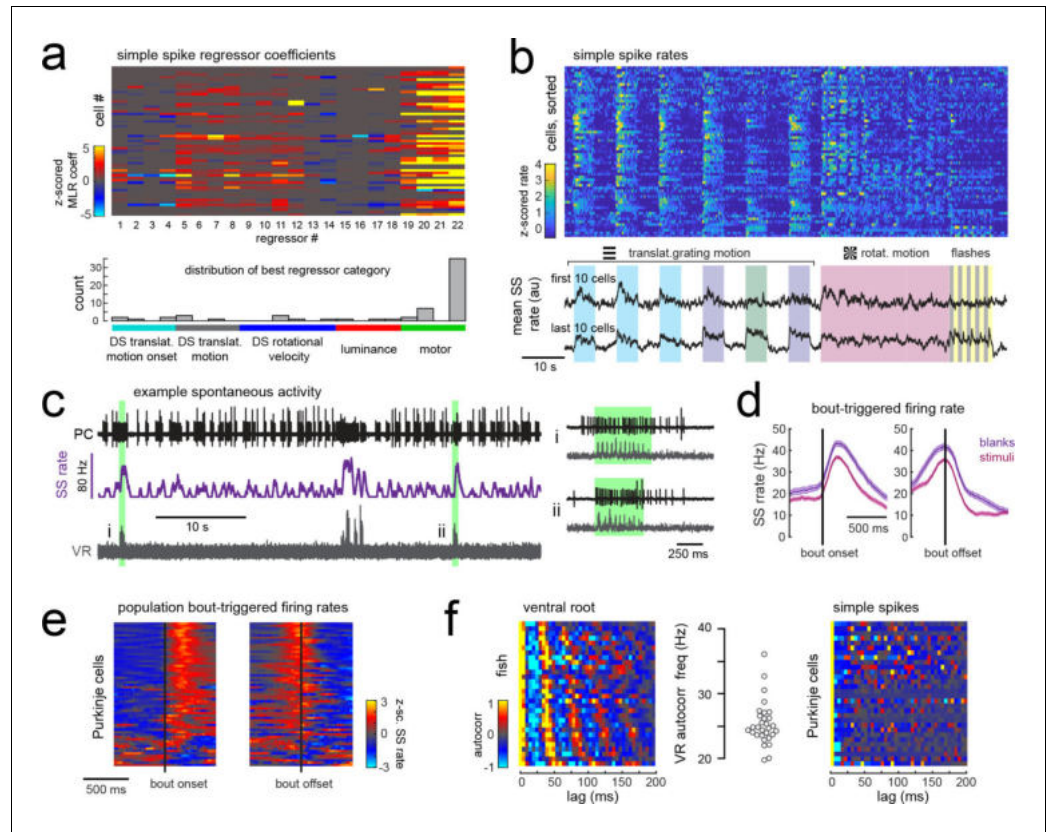
Figure 5. Simple spike rates in most Purkinje cells are increased during fictive swimming. (**a**) Above, heatmap of coefficient weights for the simple spike firing rates of 61 cells from least-squares regression with a full set of 24 stimulus- and motor-related variables (see Materials and methods for more details). Below, histogram showing the distribution of cells' highest regressor weight and the associated sensory/motor categories. (**b**) Upper panel, heatmap of z-scored simple spike rates for all 61 cells sorted by decreasing motor coefficient weight. Lower panel, the mean simple spike rate for the ten cells with the highest (upper trace) and lowest (lower trace) motor coefficient weights. (**c**) Left panel, example cell-attached Purkinje cell recording (PC, upper trace, black) from a blank trial (no stimuli) with simultaneous ventral root recording (VR, lower trace, gray, shown as a moving standard deviation). The simple spike rate is also shown (SSrate, middle trace, purple). Right, the bouts highlighted in green on an expanded timescale show the close timing of fictive bout onset and simple spike activity. (**d**) The bout on- and off-triggered mean simple spike firing rates for the cell in c) during blank recordings (purple) and stimulus trials (pink). (**e**) Z-scored heatmap of bout on- and off-triggered mean simple spike firing rates across all Purkinje cells sorted by mean firing rate in the 300 ms following bout onset. (**f**) Mean autocorrelation heatmap for simple spikes (SS, upper panel) and for ventral root recordings (VR, lower panel) for all Purkinje cells that showed spontaneous swimming bouts during blank trials (N = 30 cells from 30 fish), sorted by time to first peak in the VR autocorrelation. Right, the first significant peak in the VR autocorrelation for each recording is plotted to give the mean fictive swim frequency for each fish.

DOI: https://doi.org/10.7554/eLife.42138.016

presented (*Figure 5c*). Purkinje cells exhibit considerable spontaneous simple spike firing in the absence of any sensory stimuli or motor activity (*Hsieh et al., 2014*; *Sengupta and Thirumalai, 2015*); however fictive swim bouts consistently increased simple spike firing well above baseline levels (*Figure 5c–e*) and to an ever greater extent for spontaneous bouts in the absence of visual stimuli (p<0.01, Wilcoxon signed rank test). Aligning the mean bout-triggered simple spike rates for all Purkinje cells at bout onset and offset confirmed that the majority of cells have consistent motor-related increases in simple spike activity that begin at bout onset and return to baseline following bout offset (*Figure 5e*) although a small number of Purkinje cells instead show bout-triggered decreases in simple spike firing rates (*Figure 5e*), as observed elsewhere (*Scalise et al., 2016*). As expected for

rhythmic locomotor output, the ventral root signal was highly autocorrelated for all fish with a mean autocorrelation frequency across fish of 26.7 ± 0.7 Hz (N = 30 fish; *Figure 5f*), consistent with the slow swim bout frequency reported for restrained zebrafish larvae (*Severi et al., 2014*). The autocorrelation analyses of simple spike firing for each Purkinje cell during a spontaneous fictive bout revealed however no significant autocorrelations for simple spikes at any frequency. Unlike the modulation of simple spike firing rate seen during step phase in locomoting rats (*Sauerbrei et al., 2015*), simple spikes in zebrafish Purkinje cells do not appear to be modulated in phase with rhythmic swimming activity but are nonetheless graded by swim strength. This suggests that individual Purkinje cell firing does not encode the activation of individual muscles involved in rhythmic swimming.

Motor activity is broadly represented in granule cell signals

The timing and reliability of swim-related simple spike activity is consistent with motor efference signals from spinal locomotor circuits during fictive swimming that arrive along mossy fibers to the granule cell layer and subsequently to Purkinje cells. A disynaptic pathway from spinal premotor interneurons to the granule cells via the lateral reticular nucleus was recently found that would convey information about ongoing network activity in the spinal cord (*Pivetta et al., 2014*). There is growing evidence across species that granule cells are strongly driven by ongoing locomotor activity (*Ozden et al., 2012*; *Powell et al., 2015*; *Jelitai et al., 2016*; *Giovannucci et al., 2017*; *Knogler et al., 2017*). Furthermore, extensive electrophysiological recordings from the granule cells of the cerebellum-like circuit of the electric organ in the electric fish revealed that an overwhelming majority (>90%) of granule cells receive depolarizing motor efference signals during electric organ discharge, although this translated into spiking in only ~20% of granule cells (*Kennedy et al., 2014*).

In order to characterize motor-related granule cell activity and its potential contribution to motor-related excitation in Purkinje cells across the cerebellum, we imaged responses in the granule cell population to the same set of visual stimuli while tracking tail and eye movement (*Figure 6a*). Multi-linear regression was once again used to disambiguate responses to sensory stimuli and motor activity. Across fish (N = 7), we observed that granule cell activity was strong and widespread during swimming activity, both in the somatic layer and across the parallel fiber layer (*Figure 6a*). Granule cell activity relating to eye movements was weaker but also widespread (*Figure 6a*). These findings suggest that a large number of granule cells receive mossy fiber inputs relaying motor efference copies that drive them to fire, and they in turn drive broad motor-related activation of simple spikes in Purkinje cells (*Figure 2a,b*). These findings show more widespread motor-related representations in comparison to previous population-wide analyses of granule cell activity (*Knogler et al., 2017*) due to the abundance of behavior elicited by the current set of visual stimuli.

In order to understand the temporal patterning of swim-related motor signals in the granule cells layer, we performed additional electrophysiological recordings from randomly targeted granule cells across the cerebellum while simultaneously recording ventral root activity to identify fictive swim episodes. These recordings revealed several granule cells with negligible firing rates in the absence of motor activity but that showed large, significant increases in their spike rates during fictive bouts (N = 6/8 cells; mean firing rate at rest = 1.3 ± 0.3 Hz vs 25.7 ± 7.6 Hz during a bout; p<0.005, Wilcoxon signed rank test; *Figure 6b–d*; *Figure 6—figure supplement 1*). These granule cells had graded responses correlated with swim strength and could reach high instantaneous firing frequencies of up to 150 Hz during a fictive bout, similar to the burst firing seen in mammalian granule cells during locomotion (*Powell et al., 2015*) or whisker stimulation (*van Beugen et al., 2013*). Half of these motor-excited granule cells (N = 3/6) also showed significant autocorrelations in their spiking activity during fictive swimming (p<0.001, Ljung-Box Q-test; *Figure 6e*). The frequency of the spike autocorrelations for these cells was comparable to the fictive swim frequency obtained from the ventral root (mean difference in frequency = 1.3 ± 0.6 Hz, N = 3), suggesting that the periodicity of granule cell spiking is related to the swimming activity (*Figure 6e*). The phase of the granule cell spiking with respect to the ipsilateral ventral root activity varied however across cells, arriving either in phase, with a lag, or in antiphase (*Figure 6f*).

Together, these results suggest that motor efference copies are relayed along mossy fibers to many granule cells to drive burst firing during swimming bouts, whether fictive or real. In turn, parallel fibers deliver graded swim-related excitation to nearly all cerebellar Purkinje cells. We are confident that these are true efference signals and not motor-related sensory input from proprioception or the lateral line since the fish is paralyzed and the muscles are not moving during these

Figure 6. Granule cells across the cerebellum code for motor activity with high fidelity. (a) Heatmaps of the z-projected mean voxelwise correlation coefficients of two-photon granule cell GCaMP6s signals from multilinear regression with example sensory and motor regressors averaged across seven fish (see Materials and methods). Scale bar = 50 microns. Upper right, cartoon of experimental set-up. (b) Left, cartoon of experimental set-up. Right, upper panel, example cell-attached recording from a granule cell (gc, upper trace, black) from a blank trial with simultaneous ventral root recording (VR, lower trace, gray). The granule cell firing rate is also shown (spike rate, middle trace, orange). The bout highlighted in green (i) is shown below on an expanded timescale. (c) The bout on- (left) and off- (right) triggered mean firing rates for this granule cell during blank recordings (orange) and stimulus trials (red). (d) Z-scored heatmaps of bout on- (left) and off- (right) triggered mean firing rates in all granule cells sorted by mean firing rate in the 300 ms following bout onset (N = 8 cells from eight fish). (e) Mean autocorrelation heatmap for spikes (upper panel) and ventral root recordings (VR, lower panel) for all granule cells from d), sorted by time to first peak in the VR autocorrelation. The red arrowheads signify granule cells with significant spike autocorrelations during fictive swim bouts (N = 3; p<0.001, Ljung-Box Q-test; see Materials and methods). Right, the first significant peak in the VR autocorrelation for each recording is plotted to give the mean fictive swim frequency for each fish. The red circles are the mean spike autocorrelation frequency obtained from the three significantly autocorrelated granule cells. (f) An example bout from the cell indicated in e), which was located ipsilateral to the ventral root recording. The smoothed spike rate (red) is in antiphase with the ipsilateral fictive tail contractions (grey). See also *Figure 6—figure supplement 1*.

The following figure supplement is available for figure 6:

Figure supplement 1. Many granule cells show significant modulation of their firing rates during fictive swimming bouts.

electrophysiological experiments. The widespread increases in Purkinje cell calcium signals observed in the behaving animal during swimming (*Figure 2a,b*) therefore are likely to reflect simple spike bursts in Purkinje cells (*Figure 1—figure supplement 2*) driven by the high frequency firing of one or more presynaptic granule cells carrying motor efference information.
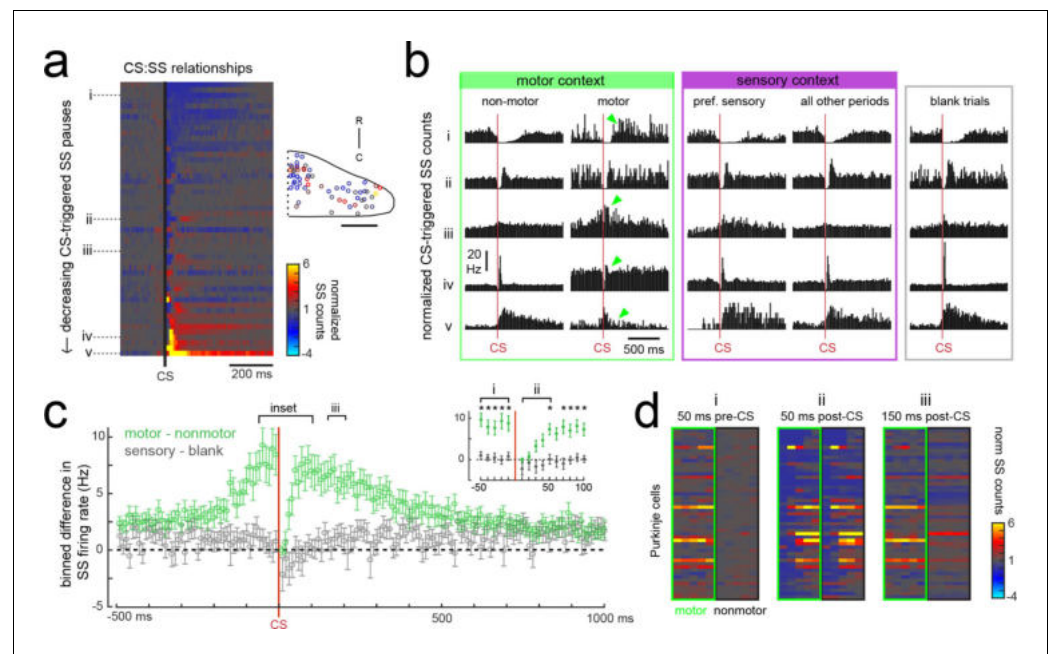

Figure 7. Purkinje cells modify their simple spike output in a complex spike- and motor context-dependent way. (a) Heatmap of complex spike-driven simple spike (CS:SS) counts for each cell normalized to the mean over 100 ms preceding a complex spike. Cells are sorted by decreasing simple spike pause and increasing excitation. The inset shows the location of these cells colored by the normalized difference in simple spiking in the 50 ms following the CS. (b) The mean complex spike-triggered simple spike count (10 ms bins) is shown for five example cells (as indicated in a) for five different contexts. Left (green box), in the presence ('motor') versus absence ('non-motor') of fictive swimming episodes. Under non-motor conditions these different Purkinje cells show, respectively, a CS-induced i) long SS pause, ii) short SS pause with rebound increase, iii) no change in SS, iv) short SS increase, and finally a v) long SS increase. Green arrows highlight changed patterns during motor context. Middle (magenta box), CS:SS relationships across preferred versus all other sensory contexts (only non-motor periods included). Right (grey box), the CS:SS relationship during blank trials (no stimuli, only non-motor periods). Vertical scale bar indicates the rate conversion for 0.2 spikes/10 ms bin (20 Hz). (c) Green markers show the mean normalized simple spike rates (calculated from 10 ms bins) for all Purkinje cells centered on the occurrence of a complex spike during a fictive bout minus those occurring at any other point (N = 51 cells). Data are mean ± SEM. Grey markers, simple spike rates centered on the occurrence of a complex spike during all sensory stimuli minus those occurring during blank trials (N = 53 cells). The dashed black line indicates zero difference between conditions. Inset, the window around complex spike onset shown on an expanded timescale. Asterisks indicate p<0.05 for motor minus nonmotor conditions (green markers) as computed by the Wilcoxon signed rank test. Grey markers, no significant differences. (d) Heat maps are shown for individual Purkinje cell binned simple spike counts over the three different 50 ms periods as indicated in e. Complex-spike triggered simple spike counts are separated for each cell for those complex spikes occurring during a fictive bout (left column of heatmaps, outlined in green) or at any other time (right column of heatmaps, outlined in black).
DOI: https://doi.org/10.7554/eLife.42138.019

The following figure supplement is available for figure 7:

Figure supplement 1. Individual Purkinje cells preferentially combine sensory and motor information.
DOI: https://doi.org/10.7554/eLife.42138.020

Purkinje cells combine sensory and motor information from distinct inputs

Our data suggests that as a population, Purkinje cells preferentially encode visual features in their complex spike activity whereas swimming activity, arriving in the form of motor efference copies, is predominantly encoded by simple spikes. Breaking this down by group, we find that Purkinje cells belonging to the three different visual complex spike phenotypes described above have simple spike activity that is correlated most strongly with motor activity (fraction of total signal from motor regressors = 0.65 ± 0.05, 0.54 ± 0.07, 0.76 ± 0.02 for the three visual complex spike phenotypes; *Figure 7—figure supplement 1a*). In contrast, for the small group of Purkinje cells with dominant motor-related complex spike phenotypes, the contribution of motor activity to simple spike activity is relatively low (0.35 ± 0.12) and simple spikes are instead broadly influenced by a combination of sensory and motor features (*Figure 7—figure supplement 1a*). This relationship holds true for individual Purkinje cells as well (*Figure 7—figure supplement 1b*). Together, these data suggest that sensory and motor information is preferentially combined in Purkinje cells from distinct sources.

Motor context alters the relationship between complex spike and simple spike activity

It is well-established that the occurrence of a complex spike can alter simple spike activity in a Purkinje cell both acutely and across longer timescales (*De Zeeuw et al., 2011*). On a short timescale, complex spikes typically cause a brief pause of tens of milliseconds in simple spike firing that can be followed by an increase or decrease in simple spikes lasting hundreds of milliseconds. The particular complex spike-triggered change in simple spiking is robust for a given Purkinje cell but varies considerably across cells (*Zhou et al., 2014*; *Zhou et al., 2015*; *Xiao et al., 2014*). Similar to previous findings, we observed heterogeneity in the relationship between complex and simple spikes across Purkinje cell recordings (*Figure 7a*). At the most extreme end, we observed complex spike-induced pauses or increases in simple spike rates in different cells that took several hundred milliseconds to return to baseline. These pauses or increases in simple spiking may be attributable to a toggling action of the complex spike to shift the Purkinje cell between 'up' and 'down' states (*Loewenstein et al., 2005*; *Sengupta and Thirumalai, 2015*). Several cells had brief pauses (tens of milliseconds) following a complex spike which left simple spikes otherwise unchanged, whereas others showed a brief increase in simple spike firing. Previous studies have suggested that the modulation of simple spike firing by a complex spike is related to the cell's location within the cerebellum (*Zhou et al., 2014*; *Zhou et al., 2015*). We did not, however, observe any clear spatial organization of the complex spike-simple spike relationship in this dataset (*Figure 7a*).

The current behavioral state of the animal should provide important contextual information for cerebellar circuits, therefore we hypothesized that the modulation of simple spikes by a complex spike might be altered in different sensory and motor contexts. In periods during which the fish was at rest (no fictive swimming), the relationship between a complex spike and the simple spike firing rate was similar whether or not visual stimuli were being presented (*Figure 7b*, 'non-motor' versus 'blank trials'). When the fish was performing a fictive swim bout however, the effect of a complex spike on simple spike output appeared diminished (*Figure 7b*, 'non-motor' versus 'motor'), which was not the case for complex spikes occurring during a cell's preferred complex spike sensory stimulus versus those occurring during all other periods (*Figure 7b*, 'pref. sensory' versus 'all other periods').

The unique effect of motor context on this relationship is likely related to the finding that many Purkinje cells have simple spike rates that are strongly excited by motor activity (*Figure 5e*), therefore a complex spike stochastically occurring during a bout would be faced with simple spikes rates that are significantly higher than baseline. Upon closer examination of the temporal window around the occurrence of a complex spike, we observed that the acute effect of a complex spike to modulate simple spike rates was identical between motor and non-motor periods for only a 50 millisecond period following the complex spike, after which time simple spiking returned to high levels correlated with ongoing behavior (*Figure 7c,d*). This temporal window was the same across cells regardless of whether the baseline modulation by a complex spike was to pause or facilitate simple spike firing. These findings suggest that the acute effect of a complex spike to change simple spike output in a Purkinje cell is temporally restricted by the behavioral state of the animal and that plasticity
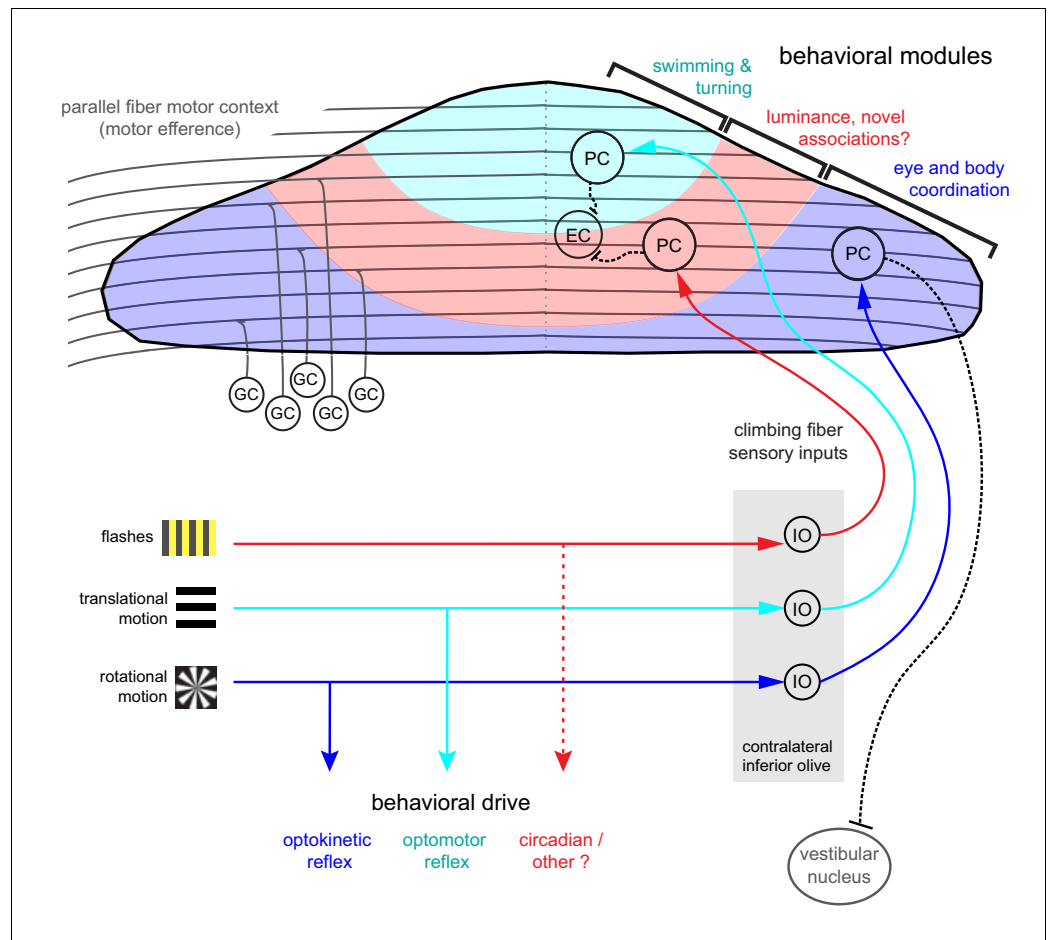
Figure 8. Organization of the larval zebrafish cerebellum Granule cells (GCs) send long parallel fibers (grey lines) that contact Purkinje cells (PCs) across the cerebellum and broadly relay motor efference copies of locomotor activity (swimming). Sensory information relating to different visual features are sent by climbing fibers of inferior olive neurons (IO) to stereotyped regions of the contralateral Purkinje cell layer. These visual stimuli contribute to several reflexive behaviors; rotational motion drives the optokinetic reflex of the eyes, translational forward motion drives the optomotor swimming reflex while others, such as luminance, may drive behavior over longer (e.g. circadian) timescales. The three distinct functional regions in the zebrafish cerebellum defined by Purkinje cell complex spike sensory responses that encode these different visual features represent putative behavioral modules. Information about the onset of directional translational motion is preferentially sent to PCs in the rostromedial region of the cerebellum (cyan) and would be important for coordinating turning and swimming, while information about the direction and velocity of rotational motion as would be needed for coordinating eye and body movements is sent to the caudolateral region (blue). The central region (red) receives information about luminance and may provide a substrate for learned sensorimotor associations. Axons from PCs (black dashed lines) of the rostromedial and central regions have mostly internal axons that contact eurydendroid cells (EC) within the cerebellar cortex. Axons from PCs in the caudolateral region have mostly external axons that exit the cerebellum and contact neurons in the caudally-located ipsilateral vestibular nucleus.
DOI: https://doi.org/10.7554/eLife.42138.021

mechanisms relying on coincident complex spike and simple spike activity will have a unique dependence on motor context (see discussion).

Discussion

In this study, we have taken advantage of an innate set of visually-driven motor behaviors in the larval zebrafish to comprehensively interrogate how Purkinje cells encode sensory and motor features

relating to these behaviors at high spatial and temporal resolution across the cerebellum. Our population imaging data across both the Purkinje cell and granule cell populations are supported by single cell electrophysiological recordings that elucidate complex spike and simple spikes. We furthermore show the robustness and specificity of these patterns across behavioral conditions regardless of whether the tail and/or eyes are freely moving or paralyzed. We show that Purkinje cells fall into anatomically clustered regions that are functionally defined by complex spike responses that convey mostly sensory information. On the other hand, simple spikes convey mostly motor-related information about tail and eye movement. During visuomotor behaviors, these two input streams converge on Purkinje cells in specific regions of the cerebellum and communicate the presence of distinct visual features together with motor context. Each of these regions therefore likely represents a behavioral module whose neural computations are used to guide sensorimotor integration and motor learning in the cerebellum.

Anatomical and functional organization of cerebellar regions

The three distinct regions formed along the rostrocaudal axis of the larval zebrafish cerebellum we define here based on distinct Purkinje cells sensory complex spike phenotypes to visual stimuli should receive topographically-specific climbing fiber inputs from the inferior olive (*Figure 8*; *Ozol et al., 1999*). The presence of these discrete complex spike response phenotypes across Purkinje cells suggests that zebrafish climbing fiber inputs from the inferior olive have undergone refinement by seven dpf to innervate only one Purkinje cell, in support of other findings (*Hsieh et al., 2014*; *Hsieh and Papazian, 2018*). Ongoing work characterizing the physiology and anatomy of inferior olive neurons and their climbing fibers (unpublished observations) supports this regional characterization and, together with studies of Purkinje cell output to eurydendroid cells, will further our understanding of these anatomical regions.

Differences in developmental timing (e.g. birthdate) are known to contribute to the formation of a topographic functional map in the cerebellum across species (*Hashimoto and Hibi, 2012*). In zebrafish, Purkinje cell development occurs in waves that map onto the same regions we describe here, beginning with a large rostromedial cluster and a smaller, caudolateral cluster and later filling in the central region to form a continuous layer (*Hamling et al., 2015*). Just like in mammals, all climbing fibers cross the midline after leaving the inferior olive and contact the somata or proximal dendrites Purkinje cells in the contralateral hemisphere of the zebrafish cerebellum (*Takeuchi et al., 2015*). The topography of early afferent climbing fiber connectivity onto Purkinje cells is likely hard-wired, as in mammals it is guided by chemical cues and does not depend on developmental activity (see *Apps and Hawkes, 2009* for review). Although all ipsilateral climbing fibers enter the cerebellar cortex as one bundle at larval stages, in the adult, additional fiber bundles are visible (*Takeuchi et al., 2015*), suggesting that other routes or types of information are added for communication between the inferior olive and cerebellar cortex at later stages. Regional differences in cytoarchitecture and patterns of molecular markers such as zebrin have also been useful for identifying related Purkinje cells into groups in the mammalian cerebellum (see *Cerminara et al., 2015* for review). Although in larval zebrafish all Purkinje cells are zebrin-positive (*Bae et al., 2009*), many other genes are expressed in restricted patterns in the zebrafish (*Takeuchi et al., 2017*) and mammalian cerebellum (*Hawkes, 2014*) that may help define the subdivision of Purkinje cells into clearly-defined subregions within the cerebellum.

The organization of the cerebellum is thought to impart distinct functional roles across regions, such that each group of Purkinje cells processes sensorimotor information relating to a different behavioral component (*Witter and De Zeeuw, 2015*). Although we only probed one sensory modality to drive behavior, zebrafish are highly visual animals that perform robust visuomotor behaviors at the larval stage, including prey capture, optokinetic and optomotor responses, and associative learning with a conditioned visual stimulus (*Easter and Nicola, 1996*; *Budick and O'Malley, 2000*; *Aizenberg and Schuman, 2011*; *Harmon et al., 2017*). Visual information is therefore a highly salient sensory modality at this age and in accordance with this strong ethological relevance we find that the complex spike sensory responses to visual stimuli provide an overarching organization of the Purkinje cell layer into putative behavioral modules (*Figure 8*). Previous studies have used confocal imaging and optogenetics to identify general regions of the cerebellum that are important for optomotor and optokinetic responses (*Matsui et al., 2014*). Our current results build on these maps with an expanded set of visual stimuli, high-resolution two-photon population imaging, and single-

cell electrophysiology, to comprehensively describe visual and motor feature coding from the level of single spikes to population activity.

We see little evidence for the encoding of multiple visual features in these complex spike responses, however we expect to find representations of features from multiple sensory modalities in individual Purkinje cells arising from the multimodality of inferior olive neurons (*Ohmae and Medina, 2015*; *Ju et al., 2018*). It will be of great interest to see if the same spatial mapping by complex spike phenotype is conserved across other sensory modalities. Many other sensory systems are active at this age and provide salient stimuli for larval zebrafish as demonstrated in behavioral studies. Larval zebrafish show innate behavioral startle responses to loud auditory cues across a range of frequencies (*Bhandiwad et al., 2013*), however functional imaging across the brain suggests that the neural coding of auditory stimuli at this stage is generic and underdeveloped in zebrafish compared to the visual modality (*Vanwalleghem et al., 2017*). In contrast, the activity of many neurons across the brain including the cerebellum are differentially modulated by vestibular inputs at larval stages (*Favre-Bulle et al., 2018*; *Migault et al., 2018*). Given the pronounced complex spike responses we observe in response to rotational motion in the Purkinje cells with axonal output to the vestibular nucleus, it is likely that the coordination of vestibular and visual inputs during rolling movements (the vestibulo-ocular reflex), critically engages the cerebellum of the larval zebrafish. Although the larval zebrafish exhibits a broad repertoire of innate behavioral responses to many other stimulus modalities including touch, the lateral line, and olfaction (see *Fero et al., 2011* for review), there is a lack of physiological data to understand how these signals are encoded in the central nervous system and the cerebellum in particular. It is furthermore conceivable that other sensory systems become more important at later developmental stages, for examples olfactory processing of cues for kin recognition and social behaviors in the juvenile fish (*Dreosti et al., 2015*) or lateral line-mediated schooling behaviors in the adult (*Miller and Gerlai, 2012*).

In support of the spatial division of the cerebellum by visual complex spike phenotypes that we show in the current study, previous findings from a completely different behavioral paradigm in larval zebrafish also found three complex spike regions with a similar organization. *Harmon et al., 2017* developed an associative learning task to pair visual stimuli with an electric shock to elicit conditioned swimming responses. They found, using single-cell electrophysiological recordings, that Purkinje cell complex spike patterns in their conditioning paradigm were spatially and functionally clustered into three regions along the rostrocaudal axis that overlap well with the regions described here. These complementary findings suggest that this regionalization is of fundamental importance across modalities and behaviors. However, experimental attempts at associative learning using auditory stimuli have been unsuccessful at this stage and even in the 6 week-old larva (*Thompson, 2016*), suggesting a prioritization of visual information for the earliest motor learning in larval zebrafish. Future studies are needed to examine how the function and organization of the zebrafish cerebellum across regions may change to reflect an increasing complexity and repertoire of sensorimotor behaviors at later developmental stages.

Complex spikes use different temporal bases to encode specific visual features important for the animal's behavioral repertoire

Our results show that that majority of Purkinje cells across the cerebellum encode visual and not motor information in their complex spike activity. We observed a remarkably discrete and complete classification of nearly all Purkinje cells (>90%) for a specific visual complex spike phenotype whose sensory nature was clearly distinguishable from motor-related signals of eye and tail behavior. These visual complex spike phenotypes were distinct between the three groups of Purkinje cells in different rostrocaudal regions. Below, we discuss how the representation of these different visual features may serve as behavioral modules that relate to the particular behavioral repertoire of the larval zebrafish and to findings from the mammalian literature.

Transient changes in the direction of translational visual motion convey information critical for driving locomotion and turning behaviors, or in the case of visual reafference, for evaluating the success of a directed behavior. In the larval zebrafish, Purkinje cells of the rostromedial cerebellum reliably encode acute, directional changes of motion in the visual field with a preferred directional tuning. During the optomotor response, fish swim to stabilize their position with respect to the visual field. Larval zebrafish also perform a variety of low and high-angle turns at this stage while exploring, performing escape maneuvers, and hunting prey, therefore complex spike signals updating the brain

about a transient change in motion in the visual field have strong ethological relevance. This population of Purkinje cells whose complex spikes encode directionally-selective motion onset are reminiscent of the directionally-tuned Purkinje cells in the oculomotor vermis of posterior lobes VI and VII in primates, where complex spike tuning organizes the cells into functional groups whose simple spikes encode real-time eye motion (*Soetedjo and Fuchs, 2006*; *Herzfeld et al., 2015*).

In the caudolateral region of the cerebellum we find Purkinje cells with strong complex spike responses to unidirectional rotational motion and axons that project primarily to the octaval (vestibular) nuclei in zebrafish (*Matsui et al., 2014*). These Purkinje cells fire complex spikes during visual motion in a temporal to nasal direction presented to the ipsilateral eye (with respect to the anatomical location of the Purkinje cell), resulting in a tonically elevated complex spike rate during visual motion in the preferred direction. This caudal region is likely the vestibulocerebellum, homologous to the mammalian flocculonodular lobe where Purkinje cells receive climbing fiber input conveying information about ongoing, opposing directional visual and rotational head motion that is used for vestibulo-ocular coordination (*Simpson and Alley, 1974*; *Ito, 1982*). Complementary imaging studies in larval zebrafish show strong, directionally-tuned responses in the activity of undefined cerebellar neurons in this same region (*Favre-Bulle et al., 2018*; *Migault et al., 2018*). Larval zebrafish perform slow steering maneuvers of the tail while navigating and also produce smooth eye movements while engaging in activities such as prey tracking (*McElligott and O'malley, 2005*), both of which result in slow changes in the visual field. In addition, zebrafish can control their eyes independently from each other, so these signals are likely to be integrated in the brain together with vestibular and body axis information to achieve coordinated movements. Notably, these zebrafish vestibulocerebellar Purkinje cells show complex spike responses not only to rotational but also to translational moving fields, which is not seen in mammals but has been observed in pigeons (*Wylie and Frost, 1991*). This finding may relate to the additional complexity of optic flow that arises during navigation in a three-dimensional world for birds and fish.

We furthermore observed that Purkinje cells in the caudolateral region have spontaneous complex spike rates an order of magnitude higher than those in the rostromedial region described above and show sustained high complex spike firing in response to their preferred stimulus. This could allow for increased temporal precision in order to generate fast and precise firing patterns as would be required when generating sensorimotor associations or coordinating smooth movements (*Porrill et al., 2013*; *Suvrathan et al., 2016*). The computation itself may in fact be different in this region since complex spikes could use conventional rate coding to encode the speed and direction of ongoing, slow movements of the visual field during behavior, as proposed by *Simpson et al., 1996* based on observations in the mammalian flocculonodular lobe across species. These findings challenge the assumption that the computations being performed across the cerebellum all follow the same rules and that the occurrence of a discrete event, rather than information about an ongoing event, is transmitted by complex spikes.

The heterogeneity of sensory complex spike coding of luminance in the intermediate region of the zebrafish cerebellum sets this group of Purkinje cells apart from the other two visual phenotypes We see both many differences in responses to luminance changes, including light/dark preference, tonic/phasic responses, latency from stimulus onset to complex spike, and receptive field size. We propose that these Purkinje cells are therefore well-suited to modulate a diversity of light-mediated behaviors in the larval zebrafish. Although the luminance stimuli in the current experiments were titrated to be moderate and thus not evoke acute behavioral responses, sudden strong decreases in luminance induce re-orienting navigational turns (*Burgess and Granato, 2007*) or escapes (*Temizer et al., 2015*) in zebrafish larvae and transient startle responses in the adult (*Easter and Nicola, 1996*), the latter two representing likely predator avoidance responses. With respect to these fast behaviors, a transient encoding of luminance change could serve to modulate these response circuits. Luminance increases spontaneous locomotor activity in larval zebrafish over longer timescales as well, which is used as a cue to regulate circadian rhythms and motivate feeding and exploratory behavior in the daytime (*Burgess and Granato, 2007*). There is also an innate preference for larval zebrafish to be in lighter areas of their environment, a behavior known as phototaxis (*Brockerhoff et al., 1995*). These latter behaviors would more likely make use of rate coding of ambient luminance, as observed in the complex spike output of some Purkinje cells, to provide sensory integration over long timescales (tens of minutes).

The differing luminance preferences and temporal dynamics across this group may furthermore be useful for learning novel associations. Indeed, a recent report by *Harmon et al., 2017* found that Purkinje cells in this central area of the larval zebrafish cerebellum (termed 'multiple complex spike cells' in this study) preferentially acquired complex spike responses to a conditioned visual stimulus during associative learning. As mentioned above, Purkinje cells in this central region are also born slightly later in development compared to the groups described above (*Hamling et al., 2015*), findings that together suggest this region may preferentially contribute to flexible or learned sensorimotor behaviors. This region may be similar to areas in the central zone (posterior lobes VI and VII) of the cerebellum in mammals, which support a wide range of behavioral functions (*Koziol et al., 2014*; *Stoodley et al., 2012*).

What signals are complex spikes encoding?

There is great debate about whether climbing fiber signals convey error, predictive, or novelty signals (see *Simpson et al., 1996* and *Streng et al., 2018* for reviews). The error hypothesis would suggest that the visually-evoked responses we observe here signal unexpected events or 'negative sensory events to be avoided' such as retinal slip (*Lang et al., 2017*). However, these signals are not necessarily a classical error signal (*Ito, 2013*), because in the current study we find that stimulus-evoked complex spikes are equally prominent in paralyzed fish as in experiments where the eyes and tail are free and track the stimulus. Furthermore, many complex spikes are robustly elicited by visual stimuli that do not acutely drive behavior, such as reverse motion or luminance changes.

Other work suggests that climbing fibers carry instructional signals for upcoming motor actions in a learned behavior, in the context of a reinforcement learning signal (*Ohmae and Medina, 2015*; *ten Brinke et al., 2015*; *Heffley et al., 2018*), or could provide the corrective drive used to initiate locomotion (*Ozden et al., 2012*). While we are not testing predictive signals in this study, it is nonetheless clear that for the complex spikes elicited during visual stimuli in our experiments do not signal an upcoming motor event. In cases when complex spikes are driven by the onset of directional translational motion, they occur with a consistently short latency (approximately 200 ms) whereas the latency to swim bout onset is much longer and more variable, and the presence of absence of these visual complex spikes across trials do not predict the occurrence of a swim bout.

Other hypotheses suggest that climbing fibers may encode novelty or salience signals related to sensory stimuli, although in fact these hypotheses do not exclude the previous ones since climbing fibers may be able to carry different types of signals by multiplexing (*Ohmae and Medina, 2015*). The complex spike responses we observe in this study do not encode all novel or salient visual stimuli as we see that responses are selective for certain visual features. In our experiments, complex spikes do not habituate but are consistently elicited by visual stimuli, across many trials and many hours, in contrast to what might be expected if complex spikes encoded novelty. It remains however to be seen how robust these responses are over longer timescales, as previous work has suggested the complex spike response to a novel sensory stimulus is subject to habituation only with repeated exposure across many days (*Ohmae and Medina, 2015*).

Since the above hypotheses were mostly developed with respect to observations in the context of cerebellar learning, the role of complex spikes may be different for innate feature coding. Our results suggest an innate coding of sensory features in climbing fiber signals in the naïve animal, consistent with observations of visual and multimodal sensory responses carried by climbing fibers in other studies in zebrafish (*Hsieh et al., 2014*; *Sengupta and Thirumalai, 2015*; *Scalise et al., 2016*; *Harmon et al., 2017*) and mammals (*Ohmae and Medina, 2015*; *Ju et al., 2018*). The complex spikes resulting from climbing fibers tuned to specific sensory features could subsequently drive the learning that underlies novel associations, including predictions, as arises when an animal experiences the repeated pairing of a complex spike-evoking stimulus and a motor event (*Ito, 2001*; *Harmon et al., 2017*). In this context, the sensory complex spike signal could be interpreted as a sensory prediction error that drives associative learning. Additional work is needed to determine how the complex spike responses encode different sensory modalities both in the naïve animal and throughout the course of learning.

Motor efference copies in the cerebellum

Our population-wide imaging and extensive electrophysiological recordings show that most Purkinje cells across the cerebellum encode the current behavioral state (motor context) of the animal through a pronounced increase in simple spikes during locomotor behaviors. We observed strong swim-related signals in granule cells and Purkinje cells during both active and fictive swimming, where zebrafish were awake but paralyzed, therefore this activity is more consistent with motor efference copy signals than proprioceptive or lateral line activation. Moreover, we found that simple spike output correlated best with the strength of ongoing swimming rather than reporting a phasic or binary locomotor state, supporting previous findings that motor parameters are linearly coded in the cerebellum (*Raymond and Medina, 2018*). Only a small minority of Purkinje cells showed a motor-related decrease in simple spiking, which may reflect the relatively small contribution of feed-forward inhibition via molecular layer interneurons. The increases in simple spike output that we observe are far less heterogeneous than the effects of locomotion on mammalian Purkinje cell simple spike firing (*Jelitai et al., 2016*; *Sauerbrei et al., 2015*) and build on previous electrophysiological samplings of Purkinje cell activity that showed increases in membrane depolarization and simple spike output during fictive swimming in zebrafish (*Sengupta and Thirumalai, 2015*; *Scalise et al., 2016*).

These results suggest that motor efference signals during whole-body locomotion (swimming) drive simple spike output in nearly all cerebellar Purkinje cells in the larval zebrafish. Our current granule cell population imaging and electrophysiological recordings in zebrafish together with other recordings and optogenetic experiments in zebrafish and mice (*Ozden et al., 2012*; *Powell et al., 2015*; *Jelitai et al., 2016*; *Giovannucci et al., 2017*; *Knogler et al., 2017*; *Albergaria et al., 2018*) provide strong evidence that the cerebellum broadly encodes intended locomotor output or signals related to it in the input layer (*Figure 6*). These findings suggest an enrichment of motor signals across parallel fiber inputs, though some regional specialization of signals in limbed vertebrates may be needed to coordinate different limb networks. Future work is required to investigate the origin of mossy fibers carrying eye and tail motor efference copies to the zebrafish cerebellum and how these signals are transformed by subsequent processing stages in cerebellar circuits.

Complex spike - simple spike relationships

We observed that the dominant action of motor activity on simple spiking acutely changes how complex spikes and simple spikes interact in Purkinje cells. During non-locomotor periods, complex spikes have the ability to consistently increase or pause simple spiking for several hundreds of milliseconds in different Purkinje cells. Under motor-driven conditions of high simple spike rates, however, a complex spike resets simple spike activity for only a brief (<50 ms) window in all Purkinje cells before simple spikes return to their previous high rate. This is likely due to the overwhelming excitatory influence of locomotor activity carried by parallel fibers that drives simple spiking across the Purkinje cell population at high rates. When faced with these high simple spike rates, a complex spike arriving during motor activity therefore has a limited influence over simple spike output. The narrowing of this temporal window may serve to make finer adjustments of motor activity through very acute perturbations in network activity.

Across longer timescales, sensorimotor behaviors needs to be adjusted during development, experience, and learning, so that an animal can adapt to suit a changing environment or context. In a developmental context, the cerebellum may be actively engaged in refining and maintaining sensorimotor behaviors as the physiology of neural circuits, muscles, and sensory appendages matures. In the context of supervised cerebellar learning, classical theories predict that the coincident activation of a climbing fiber input and parallel fiber synapses drives long-term depression at the active parallel fiber to Purkinje cell synapses, leading to motor learning (*Ito, 2001*; but see *Bouvier et al., 2018*). Synaptic plasticity mechanisms both at other synapses and involving other cerebellar neurons (e.g. interneurons) are also likely to contribute (see *Gao et al., 2012* for review). We propose that motor efference signals during swimming and eye movements are widely broadcasted across the cerebellum to Purkinje cells because these are the most relevant signals not only for coordinating ongoing behaviors but also for driving plasticity. The enrichment of motor-related activity across the granule cell layer and subsequent broad excitation of Purkinje cells would support learned associations between motor behaviors and any relevant sensory information carried by regionally-specially

climbing fiber input. Indeed, recent work by *Albergaria et al., 2018* supports this idea by showing that a generalized increase in granule cell excitation during either locomotion or optogenetic stimulation enhances cerebellar learning in a paradigm for eyeblink conditioning. The amenability of the zebrafish cerebellum to in vivo physiological and behavioral recordings together with the hypotheses raised by this study should make it an attractive system to study the rules of cerebellar plasticity and learning in the future.

Outlook

Our results reveal a strong spatial organization of visual feature encoding in the Purkinje cell population into three rostrocaudal functional regions receiving different climbing fiber inputs. These regions are each involved in processing visual information relating to distinct motor behaviors and as such exhibit unique temporal features in sensory coding. Broad excitation from granule cells is layered on these regions during locomotor activity as a contextual signal. We believe that the system of granule cells and Purkinje cells together thus forms the substrate for cerebellar modules modulating innate and learned motor behaviors. These and other recent findings (*Matsui et al., 2014*; *Harmon et al., 2017*) provide a promising outlook for using the zebrafish as a model organism for understanding motor control and learning in the cerebellum.

Materials and methods

Experimental model and subject details

Zebrafish (*Danio rerio*) were maintained at 28 ˚C on a 14 hr light/10 hr dark cycle using standard protocols. All animal procedures were performed in accordance with approved protocols set by the Max Planck Society and the Regierung von Oberbayern (TVA 55-2-1-54-2532-82-2016). All experiments were performed using larvae at 6–8 dpf of as yet undetermined sex.

To label Purkinje cells specifically, we made use of the *aldoca* promoter and the carbonic anhydrase 8 (ca8) enhancer element as published previously (*Takeuchi et al., 2015*; *Matsui et al., 2014*). For electrophysiological recordings in Purkinje cells, *aldoca*:GFF;mn7GFF;UAS:GFP fish were used (*Takeuchi et al., 2015*; *Asakawa et al., 2008*; *Asakawa et al., 2013*), with Tg(gSAIzGFFM765B); UAS:GFP and Tg(gSAG6A); UAS:GFP fish additionally used for granule cell recordings (*Takeuchi et al., 2015*). For calcium imaging experiments with granule cells, Tg(gSA2AzGFF152B); UAS:GCaMP6s fish were used (*Takeuchi et al., 2015*; *Thiele et al., 2014*). For calcium imaging experiments in Purkinje cells, we cloned GCaMP6s (*Chen et al., 2013*) downstream of the *ca8* enhancer with an E1b minimal promoter referred hereafter as PC:GCaMP6s. We injected PC: GCaMP6s together with *tol2* mRNA in one cell stage embryos (25 ng/µl each), screened at six dpf for expression in the cerebellum, and raised strong positive fish to adulthood. Positive F1 progeny were used for all imaging experiments. For simultaneous electrophysiological and imaging experiments, we injected PC:GCaMP6s without *tol2* mRNA to achieve sparse, single-cell labelling. For anatomical experiments, we created a construct harboring a bright GFP variant mClover3 (*Bajar et al., 2016*) tagged with a membrane targeting signal (Fyn). This construct is termed PC:Fyn-mClover3. Injections were done as described for sparse GCaMP6s labelling in fish expressing *aldoca*:gap43-mCherry to allow registration across fish. For Purkinje cell counting, we created a stable transgenic line as described above where a nuclear localization signal (NLS) is fused to the N-terminus of GCaMP6s (PC:NLS-GCaMP6s) to restrict GCaMP6s to the nucleus.

Visual stimuli

For functional imaging experiments, trials were presented that consisted of the following stimuli, in non-randomized order: Black and white whole-field gratings were presented with motion in the forward direction at slow, medium, and fast speeds (3, 10, and 30 mm/s, respectively), for five seconds each with a pause of five seconds between stimuli, followed by reverse, leftward, and rightward moving gratings of the same duration and at medium speed. Grating remained static between stimuli. Black and white windmill patterns were rotated at 0.2 Hz with changing velocity that followed a sine function. Windmill patterns were presented across the whole field as well as for each half of the visual field. Flashes covered the whole visual field and switched between maximum luminance and darkness. For electrophysiological recordings, stimuli were similar as for functional imaging with the

exception that the stimulus set had shorter pauses between stimuli and that fewer repetitions of the rotating windmill stimulus were presented. Blank trials consisting of static gratings were also interspersed with stimuli trials to obtain baseline responses. For one experiment (*Figure 4—figure supplement 1g*) the fish was also presented with a series of whole-field black or white flashes of various durations (50–5000 ms) against a baseline intermediate luminance.

Functional population imaging

Volumetric functional imaging in the larval zebrafish cerebellum was performed as previously described in *Knogler et al., 2017*. Briefly. 6–8 dpf nacre (*mitfa -/-*) transgenic zebrafish larvae with GCaMP6s expressed in Purkinje cells were embedded in 1.5–2.5% agarose prior to imaging. Neural activity was recorded with a custom-built two-photon microscope. A Ti- Sapphire laser (Spectra Physics Mai Tai) tuned to 905 nm was used for excitation. Larval brains were systematically imaged while presenting visual stimuli (see below) at 60 frames per second using a Telefunken microprojector controlled by custom Python software and filtered (Kodak Wratten No.25) to allow for simultaneous imaging and visual stimulation. We acquired the total cerebellar volume by sampling each plane at ~5 Hz. After all stimuli were shown in one plane, the focal plane was shifted ventrally by 1 µm and the process was repeated. Tail and eye movement was tracked throughout with 850 nm infrared illumination and customized, automated tracking software. Behavior was imaged at up to 200 frames per second using an infrared-sensitive charge-coupled device camera (Pike F032B, Allied Vision Technologies) and custom written software in Python.

Image processing

Image analysis was performed with MATLAB (MathWorks) and Python similar to *Knogler et al., 2017*. Python analysis used scikit-learn and scikit-image (*Pedregosa et al., 2012*; *van der Walt et al., 2014*). Volumetrically-acquired two-photon data was aligned first within a plane then across planes to ensure that stacks were aligned to each other with subpixel precision. Any experiments during which the fish drifted significantly in z were stopped and the data discarded. The boundary of the cerebellum was manually masked to remove external signals such as skin autofluoresence. All signals from all planes were extracted for voxelwise analysis (mean of approximately 350 billion ± 10 billion for 5 fish with 100 planes with an additional 118 billion for a sixth fish with only 34 planes). Purkinje cell ROI activity traces were extracted using automated algorithms based on local signal correlations between pixels (see *Portugues et al., 2014* for details) and used for principal component analysis (see Materials and methods below). Tail activity during imaging experiments was processed to yield a vigor measurement (standard deviation of a 50 ms rolling buffer of the tail trace) that was greater than zero when the fish is moving. Independent left and right eye position and velocity were obtained from eye tracking data.

Single cell Purkinje cell imaging

Sparse labelled Purkinje cells expressing GCaMP6s were used to perform two-photon imaging as described above to identify any signal compartmentalization (*Figure 1—figure supplement 2*). Visual stimuli consisting of reverse and forward moving gratings were probed to evoke signals in Purkinje cells. For five Purkinje cells across three fish, ROIs for soma and parts of the dendrite were drawn manually and Calcium traces were extracted using custom-written software in Python. The most distal dendritic ROI was correlated with somatic ROI to determine the correlation coefficient for each cell.

Electrophysiological neural recordings

Cell-attached electrophysiological recordings were performed in 6–8 dpf zebrafish as previously described (*Knogler et al., 2017*) using an Axopatch Multiclamp 700B amplifier, a Digidata series 1550 Digitizer, and pClamp nine software (Axon Instruments, Molecular Devices). Data were acquired at 8.3 kHz using Clampex 10.2. Wild-type or transgenic zebrafish larvae with GFP-positive Purkinje cells and motor neurons were used for most recordings (see subject details above).

Larvae were paralyzed in bath-applied buffered 1 mg/ml alpha-bungarotoxin (Cayman Scientific, Concord, CA) and embedded in 1.5% low melting point agarose in a 35 mm petri dish. External solution was composed of Evans solution (134 mM NaCl, 2.9 mM KCl, 2.1 mM CaCl2, 1.2 mM

MgCl2, 10 mM glucose, 10 mM HEPES, pH 7.8 with NaOH). Electrodes for neuron recordings (6–12 MΩ) were pulled from thick-walled borosilicate glass with filament and were filled with the following intracellular solution (in mM): 105 D-gluconic acid, 16 KCl, 2 MgCl2, 10 HEPES, and 10 EGTA, adjusted to pH 7.2, 290 mOsm (*Drapeau et al., 1999*). Sulforhodamine B (0.1%) was included in the intracellular solution to visualize the electrode. The skin overlying the cerebellum was carefully removed with a glass electrode prior to recording. Post-recording fluorescent images of GFP-positive Purkinje cells and the recording electrode (visualized with an RFP filter) as well as bright-field images to confirm cell identity and map somatic location were acquired with an epifluorescent Thor-Labs camera controlled by Micromanager.

Electrophysiological data were analyzed offline with Clampfit 10.2 software (Molecular Devices) and Matlab (Mathworks, Natick MA). Cell-attached traces were high-pass filtered at 1–10 Hz and complex spikes and simple spike were automatically extracted by setting a threshold for each type of spike in that recording. A 2.5 ms period was blanked following each complex spike so that the complex spike waveform did not cross the simple spike threshold. Baseline firing rates were calculated from blank trials where no visual stimuli were presented or from the two second period at the beginning of each trial prior to the first stimulus onset if no blanks were obtained.

For experiments with simultaneous calcium imaging, stochastically-labeled single Purkinje cells expressing GCaMP6s were recorded with an epifluorescent backlit-CMOS camera (Photometrix Prime 95B) at 11.5 fps controlled by Micromanager and triggered by pClamp software during electrophysiological recordings. No visual stimuli were shown in these experiments. Fluorescent Purkinje cell activity was processed by manual ROI extraction. Extracted complex spike and simple spike rates from simultaneous electrophysiology traces were convolved with a GCaMP6 kernel for comparison with the fluorescent signal.

For electrophysiological recordings in the semi-paralyzed animal, larval zebrafish were embedded in 2% low-melting point agarose and injected with 0.5 mg/ml alpha-bungarotoxin in the caudal tip of the tail. This method reduces the trunk contractions during swimming but preserved full eye movement. The agarose around the eyes was removed and the fish was lit from below with 850 nm infrared illumination to allow for good image contrast of the eyes. Eye movement was recorded during simultaneous electrophysiological recordings and tracked offline with customized, automated software to extract independent trajectories for each eye.

Ventral root recordings

To obtain extracellular ventral root recordings, a thin-walled borosilicate glass electrode with a large opening (approximately a quarter of the width of a somite) was first used to remove a small section of skin overlying the horizontal myotomes of the spinal cord around the fifth spinal somite. The electrode was then cleared with positive pressure and positioned over the terminals of the ventral root with gentle suction to ensure good signal to noise.

Motor activity was extracted as a moving standard deviation of the ventral root trace. A threshold was then applied to identify ventral root activity that would correspond to motor output on the side of the animal ipsilateral to the recording electrode. To extract a binarized trace of swimming bouts, ventral root activity separated by an interval of less than 100 ms was considered to be part of the same bout. The vigor trace was median filtered to extrapolate vigor information across the entire bout. Peaks in the lag of the autocorrelation analysis of the thresholded, binarized signal was used to extract fictive swim frequency.

Multilinear regression

Briefly, this analysis involves three steps. First, we processed and extracted physiological signals from imaging data and electrophysiological recordings (see above). Second, we used each different feature of the visual stimulus or motor behavior, such as rotational clockwise visual motion velocity, or the strength of the swimming bouts across a trial, to build a vector of values for each trial convolved with the temporal dynamics of the signal (calcium signal or firing rate). These feature vectors are termed regressors. Third, we performed multilinear regression to quantify the contribution of these different features to the signal of interest. This step included parameter validation to ensure that the results of the analysis are robust. Following this process, each signal is assigned a vector of

coefficient weights that can be multiplied by the set of regressors to best recapitulate the activity of that signal.

Motor regressors were computed for each trial from the behavioral parameters obtained from eye and tail motor information in imaging and electrophysiology experiments (see above). Motor regressors for swimming were created to capture various features including bout onset, offset, duration, and vigor. Eye motor regressors captured directional velocity of each eye independently. Sensory regressors for each type of experiment were the same for all cells and were created using features including the duration, direction, and velocity of moving stimuli as well as luminance (see *Figure 1—figure supplement 2* and *Figure 3—figure supplement 1* for full regressor lists for imaging and electrophysiology).

For functional imaging data, regressors were convolved with a GCaMP6s kernel, modeled as a single exponential function with time decay constant tau = 1600 ms. The tau for this kernel was derived from the average single exponential fit of the fluorescence peak produced by a single complex spike as ascertained by simultaneously recorded GCaMP6s and electrophysiological signals (*Figure 1—figure supplement 2*, N = 8 cells). Regressors were normalized and passed to the scikit-learn function LinearRegression to compute the mulilinear regression coefficients, which was sufficient to accurately recapitulate the calcium traces (mean coefficient of multiple determination = 0.46 ± 0.02).

The higher sampling rates of electrophysiological recordings (8.3 KHz) allowed us to create additional regressors that captured more subtle features in the visual stimuli, for example the onset of translational motion in a given direction. The window for these regressors spanned a 500 ms period beginning at stimulus onset. Our previous electrophysiological recordings in granule cells have suggested a latency of ~100–200 ms for visual input to arrive at the input layer of the cerebellum (*Knogler et al., 2017*) similar to the mean latency of 126 ms reported for visual responses in the mouse inferior olive (*Ju et al., 2018*). Since most sensory stimuli were presented for longer periods (gratings for 5 s, windmill stimuli for 10 s, flashes for 1 s), this short window was designed to be sufficiently long to capture onset-related signals that face synaptic delays, but also clearly distinguish between responses that are transient at stimulus onset or last for the duration of the stimulus. Windmill stimuli had sinusoidal velocity and smoothly changed direction, thus multiple regressors were built for these stimuli that represented graded velocity, binary motion in a given direction, as well as change of direction. These motor and visual regressors were then convolved with a 20 ms filter to match the convolution of spiking into firing rates.

In order to best analyze our electrophysiological data with this extended set of regressors, we implemented a variant of lasso regression known as elastic net regularization using the function *lasso* from MATLAB. This is a useful fitting method for linear regression using generalized penalties that has been shown to be robust and gives sparse coefficient weight distributions such that in practice many regressor coefficients are zero (*Zou and Hastie, 2005*; *Tibshirani, 2011*; *Dean et al., 2015*).

Documentation from MATLAB (r2018b) gives the following formulation:

'Elastic net solves the problem

$$\min_{\beta_0, \beta} \left(\frac{1}{2N} \sum_{i=1}^{N} \left(y_i - \beta_0 - x_i^T \beta \right)^2 + \lambda P_a(\beta) \right), \text{ where}$$

$$P_a(\beta) = \frac{(1-\alpha)}{2} \beta_2^2 + \alpha \beta_1 = \sum_{j=1}^{p} \left(\frac{(1-\alpha)}{2} \beta_j^2 + \alpha \beta_j \right).$$

- N is the number of observations.
- y_i is the response at observation i.
- x_i is data, a vector of length p at observation i.
- λ is a nonnegative regularization parameter corresponding to one value of Lambda.
- The parameters β_0 and β are a scalar and a vector of length p, respectively.
- The penalty term $P_a(\beta)$ interpolates between the L^1 norm of β and the squared L^2 norm of β.'

Alpha values of 0.2 were used which represent an elastic net optimization with only modest sparsification, approaching ridge regression. Increasing the alpha parameter to move closer to an elastic net optimization did not significantly alter the main regressor weights. As the regularization coefficient Lambda increases, the number of nonzero components for regressor weights decreases. Lambda was selected by assessing the lowest total root mean squared error across the dataset following iterative regression with different parameter values: 0.9 for complex spike analyses and 0.8 for simple spike analyses. Both alpha and Lambda parameters were robust across a range of values

for the distribution of coefficient weights. The same procedure was used to obtain both Purkinje cell and granule cell coefficient weights.

For analyses of both imaging and electrophysiological data, multilinear regression produced a vector of coefficient weights for all regressors for the activity of each cell/voxel. In the latter case, a separate set of coefficient weights was obtained for complex spikes and simple spikes. The estimated weights for each regressor for a given cell/voxel can take positive or negative values (or zero). Negative weights are interpretable as a relay through inhibitory neurons.

Purkinje cell maps (*Figure 2a*) shows mean z-projections of the regressor coefficients from a representative fish. Granule cell maps (*Figure 6a*) are means of seven morphed fish and were manually masked either for parallel fibers and granule cell somata to show potential differences in the signal topography. To further dissociate motor and sensory responses for sensory stimuli that strongly drive a particular behavior (translational motion and swimming, or rotational motion and left/right eye velocities), we used a maximum intensity projection of respective sensory and motor regressor maps and colored a pixel depending on whether sensory (magenta) or motor (green) regressors explain this pixel better with a given minimum distance. Differences that are below that minimum distance or are uncorrelated are colored white. Despite the slow time constant for the calcium signal decay, the variability of tail and eye movements across trials, including their onset, duration, and presence/absence, was sufficient to assign clear sensory or motor origins to the majority of these voxels.

For detailed electrophysiological analyses of the different classes of visual complex spike responses for Purkinje cells, we included for analyses all cells for which that regressor coefficient weight was significant. To determine which Purkinje cells showed significant responses to luminance, we used autocorrelation analyses of complex spike rates during whole-field flashes only and assessed significance using the Ljung-Box Q-test. For analysis of complex spikes and motor activity, we analyzed all cells with significant, nonzero motor regressor weights for complex spike activity. When examining the relationship between complex spikes and simple spike rates in individual Purkinje cells, cells with less than ten complex spikes for any condition (e.g. motor versus non-motor) were excluded from analysis.

Our multilinear regression analyses were carefully chosen in place of a series of separate simple regressions which would not provide useful or even correct insight into the question of which features these neurons are encoding. Multilinear regression is therefore preferred statistical method when considering which of multiple features contribute to a given signal and to what degree. However, as with any analysis, one must acknowledge the potential caveats or considerations when using this method (see *Slinker and Glantz, 2008* for review). For example, although multilinear regression assumes a simple addition of the regressor multiplied by the coefficient values, different sensory and/or motor features could interact nonlinearly to influence a cell's firing rate. Models do exist that incorporate nonlinearity (interaction terms), however these terms will highly correlate with each of the variables used to create the product and artificially introduce multicollinearity. Therefore since the R^2 values of the linear fits were reasonable, we did not explore these models. The complete set of regressors used for electrophysiological analysis nonetheless face the consideration that even in a linear model some regressors will be correlated with each other (for example, stimulus onset and duration, or swim strength and duration). We addressed this concern in two ways. First, we explored a wide range of possible regressors, both quantitative and categorical, then we dropped unnecessary and redundant regressors that consistently gave small or zero coefficient values. This was done through variable selection methods to select the optimal pool of regressors. Second, we used the elastic net optimization of lasso with low alpha values that approach ridge regression, which specifically helps to sparsify the coefficients rather than split coefficient weights between correlated regressors.

Principal component analysis (PCA)

We performed PCA on the vector of correlations with all regressors for all automatically segmented ROIs and all fish. This correlation vector representation was clustered in the PC space in 10 clusters using *k*-means. This number was chosen because 10 PCs already explained ~90% of the variance. All voxels were then colored in according to the cluster they belonged to.

The anatomical clustering and stereotypy indices were calculated as follows. For the anatomical clustering index, the average distance between ROIs of the same cluster within a fish was compared

against the average distance between an ROI from that cluster and a randomly chosen ROI from that fish. The inverse ratio of these two quantities is the anatomical clustering index. The stereotypy index is computed similarly. In this case, the average distance between an ROI from a particular cluster and fish and other ROIs from that same cluster but other fish is compared against the distance between an ROI from that same cluster and fish and other ROIs from other clusters and fish. Again, the inverse ratio of these two quantities is the stereotypy index. To summarize, the index is a comparison of average distance within a condition to average distance without the restraint of that condition.

Purkinje cell morphology

Sparsely labelled Purkinje cells were imaged using a 20x water immersion objective with 1 NA (Zeiss) on a confocal microscope (LSM 700, Carl Zeiss, Germany). High resolution stacks of Purkinje cells were deconvolved using Richardson-Lucy algorithm and artifacts were removed manually. Purkinje cell axonal projections were traced using NeuTube (*Feng et al., 2015*) and the Simple Neurite Tracer plugin for FIJI (*Longair et al., 2011*). SWC files were converted to line stacks and post-processed using custom written software in Python. Individual axonal projections were morphed together to a reference brain using *aldoca*:gap43-mCherry as a reference and CMTK as morphing tool (*Rohlfing and Maurer, 2003*). Dendritic planarity was assessed by performing principal component analysis on binarized dendritic morphologies. The ratio of the third principal component to the second was used to determine planarity (planar dendrites have ratios approaching 0, whereas nonplanar dendrites have ratios approaching 1).

Purkinje cell counting

We imaged three individual PC:NLS-GCaMP6s transgenic fish line at seven dpf using confocal microscopy as described for morphological experiments above. In this line, GCaMP6s is restricted to the nucleus and approximates a sphere. Consequently, we used 3D template matching using a 3D (spherical) Gaussian to find individual nuclei using custom written software in Python. False positives were removed and missed cells were added manually.

Quantification and statistical analysis

Data were analyzed in MATLAB and Python with custom software (*Knogler, 2019*; copy archived at https://github.com/elifesciences-publications/Knogler_etal_2019_eLife).

Values given in the text are mean ± standard error of the mean. Baseline complex spike firing rates for groups of Purkinje cells sorted by complex spike phenotype were compared by one-way ANOVA, followed by pairwise *post hoc* analyses using Bonferroni post hoc correction. The nonparametric Wilcoxon signed rank test was used on paired nonparametric datasets. Details of statistical analyses are found in the text and figure legends.

Data/resource sharing

Example electrophysiological datasets are available at https://zenodo.org/record/1494071. An example imaging dataset is available at https://zenodo.org/record/1638807. Further information and requests for data, resources, and reagents should be directed to Ruben Portugues (rportugues@neuro.mpg.de).

Additional information

Funding

Funder	Grant reference number	Author
Alexander von Humboldt-Stiftung		Laura D Knogler
Carl Friedrich von Siemens Foundation		Laura D Knogler
Fonds de Recherche du Québec - Santé		Laura D Knogler
Max-Planck-Gesellschaft	Open-access funding	Laura D Knogler Andreas M Kist Ruben Portugues
International Max Planck Research School for Life Sciences		Andreas M Kist
Joachim Herz Stiftung		Andreas M Kist
Deutsche Forschungsgemeinschaft	PO 2105/2-1	Laura D Knogler Andreas M Kist Ruben Portugues

Author contributions

Author ORCIDs

Laura D Knogler ![ORCID] https://orcid.org/0000-0001-7111-9832
Andreas M Kist ![ORCID] http://orcid.org/0000-0003-3643-7776
Ruben Portugues ![ORCID] http://orcid.org/0000-0002-1495-9314

Ethics

Animal experimentation: All procedures involving animals were in accordance with the Max Planck Society guidelines and approved by the Regierung von Oberbayern (TVA# 55-2-1-54-2532-82-2016)

Decision letter and Author response

Decision letter https://doi.org/10.7554/eLife.42138.024
Author response https://doi.org/10.7554/eLife.42138.025

Additional files

Supplementary files

• Transparent reporting form
DOI: https://doi.org/10.7554/eLife.42138.022

Data availability

Example electrophysiological datasets are available at https://zenodo.org/record/1494071. An example imaging dataset is available at https://zenodo.org/record/1638807. MATLAB code for electrophysiological analysis available via GitHub (https://github.com/portugueslab/Knogler_etal_2019_eLife; copy archived at https://github.com/elifesciences-publications/Knogler_etal_2019_eLife).

References

Ahrens MB, Li JM, Orger MB, Robson DN, Schier AF, Engert F, Portugues R. 2012. Brain-wide neuronal dynamics during motor adaptation in zebrafish. *Nature* **485**:471–477. DOI: https://doi.org/10.1038/nature11057, PMID: 22622571

Aizenberg M, Schuman EM. 2011. Cerebellar-dependent learning in larval zebrafish. *Journal of Neuroscience* **31**: 8708–8712. DOI: https://doi.org/10.1523/JNEUROSCI.6565-10.2011, PMID: 21677154

Albergaria C, Silva NT, Pritchett DL, Carey MR. 2018. Locomotor activity modulates associative learning in mouse cerebellum. *Nature Neuroscience* **21**:725–735. DOI: https://doi.org/10.1038/s41593-018-0129-x, PMID: 29662214

Albus JS. 1971. A theory of cerebellar function. *Mathematical Biosciences* **10**:25–61. DOI: https://doi.org/10.1016/0025-5564(71)90051-4

Apps R. 1999. Movement-related gating of climbing fibre input to cerebellar cortical zones. *Progress in Neurobiology* **57**:537–562. DOI: https://doi.org/10.1016/S0301-0082(98)00068-9, PMID: 10215101

Apps R, Hawkes R. 2009. Cerebellar cortical organization: a one-map hypothesis. *Nature Reviews Neuroscience* **10**:670–681. DOI: https://doi.org/10.1038/nrn2698, PMID: 19693030

Asakawa K, Suster ML, Mizusawa K, Nagayoshi S, Kotani T, Urasaki A, Kishimoto Y, Hibi M, Kawakami K. 2008. Genetic dissection of neural circuits by Tol2 transposon-mediated Gal4 gene and enhancer trapping in zebrafish. *PNAS* **105**:1255–1260. DOI: https://doi.org/10.1073/pnas.0704963105, PMID: 18202183

Asakawa K, Abe G, Kawakami K. 2013. Cellular dissection of the spinal cord motor column by BAC transgenesis and gene trapping in zebrafish. *Frontiers in Neural Circuits* **7**:1–14. DOI: https://doi.org/10.3389/fncir.2013.00100, PMID: 23754985

Badura A, Schonewille M, Voges K, Galliano E, Renier N, Gao Z, Witter L, Hoebeek FE, Chédotal A, De Zeeuw CI. 2013. Climbing fiber input shapes reciprocity of purkinje cell firing. *Neuron* **78**:700–713. DOI: https://doi.org/10.1016/j.neuron.2013.03.018, PMID: 23643935

Bae YK, Kani S, Shimizu T, Tanabe K, Nojima H, Kimura Y, Higashijima S, Hibi M. 2009. Anatomy of zebrafish cerebellum and screen for mutations affecting its development. *Developmental Biology* **330**:406–426. DOI: https://doi.org/10.1016/j.ydbio.2009.04.013, PMID: 19371731

Bajar BT, Wang ES, Lam AJ, Kim BB, Jacobs CL, Howe ES, Davidson MW, Lin MZ, Chu J. 2016. Improving brightness and photostability of green and red fluorescent proteins for live cell imaging and FRET reporting. *Scientific Reports* **6**:1–12. DOI: https://doi.org/10.1038/srep20889, PMID: 26879144

Bhandiwad AA, Zeddies DG, Raible DW, Rubel EW, Sisneros JA. 2013. Auditory sensitivity of larval zebrafish (Danio rerio) measured using a behavioral prepulse inhibition assay. *Journal of Experimental Biology* **216**:3504–3513. DOI: https://doi.org/10.1242/jeb.087635, PMID: 23966590

Bouvier G, Aljadeff J, Clopath C, Bimbard C, Ranft J, Blot A, Nadal J-P, Brunel N, Hakim V, Barbour B. 2018. Cerebellar learning using perturbations. *eLife* **7**:53785. DOI: https://doi.org/10.7554/eLife.31599

Brockerhoff SE, Hurleyt JB, Janssen-bienholdt U, Neuhauss SCF, Driever W, Dowling JE. 1995. System defects. *Neurobiology* **92**:10545–10549.

Budick SA, O'Malley DM. 2000. Locomotor repertoire of the larval zebrafish: swimming, turning and prey capture. *The Journal of Experimental Biology* **203**:2565–2579. PMID: 10934000

Burgess HA, Granato M. 2007. Modulation of locomotor activity in larval zebrafish during light adaptation. *Journal of Experimental Biology* **210**:2526–2539. DOI: https://doi.org/10.1242/jeb.003939, PMID: 17601957

Cerminara NL, Lang EJ, Sillitoe RV, Apps R. 2015. Redefining the cerebellar cortex as an assembly of non-uniform purkinje cell microcircuits. *Nature Reviews Neuroscience* **16**:79–93. DOI: https://doi.org/10.1038/nrn3886, PMID: 25601779

Cerminara NL, Apps R. 2011. Behavioural significance of cerebellar modules. *The Cerebellum* **10**:484–494. DOI: https://doi.org/10.1007/s12311-010-0209-2, PMID: 20838949

Chen TW, Wardill TJ, Sun Y, Pulver SR, Renninger SL, Baohan A, Schreiter ER, Kerr RA, Orger MB, Jayaraman V, Looger LL, Svoboda K, Kim DS. 2013. Ultrasensitive fluorescent proteins for imaging neuronal activity. *Nature* **499**:295–300. DOI: https://doi.org/10.1038/nature12354, PMID: 23868258

Crepel F, Mariani J, Delhaye-Bouchaud N. 1976. Evidence for a multiple innervation of purkinje cells by climbing fibers in the immature rat cerebellum. *Journal of Neurobiology* **7**:567–578. DOI: https://doi.org/10.1002/neu.480070609, PMID: 1003202

De Zeeuw CI, Hoebeek FE, Bosman LW, Schonewille M, Witter L, Koekkoek SK. 2011. Spatiotemporal firing patterns in the cerebellum. *Nature Reviews Neuroscience* **12**:327–344. DOI: https://doi.org/10.1038/nrn3011, PMID: 21544091

Dean P, Porrill J, Kingdom U. 2015. At the edge of chaos : how cerebellar granular layer network dynamics can provide the basis for temporal filters. *PLoS Computational Biology*:1–28. DOI: https://doi.org/10.1371/journal.pcbi.1004515

Dizon MJ, Khodakhah K. 2011. The role of interneurons in shaping purkinje cell responses in the cerebellar cortex. *Journal of Neuroscience* **31**:10463–10473. DOI: https://doi.org/10.1523/JNEUROSCI.1350-11.2011, PMID: 21775592

Drapeau P, Ali DW, Buss RR, Saint-Amant L. 1999. In vivo recording from identifiable neurons of the locomotor network in the developing zebrafish. *Journal of Neuroscience Methods* **88**:1–13. DOI: https://doi.org/10.1016/S0165-0270(99)00008-4, PMID: 10379574

Dreosti E, Lopes G, Kampff AR, Wilson SW. 2015. Development of social behavior in young zebrafish. *Frontiers in Neural Circuits* **9**. DOI: https://doi.org/10.3389/fncir.2015.00039, PMID: 26347614

Easter SS, Nicola GN. 1996. The development of vision in the zebrafish (Danio rerio). *Developmental Biology* **180**:646–663. DOI: https://doi.org/10.1006/dbio.1996.0335, PMID: 8954734

Eccles JC, Ito M, Szentagothai J. 1967. *The Cerebellum as a Neuronal Machine*. springer.

Favre-Bulle IA, Vanwalleghem G, Taylor MA, Rubinsztein-Dunlop H, Scott EK. 2018. Cellular-Resolution imaging of vestibular processing across the larval zebrafish brain. *Current Biology* **28**:3711–3722. DOI: https://doi.org/10.1016/j.cub.2018.09.060, PMID: 30449665

Feng L, Zhao T, Kim J. 2015. neuTube 1.0: a new design for efficient neuron reconstruction software based on the SWC format. *eNeuro* **2**. DOI: https://doi.org/10.1523/ENEURO.0049-14.2014, PMID: 26464967

Fero K, Yokogawa T, Burgess HA. 2011. The Behavioral Repertoire of Larval Zebrafish. In: Kalueff A , Cachat J. M (Eds). *Zebrafish Models in Neurobehavioral Research*. Totowa, NJ: Humana Press. p. 249–291. DOI: https://doi.org/10.1007/978-1-60761-922-2_12

Gao Z, van Beugen BJ, De Zeeuw CI. 2012. Distributed synergistic plasticity and cerebellar learning. *Nature Reviews Neuroscience* **13**:619–635. DOI: https://doi.org/10.1038/nrn3312, PMID: 22895474

Giovannucci A, Badura A, Deverett B, Najafi F, Pereira TD, Gao Z, Ozden I, Kloth AD, Pnevmatikakis E, Paninski L, De Zeeuw CI, Medina JF, Wang SS. 2017. Cerebellar granule cells acquire a widespread predictive feedback signal during motor learning. *Nature Neuroscience* **20**:727–734. DOI: https://doi.org/10.1038/nn.4531, PMID: 28319608

Hamling KR, Tobias ZJ, Weissman TA. 2015. Mapping the development of cerebellar purkinje cells in zebrafish. *Developmental Neurobiology* **75**:1174–1188. DOI: https://doi.org/10.1002/dneu.22275, PMID: 25655100

Harmon TC, Magaram U, McLean DL, Raman IM. 2017. Distinct responses of purkinje neurons and roles of simple spikes during associative motor learning in larval zebrafish. *eLife* **6**:e22537. DOI: https://doi.org/10.7554/eLife.22537, PMID: 28541889

Harvey RJ, Napper RM. 1991. Quantitative studies on the mammalian cerebellum. *Progress in Neurobiology* **36**:437–463. DOI: https://doi.org/10.1016/0301-0082(91)90012-P, PMID: 1947173

Hashimoto M, Hibi M. 2012. Development and evolution of cerebellar neural circuits. *Development, Growth & Differentiation* **54**:373–389. DOI: https://doi.org/10.1111/j.1440-169X.2012.01348.x, PMID: 22524607

Hawkes R. 2014. Purkinje cell stripes and long-term depression at the parallel fiber-Purkinje cell synapse. *Frontiers in Systems Neuroscience* **8**:1–11. DOI: https://doi.org/10.3389/fnsys.2014.00041, PMID: 24734006

Heffley W, Song EY, Xu Z, Taylor B, Hughes MA, McKinney A, Joshua M, Hull C. 2018. Coordinated cerebellar climbing fiber activity is gated by behavioral context in a voluntary motor regime. *Nature Neuroscience*.

Herzfeld DJ, Kojima Y, Soetedjo R, Shadmehr R. 2015. Encoding of action by the purkinje cells of the cerebellum. *Nature* **526**:439–442. DOI: https://doi.org/10.1038/nature15693, PMID: 26469054

Hsieh JY, Ulrich B, Issa FA, Wan J, Papazian DM. 2014. Rapid development of purkinje cell excitability, functional cerebellar circuit, and afferent sensory input to cerebellum in zebrafish. *Frontiers in Neural Circuits* **8**:1–12. DOI: https://doi.org/10.3389/fncir.2014.00147, PMID: 25565973

Hsieh J-Y, Papazian DM. 2018. Extracellular Loose-Patch Recording of Purkinje Cell Activity in Awake Zebrafish and Emergence of Functional Cerebellar Circuit. In: Sillitoe R. V (Ed). *Extracellular Recording Approaches*. New York, NY: Springer. p. 207–224. DOI: https://doi.org/10.1007/978-1-4939-7549-5_11

Ito M. 1972. Neural design of the cerebellar motor control system. *Brain Research* **40**:81–84. DOI: https://doi.org/10.1016/0006-8993(72)90110-2, PMID: 4338265

Ito M. 1982. Cerebellar control of the vestibulo-ocular reflex–around the flocculus hypothesis. *Annual Review of Neuroscience* **5**:275–297. DOI: https://doi.org/10.1146/annurev.ne.05.030182.001423, PMID: 6803651

Ito M. 2001. Cerebellar long-term depression: characterization, signal transduction, and functional roles. *Physiological Reviews* **81**:1143–1195. DOI: https://doi.org/10.1152/physrev.2001.81.3.1143, PMID: 11427694

Ito M. 2006. Cerebellar circuitry as a neuronal machine. *Progress in Neurobiology* **78**:272–303. DOI: https://doi.org/10.1016/j.pneurobio.2006.02.006, PMID: 16759785

Ito M. 2013. Error detection and representation in the olivo-cerebellar system. *Frontiers in Neural Circuits* **7**:1. DOI: https://doi.org/10.3389/fncir.2013.00001, PMID: 23440175

Jelitai M, Puggioni P, Ishikawa T, Rinaldi A, Duguid I. 2016. Dendritic excitation–inhibition balance shapes cerebellar output during motor behaviour. *Nature Communications* **7**:1–13. DOI: https://doi.org/10.1038/ncomms13722

Ju C, Bosman LWJ, Hoogland TM, Velauthapillai A, Murugesan P, Warnaar P, Negrello M, De ZCI. 2018. Neurons of the inferior olive respond to broad classes of sensory input while subject to homeostatic control. *bioRxiv*. DOI: https://doi.org/10.1101/379149

Kennedy A, Wayne G, Kaifosh P, Alviña K, Abbott LF, Sawtell NB. 2014. A temporal basis for predicting the sensory consequences of motor commands in an electric fish. *Nature Neuroscience* **17**:416–422. DOI: https://doi.org/10.1038/nn.3650, PMID: 24531306

Kitamura K, Kano M. 2013. Dendritic calcium signaling in cerebellar purkinje cell. *Neural Networks* **47**:11–17. DOI: https://doi.org/10.1016/j.neunet.2012.08.001, PMID: 22985934

Knogler LD, Markov DA, Dragomir EI, Štih V, Portugues R. 2017. Sensorimotor representations in cerebellar granule cells in larval zebrafish are dense, spatially organized, and Non-temporally patterned. *Current Biology* **27**:1288–1302. DOI: https://doi.org/10.1016/j.cub.2017.03.029, PMID: 28434864

Knogler LD. 2019. Knogler_etal_2019_eLife. 8e0a14a. Github. https://github.com/portugueslab/Knogler_etal_2019_eLife

Koziol LF, Budding D, Andreasen N, D'Arrigo S, Bulgheroni S, Imamizu H, Ito M, Manto M, Marvel C, Parker K, Pezzulo G, Ramnani N, Riva D, Schmahmann J, Vandervert L, Yamazaki T. 2014. Consensus paper: the cerebellum's Role in Movement and Cognition. *The Cerebellum* **13**:151–177. DOI: https://doi.org/10.1007/s12311-013-0511-x

Lang EJ, Apps R, Bengtsson F, Cerminara NL, De Zeeuw CI, Ebner TJ, Heck DH, Jaeger D, Jörntell H, Kawato M, Otis TS, Ozyildirim O, Popa LS, Reeves AM, Schweighofer N, Sugihara I, Xiao J. 2017. The roles of the olivocerebellar pathway in motor learning and motor control. A consensus paper. *The Cerebellum* **16**:230–252. DOI: https://doi.org/10.1007/s12311-016-0787-8, PMID: 27193702

Lev-Ram V, Miyakawa H, Lasser-Ross N, Ross WN. 1992. Calcium transients in cerebellar purkinje neurons evoked by intracellular stimulation. *Journal of Neurophysiology* **68**:1167–1177. DOI: https://doi.org/10.1152/jn.1992.68.4.1167, PMID: 1432076

Loewenstein Y, Mahon S, Chadderton P, Kitamura K, Sompolinsky H, Yarom Y, Häusser M. 2005. Bistability of cerebellar purkinje cells modulated by sensory stimulation. *Nature Neuroscience* **8**:202–211. DOI: https://doi.org/10.1038/nn1393, PMID: 15665875

Longair MH, Baker DA, Armstrong JD. 2011. Simple neurite tracer: open source software for reconstruction, visualization and analysis of neuronal processes. *Bioinformatics* **27**:2453–2454. DOI: https://doi.org/10.1093/bioinformatics/btr390, PMID: 21727141

Marr D. 1969. A theory of cerebellar cortex. *The Journal of Physiology* **202**:437–470. DOI: https://doi.org/10.1113/jphysiol.1969.sp008820, PMID: 5784296

Masino MA, Fetcho JR. 2005. Fictive swimming motor patterns in wild type and mutant larval zebrafish. *Journal of Neurophysiology* **93**:3177–3188. DOI: https://doi.org/10.1152/jn.01248.2004, PMID: 15673549

Mathews PJ, Lee KH, Peng Z, Houser CR, Otis TS. 2012. Effects of climbing fiber driven inhibition on purkinje neuron spiking. *Journal of Neuroscience* **32**:17988–17997. DOI: https://doi.org/10.1523/JNEUROSCI.3916-12.2012, PMID: 23238715

Matsui H, Namikawa K, Babaryka A, Köster RW. 2014. Functional regionalization of the teleost cerebellum analyzed in vivo. *PNAS* **111**:11846–11851. DOI: https://doi.org/10.1073/pnas.1403105111, PMID: 25002482

McElligott MB, O'malley DM. 2005. Prey tracking by larval zebrafish: axial kinematics and visual control. *Brain, Behavior and Evolution* **66**:177–196. DOI: https://doi.org/10.1159/000087158, PMID: 16088102

Migault G, van der Plas TL, Trentesaux H, Panier T, Candelier R, Proville R, Englitz B, Debrégeas G, Bormuth V. 2018. Whole-Brain calcium imaging during physiological vestibular stimulation in larval zebrafish. *Current Biology* **28**:3723–3735. DOI: https://doi.org/10.1016/j.cub.2018.10.017, PMID: 30449666

Miller N, Gerlai R. 2012. From schooling to shoaling: patterns of collective motion in zebrafish (Danio rerio). *PLoS ONE* **7**:e48865. DOI: https://doi.org/10.1371/journal.pone.0048865, PMID: 23166599

Ohmae S, Medina JF. 2015. Climbing fibers encode a temporal-difference prediction error during cerebellar learning in mice. *Nature Neuroscience* **18**:1798–1803. DOI: https://doi.org/10.1038/nn.4167, PMID: 26551541

Ozden I, Dombeck DA, Hoogland TM, Tank DW, Wang SS. 2012. Widespread state-dependent shifts in cerebellar activity in locomoting mice. *PLoS ONE* **7**:e42650. DOI: https://doi.org/10.1371/journal.pone.0042650, PMID: 22880068

Ozol K, Hayden JM, Oberdick J, Hawkes R. 1999. Transverse zones in the vermis of the mouse cerebellum. *The Journal of Comparative Neurology* **412**:95–111. DOI: https://doi.org/10.1002/(SICI)1096-9861(19990913)412:1<95::AID-CNE7>3.0.CO;2-Y, PMID: 10440712

Palay SL, Chan-Palay V. 1974. *Cerebellar Cortex: Cytology and Organization*. New York: Springer-Verlag. DOI: https://doi.org/10.1007/978-3-642-65581-4

Pedregosa F, Varoquaux G, Gramfort A, Michel V, Thirion B, Grisel O, Blondel M, Prettenhofer P, Weiss R, Dubourg V, Vanderplas J, Passos A, Cournapeau D, Brucher M, Perrot M, É D. 2012. Scikit-learn: machine learning in python. *Journal of Machine Learning Research* **12**:2825–2830.

Pivetta C, Esposito MS, Sigrist M, Arber S. 2014. Motor-circuit communication matrix from spinal cord to brainstem neurons revealed by developmental origin. *Cell* **156**:537–548. DOI: https://doi.org/10.1016/j.cell.2013.12.014, PMID: 24485459

Porrill J, Dean P, Anderson SR. 2013. Adaptive filters and internal models: multilevel description of cerebellar function. *Neural Networks* **47**:134–149. DOI: https://doi.org/10.1016/j.neunet.2012.12.005, PMID: 23391782

Portugues R, Feierstein CE, Engert F, Orger MB. 2014. Whole-brain activity maps reveal stereotyped, distributed networks for visuomotor behavior. *Neuron* **81**:1328–1343. DOI: https://doi.org/10.1016/j.neuron.2014.01.019, PMID: 24656252

Powell K, Mathy A, Duguid I, Häusser M. 2015. Synaptic representation of locomotion in single cerebellar granule cells. *eLife* **4**:e07292. DOI: https://doi.org/10.7554/eLife.07290

Raman IM, Bean BP. 1997. Resurgent sodium current and action potential formation in dissociated cerebellar purkinje neurons. *The Journal of Neuroscience* **17**:4517–4526. DOI: https://doi.org/10.1523/JNEUROSCI.17-12-04517.1997, PMID: 9169512

Ramirez JE, Stell BM. 2016. Calcium imaging reveals coordinated simple spike pauses in populations of cerebellar purkinje cells. *Cell Reports* **17**:3125–3132. DOI: https://doi.org/10.1016/j.celrep.2016.11.075, PMID: 28009283

Raymond JL, Medina JF. 2018. Computational principles of supervised learning in the cerebellum. *Annual Review of Neuroscience* **41**:233–253. DOI: https://doi.org/10.1146/annurev-neuro-080317-061948, PMID: 29986160

Rohlfing T, Maurer CR. 2003. Nonrigid image registration in shared-memory multiprocessor environments with application to brains, breasts, and bees. *IEEE Transactions on Information Technology in Biomedicine* **7**:16–25. DOI: https://doi.org/10.1109/TITB.2003.808506, PMID: 12670015

Sauerbrei BA, Lubenov EV, Siapas AG. 2015. Structured variability in purkinje cell activity during locomotion. *Neuron* **87**:840–852. DOI: https://doi.org/10.1016/j.neuron.2015.08.003, PMID: 26291165

Scalise K, Shimizu T, Hibi M, Sawtell NB. 2016. Responses of cerebellar purkinje cells during fictive optomotor behavior in larval zebrafish. *Journal of Neurophysiology* **116**:2067–2080. DOI: https://doi.org/10.1152/jn.00042.2016, PMID: 27512018

Sengupta M, Thirumalai V. 2015. AMPA receptor mediated synaptic excitation drives state-dependent bursting in purkinje neurons of zebrafish larvae. *eLife* **4**:e09158. DOI: https://doi.org/10.7554/eLife.09158

Severi KE, Portugues R, Marques JC, O'Malley DM, Orger MB, Engert F. 2014. Neural control and modulation of swimming speed in the larval zebrafish. *Neuron* **83**:692–707. DOI: https://doi.org/10.1016/j.neuron.2014.06.032, PMID: 25066084

Simpson JI, Wylie DR, De Zeeuw CI. 1996. On climbing fiber signals and their consequence(s). *Behavioral and Brain Sciences* **19**:384–398. DOI: https://doi.org/10.1017/S0140525X00081486

Simpson JI, Alley KE. 1974. Visual climbing fiber input to rabbit vestibulo-cerebellum: a source of direction-specific information. *Brain Research* **82**:302–308. DOI: https://doi.org/10.1016/0006-8993(74)90610-6, PMID: 4441896

Slinker BK, Glantz SA. 2008. Multiple linear regression: accounting for multiple simultaneous determinants of a continuous dependent variable. *Circulation* **117**:1732–1737. DOI: https://doi.org/10.1161/CIRCULATIONAHA.106.654376, PMID: 18378626

Soetedjo R, Fuchs AF. 2006. Complex spike activity of purkinje cells in the oculomotor vermis during behavioral adaptation of monkey saccades. *Journal of Neuroscience* **26**:7741–7755. DOI: https://doi.org/10.1523/JNEUROSCI.4658-05.2006, PMID: 16855102

Stoodley CJ, Valera EM, Schmahmann JD. 2012. Functional topography of the cerebellum for motor and cognitive tasks: an fMRI study. *NeuroImage* **59**:1560–1570. DOI: https://doi.org/10.1016/j.neuroimage.2011.08.065, PMID: 21907811

Streng ML, Popa LS, Ebner TJ. 2018. Complex spike wars: a new hope. *The Cerebellum* **17**:735–746. DOI: https://doi.org/10.1007/s12311-018-0960-3, PMID: 29982917

Suvrathan A, Payne HL, Raymond JL. 2016. Timing Rules for Synaptic Plasticity Matched to Behavioral Function. *Neuron* **92**:959–967. DOI: https://doi.org/10.1016/j.neuron.2016.10.022, PMID: 27839999

Takeuchi M, Matsuda K, Yamaguchi S, Asakawa K, Miyasaka N, Lal P, Yoshihara Y, Koga A, Kawakami K, Shimizu T, Hibi M. 2015. Establishment of Gal4 transgenic zebrafish lines for analysis of development of cerebellar neural circuitry. *Developmental Biology* **397**:1–17. DOI: https://doi.org/10.1016/j.ydbio.2014.09.030, PMID: 25300581

Takeuchi M, Yamaguchi S, Sakakibara Y, Hayashi T, Matsuda K, Hara Y, Tanegashima C, Shimizu T, Kuraku S, Hibi M. 2017. Gene expression profiling of granule cells and purkinje cells in the zebrafish cerebellum. *Journal of Comparative Neurology* **525**:1558–1585. DOI: https://doi.org/10.1002/cne.24114, PMID: 27615194

Temizer I, Donovan JC, Baier H, Semmelhack JL. 2015. A visual pathway for Looming-Evoked escape in larval zebrafish. *Current Biology* **25**:1823–1834. DOI: https://doi.org/10.1016/j.cub.2015.06.002, PMID: 26119746

ten Brinke MM, Boele HJ, Spanke JK, Potters JW, Kornysheva K, Wulff P, IJpelaar AC, Koekkoek SK, De Zeeuw CI. 2015. Evolving models of pavlovian conditioning: cerebellar cortical dynamics in awake behaving mice. *Cell Reports* **13**:1977–1988. DOI: https://doi.org/10.1016/j.celrep.2015.10.057, PMID: 26655909

Thiele TR, Donovan JC, Baier H. 2014. Descending control of swim posture by a midbrain nucleus in zebrafish. *Neuron* **83**:679–691. DOI: https://doi.org/10.1016/j.neuron.2014.04.018, PMID: 25066082

Thompson AW. 2016. PhD Thesis, University of Queensland. Library Search. https://espace.library.uq.edu.au/view/UQ:376894

Tibshirani R. 2011. Regression shrinkage and selection via the lasso: a retrospective. *Journal of the Royal Statistical Society: Series B* **73**:273–282. DOI: https://doi.org/10.1111/j.1467-9868.2011.00771.x

van Beugen BJ, Gao Z, Boele HJ, Hoebeek F, De Zeeuw CI. 2013. High frequency burst firing of granule cells ensures transmission at the parallel fiber to purkinje cell synapse at the cost of temporal coding. *Frontiers in Neural Circuits* **7**:95. DOI: https://doi.org/10.3389/fncir.2013.00095, PMID: 23734102

van der Walt S, Schönberger JL, Nunez-Iglesias J, Boulogne F, Warner JD, Yager N, Gouillart E, Yu T, scikit-image contributors. 2014. scikit-image: image processing in Python. *PeerJ* **2**:e453. DOI: https://doi.org/10.7717/peerj.453, PMID: 25024921

Vanwalleghem G, Heap LA, Scott EK. 2017. A profile of auditory-responsive neurons in the larval zebrafish brain. *Journal of Comparative Neurology* **525**:3031–3043. DOI: https://doi.org/10.1002/cne.24258, PMID: 28599354

Witter L, De Zeeuw CI. 2015. Regional functionality of the cerebellum. *Current Opinion in Neurobiology* **33**:150–155. DOI: https://doi.org/10.1016/j.conb.2015.03.017, PMID: 25884963

Wylie DR, Frost BJ. 1991. Purkinje cells in the vestibulocerebellum of the pigeon respond best to either translational or rotational wholefield visual motion. *Experimental Brain Research* **86**:229–232. DOI: https://doi.org/10.1007/BF00231059, PMID: 1756795

Xiao J, Cerminara NL, Kotsurovskyy Y, Aoki H, Burroughs A, Wise AK, Luo Y, Marshall SP, Sugihara I, Apps R, Lang EJ. 2014. Systematic regional variations in purkinje cell spiking patterns. *PLoS ONE* **9**:e105633. DOI: https://doi.org/10.1371/journal.pone.0105633, PMID: 25144311

Zhou H, Lin Z, Voges K, Ju C, Gao Z, Bosman LW, Ruigrok TJ, Hoebeek FE, De Zeeuw CI, Schonewille M. 2014. Cerebellar modules operate at different frequencies. *eLife* **3**:e02536. DOI: https://doi.org/10.7554/eLife.02536, PMID: 24843004

Zhou H, Voges K, Lin Z, Ju C, Schonewille M. 2015. Differential purkinje cell simple spike activity and pausing behavior related to cerebellar modules. *Journal of Neurophysiology* **113**:2524–2536. DOI: https://doi.org/10.1152/jn.00925.2014, PMID: 25717166

Zou H, Hastie T. 2005. Regularization and variable selection via the elastic net. *Journal of the Royal Statistical Society: Series B* **67**:301–320. DOI: https://doi.org/10.1111/j.1467-9868.2005.00503.x

Figures and figure supplements

Motor context dominates output from purkinje cell functional regions during reflexive visuomotor behaviours
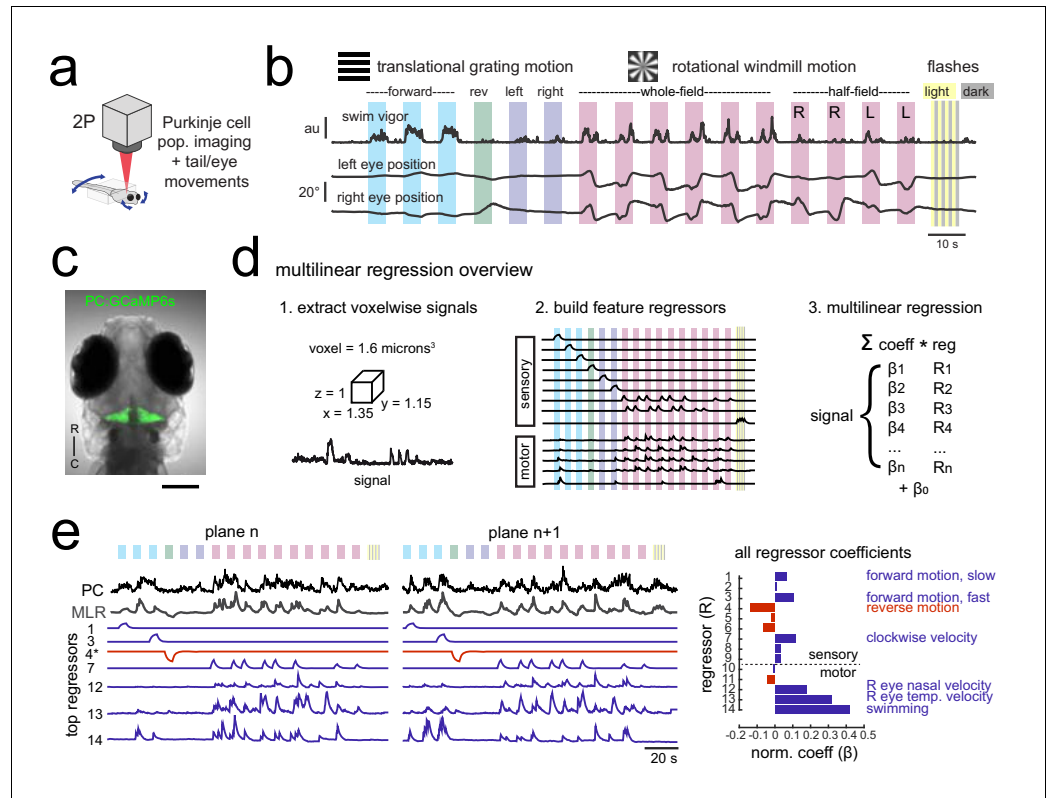
Laura D Knogler *et al*

Figure 1. Using population imaging and multilinear regression to describe feature responses across the Purkinje population during visuomotor behaviors. (a) Cartoon of the embedded zebrafish preparation under the two-photon microscope with freely-moving eyes and tail. (b) Overview of the visual stimuli presented to the awake, behaving zebrafish during volumetric two-photon calcium imaging. See Materials and methods for further details. The mean swimming activity and eye position for a representative fish across an entire experiment is shown (N = 100 trials). (c) Composite bright field image of a seven dpf zebrafish larva from a dorsal view showing Purkinje cells expressing GCaMP6s driven by a ca8 enhancer element. Scale bar = 100 microns. (d) Overview of the multilinear regression analysis. See Materials and methods for additional details and see *Figure 1—figure supplement 1* for full list of regressors. (e) Left panels, example calcium signal from a Purkinje cell across two planes (black trace) can be well recapitulated through multilinear regression (MLR, grey trace; $R^2 = 0.77$). The regressors with the seven largest coefficients (β) are shown below scaled in height and colored by their β value (blue = positive, red = negative). The asterisk for regressor four refers to a negative value of β which results in an inverted regressor. Right, a bar graph quantifying the normalized β values for all regressors for this cell with the regressors shown at left labelled. See also *Figure 1—figure supplements 1* and *2*.

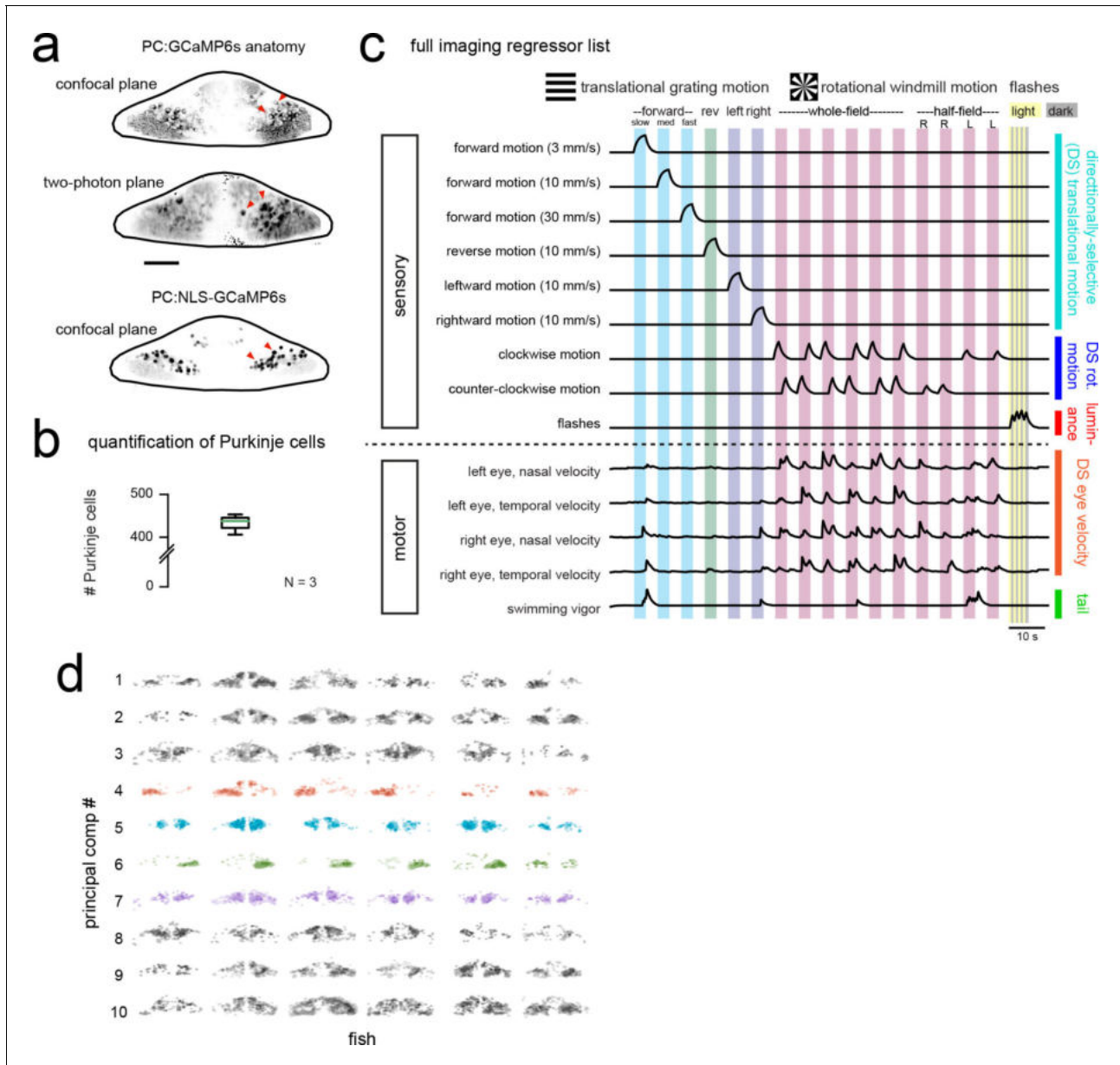DOI: https://doi.org/10.7554/eLife.42138.002

Figure 1—figure supplement 1. Functional imaging anatomy and full regressor list. (a) Single imaging planes showing PC:GCaMP6s fluorescence as obtained from confocal imaging (upper panel) and during two-photon experiments (middle panel). Lower panel, a single confocal imaging plane from a PC:NLS-GCaMP6s fish where GCaMP is restricted to the nucleus. Red arrowheads indicate example Purkinje cell somata. Scale car = 25 microns. (b) Quantification of Purkinje cells in the entire cerebellum at seven dpf as counted in the PC:NLS-GCaMP6s line. N = 3 fish. (c) The complete set of regressors used in analysis of calcium imaging data. Individual regressors fall into one of five categories (three sensory and two motor), as indicated by the categories at right. Tail and eye motor regressors are calculated for each imaging plane based on the motor activity during that trial, therefore a representative example from one trial in the dataset is shown here. See also *Videos 1* and *2* for example imaging trials with the sequence of visual stimuli displayed. (d) Projections of the first ten principal components of Purkinje cell activity in response to experimental stimuli across all fish (N = 6; see Materials and methods), ordered in increasing variance explained. Components that show a high degree of anatomical clustering are colored. Colors are arbitrarily chosen.
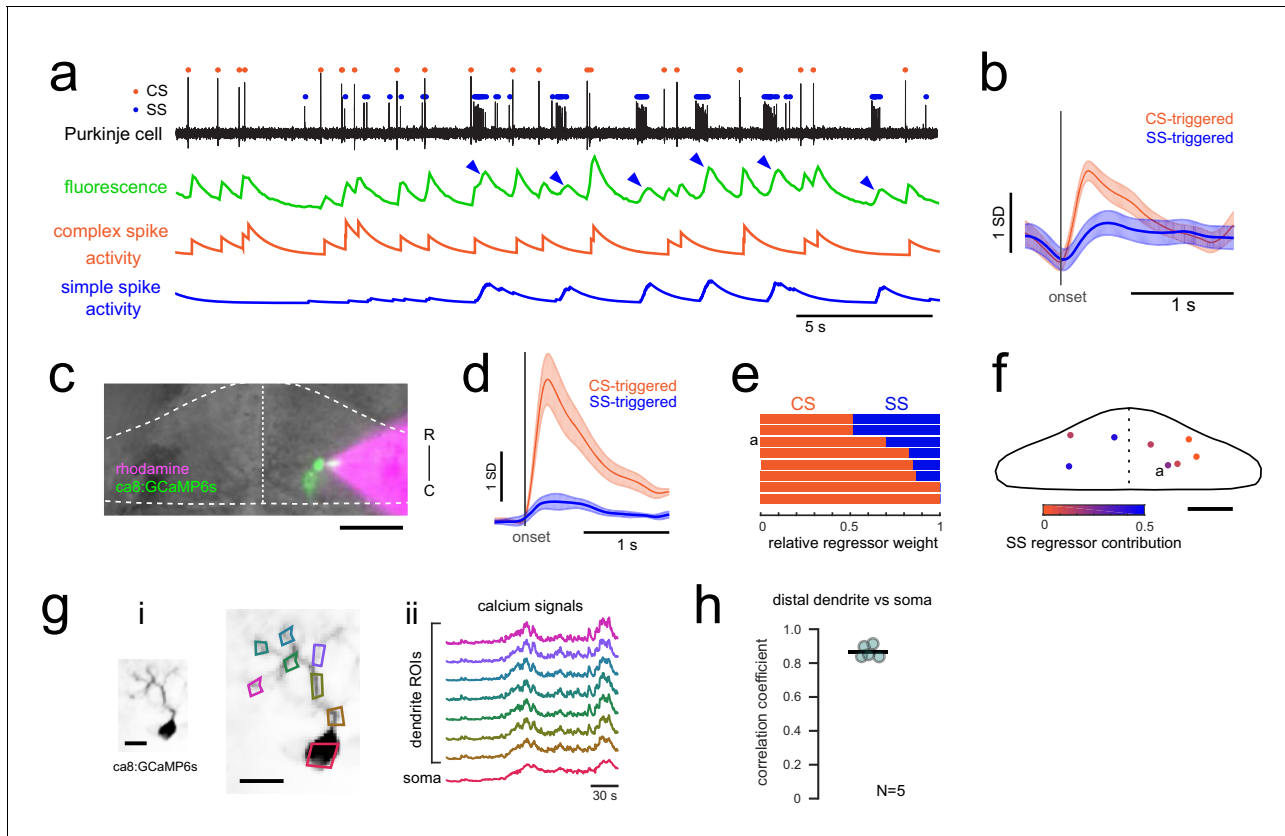
DOI: https://doi.org/10.7554/eLife.42138.003

Figure 1—figure supplement 2. Calcium signals report complex spikes reliably but can also report simple spike bursts. (a) Example cell-attached electrophysiological recording (ephys, black trace) and simultaneously recorded fluorescence trace (green) from a Purkinje cell expressing GCaMP6s under the Purkinje cell-specific ca8 enhancer. All complex spikes (orange dots) are accompanied by an increase in fluorescence as shown as a deflection in the fluorescence trace that accounts for every peak in the complex spike regressor (orange trace, spike rate convolved with GCaMP kernel). In contrast, only high frequency bursts of simple spikes (blue dots) influence the fluorescence signal (indicated by blue arrowheads). (b) The mean spike-triggered fluorescence signal and standard deviation is plotted for the example cell from a) for complex and simple spike bursts (N = 25 each). (c) A composite epifluorescent image showing a bright field dorsal view of the cerebellum together with single-cell GCaMP expression in the Purkinje cell from the previous panels and the rhodamine-filled electrode contacting this cell. The outline and midline of the cerebellum is indicated by the dashed white line. Scale bar = 50 microns. (d) The mean spike-triggered fluorescence signal and standard error is plotted for eight cells (N = 6 fish) for complex and simple spike bursts. (e) The relative contribution of the complex spike (CS) and simple spike (SS) regressors (spike rates convolved with the GCaMP kernel) to the fluorescence signal in each cell as determined by least squares regression (see Materials and methods) across the eight cells. The example cell from a) is indicated. (f) The location of all example cells, color-coded by relative SS regressor contribution. (g) Overview of i) the morphology of a singly-labelled Purkinje cell and the subcellular regions of interest (ROIs) with ii) corresponding calcium signals obtained from high resolution two-photon imaging (see Materials and methods). Scale bars = 20 microns. (h) Quantification of the correlation coefficient between the calcium signal from the most distal dendritic segment and the soma. N = 5 cells from three fish.
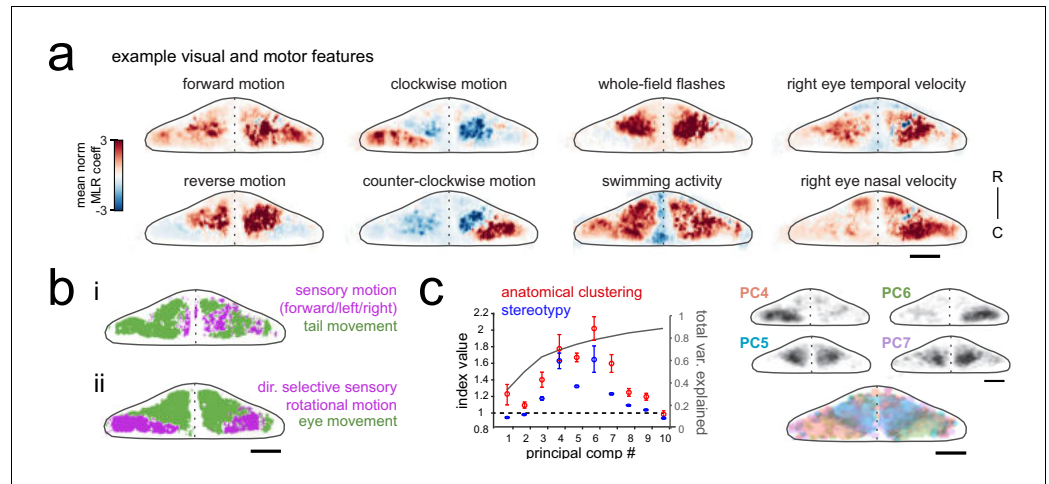
DOI: https://doi.org/10.7554/eLife.42138.007

Figure 2. Purkinje cell activity is functionally clustered across the cerebellum. (a) Heatmaps of the z-projected mean voxelwise correlation coefficients from multilinear regression (MLR) with example sensory and motor regressors for a representative fish (see Materials and methods). Scale bar = 50 microns. (b) Voxels from the example fish in a) are colored according to whether the best regressor for correlated sensory stimuli and motor events (including i) swimming and ii) eye movement) are sensory (magenta), motor (green), or equal/uncorrelated (white). (c) Left, quantification of principal component analysis, clustering, and stereotypy of Purkinje cell responses. Left axis, index values across the first ten principal components with respect to the anatomical clustering of principal components within a fish (red line) and the stereotypy of these clusters across fish (blue line). Dotted black line shows an index value of 1 (equivalent to chance). Right axis, total variance explained across principal components. Right panel, mean spatial mapping of the four principal components with the highest index values for anatomical clustering and stereotypy as individual maps (above) and composite (below). Colors are arbitrarily chosen.
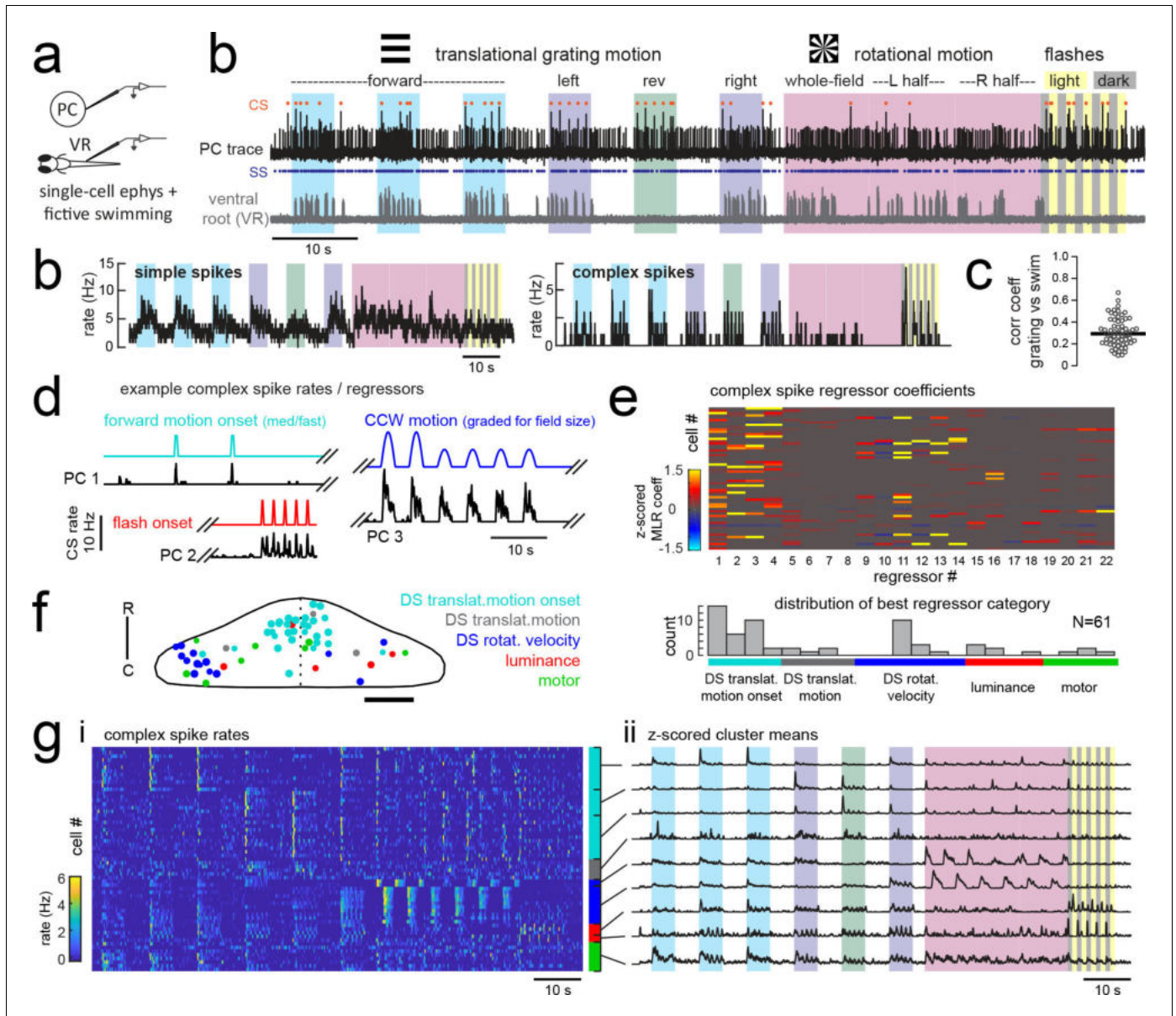
DOI: https://doi.org/10.7554/eLife.42138.006

Figure 3. Electrophysiological recordings from Purkinje cells reveal distinct complex spike responses that can be grouped into four primary response types corresponding to sensory or motor features. (a) Cartoon of the embedded, paralyzed zebrafish preparation used for simultaneous Purkinje cell (PC) electrophysiology with fictive swimming patterns extracted from the ventral root (VR). (b) Example single trial from a cell-attached Purkinje cell (PC) recording (upper trace, black) with simultaneous ventral root recording (lower trace, gray, shown as a moving standard deviation). Complex spikes in the PC are indicated by orange dots above the trace and simple spikes are indicated by blue dots below the trace. Stimuli are color-coded as before (see *Figure 1* and Materials and methods for more details). (b) Left, the mean simple spike (SS) and complex spike (CS) rate for the cell shown in (a) across five trials. Right, the correlation coefficients of forward, left and rightward grating motion with the trial by trial fictive swim activity for all fish. (c) Plot of the correlation coefficient for each fish between the regressor for concatenated swimming activity during moving forward, left, and right gratings across all trials and the summed sensory regressor for forward, left, and right grating motion. The mean is indicated by the black bar. (d) Example mean complex spike rate extracts from three different Purkinje cells showing the temporal similarity of firing dynamics with visual feature regressors. (e) Above, heatmap of coefficient weights for the complex spike firing rates of 61 cells from z-scored least-squares multilinear regression (MLR) with a full set of 24 stimulus- and motor-related variables (see Materials and methods). Below, histogram showing the distribution of cells' highest regressor weight. (f) Location of these cells across all fish mapped onto a reference cerebellum (dorsal view). The color indicates the highest MLR coefficient weight for that cell while the size indicates the degree to which that coefficient contributes to the overall firing rate respective to the others, where the biggest circles = 100%. Scale bar = 50 microns. (g) Left, heatmap of complex spike rates for all 61 cells clustered according to the category of their

Figure 3 continued on next page

Figure 3 continued

highest MLR coefficient weight (e.g. luminance, rotational motion, swimming). Colored bars at right indicate complex spike category as indicated in previous panels. Right, the mean z-scored complex spike rate from each cluster. See also *Figure 3—figure supplements 1* and *2*.
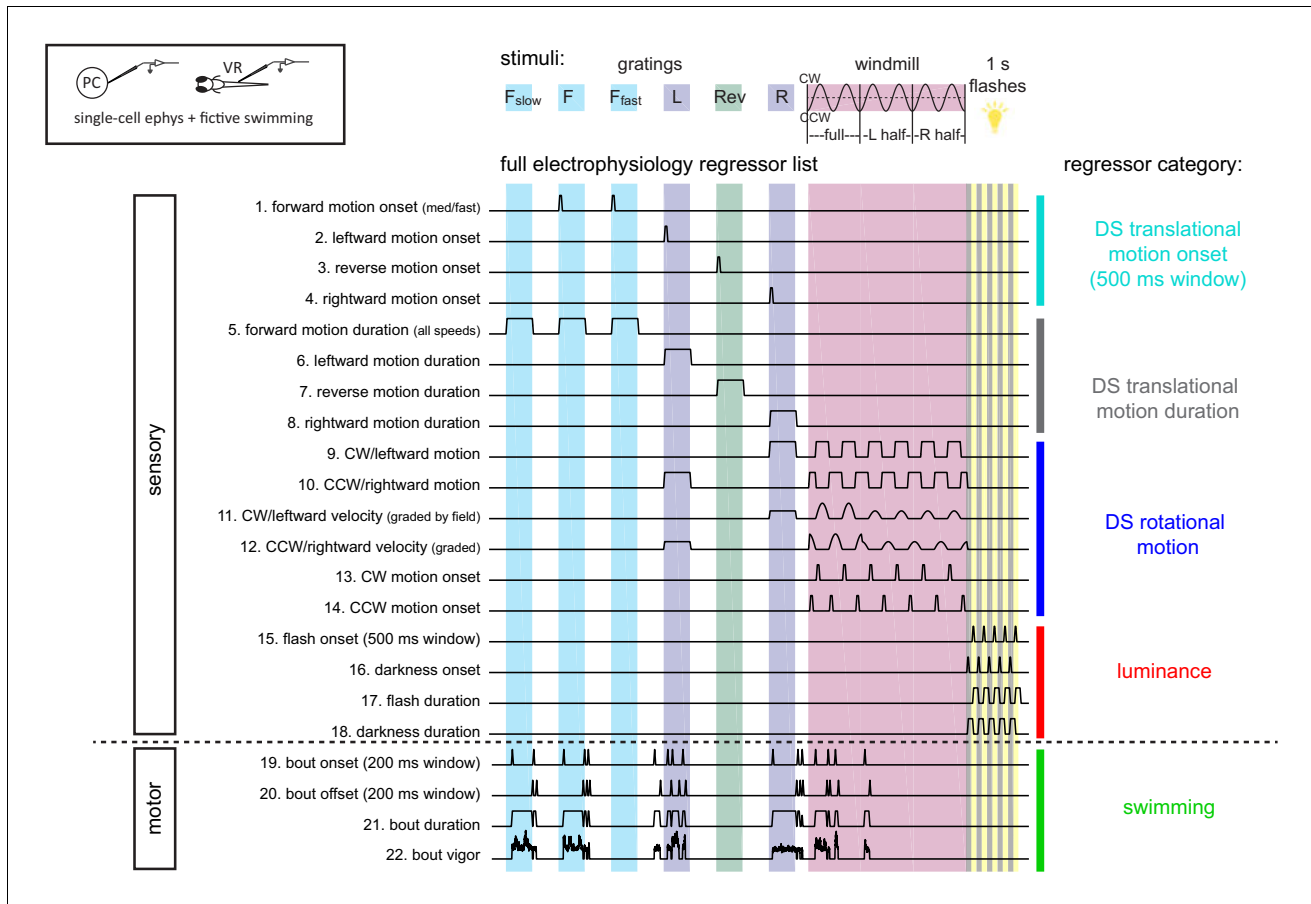
Figure 3—figure supplement 1. Sensory and motor regressors used for multilinear least-squares regression with electrophysiological recordings Top left, cartoon of recording setup. Top center, description of stimuli used in the electrophysiological experiments (see Materials and methods and *Figure 2* for details). Gratings speeds are 10 mm/s with additional slow (F_{slow}, 3 mm/s) and fast (F_{fast}, 30 mm/s) speeds for forward grating stimuli. The windmill stimulus rotated at sinusoidal velocities in the clockwise (CW) and counter-clockwise (CCW) directions with a frequency of 0.2 Hz. Six total periods were shown, with the first two periods being whole-field windmills, the second two periods restricted to the left visual field only, and the final two periods restricted to the right visual field only. Below, the complete set of regressors used in analysis of electrophysiological data. Individual regressors fall into one of five categories (four visual or one motor), as indicated by the colored bars and category names at the right, pertaining to either sensory or motor features as categorized at left. Regressors 19–21 are calculated for each cell based on the motor activity in that trial, therefore a representative example from one trial in the dataset is shown here.
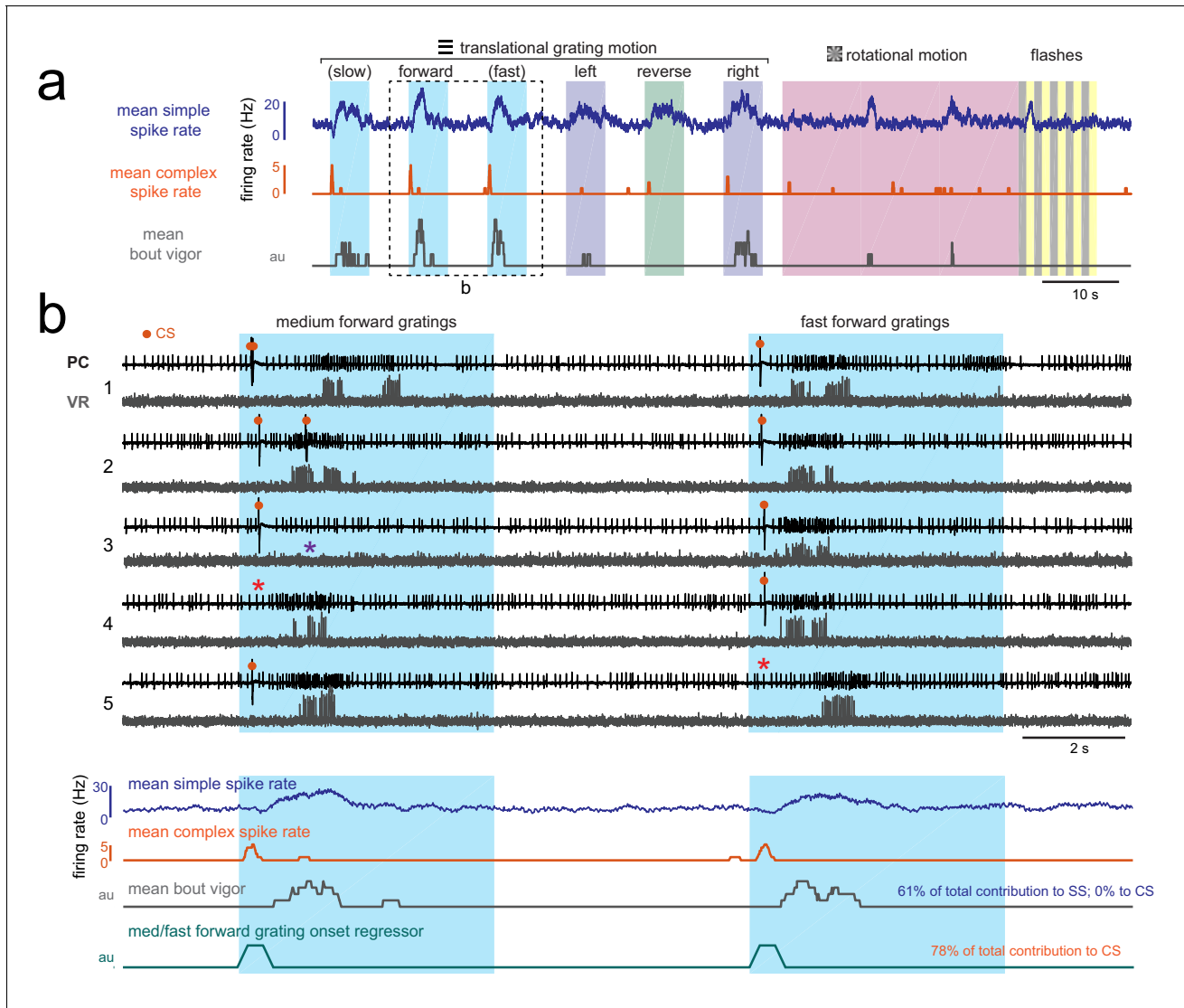
DOI: https://doi.org/10.7554/eLife.42138.010

Figure 3—figure supplement 2. Visually-evoked swimming responses to forward gratings are episodic, vary across trials, and are clearly resolvable from visual responses. (a) Shown is the mean simple spike rate (upper trace, blue), complex spike rate (middle trace, orange), and swim bout vigor (lower trace, grey) across trials for an example fish. The compressed time scale and trial averaging suggests that visual and motor responses to forward-moving gratings may be correlated with each other as well as with both simple and complex spike rates. Multilinear analysis (summarized in text at right) finds however that the coefficient weights for motor regressors are large for simple spike activity across trials while they are zero for complex spike activity. Conversely, direction motion onset regressors for visual motion contribute to the majority of the complex spike activity and to less than 5% of simple spike activity. (b) Upper traces, the boxed area in (a) is shown on an expanded timescale and for five individual trials (numbered at left) in order to better show the temporal structure of neural and behavioral responses to visual stimuli. Excerpts from cell-attached recordings from this Purkinje cell (PC) and simultaneous ventral root (VR) show reliable complex spikes elicited at visual motion onset and swim bouts of varying durations and strength evoked at different latencies (up to two seconds) from visual stimulus onset. Note that trials occur where the visual stimulus can fail to elicit a complex spike (red asterisks) or a bout (purple asterisk). Lower traces, the average traces from these stimuli are also shown on an expanded timescale to drive home the point that although average activity may look correlated, the variability of visually-evoked behaviors across trials allows multilinear regression to clearly separate visual and motor responses in simple spike and complex spike activity. The forward motion onset regressor, which captures spiking responses in the 500 ms window following visual stimulus onset, is also shown for comparison.
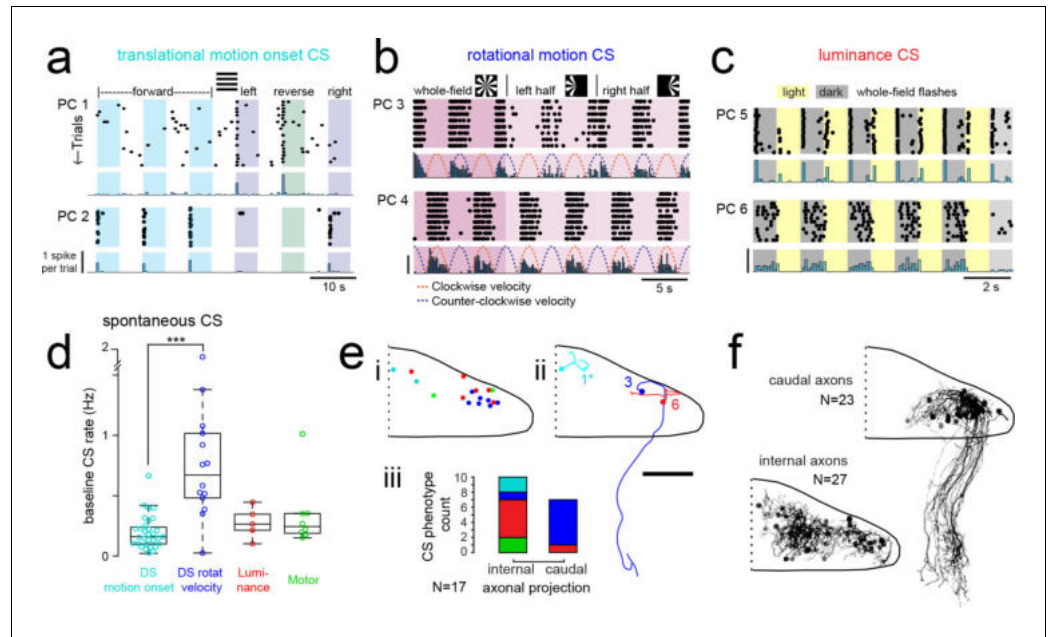
DOI: https://doi.org/10.7554/eLife.42138.011

Figure 4. Purkinje cells in different regions show complex spike responses that encode different visual features and one group sends outputs to a different downstream region. (a) Raster plot (upper left panels) and histogram (lower left panels, 500 ms bins) of complex spikes occurring across trials during translational whole-field motion of black and white bars in all four cardinal directions for two example Purkinje cells (PC). Numbers assigned to PCs for this and panels b-c are arbitrary. (b) Raster plot (upper left panels) and histogram (lower left panels, 100 ms bins) of complex spikes occurring across trials during whole- and half-field bidirectional rotational motion of a black and white windmill for an example cell. The dashed lines over the histogram show the velocity of the stimulus in each direction across the trial. (c) Raster plot (upper left panels) and histogram (lower left panels, 100 ms bins) of complex spikes occurring across trials during whole-field light/dark flashes for two example cells, (i) and ii). (d) A box plot of complex spike firing rates during blank trials (no visual stimuli) for cells grouped by their sensory or motor complex spike category (see *Figure 2*). N = 31, 14, 5, 8. Asterisks indicate significance (one-way ANOVA with Bonferroni post hoc correction, p<0.001). j (i) The location of cells colored by complex spike phenotype are plotted onto a flattened dorsal view of the cerebellum with all coordinates flipped to the right half of the cerebellum. e (ii) Three example maximum projection images of traced axonal morphology from stochastically-labelled, Fyn-mClover3-expressing Purkinje cells for which electrophysiological recordings were also obtained. Labels for each cell refer to the electrophysiological traces in panels a-c. The asterisk for cell a) indicates that these coordinates were flipped to the right half of the cerebellum. Scale bar = 50 microns. e (iii) Categorical grouping of complex spike phenotypes for internal versus caudal axonal projections. N = 17 cells from 17 fish. (f) Morphed Purkinje cell axonal morphologies from single-cell labelling across fish (N = 50 cells) can be grouped into two populations based on axonal projection (as for e iii). N = 27 cells with internal axons, N = 23 cells with caudal axons. See also *Figure 4—figure supplement 1*.
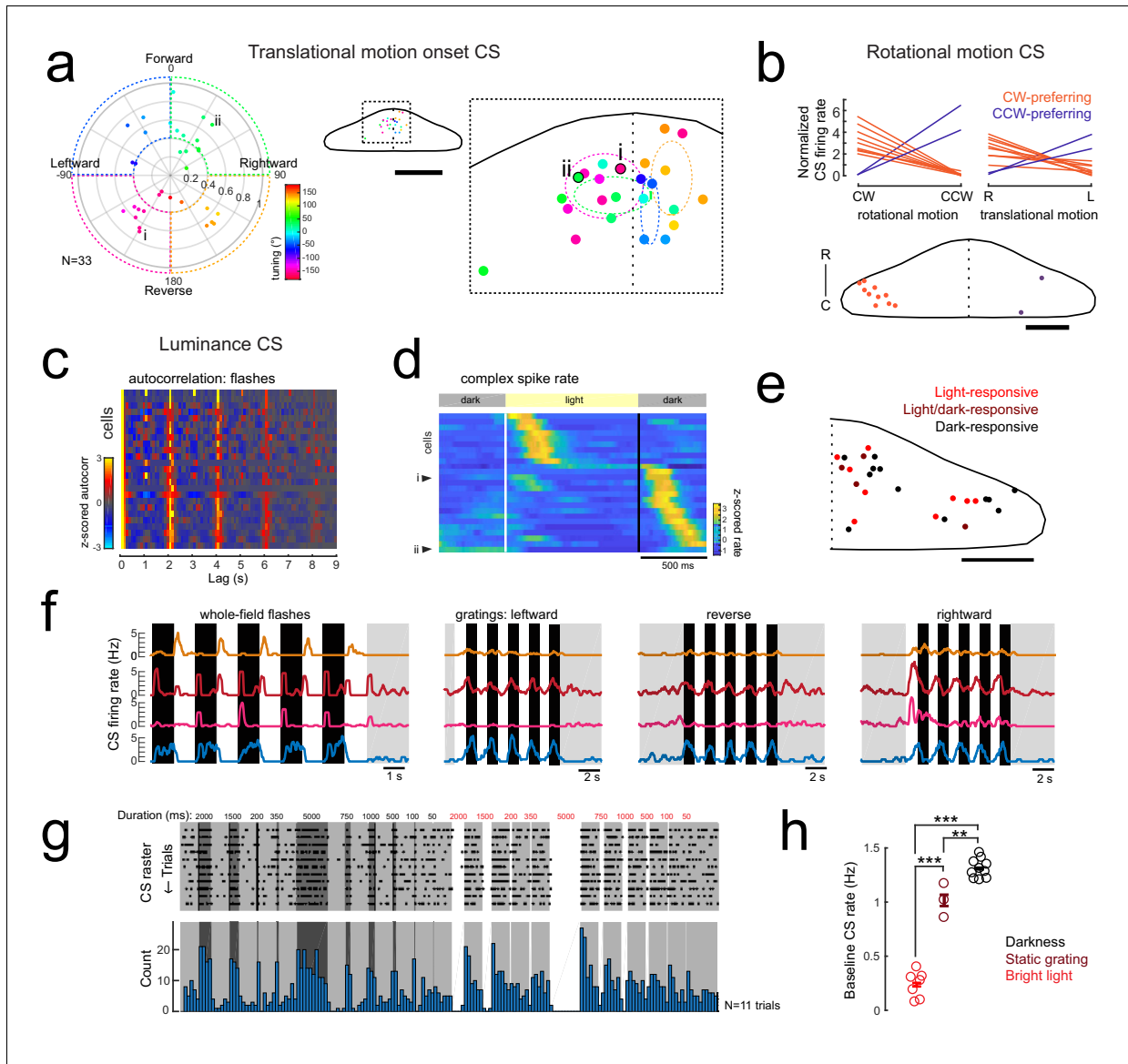DOI: https://doi.org/10.7554/eLife.42138.012

Figure 4—figure supplement 1. Complex spike responses encode specific aspects of visual features. (**a**) Left, polar plot of all Purkinje cells with a significant contribution to complex spike activity from the onset of translational motion in a given direction (N = 33/61 cells). The tuning of the cells is indicated by the polar coordinates as well as the marker color, with 0° indicating forward motion. The distance from the center indicates the direction selectivity index of the cell (see Materials and methods). Dashed areas indicate the four quadrants used for binning. Right, the location of all cells with this complex spike phenotype within the quadrants are plotted onto a flattened dorsal view of the cerebellum (example cells i and ii from *Figure 3a* are indicated and outlined in black). The overview shows the zoomed-in region of the rostromedial cerebellum. Colors indicate tuning preference as shown at left. Dotted ellipses indicate the boundary for the mean location and SEM for each group of similarly tuned cells. Scale bar = 100 microns for overview, 500 microns for cropped zoom. (**b**) Upper plots, the mean complex spike firing rate (normalized to baseline, dotted black line) of all Purkinje cells with significant coefficient weights for rotational motion regressors (N = 11) is shown for both the duration of rotational motion in a given direction (left plot) and the duration of leftward and rightward translational motion (right plot). Two distinct groups are clearly seen that prefer either clockwise and rightward motion (orange lines) or counter-clockwise and leftward motion (blue lines). Lower panel, the location of all cells with this complex spike phenotype are plotted onto a flattened dorsal view of the cerebellum. Colors indicate rotational motion preference. Scale bar = 50 microns. (**c**) Left, all luminance-responsive cells as determined by significant autocorrelation values for whole-field flashes for the 2 s lag (N = 25/61) are plotted in a heat map sorted by maximum autocorrelation value for the 2 s lag. Cells are ordered by peak autocorrelation at 2 s. (**d**) Z-scored complex spike firing rates for all luminance-responsive Purkinje cells averaged across flash repetitions and sorted by the timing of their peak firing rate are shown as a heatmap. Black lines mark the transition from dark to light and back again as indicated by the grey bars above. Example cells from *Figure 3c* are indicated. N = 25 cells. (**e**) The location of all cells with a luminance complex spike phenotype are plotted onto a flattened dorsal view of the cerebellum with all

Figure 4—figure supplement 1 continued on next page

Figure 4—figure supplement 1 continued

coordinates flipped to the right half of the cerebellum. Colors indicate the preference for light or dark flashes (or both). Scale bar = 50 microns. (**f**) Four example Purkinje cell mean complex spike firing rates in response to whole-field flashes (left) and three directions of moving gratings (right) show different responses to global versus local luminance changes. (**g**) Additional recordings from a luminance-responsive Purkinje cell (see *Figure 3cii*) during the presentation of whole-field black (here shown as dark grey) and white flashes of various durations (50–5000 ms) from a baseline intermediate luminance (light grey). Upper panel, raster plot of complex spikes across trials (N = 11). Lower panel, complex spike count histogram. This cell produces has a clear sustained increase in complex spike activity during darkness whereas complex spike activity is nearly absent during bright flashes. (**h**) Quantification of the baseline complex spike firing rate of the cell in g) in the absence of changing visual stimuli for periods of tens of minutes for three different whole-field luminance levels. Three asterisks indicate $p < 0.001$ and two indicate $p < 0.01$ as calculated by one-way ANOVA with Bonferroni post hoc correction.
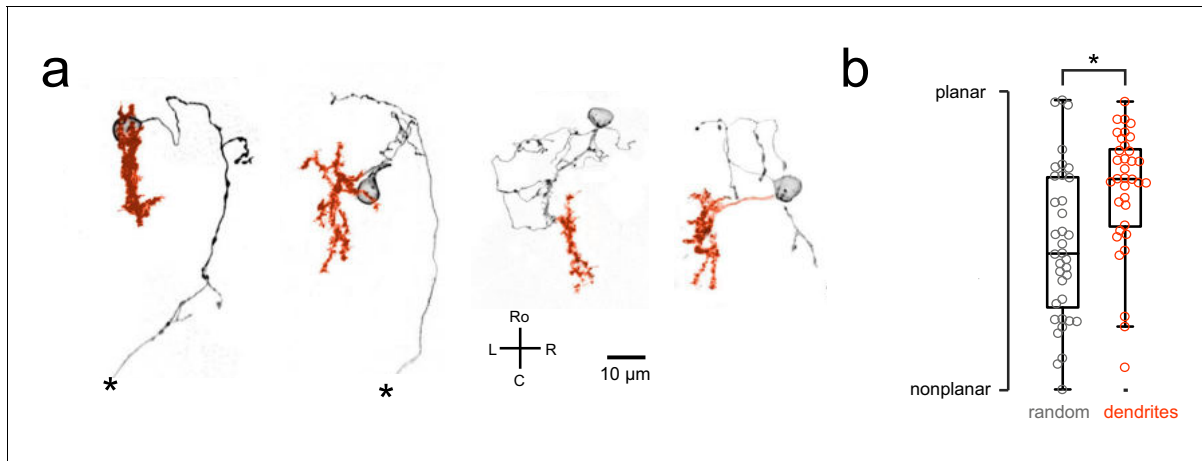
DOI: https://doi.org/10.7554/eLife.42138.013

Figure 4—figure supplement 2. Purkinje cell dendrites show a mostly planar morphology. (a) Four example Purkinje cell morphologies obtained by single-cell labeling (see Materials and methods) are shown with their soma and axon in black and dendrites in orange. Asterisks indicate a truncated axon. (b) Quantification of dendritic morphology as measured by determining the principal axes (see Materials and methods) shows that dendrites are significantly more planar than chance (p<0.01, Wilcoxon signed rank test).

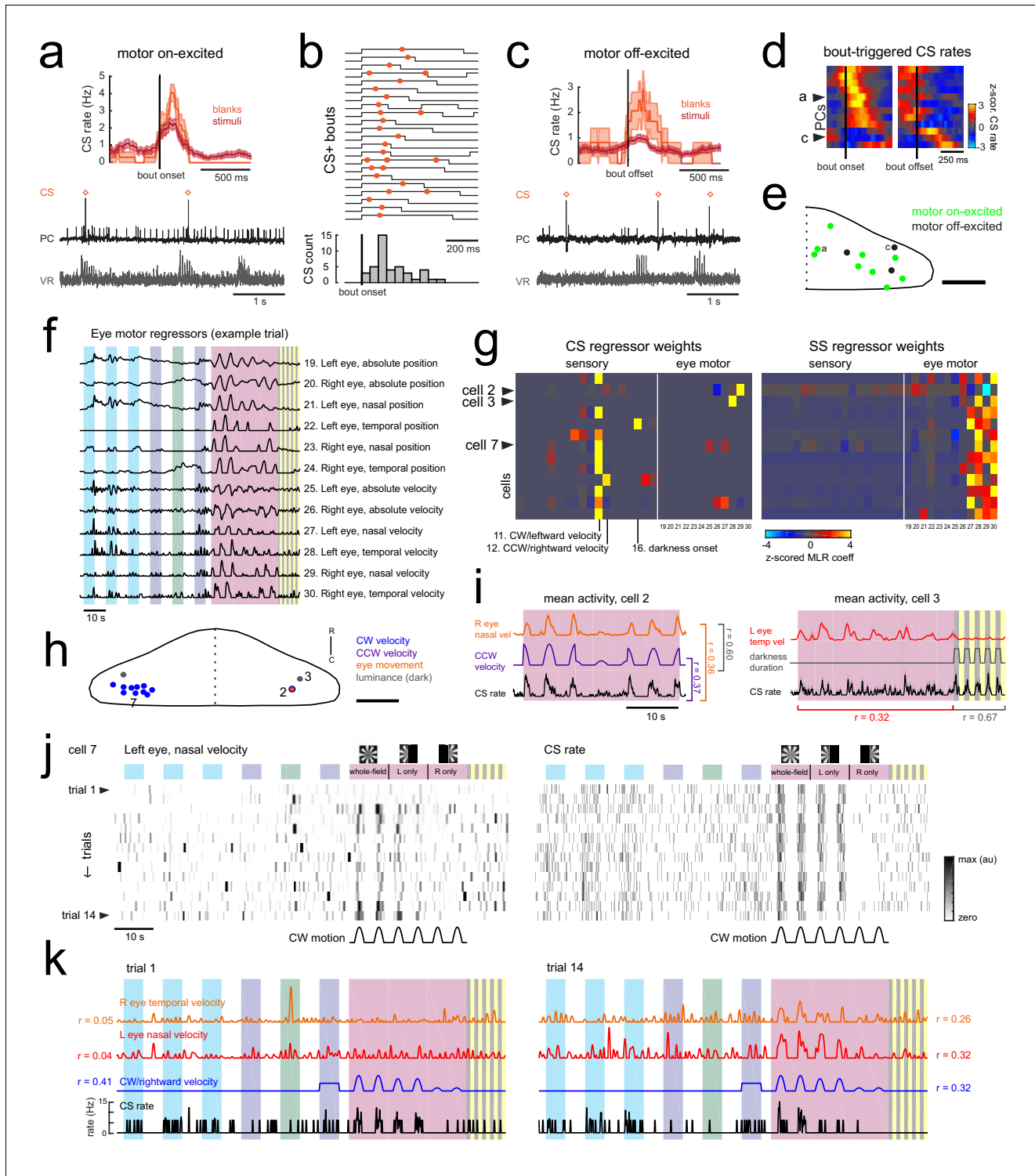**Figure 4—figure supplement 3.** Motor-related complex spikes are rare. (**a**) Upper plot, the mean bout-triggered complex spike rate with shaded SEM for this cell for all swim bouts during the blank recordings (no stimuli presented, orange trace) and during trials with visual stimuli (red trace). N = 16 bouts (blanks), 76 bouts (stimuli). Lower traces, example excerpt from a blank recording from this Purkinje cell (PC, black trace) with simultaneous ventral root recording (VR, gray trace, shown as a moving standard deviation). Complex spikes are indicated by orange dots above the trace. (**b**) Upper traces, a subset of bouts are plotted aligned to bout onset for swim episodes during which a complex spike (orange dot) occurred. Below, a normalized histogram for all CS-positive bouts in this recording show that the majority of the complex spikes are triggered in the period 100–150 ms following bout

Figure 4—figure supplement 3 continued on next page

Figure 4—figure supplement 3 continued

onset (N = 34/76 CS-positive bouts). (**c**) Upper plot, the mean bout off-triggered complex spike rate with shaded SEM for this cell for blank and visual stimuli trials. N = 12 bouts (blanks), 468 bouts (stimuli). Lower traces, example excerpt from a blank electrophysiological recording from this cell. (**d**) Heatmap of bout on- and off-triggered mean complex spike rates for all cells with significant motor coefficients arranged by peak CS firing rate from bout onset. The lower three rows correspond to cells that have a decrease in CS activity during bouts which increases following bout offset. The example cells from a) and c) are indicated. (**e**) The locations of these Purkinje cells with CS activity correlated with bout onset (green) or bout offset (black) are plotted on the right lobe of a reference cerebellum (some coordinates were flipped from left to right). The example cells from a) and c) are indicated. Scale bar = 50 microns. (**f**) The 12 eye motor regressors used for multilinear least squares regression (MLR) of electrophysiological data with eye movements in the semi-paralyzed zebrafish (see Materials and methods for details; see *Figure 1—figure supplement 2* for the description of sensory regressors). All eye motor regressors are calculated for each cell based on the motor activity of each eye (tracked independently) in that trial. A representative set of regressors computed from eye movement in one trial in the dataset is shown here. (**g**) Heatmap of all 30 regressor coefficient weights (18 sensory and 12 eye motor) for the complex spike (left) and simple spike (right) firing rates of 13 cells (N = 11 fish). The sensory regressors with the largest coefficient weights for complex spike rates are indicated. For complex spike phenotypes, 11/13 Purkinje cells have a stronger 'sensory' phenotype, whereas 13/13 Purkinje cell have a simple spike 'motor' phenotype. The two remaining Purkinje cells with a motor complex spike phenotype are indicated as ci and cii (arrowheads). (**h**) Location of all cells, color-coded for complex spike phenotype as determined by MLR and additional analyses (see subsequent panels). Scale bar = 50 microns. (**i**) Left, mean activity and SEM for the complex spike rate and best eye movement regressor excerpted from the rotational stimulus portion of the experiment for Purkinje cell two as indicated in g) and classified as having a motor complex spike phenotype. The single correlation coefficient between the best motor and sensory regressors across trials are very high (r = 0.60 across the full trial). Right, mean activity and SEM for the complex spike rate and best eye movement regressor excerpted from the rotational stimulus and flash portion of the experiment for Purkinje cell three as indicated in b) and the only other cell classified as having a 'motor' complex spike phenotype. The single correlation coefficient values for the complex spike rate with the indicated regressors across trials for just the rotational stimulus period or just the luminance period are shown. (**j**) Heatmap of eye movement (left eye, nasal) and complex spike rates across all trials of an experiment for a representative Purkinje cell in the left caudolateral cerebellum (cell seven as indicated in g,h). Note the variability of the eye movement across trials (left) compared to the complex spike rate (right). Clockwise velocity is indicated for reference. (**k**) The best motor regressors for each eye and the best sensory regressor are plotted against the complex spike rate of the cell in j) for the first (left) and last (right) trial of the experiment. Single correlation coefficient values are shown between each regressor and the complex spike rate for this trial. Time scale is same as for j).
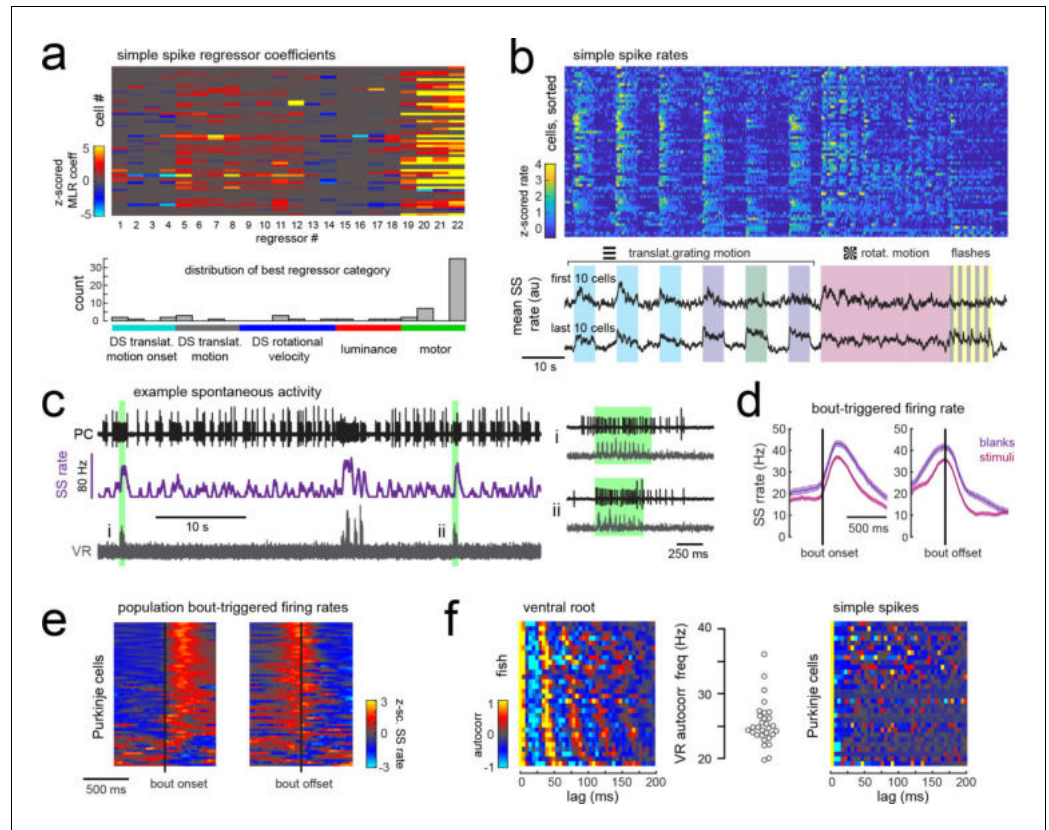
DOI: https://doi.org/10.7554/eLife.42138.015

Figure 5. Simple spike rates in most Purkinje cells are increased during fictive swimming. (a) Above, heatmap of coefficient weights for the simple spike firing rates of 61 cells from least-squares regression with a full set of 24 stimulus- and motor-related variables (see Materials and methods for more details). Below, histogram showing the distribution of cells' highest regressor weight and the associated sensory/motor categories. (b) Upper panel, heatmap of z-scored simple spike rates for all 61 cells sorted by decreasing motor coefficient weight. Lower panel, the mean simple spike rate for the ten cells with the highest (upper trace) and lowest (lower trace) motor coefficient weights. (c) Left panel, example cell-attached Purkinje cell recording (PC, upper trace, black) from a blank trial (no stimuli) with simultaneous ventral root recording (VR, lower trace, gray, shown as a moving standard deviation). The simple spike rate is also shown (SSrate, middle trace, purple). Right, the bouts highlighted in green on an expanded timescale show the close timing of fictive bout onset and simple spike activity. (d) The bout on- and off-triggered mean simple spike firing rates for the cell in c) during blank recordings (purple) and stimulus trials (pink). (e) Z-scored heatmap of bout on- and off-triggered mean simple spike firing rates across all Purkinje cells sorted by mean firing rate in the 300 ms following bout onset. (f) Mean autocorrelation heatmap for simple spikes (SS, upper panel) and for ventral root recordings (VR, lower panel) for all Purkinje cells that showed spontaneous swimming bouts during blank trials (N = 30 cells from 30 fish), sorted by time to first peak in the VR autocorrelation. Right, the first significant peak in the VR autocorrelation for each recording is plotted to give the mean fictive swim frequency for each fish.
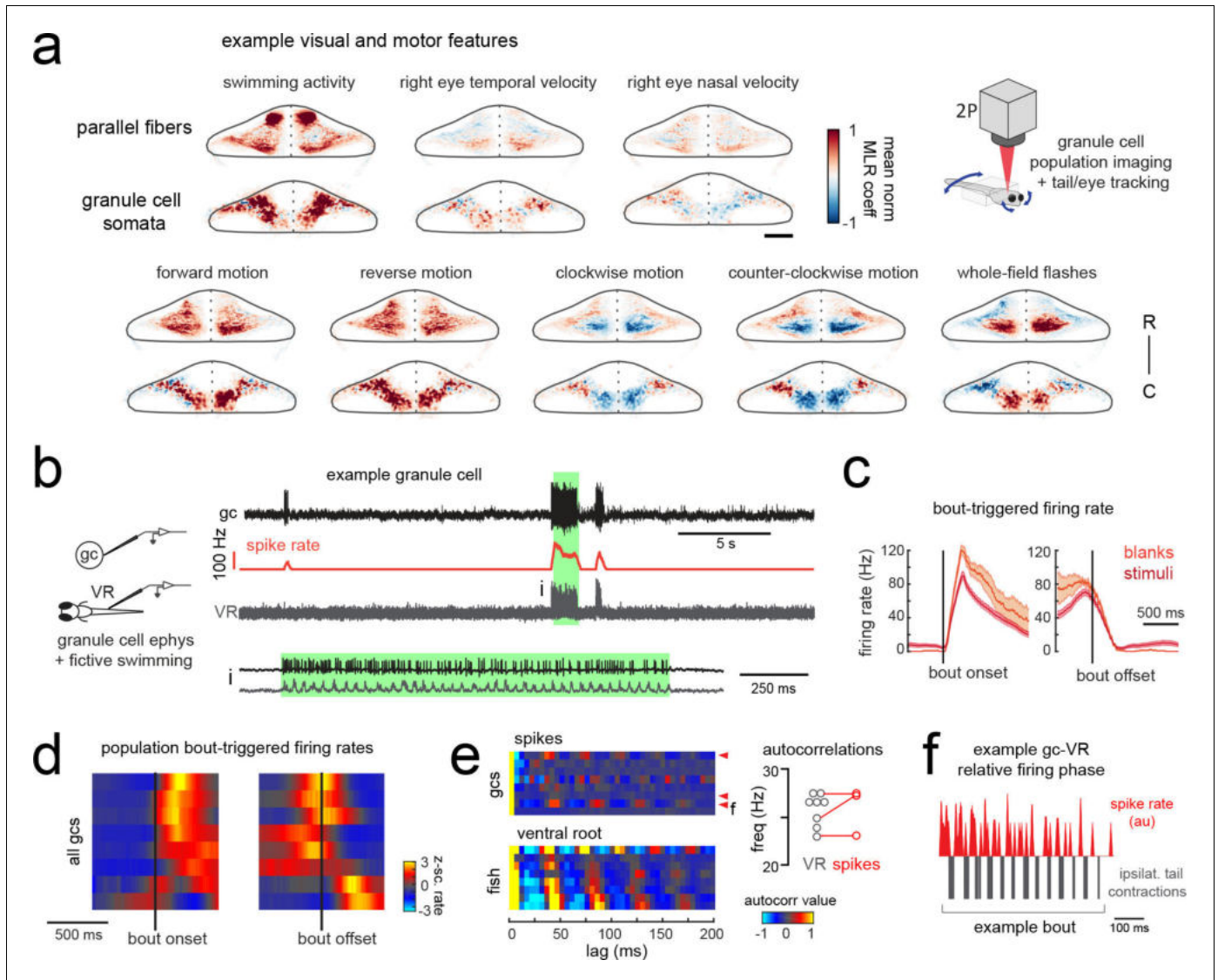
DOI: https://doi.org/10.7554/eLife.42138.016

Figure 6. Granule cells across the cerebellum code for motor activity with high fidelity. (a) Heatmaps of the z-projected mean voxelwise correlation coefficients of two-photon granule cell GCaMP6s signals from multilinear regression with example sensory and motor regressors averaged across seven fish (see Materials and methods). Scale bar = 50 microns. Upper right, cartoon of experimental set-up. (b) Left, cartoon of experimental set-up. Right, upper panel, example cell-attached recording from a granule cell (gc, upper trace, black) from a blank trial with simultaneous ventral root recording (VR, lower trace, gray). The granule cell firing rate is also shown (spike rate, middle trace, orange). The bout highlighted in green (i) is shown below on an expanded timescale. (c) The bout on- (left) and off- (right) triggered mean firing rates for this granule cell during blank recordings (orange) and stimulus trials (red). (d) Z-scored heatmaps of bout on- (left) and off- (right) triggered mean firing rates in all granule cells sorted by mean firing rate in the 300 ms following bout onset (N = 8 cells from eight fish). (e) Mean autocorrelation heatmap for spikes (upper panel) and ventral root recordings (VR, lower panel) for all granule cells from d), sorted by time to first peak in the VR autocorrelation. The red arrowheads signify granule cells with significant spike autocorrelations during fictive swim bouts (N = 3; p<0.001, Ljung-Box Q-test; see Materials and methods). Right, the first significant peak in the VR autocorrelation for each recording is plotted to give the mean fictive swim frequency for each fish. The red circles are the mean spike autocorrelation frequency obtained from the three significantly autocorrelated granule cells. (f) An example bout from the cell indicated in e), which was located ipsilateral to the ventral root recording. The smoothed spike rate (red) is in antiphase with the ipsilateral fictive tail contractions (grey). See also *Figure 6—figure supplement 1*.
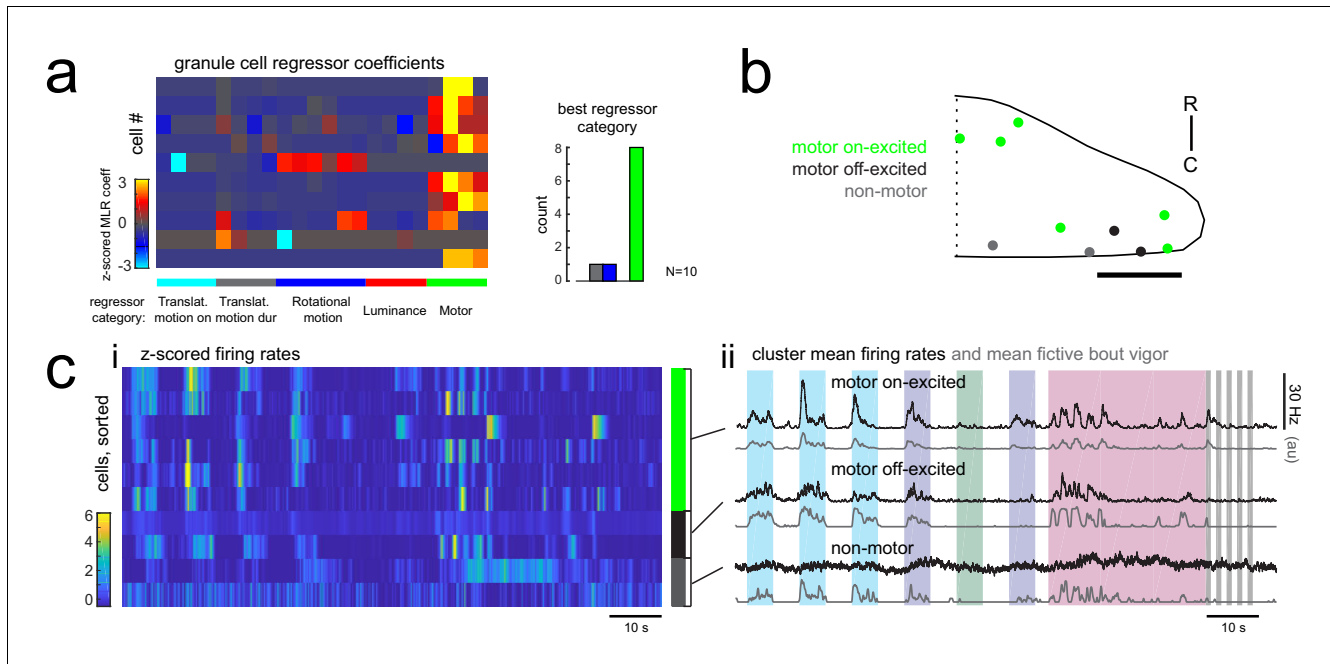
DOI: https://doi.org/10.7554/eLife.42138.017

Figure 6—figure supplement 1. Many granule cells show significant modulation of their firing rates during fictive swimming bouts. (a) Left, matrix of multilinear regressor coefficients for granule cell firing rates from all 10 cell-attached electrophysiological recordings with simultaneous fictive behavior in response to the same sensory stimuli as shown in *Figure 2a*. Right, histogram of cell counts for each best regressor category (as color-coded at left). (b) Location of granule cells across all fish mapped onto a reference cerebellum (dorsal view) and colored according to their motor phenotype. All coordinates are flipped onto the right hemisphere. Scale bar = 50 microns. (c) Left, heatmap of z-scored mean firing rates for all granule cells sorted by decreasing motor regressor coefficient. Colored bars at right indicate cells whose firing rate is positively modulated by bout duration (green), by bout offset (black), or by neither (grey). Right, cluster mean granule cell firing rates (black) and mean fictive bout vigor (grey).
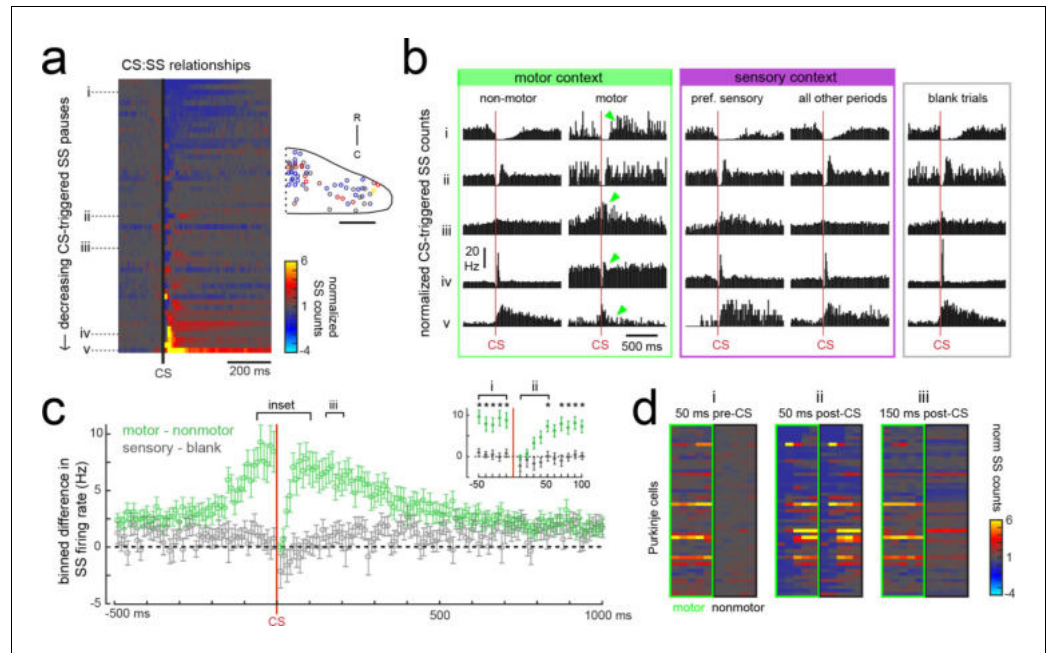DOI: https://doi.org/10.7554/eLife.42138.018

Figure 7. Purkinje cells modify their simple spike output in a complex spike- and motor context-dependent way. (a) Heatmap of complex spike-driven simple spike (CS:SS) counts for each cell normalized to the mean over 100 ms preceding a complex spike. Cells are sorted by decreasing simple spike pause and increasing excitation. The inset shows the location of these cells colored by the normalized difference in simple spiking in the 50 ms following the CS. (b) The mean complex spike-triggered simple spike count (10 ms bins) is shown for five example cells (as indicated in a) for five different contexts. Left (green box), in the presence ('motor') versus absence ('non-motor') of fictive swimming episodes. Under non-motor conditions these different Purkinje cells show, respectively, a CS-induced i) long SS pause, ii) short SS pause with rebound increase, iii) no change in SS, iv) short SS increase, and finally a v) long SS increase. Green arrows highlight changed patterns during motor context. Middle (magenta box), CS:SS relationships across preferred versus all other sensory contexts (only non-motor periods included). Right (grey box), the CS:SS relationship during blank trials (no stimuli, only non-motor periods). Vertical scale bar indicates the rate conversion for 0.2 spikes/10 ms bin (20 Hz). (c) Green markers show the mean normalized simple spike rates (calculated from 10 ms bins) for all Purkinje cells centered on the occurrence of a complex spike during a fictive bout minus those occurring at any other point (N = 51 cells). Data are mean ± SEM. Grey markers, simple spike rates centered on the occurrence of a complex spike during all sensory stimuli minus those occurring during blank trials (N = 53 cells). The dashed black line indicates zero difference between conditions. Inset, the window around complex spike onset shown on an expanded timescale. Asterisks indicate p<0.05 for motor minus nonmotor conditions (green markers) as computed by the Wilcoxon signed rank test. Grey markers, no significant differences. (d) Heat maps are shown for individual Purkinje cell binned simple spike counts over the three different 50 ms periods as indicated in e). Complex-spike triggered simple spike counts are separated for each cell for those complex spikes occurring during a fictive bout (left column of heatmaps, outlined in green) or at any other time (right column of heatmaps, outlined in black).
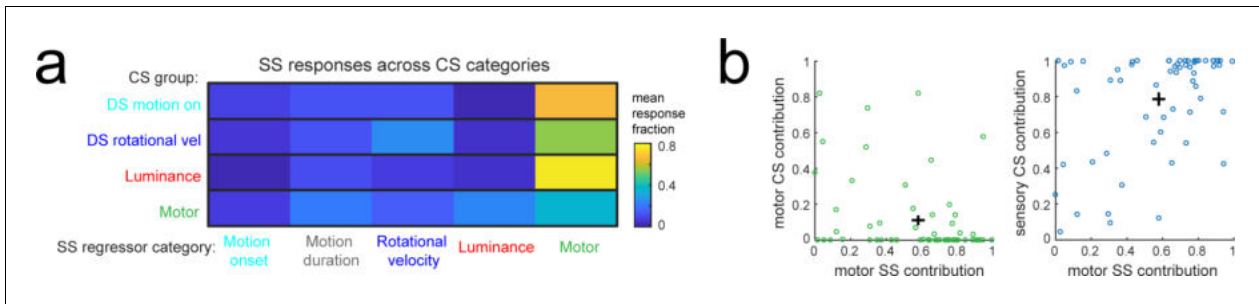
Figure 7—figure supplement 1. Individual Purkinje cells preferentially combine sensory and motor information. (a) The mean fraction of the simple spike (SS) response contributed by each regressor computed for each of the four Purkinje cell complex spike (CS) groups. (b) Left, scatterplot of the fraction of complex spike versus simple spike activity accounted for by motor regressors. Right, the fraction of simple spike activity accounted for by motor regressors versus the fraction of complex spike activity accounted for by all sensory regressors.
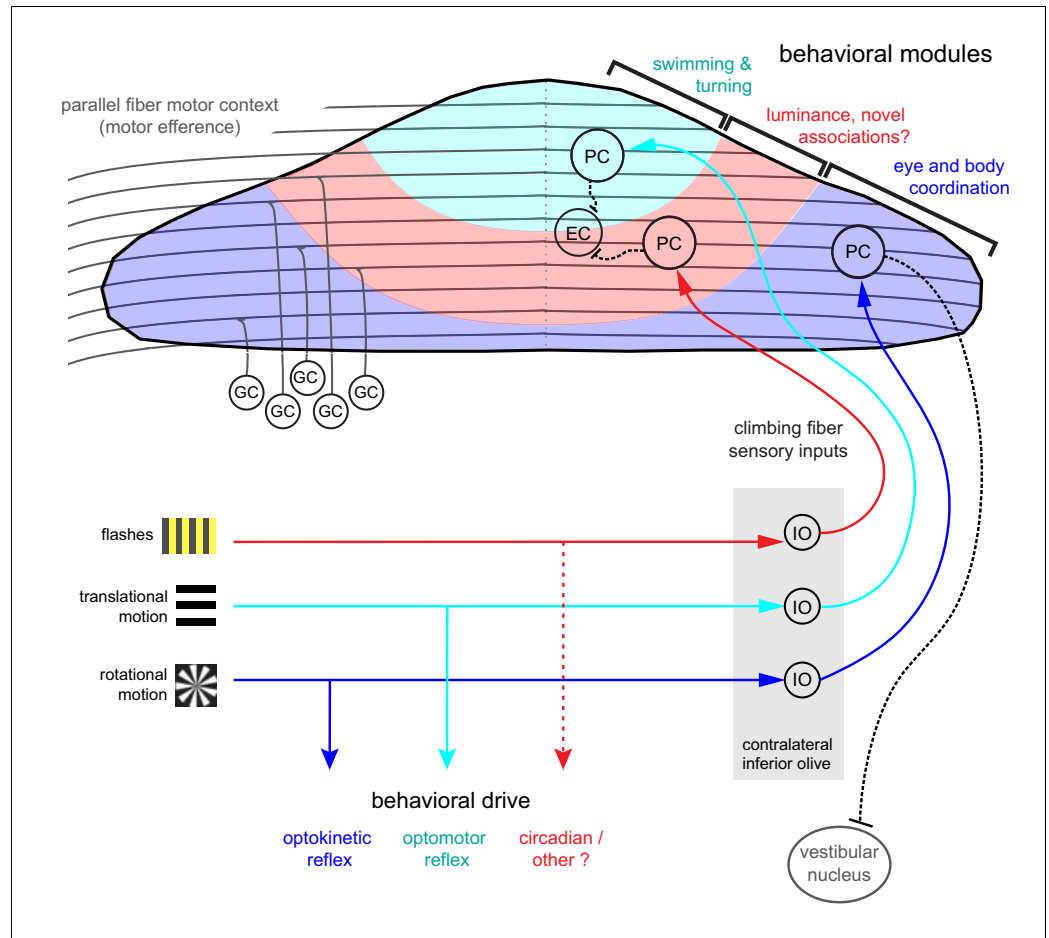
DOI: https://doi.org/10.7554/eLife.42138.020

Figure 8. Organization of the larval zebrafish cerebellum Granule cells (GCs) send long parallel fibers (grey lines) that contact Purkinje cells (PCs) across the cerebellum and broadly relay motor efference copies of locomotor activity (swimming). Sensory information relating to different visual features are sent by climbing fibers of inferior olive neurons (IO) to stereotyped regions of the contralateral Purkinje cell layer. These visual stimuli contribute to several reflexive behaviors; rotational motion drives the optokinetic reflex of the eyes, translational forward motion drives the optomotor swimming reflex while others, such as luminance, may drive behavior over longer (e.g. circadian) timescales. The three distinct functional regions in the zebrafish cerebellum defined by Purkinje cell complex spike sensory responses that encode these different visual features represent putative behavioral modules. Information about the onset of directional translational motion is preferentially sent to PCs in the rostromedial region of the cerebellum (cyan) and would be important for coordinating turning and swimming, while information about the direction and velocity of rotational motion as would be needed for coordinating eye and body movements is sent to the caudolateral region (blue). The central region (red) receives information about luminance and may provide a substrate for learned sensorimotor associations. Axons from PCs (black dashed lines) of the rostromedial and central regions have mostly internal axons that contact eurydendroid cells (EC) within the cerebellar cortex. Axons from PCs in the caudolateral region have mostly external axons that exit the cerebellum and contact neurons in the caudally-located ipsilateral vestibular nucleus.
DOI: https://doi.org/10.7554/eLife.42138.021